Title

The Saga of Light-Matter Interaction and Magneto-optical Effects. Applications to Atomic Magnetometry, Laser-cooled Atoms, Atomic Clocks, Geomagnetism, and Plant Bio-magnetism

Permalink

https://escholarship.org/uc/item/1z04r0xj

Author

Corsini, Eric P.

Publication Date

2012

Peer reviewed|Thesis/dissertation

The Saga of Light-Matter Interaction and Magneto-optical Effects
Applications to Atomic Magnetometry,
Laser-cooled Atoms, Atomic Clocks,
Geomagnetism, and
Plant Bio-magnetism

by

Eric P. Corsini

A dissertation submitted in partial satisfaction of the

requirements for the degree of

Doctor of Philosophy

in

Physics

in the

Graduate Division

of the

University of California, Berkeley

Committee in charge:

Professor Dr. hab. Wojciech Gawlik, Co-Chair
Professor Dmitry Budker, Co-Chair
Professor Eugene D. Commins
Professor Grigory Isaakovich Barenblatt
Professor Holger Müller

Spring 2012

The Saga of Light-Matter Interaction and Magneto-optical Effects

Applications to Atomic Magnetometry,
Laser-cooled Atoms, Atomic Clocks,
Geomagnetism, and
Plant Bio-magnetism

by

Eric P. Corsini

Abstract

The Saga of Light-Matter Interaction and Magneto-optical Effects

Applications to Atomic Magnetometry,
Laser-cooled Atoms, Atomic Clocks,
Geomagnetism, and
Plant Bio-magnetism

by

Eric P. Corsini

Doctor of Philosophy in Physics

University of California, Berkeley

Professor Dr. hab. Wojciech Gawlik, Co-Chair

Professor Dmitry Budker, Co-Chair

The quest to expand the limited sensorial domain, in particular to bridge the inability to gauge magnetic fields near and far, has driven the fabrication of remedial tools. The interaction of ferromagnetic material with a magnetic field had been the only available technique to gauge that field for several millennium. The advent of electricity and associated classical phenomena captured in the four Maxwell equations, were a step forward. In the early 1900s, the model of quantum mechanics provided a two-way leap forward. One came from the newly understood interaction of light and matter, and more specifically the three-way coupling of photons, atoms' angular momenta, and magnetic field, which are the foundations of atomic magnetometry. The other came from magnetically sensitive quantum effects in a fabricated energy-ladder form of matter cooled to a temperature below that of the energy steps; these quantum effects gave rise to the superconducting quantum interference device (SQUID). Research using atomic magnetometers and SQUIDs has resulted in thousands of publications, text books, and conferences. The current status in each field is well described in Refs. [48, 49, 38, 42] and all references therein. In this work we develop and investigate techniques and applications pertaining to atomic magnetometry.

[Full text: tbd.com or eric.corsini@gmail.com].

To Marianne, ma compagne [1]
and to my parents[2]
whose emotional and intellectual support made
this work possible.

---

[1] Phi-Beta-Kappa, B.A., M.A., U.C. Santa Barbara; from California, a world traveler, with a mind opened to the challenges of interacting with other cultures and languages, and active in two ways at opening young minds to those challenges; first through her position as a foreign language high school teacher, and second through her position as department Chair, reminding the education hierarchy of the essentiality of learning early on that we are a family of distinct cultures (Fig. E.1).

[2] Restored a 300-year old home built on seven acres, planted 5000^+ trees, and many kinds of flowers. They fostered in their children the spirit of curiosity and the drive to push boundaries. The first “real” toy they offered me at age three was a hammer, some nails and a few wooden planks, with which I later made a small hut. Because of the fostering they provided, by age sixteen I was licensed to fly a 2-seater Jodel airplane (several years before being legally allowed to hold a drivers licence), was licensed to fly and able to keep a glider aloft in excess of five hours, had learned to program a computer (now obsolete - in the early days of computers) at the “Jean-Perrin” science museum in a programming language called P.A.F., had grown my own garden complete with Petunia flowers, carrots, lettuce, red radishes..., and had learned to mend and sew. These early realizations are a tribute to the investigative spirit they passed on, and the foundation to this dissertation. But their fostering started even earlier, when they chose against the fashion of the day, to build a stroller facing forward, to the world, whereas the ones available for purchase had the child facing the other way, towards the parent (Fig. E.1).

Contents

List of Figures

List of Tables

Acknowledgments

Completion of this work was made possible by the generous help, lessons, and inspirations I received from my juniors, peers, and seniors listed below. The particular inspiration each provided is an intrinsic part of this work, and as such, is documented and described in these acknowledgements and corresponding appendices.

In particular I am deeply indebted to my colleague Victor Acosta who shared with me, not only his scientific insight, but also his daily-life common sense, a personal reminder that idealism has to be subjected to realism (Appendix B - Fig. B.4).I re-learned the obvious fact that life is not meant to be fair but meant to be lived and that expecting otherwise is seeking utopia. The corollary is that one need not contribute to the unfairness but must accept it as an intrinsic part of real life, move forward in good spirit, and thank adversity, rather than resent it [45].

I also thank Micah Ledbetter (postdoc) whose ability to combine high quality apparatus building with a rapid transition to data taking and publication, was a constant reminder that my penchant for building with perfection and multi-functionality needed to be subordinated to the main goal of scientific research, which is to publish results. He also initiated me to the grueling five mile, one thousand feet inclined, fire-trail run (Appendix B - Fig. B.3), which goes from the base of the Berkeley hill where is constructed the UC Berkeley campus, to the top of the hill at the U.C. Berkeley Space Science Lab bus stop (for the downhill [free to students] bus ride).

James Higbie (postdoc), with whom I took my first steps as a graduate student experimentalist, provided another source of inspiration with his unique ability of bringing an apparatus to proof of principle functionality by means of a minimalist's construction style and a sharp sense for computer modeling.

Brian Patton's (postdoc) eloquent delivery of scientific ideas showed me that good science is complete only when presented in a readily accessible, clear, concise, and understandable format.

Many thanks to Kostya Tsigutkin (postdoc), for his welcoming smile and readiness to answer a wide range of questions, to Geoffrey Iwata (UC Berkeley undergraduate student - Fig. 4.18) whom I mentored and who is moving on to the University of Columbia (after deciding against the university of Chicago); to Duy Le Ba, another UC Berkeley undergraduate student whom I briefly mentored; his gentle demeanor, and bright mind made interacting with him a privilege; to Andrey Shmakov (UC undergraduate student) with whom I interacted and who provided valuable input connected to the work pertaining to Chapter 6; to my peers and colleagues Dmitry Dounas-Frazer, Nathan Leefer, Pauli Kehayias, Damon English, a renaissance classical-genre singer, Simon Rochester, a Mathematica expert, and Andrew Park, a computer whiz; and to visiting postdocs Christian Weber, Szymon Pustelny, Przemyslaw (Pzemek) Wlodarczyk, Andrei Jarmola, Ran Fisher, Kasper Jensen, for the lively coffee breaks, tours of the Northern California country-side, and evening lap-swim workouts at the UC Berkeley RSF[3] pool (Fig. D.1), and to Amir Waxman for the many grueling fire trail runs we did together (Appendix B - Fig. B.2).

In our entering class, I thank Miguel Daal and Erin Quealy for the mutual support we provided each other preparing for the Preliminaries exams and Thomas (Tom) Purdy and Jay Deep Sau for their heartfelt friendships.

In the physics department's technical support teams, I specifically thank Mike Brown, Carlisle Warner, and Marco Ambrosini (physics department machine shop - Appendix C - Fig. C.2) for their meticulous machining and guidance in that field; similarly I thank John Davis, LeVern Garner, and David Gallegos, (physics department electronic shop - Appendix C - Fig. C.1) for sharing their electronics expertise; I thank Mike (Misha) Solarz, "independent contractor" for his help assembling the work space described in Chapter 5 (Appendix B - Fig. B.4), I also thank Joseph Kant (physics department student machine shop) for the meticulous and comprehensive machine shop course revolving around making a small hammer which parts incorporates a wide range of

---

[3] Recreational Sports facilities

lathing and milling techniques (finishing the hammer grants unlimited student machine-shop access - Fig. C.2).

In the physics department student support services (Appendix B - Fig. B.4), I thank the indispensable contributions of Anne Takizawa (Student Affairs Officer), of Donna Sakima (Graduate Student Affairs Officer), and of Claudia Trujillo (Undergraduate Adviser). In the Physics Department academic leadership, I wish to Chair Frances Hellman, who oversaw the Physics Department's turn around from the 2002 outside panel review's "genteel decline" diagnostic to the recent top NRC ranking, and who led the 2012 outside panel review (results pending). In the physics department management services I wish to thank Stephen Pride-Raffel (Appendix B - Fig. B.4) for (on numerous occasions) expediting equipment and parts purchases, Anthony Vitan, Katalin Markus, Eleanor Crump, and Tom Colton. In the university management services I thank Cassandra Hill in the Graduate Division for her expert guidance in the logistics pertaining to dissertation requirements and filing, I thank Dorothy Jones in the Registrar's department. In the university housing services I offer a warm thank you to Susana Wong (Appendix B - Fig. B.4) for her cheerful and uplifting demeanor and expert help and organization in housing administrative matters. In the recreational sports department, I thank Brigitte Lossing for her diligence at providing evening lap-swimmers additional pool open hours (Appendix D - Fig. D.1). Last, in this paragraph, I wish to thank Elvia Palabrica, one of the many dedicated persons, working late into the night, to meticulously keep the physics building spotless; she always offered an easy solution to solve building supplies issues, and blended her hard work with a cheerful personality.

Many thanks to Mark Prouty, Geometrics Inc. COO and Director, for the generous loan of a G858 commercial atomic magnetometer; he took the time after a long day's work to bring the magnetometer's power supply just in time to make possible the first attempted plant biomagnetism measurement (Ch. 7) of "Truly" (the bunga bangkai corpse-flower) as it started opening its bloom.

Thanks also go to the UC Botanical garden staff and in particular to Holly Forbes, Nancy Nelson, and to Paul Licht, director. Their generous loan of the garden's "research plateau", and access to the garden, made possible several sensitive magnetic field measurements including the one on plant biomagnetism (Ch. 7).

I also thank my co-PI and co-dissertation Chair, Dr. Dmitry Budker, for introducing me to AMO physics, and to a captivating branch of that science. I also thank him for the opportunities he generously afforded me to attend international conferences. His extensive grasp of the field combined with his ability to extract and synthesize from a vast sea of information the key idea leading to new science and publications, was an inspiration; as were his musical talents, playing so as to soothe the soul and the heart.

Not forgetting the dissertation and qualification-exam committees members (Appendix A, Figs. A.1 & A.2), I thank in particular Dr. Eugene Commins, for his very carefully thought-out explanation and approach to teaching graduate-level quantum mechanics class; his teaching talent twice earned him the U.C. Berkeley Distinguished Teaching Award in the Physical Sciences (the only U.C. Berkeley professor to earn it twice - Appendix B - Fig. B.3). I also thank him for the summer reading class he generously granted me, and for his guidance in the qualification exam preparation and the dissertation writing. I thank Dr. Grigory Isaakovich Barenblatt for his applied mathematics course (Appendix B - Fig. B.3), his novel ideas on very tough problems like fractures and turbulence [91, 36, 25], and the inspiration provided by the courage he exercised in advancing a theory on turbulent flows that went contrary to the deeply entrenched and accepted belief[4,5]. Turbulent flows is a topic in another line of research in which I may one day venture.

---

[4] Dr. Barenblatt, Math 275 U.C. Berkeley Spring 2012 on April 12th 2012 (9:30-11:00am class): "In such cases one goes through three stages. The first stage: "It is wrong". The second stage: "It is correct but of no importance". The third stage: "It is correct and of importance but it was not him who did it first".

[5] The fatal puncture of the wing leading edge of the space shuttle Columbia on January 1986 may have been avoided had the computer simulation (completed prior to shuttle re-entry) of the impact by the foam

Many thanks to Dr. Holger Müller for the inspiration he provided by his "let's do it" attitude in life and in research, for taking time to appraise and guide me in my work, and for the motivating example of advancing novel ideas to test Einstein's Equivalence Principle in the face of contrary belief and disputative questions from prominent members in that field, in particular at the 2010-I.C.A.P. International Conference in Cairns, Queensland, Australia (Appendix A - Fig. B.2). Last, is Dr. Charles Townes, member of the qualification exam committee, Physics 1964-Nobel Laureate, and discoverer (in 1954) of the maser, the forerunner of the laser, an essential component throughout this work; I thank him for the example of living the full working life, he lives and inspires in us all, continuing research and giving conferences well past the age of ninety.

I thank the Physics Department, the Math Department, and the university of California, Berkeley, for providing a world renowned, and top ranked programs in physics (Appendix B - Fig. B.1) and mathematics, and in many fields of science and humanities. Upon beginning my years as a graduate student, I was awestruck by the numerous talented physics and mathematics instructors and the quality of the research programs. In particular I thank Dr. Littlejohn, in the Physics Department, for the choreographed delivery of clear and concise advanced topics in physics (Appendix B - Fig. B.4). I thank Dr Lawrence Craig Evans for his clear and concise courses on Partial Differential Equations, I thank the NDSEG fellowship program for awarding me a three-year fellowship which allowed me to freely investigate courses in mathematics and physics. I also thank the physics teaching-assistant program for graduate students, which allows them to be an integral part, and to contribute to the instruction of the nation's and world's top ranking undergraduate students. Preparing for and delivering section-lectures, midterm and final review sessions, and occasionally subbing for the instructor at the main lecture, facing 200 sharp and bright minds, were valuable and memorable experiences.

Moving eastward 6,000 miles, I thank my other co-PI and co-dissertation Chair, Dr. hab. Wojciech Gawlik, who, under the joint Kraków-Berkeley Atomic Physics and Photonics Laboratory[6] (Fig. A.2), opened the doors of his research laboratory at the Jagiellonian University in Kraków, affording me the opportunity to learn and work with laser-cooled atoms (Dr Gawlik's group is the first to realize a BEC in Poland). I thank him further for being an observer-member of my qualification exam committee, by means of Skype teleconference late into the night in his time-zone (Appendix B - Fig. B.2). I also thank him and his wife, "Danka", for welcoming me in their home and for the skiing week-end (Appendix B - Fig. B.3). The nearly five-month visit (the most fruitful months of my graduate student career) concluded with the first observation of nonlinear Faraday rotation with "MOT"-cooled atoms [**Phys. Rev. A 81, 053420 (2010)**].

Many thanks to my colleagues and seniors in Kraków, in particular to Jerzy (Jurek) Zachorowski for sharing his extensive knowledge of the field of cold atoms, for his personal invitation to the close viewing of the twelve-person rope-pulled ringing of the 9.6-tonnes, ~500 years old, Zygmunt Royal Bell at the Wavel Castle (he is one of the twelve life-time appointed bell ringers - [Appendix B - Fig. B.3]), and for the long bike ride in the Polish country side, and to his wife Dorota Zachorowska for the dinner later that day; to Joseph Flagga for his electronic expertise; to Danuta Myrek for managing the logistics pertaining to my visit; to Piotr Czapla, the concierge of the physics building, for opening the main door late at night; to Michal Zawada for the one-week assignment at the Polish National Laboratory for A.M.O. physics in Torun, where he manages, under the direction of Dr. W. Gawlik the first BEC apparatus in Poland; to my colleagues Krzysztof Brzozowski (and fiancé Anna Barzyńska - now Brzozowska) , Marcin Bober, Krystian Sycz, Barbara Wajnchold, Leszek Krzemień (and fiancé Anna Stachulak - now Stachulak-Krzemień"), and Adam

---

debris from the main tank, included a power-law dependence of the flow velocity on the Reynolds number (as opposed to the accepted logarithmic law) [91, 24].

[6] Funded in turn by the NSF Global Scientists project for joint research grant; by the NATO grant Science 4 Peace; and by the NATO grant [PST.CLG98362] for cooperation between Berkeley, Riga (Latvia), Kraków (Poland) and the NRC US-Poland Twinning grant

Wojciechowski's fiancé, Joanna (Asia) Symula (now - Wojciechowska), for sharing the comfort of their own homes and families, barbecues at their parents' chalets, hikes in the Bielsko mountains (Appendix B - Fig. B.4), and the loan of a mountain-bike; and to my many other physics colleagues whom I met more closely during the three-day physics department hike, which terminated with roasting sausages at a bon-fire, high in the snowed-in Tatra mountains (Appendix B - Fig. B.3).

Moving back to California, I acknowledge the solid foundation laid by the professors in my undergraduate education at the high ranking physics department at UC Santa Barbara (which was the recipient of four physics/chemistry Nobel prizes during [or near] my undergraduate tenure [Dr W. Kohn (chemistry-1998), Dr A. Heeger (chemistry-2000), and Dr H. Kroemer (physics 2000), and Dr. D. Gross (physics-2004)]). In particular I thank Dr G. Halers in non-equilibrium soft condensed matter physics and statistical mechanics, Dr A. Cleland, in quantum systems and classical mechanics, Dr. Elizabeth Gwinn, in condensed matter physics and quantum mechanics, Dr H. Nelson, in particle physics, Dr J. Hartle, in general relativity, Dr A. Ludwig in theoretical condensed matter and mathematical physics, and Dr O. Blaes for his enthusiastic and charismatic presentation of cosmology. Similarly I thank the professors in the mathematics department, Dr Alexandros Alevras, in a three-quarter-long Real-analysis course, Dr T. Sideris, in complex analysis and Differential Geometry, Dr Bisch Dietmar, in Rings, Fields, and Group Theory, Dr K Millett in Topology, and Dr Xianzhe Dai in lower division mathematics. I also thank the College of Creative Studies at UC Santa Barbara, a small college within the university, catering to ~300 curious and motivated students, giving them complete and unrestricted freedom to explore courses offered by the university, sheltering their students from the more restrictive university bureaucracy, and offering to their students advanced topics courses in physics and mathematics in ten-student class-size settings. Within that college I thank Dr. R. Freedman (author of a lower-division physics excellent introductory text book) for his clear and concise instruction in introductory physics, Dr. F. Roig for his advanced topic courses in general relativity, College Provost Bill Ashby, Leslie Campbell and Frank Bauman in the college administration, orchestrating the logistics for students to enjoy a unique learning experience. It is the college of creative studies' unique learning setting which allowed me to complete two non-overlapping degrees in physics and mathematics with highest honors.

Moving further back in time I thank the Hancock Community College, for the dedicated instructors[7] in physics, philosophy (Dr. Klaus Fisher), literature, history (Gary Bierly), mathematics, electronics, and computer science. Yet further back in time I thank my high school and junior high school mathematics and physics instructors; in particular my junior high physics instructor. His name I do not recall, but he awakened in a small class, the spirit of scientific curiosity. One memorable experiment was separating water (with a pinch of salt added as a catalyst), into oxygen and hydrogen, into a thick, soft and heavy green-plastic bottle. With a light bulb filament inserted in the neck of the bottle and connected to the end of a ~10 m cord, hiding behind tables, we connected the cord into the socket. A loud explosive noise ensued and the bottle flew up to the ceiling, undamaged, upright and propelled like a rocket; ten pairs of science-struck early-teenager eyes gazing at the non-destructive application of the chemical energy calculations they had just previously completed.

Back to the present at UC Berkeley, I wish to thank visiting professor, Mikhail Balabas from the S. I. Vavilov State Optical Institute, St. Petersburg, 199034 Russia, who, during several three-to-four month long visits with our group, shared his unique combination of scientist and artist glass-blower talents. He is one of the few in the world to make the anti-relaxation paraffin and alkene coated cells, which is one of the three ways (Ch. 1) existing today to preserve atomic spin polarization. The mechanism by which the coating works has puzzled scientists for the last fifty years and continues doing so [22, 128, 127, 113]. His combined talents allow him to probe the elusive cell-wall coating anti-relaxation mechanism and has guided him to recently devise a new coating one hundred times more effective than the paraffin coating which had prevailed for the last

---

[7] All names - and correct spelling - were not be obtained at the time of the submission of the dissertation.

fifty years. Watching him meticulously working with two simple tools (Fig. 5.6 and Appendix B - Fig. B.2)) a custom- and Russian-made glass-blower torch and 2) an oven which he constructed out of a two nested tin containers, separated with insulating wool, with heating rods and a fan in the inner vessel to produce a homogeneous heat distribution, provided the example that complex physics mechanisms are sometimes solved solely with intuition and simple tools, without the need of elaborate technology. I thank him for his scientific guidance (in the work of Ch. 6), his peaceful demeanor, and for the many cups of espresso he shared with me in his office.

Listed last are the two mentors to whom I owe the most for my growth as a scientist, physicist, and graduate student experimentalist, and who were central to the successful completion of this dissertation.

The first, Adam Wojciechowski, a graduate student at the Jagiellonian University (working under Dr. W. Gawlik), who guided me through a rapid leaning curve in cold atom physics during my visit in Kraków. He also shared his unusually extensive knowledge of Polish history and culture. In Zakhopane he introduced me to the traditional Oscypek smoked cheese; from there we hiked together through the Tatra mountains (Morskie Oko being one of our destinations [Appendix B - Fig. B.2]) tramping through blizzards, snow and ice, and sometimes sunshine. The day we parted we crossed arms at Lake Zakrzowek, each upping a shot of herbal and spice flavored Ukrainian vodka, therefore sealing a fruitful and successful first encounter.

The second, Todor Karaulanov, a postdoc at U.C. Berkeley, who generously shared his encyclopedic scientific knowledge and insight, and provided his moral support and mentorship though several years of my research at Berkeley (Appendix B - Fig. B.2). He re-enforced my conviction, through his personal example, that no matter what the struggle may be, the world of atomic physics is truly fascinating.

Preface

The present doctoral dissertation was completed under the co-chairmanship, guidance, and supervision of:

1) Physics Professor Dmitry Budker at the University of California, Berkeley[8,9,10]

2) Physics Professor Dr. hab. Wojciech Gawlik at the Jagiellonian University in Kraków, Poland[7,8,11],

and meets the criteria and standards expected by each co-Chairman.

This work is an investigation in "Atomic Magnetometry", a subset of the field of "Magneto-optical Effects", itself a subset of the vast field called "Light-Matter interaction". The work is presented in seven Chapters.

- Chapter One, is a brief introduction, historical overview and perspective of magneto-optical effects, starting with the linear Faraday effect, to a host of nonlinear effects, from which evolved atomic magnetometry, the study of which started in the 1950s.
- Chapter Two, presents the first observation of nonlinear Faraday rotation with laser-cooled atoms, one result of which makes visually manifest both linear and nonlinear Faraday rotations in one measurement.
- Chapter Three, develops a novel idea applicable to self-oscillating magnetometers.
- Chapter Four, Part I, shows the construction of a multi-configurable and field-able atomic magnetometer platform.
- Chapter Four, Part II, presents preliminary in-the-field measurements (using the above field-able device) to exemplify the multi-configurability of the device and the many

---

[8] Address: University of California, Berkeley, Physics Dept. MS:7300, Berkeley, CA, 94720, USA;
tel: 510-643 1829; email:budker@berkeley.edu; web-page: budker.berkeley.edu

[9] The present co-Chairmanship and co-adviser-ship in under the umbrella of the joint Krakó-Berkeley Photonics and Atomic Physics Laboratory and collaboration.

[10] The present dissertation is the second instance of a dissertation with co-advisorship and co-Chairmanship by Dr. Gawlik and Dr. Budker. The first was Dr. S. Pustelny's doctoral dissertation, awarded in 2007 by the Jagiellonian University, with Dr. Gawlik and Dr. Budker, acting as co-advisers and co-Chairs.

[11] Address: Zakłlad Fotoniki, Instytut Fizyki UJ, Reymonta 4, 30-059 Kraków, Poland;
tel. +48-12-6635656; Fax: +48-12-6338494; email: gawlik@uj.edu.pl; web-page: www.if.uj.edu.pl/ZF

facets and challenges of Earth's field atomic magnetometry (in particular, in the self-oscillating magnetometer configuration of Chapter Three).

- Chapter Five, Part I, takes us back to the lab to show the construction of a multi-configurable shielded magnetometer platform, one purpose of which is to investigate, in a well controlled environment, optimization techniques for application of atomic magnetometry applications in the field.

- Chapter Five, Part II, presents preliminary measurements to exemplify the use of the in-lab multi-configurable magnetometer platform, and to confirm the complex and challenging physics pertaining to finite magnetic field atomic magnetometry.

- Chapter Six, explores the use of one of the many configurations possible with the in-lab device of Chapter Five, to investigate the properties of a novel atomic spin-polarization anti-relaxation coating identified by Balabas *et al* in 2010, exhibiting two orders of magnitudes improvement over the paraffin coatings, which have been at the forefront since the 1950s. The investigation touches on applications in magnetometry and in time and frequency standards.

- Chapter Seven, reports on the measurement of plant biomagnetism (magnetophytography) in the six-foot tall inflorescence "Trudy", with a commercial atomic magnetometer (Geometrics Inc. G858)[12]. "Trudy" is an Indonesian-jungle native "bunga-bangkai" corpse-flower, residing at the U.C Botanical Garden. The measurement was performed and spanned "Trudy's " twelve-hour, once-every-six-year bloom, during which "bunga-bangkai" corpse-flowers exhibit strong cadaverine and putrecine scents, and surface temperatures rising to 30°. The ensuing publication, although modest in its results (reporting an upper bound on Trudy's magnetic field), drew a response, from the scientific and broad-community, larger than did the rest of this work, including an article in the Berkeleyan newspaper, a podcast on the APS website [9], and a free e-book by Caltech Authors.

  The wide response to the plant biomagnetism measurement, and the several applications for atomic magnetometers explored and suggested in this work, provide evidence that the ability to make sensitive measurements of magnetic fields opens a realm, to which our senses are otherwise blind, yet which we yearn to better understand.

---

[12] The measurement covered a 3-day span to record a baseline before and after the bloom period - a length of time better suited for a commercial device at this development stage.

To supplement the acknowledgments section and to recognize the specific contributions of my peers and seniors whose collaboration made this work possible, specific recognition is given in the caption of each figure. Broader acknowledgments are given at the end of each chapter. An overview of the acknowledgments/contributions are given below.

- Chapter Two, (First observation of Nonlinear Faraday rotation with laser-cooled atoms) was managed by graduate student A. Wojciechowski who led me through a rapid learning curve in cold atom physics. He allowed me to run a good part of the experiment; His guidance, mentorship, and management of the experiment were essential to the results. He is rightfully the first author in the resulting publication [**Phys. Rev. A 81, 053420 (2010)**] and the main results are part of his Ph.D. dissertation. the Chapter touches on practical applications of this first observation.
- Chapter Three (A self-oscillating, all-optical, atomic magnetometer with high dynamic range and large bandwidth) was managed by postdoc James Higbie (with whom I made my first steps as a graduate student experimentalist) and with close participation of our PI Dr. Budker. James Higbie is rightfully the first author in the resulting publication [**Rev. Sci. Instrum. 77(11):113106, 2006.**].
- Chapter Four, Part I, (Design and construction of a fieldable and multi-configurable optical platform) was my work with the help of valuable discussions with the physics machine and electronic shops staff (no specific recognition is given in the captions). In particular, many thanks to Mike Brown who patiently veered my mechanical designs to more feasible formats. A small instrumentation publication is in the planning stage.
- Chapter Four, Part II, (Preliminary measurements using the fieldable optical platform in its first iteration and then in the one described in Part I). This long-running project (2006-2008) was first managed by postdoc J. Higbie (2006 to mid-2007), then by myself (mid-2007-2008), with the close participation of our PI Dr. Budker; the other collaborators were Chris Hovde (Southwest Sciences), Todor Karaulanov, and Brian Patton who joined mid-2008. Brian Patton took the management of the apparatus in 2009 after I turned to the work described in Chapter Five.
- Chapter Five, Part I, (Design and construction of a multi configurable in-lab magnetometer platform) was my work, with the help of valuable discussions with the physics machine and electronics shops staff (no specific recognition is given in the captions). Many thanks to Carllisle Warner, to Michael (Misha) Solarz, and to LeVern Garner.
- Chapter Five, Part II, (Preliminary measurements with the magnetometer platform described in Part I) was my work, with the mentorship of postdoc T. Karaulanov, guidance from our P.I. Dr. Budker, and with valuable discussions with M. Balabas, V. Acosta, M. Ledbetter, B. Patton, K. Tsigutkin, and D. Dounas-Fraser. A small instrumentation publication combining Chapter Five Parts I & II is in the planning stage.
- Chapter Six (Hyperfine frequency shift and Zeeman relaxation in alkali vapor cells with anti-relaxation alkene coating) was my work with the mentorship of postdoc T. Karaulanov, collaboration and guidance by visiting professor M. Balabas and by our P.I. Dr. Budker, and with valuable discussions with V. Acosta, M. Ledbetter, B. Patton, K. Tsigutkin, and D. Dounas-Fraser. A publication is near-completion [Authors: E Corsini, M. Balabas, T. Karaulanov, and D. Budker]
- Chapter Seven (Search for plant biomagnetism with a sensitive magnetometer.) was completed by a wide collaboration. However the blooming of “Trudy”, the corpse flower, happened to coincide with most collaborators’ summer holidays except for my own, for Caltech visiting undergraduate student Brian Lester, for Mark Prouty (Geometric Inc. COO and Director)

who took time after work to deliver the magnetometer power supply and connector at 6pm, for Marianne, who agreed to cancel her plans so as to serve as taxi-driver that evening, and for Nancy Nelson (U.C. Berkeley garden staff) who re-opened the garden gate at 8:30pm upon Marianne's subtle request. The fortuitous combination allowed me to make a continuous three-day data recording starting at 9:00pm, the very beginning of the flower's bloom (Fig. 7.8). I subsequently performed the data analysis and wrote the article [**Jour. of Appl. Phys. 109 (2011)**], with guidance from Victor Acosta and from our P.I. Dr. Budker; and with the wider collaboration of postdoc Brian Patton, M. Prouty, and undergraduate students N. Baddour and B. Lester.

Chapter 1

Atomic Magnetometry Selected Points of Interest

1.1 Historical overview

The origin of atomic magnetometry dates back to the birth of modern physics. Two branches emerged. One pertains to the high end of the energy spectrum, in which, to first order, observations are described by the four-dimensional Minkowski metric. The other, relevant to this work, pertains to the low end of the energy spectrum. At low energy, observables of a system are described by non-commutative operators acting on vectors in a Hilbert space. From the "Quantum Mechanics" model emerged new fundamental quantities and new force-fields; light was also found to have both wave and particulate characters.

One fundamental quantity of interest to this work is the intrinsic angular momentum (spin) of fundamental particles and of photons. The combined spin and charge of the electron and of the nucleons, and the spin bearing and particulate nature of light, are at the heart of atomic magnetometry.

As shown on Fig. 1.1, non commutativity of observables led to the quantization of the energy level of the atom. Relativistic corrections, interaction of electron spin and electron angular momentum, and the interaction of electron spin and nucleon spins, led to further splitting of the quantized energy levels, each one lifting the degeneracy of the (Hamiltonian) energy operator's eigen-values. One of the two key elements in atomic magnetometry is the interaction of the atomic spin with an external magnetic field; that interaction lifts the final energy-level degeneracy into Zeeman energy sub-levels. The second key element is optical pumping, a subset of the vast field of "light-matter interaction".

This chapter touches on a few points of interest germane to this dissertation. Detailed coverage of the science underlying the interaction of light and matter in the presence of a magnetic field is presented in depth in many texts and review articles including references [63, 44, 82, 38] (and all references therein).

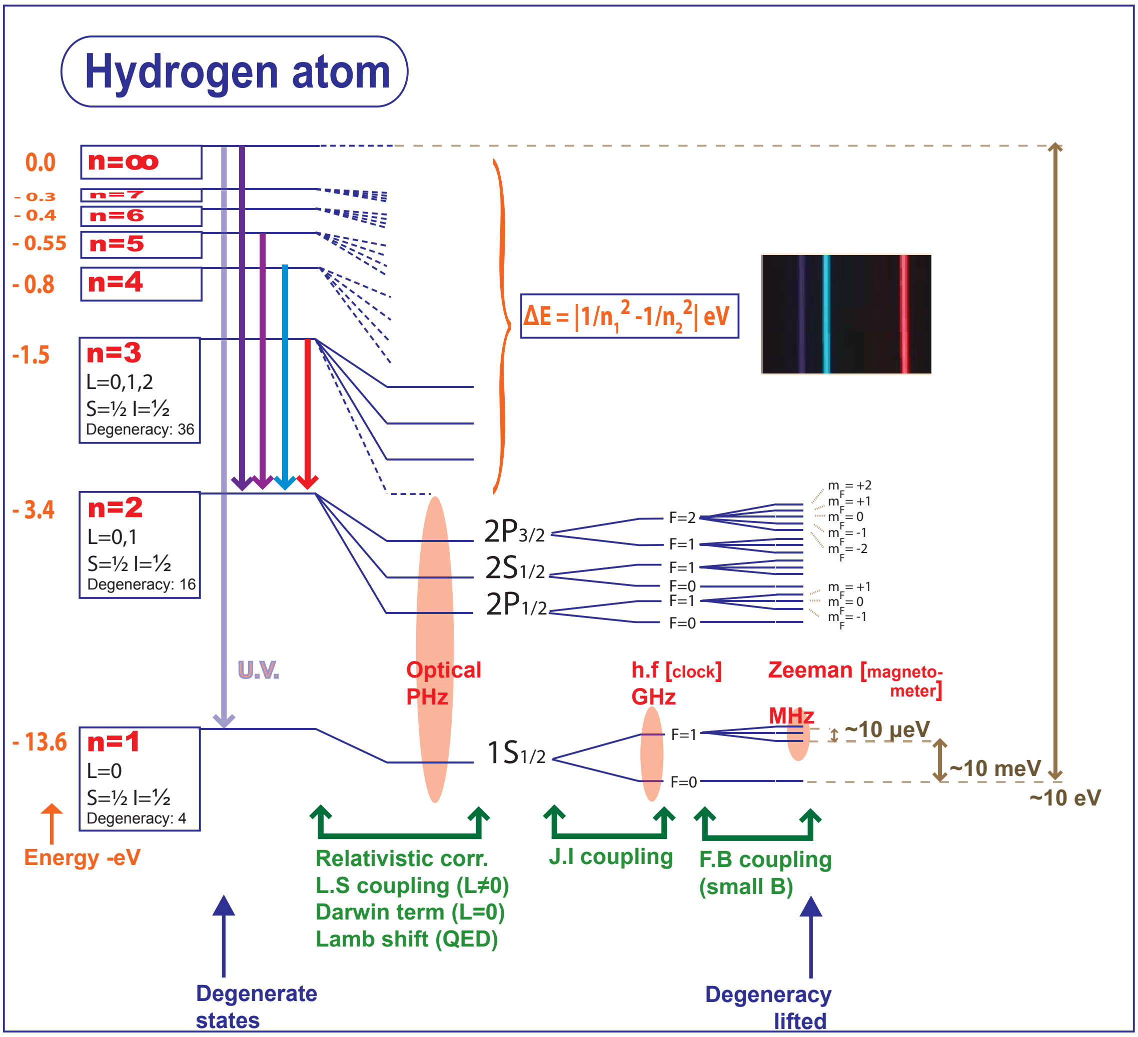

Figure 1.1: Magnetometry - origin. The non-commutativity of observables lead to energy level quantization in the hydrogen atom. Successively smaller energy interactions lift the degeneracy of the quantized energy levels. The last one, the Zeeman sub-levels' coupling to the magnetic lifts the Zeeman level degeneracy and (alongside with optical pumping) is at the heart of atomic magnetometry.

1.2 Atomic magnetometry: energy, frequency and wavelength-equivalent perspective

Atomic magnetometry pertains to very low energies, which are as cold as the largest particle accelerator is hot. The sensitivity of atomic magnetometers, in energy-equivalent units, is eight orders of magnitude colder still ($10^{-21}eV$). A ladder-depiction of energies pertaining to current research is shown in Fig. 1.2.

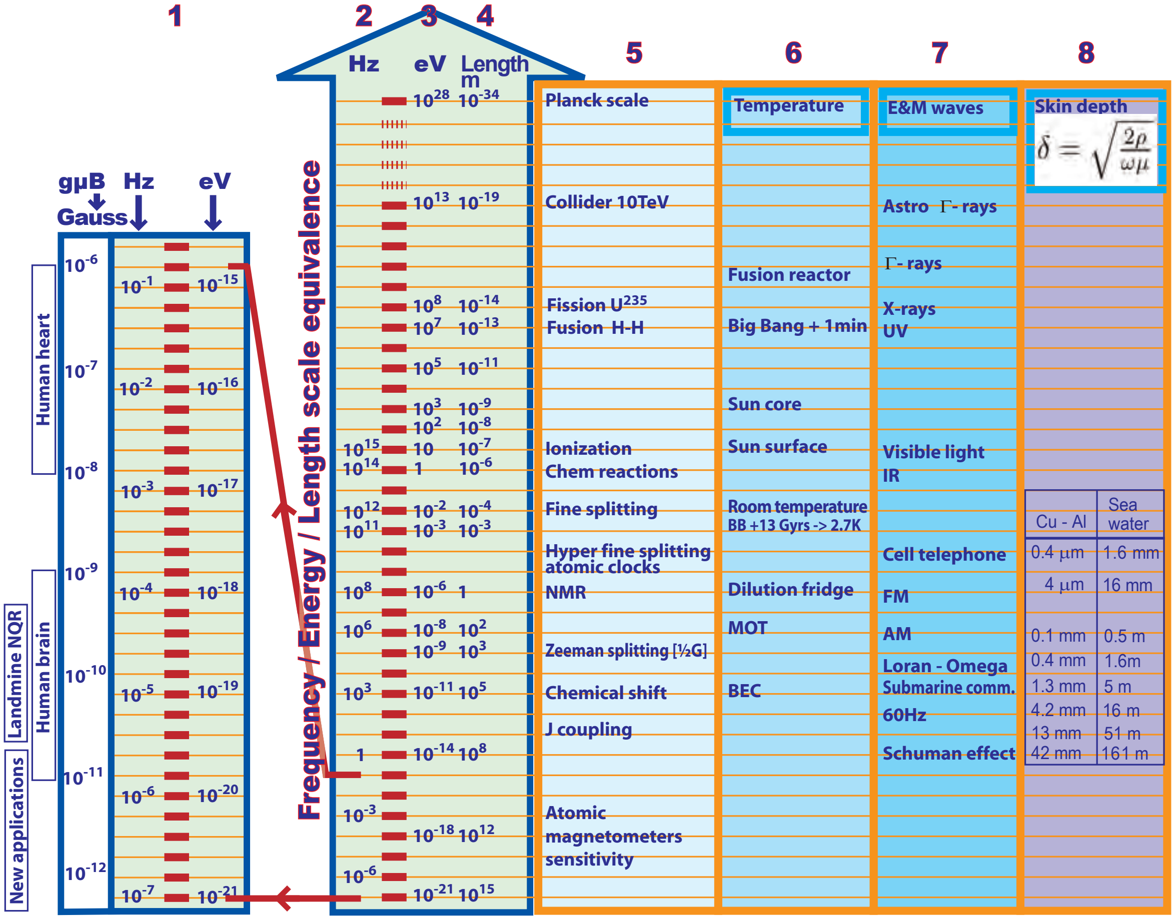

Figure 1.2: Magnetometry - Energy equivalence perspective. The scale ranges from the LHC (the Planck scale is shown not-to-scale) down to the world's record in atomic magnetometer sensitivity set in 2010 by the Romalis group at Princeton [59]. The scale is given in equivalent units of 2: frequency (Hz), 3: energy (eV), 4: wavelength (m), 5: atomic processes, and partially in 6: temperature, 7: electromagnetic processes, and 8: electromagnetic skin depths. Col. 1: is a scaled up section pertaining to the range of atomic magnetometer sensitivity and applications pertaining to it, which include biomagnetism, NQR, and new domains in physics.

1.3 The "Atomic magnetometry" Hamiltonian - Interaction with a static magnetic field

The hydrogenic atom Hamiltonian is the operator of interest to atomic magnetometry with alkali atoms. In particular the term (H_{B}), which couples the electron's and nucleus' magnetic moments (atomic spin) to an external magnetic field, and which lifts the hyperfine F-sub levels (2F+1) degeneracy,

$$H_B = \frac{\mu_B}{\hbar}(g_s\mathbf{S} + g_L\mathbf{L} + g_I\mathbf{I})\mathrm{B}, \tag{1.1}$$

where μ_B is the Bohr magneton, $\hbar$ is the Planck constant, g_s, g_L, and g_I, are the electron spin, orbital, and nuclear Landé g-factors, respectively. To first order g_L is corrected by the ratio of the electron and nuclear masses,

$$g_L = 1 - \frac{m_e}{m_{nuc}}. \tag{1.2}$$

The experimentally measured values of g_s and g_I in ^{87}Rb and ^{85}Rb are given in Tables 1.1 & 1.2[11].

Spin g-factor	g_s	2.0023193043622(15	[1]
Orbital g-factor	g_L	0.99999369	
Fine structure g-factor	$g_J(5^2\mathbf{S}_{1/2})$	2.00233113(20)	[20]
	$g_J(5^2\mathbf{P}_{1/2})$	0.666	
	$g_J(5^2\mathbf{P}_{3/2})$	1.3362(13)	[20]
	g_I	-0.000995141 4(10)	

Table 1.1: Electron Landé g-factors in ^{87}Rb

Spin g-factor	g_s	2.0023193043622(15	[1]
Orbital g-factor	g_L	0.99999354	
Fine structure g-factor	$g_J(5^2\mathbf{S}_{1/2})$	2.00233113(20)	[20]
	$g_J(5^2\mathbf{P}_{1/2})$	0.666	
	$g_J(5^2\mathbf{P}_{3/2})$	1.3362(13)	[20]
	g_I	-0.00029364000(60)	

Table 1.2: Electron Landé g-factors in ^{85}Rb

To simplify evaluating H_B, the eigen-basis used is the one in which the magnetic field coupling to the electron magnetic moment is a small perturbation (linear in that basis). If the perturbation is small compared to the fine splitting, one chooses the J basis,

$$H_B = \frac{\mu_B}{\hbar}(g_J J_z + g_I I_z)B_z, \tag{1.3}$$

where the magnetic field is taken to be in the z direction.

Similarly if the perturbation is small compared to the hyperfine splitting, one chooses the F basis,

$$H_B = \frac{\mu_B}{\hbar} g_F F_z B_z. \tag{1.4}$$

In equations 1.3 & 1.1 g_J and g_F are given to first order by

$$\begin{aligned} g_J &= g_L \frac{J(J+1) - S(S+1) + L(L+1)}{2J(J+1)} + g_s \frac{J(J+1) + S(S+1) - L(L+1)}{2J(J+1)} && (1.5) \\ &\simeq 1 + \frac{J(J+1) + S(S+1) - L(L+1)}{2J(J+1)} && (1.6) \\ g_F &= g_J \frac{F(F+1) - I(I+1) + J(J+1)}{2F(F+1)} + g_I \frac{F(F+1) + I(I+1) - J(J+1)}{2F(F+1)} && (1.7) \\ &\simeq g_J \frac{F(F+1) - I(I+1) + J(J+1)}{2F(F+1)}, && (1.8) \end{aligned}$$

where the approximate expressions for g_J and g_F come from taking the values $g_s \sim 2$ and $g_L \simeq 1$, and from ignoring the effect of the nuclear term (a correction at the 0.1% level).

Equation 1.4 describes an interaction (the “anomalous Zeeman effect”) in which the Hamiltonian H_B linearly perturbs the hyperfine Hamiltonian H_{hf} and splits the Zeeman sub-levels degeneracy by an energy,

$$\Delta E|F, m_F >= \mu_B g_F m_F B_z. \tag{1.9}$$

Equation 1.3 describes an interaction (the “Paschen-Back effect”) which, to lowest order, shifts the Zeeman sub-levels energies by

$$\begin{aligned} E|J, m_J, I, m_I > \; &= A_{hf} m_J m_I \\ &\quad + B_{hf} \frac{3(m_J m_I)^2 + \frac{3}{2} m_J m_I - I(I+1)J(J+1)}{2J(2J-1)(2I-1)} \\ &\quad + \mu_B (g_J m_J + g_I m_I) B_z. \end{aligned} \tag{1.10}$$

The problem is more difficult for intermediate Zeeman energy shifts, but is greatly simplified in the ground state. The solution is given by the “Breit Rabi” formula [11].

$$E|J = 1/2, m_J, I, m_I >= \Delta E_{hf} \frac{I}{2I+1} \pm \frac{1}{2}(g_J + 2I g_I)\mu_B B. \tag{1.11}$$

Equations 1.9 and 1.11 are referred to in subsequent chapters. In particular they:

- Quantify the Larmor frequency (central to atomic magnetometry).
- Quantify the nonlinear Zeeman effect (NLZ) at Earth’s magnetic field, which when evaluated $\Delta m = 1$, at 500 mG, for ^{87}Rb and for Cs is approximately 18 Hz and 3 Hz, respectively.
- Quantify the quadratic “clock” transition ($m_F = 0 \rightarrow m'_F = 0$) frequency shift, Δ_{clock}, which has no linear correction,

$$\Delta_{clock} = \frac{(g_J - g_I)^2 \mu_B^2}{2\hbar \Delta E_{hf}} B^2. \tag{1.12}$$

1.4 Linear Faraday Rotation

Linear Faraday rotation is the first consequence of the Zeeman sub-level splitting and is depicted in Fig. (1.3). The splitting causes the resonant absorption peaks of the opposite helicity components of linear polarized light, to be are shifted with respect to each other. The shift is made explicit in the Kramers-Kronig dispersion relations which are derived from the classical model of N damped harmonic oscillators with mass m, damping factor b, spring constant k, and charge q under the influence of a driving force qE. $E = E_o e^{i\omega t}$ is the amplitude of the electric field of an incident electromagnetic wave of frequency ω.

With $E = E_x$, the corresponding differential equation is (in CGS units and setting factors of c, π, and 4π=1)

$$m\ddot{x} + b\dot{x} + kx = qE_o e^{i\omega t} \tag{1.13}$$

which generates a macroscopic polarization

$$P = Nqx = N\frac{q^2 E_o e^{i\omega t}}{m(\omega_o^2 - \omega^2 + i\gamma\omega}, \tag{1.14}$$

where $\gamma = b/m$ and $\omega_o = \sqrt{k/m}$.
P is also derived from the Maxwell's equations,

$$P = (\epsilon - 1)E \tag{1.15}$$

For a magnetic permeability, $\mu \simeq$1, the index of refraction, $n \simeq \sqrt{\epsilon}$. Combining Eqs. 1.14 and 1.15 we get,

$$n = \sqrt{1 + \frac{Nq^2}{m(\omega_o^2 - \omega^2 + i\gamma\omega)}}. \tag{1.16}$$

With $n \simeq 1$, Eq. 1.16 simplifies to

$$n = 1 + \frac{Nq^2}{2m(\omega_o^2 - \omega^2 + i\gamma\omega)}. \tag{1.17}$$

Separating the real part (leading to dispersion) and the imaginary part (leading to absorption), and for small $\Delta_\omega = \omega_o - \omega$, we obtain the Kramers-Kronig dispersion relations (n(w), the dispersive components and $\alpha(\omega)$, the absorptive component) valid in the neighborhood of an optical transition.

$$\begin{aligned} n(\omega) &\propto \frac{\omega_o - \omega}{(\Delta\omega)^2 + (\gamma/2)^2}, && (1.18) \\ \alpha(\omega) &\propto \frac{\gamma}{(\Delta\omega)^2 + (\gamma/2)^2}. && (1.19) \end{aligned}$$

The characteristic width of these dispersion curves is Lorentzian and corresponds the FWHM of the absorbtion line. The thermal motion and vapor pressure of the atoms,

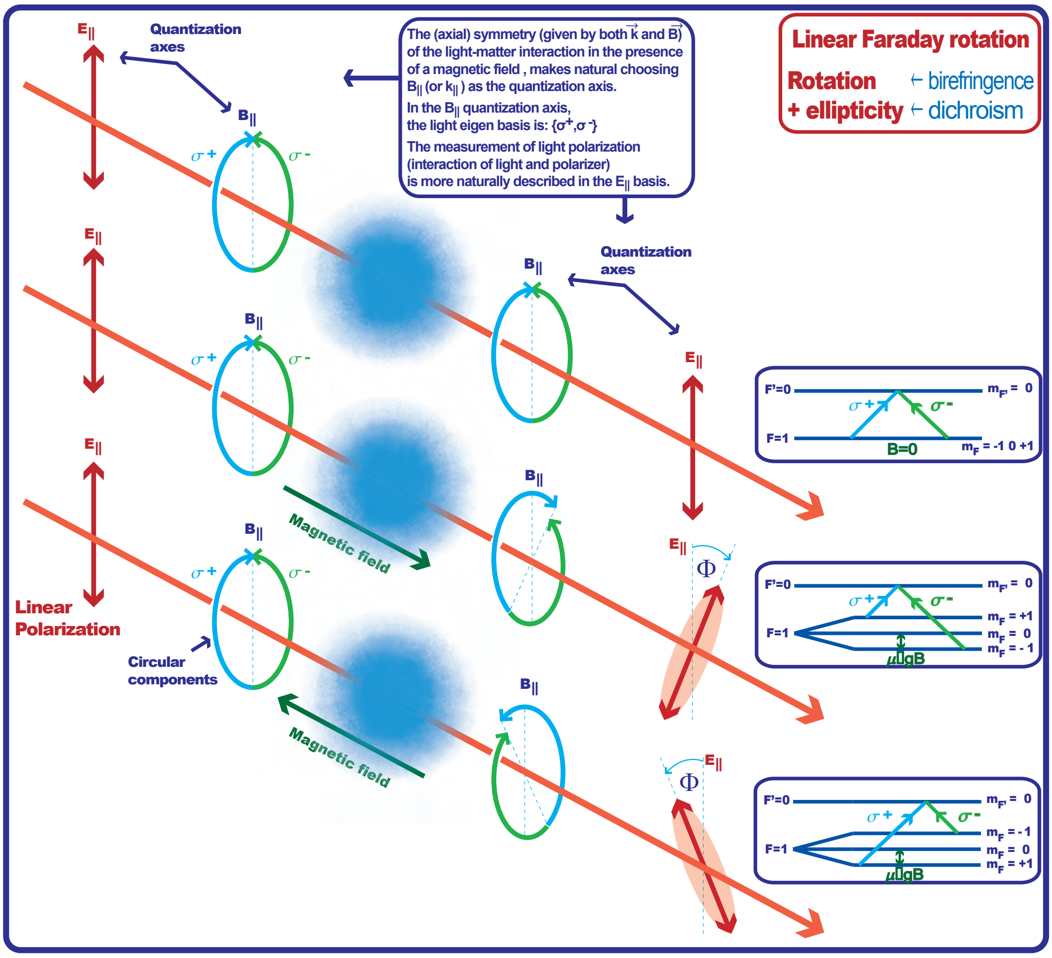

The (axial) symmetry (given by both $\vec{k}$ and $\vec{B}$) of the light-matter interaction in the presence of a magnetic field , makes natural choosing $B_{||}$ (or $k_{||}$) as the quantization axis.

In the $B_{||}$ quantization axis, the light eigen basis is: $\{\sigma^+,\sigma^-\}$

The measurement of light polarization (interaction of light and polarizer) is more naturally described in the $E_{||}$ basis.

Figure 1.3: Linear Faraday Rotation: DAVLL. Linearly polarized light is the sum of two opposite helicity components (σ^+, σ^-). The "natural" quantization axis is $B_{||}$ in which the eigen-basis $=$ σ^+, σ^-. The two components have different indices of refraction due to the splitting of the Zeeman under the action of the magnetic-field in the alkali medium. In conclusion the interaction of light, matter, and magnetic field, induces circular dichroism and circular birefringence in the alkali medium and adds components of ellipticity and rotation to the linear polarization. The application od linear Faraday rotation is achieved with a balanced polarimeter (which may be supplemented with a $\lambda/4$ plate), or a cross polarizer, which extracts the rotation or the ellipticity, yielding a zero crossing within the Doppler broadened absorption line, applicable to an optical frequency feedback mechanism.

Doppler and pressure broaden the profile into a Voigt profile (of the order of 1 GHz, compared to ~10 MHz for the natural linewidth described above) but lead to qualitatively the same observation.

The splitting of the Zeeman sublevels shifts the (Doppler broadened) resonant absorption of the left and right circular polarizations, and results in circular birefringence and circular dichroism causing rotation and ellipticity of a linearly polarized weak probe light as depicted in figure (1.3).

1.5 Nonlinear Faraday rotation or nonlinear magneto-optical rotation (NMOR)

With the previous section we concluded the “simple and linear” Quantum mechanics. In this section we add and step into the more complex subject of nonlinear effects based on optical pumping. Whereas the Zeeman splitting, or equivalently the Larmor frequency, is a measure of the magnetic field (the center of the resonance), the nonlinear effect, associated to optical pumping, is responsible for the width of the resonance, which limits how well the center of the resonance can be measured, and ultimately limits the atomic magnetometer sensitivity.

The combination of the Zeeman splitting and optical pumping led to the discovery of NMOR, which ignited research in atomic magnetometry. Detailed discussions of optical pumping [82], zero magnetic-field NMOR resonances [40, 43], and finite-field resonances which occur when the pumping laser light is amplitude modulated [41] (AM-NMOR or AMOR), or frequency modulated (FM-NMOR) [74], have been presented in prior work hereby cited.

In short a NMOR resonance occurs when optical pumping causes an atomic vapor to become dichroic (or birefringent), so that a subsequent probe light experiences polarization rotation. For the NMOR resonances considered in this work, both pump and probe are linearly polarized and therefore primarily produce and detect atomic alignment. Or the pump is circularly polarized and the probe is linear polarized and therefore produce and detect orientation. The magnetic-field dependence originates from the fact that the atomic spins undergo Larmor precession Ω_{L} which modifies the dichroic (or birefringent) characteristics of the medium.

To produce a macroscopic alignment with a weak optical pumping there are two regimes. The first is when the Larmor precession frequency is small compared to the spin relaxation rate; in this regime a continuous pump can be used. The second is when the Larmor precession frequency is large compared to the spin relaxation rate; in this regime the pump is made synchronous (or nearly synchronous) with the precession (stroboscopic pumping). In the second regime the modulation of the pump is achieved by modulating the amplitude of the pump light (AM-NMOR or AMOR [41]) or by modulating the optical-frequency (FM-NMOR [74]). If the optical-pumping rate is modulated at a frequency $2\Omega_{\mathrm{L}}$, for alignment, and Ω_{L}, for orientation, then the optical-rotation angle of the probe polarization will in general also oscillate at frequency $2\Omega_{\mathrm{L}}$ (due to the two-fold degeneracy of linearly polarized light) and at frequency Ω_{L}, respectively. By sweeping the pump light modulation frequency, the NMOR resonance is observed as a resonant peak in the rotation-angle amplitude of the probe light polarization.

1.6 Preserving atomic polarization and adsorption

Once atomic polarization has been achieved there are three leading techniques to preserve it:

- Anti-relaxation coatings which preserve atomic polarization up to 10,000 atom-wall bounces (and more recently up to 10^6 bounces[23]). This technique is the one pertaining to Chapters 3, 4, 5, and 7.

- Buffer gas, which slows the diffusion of polarized atoms to the cell wall (uncoated-wall collisions are depolarizing).
- Cooling and trapping the atoms (removing the container's walls and therefore wall-collisions) which is presented in Chapter 2.

Anti-relaxation coatings have yet another interaction of interest with alkali atoms: adsorption and/or absorption. That interaction touches on the larger domain of surface science, and is the topic of Chapter 6.

1.7 Conclusion

The idea, the precursor experiments, and the discovery of nonlinear magneto-optical effects (from which NMOR was derived), were pioneered in the 1950s, 1960s, 1970s, and 1980s with Kasler, Dehmelt, Bell and Bloom, Cohen-Tanoudji, Bouchiat *et al*, Gawlik *et al*, Budker *et al* (among several others) [62, 117, 31, 28, 67, 137, 34, 62, 61, 117, 28, 27, 31, 73, 75, 38], and heralded atomic magnetometry. With the advent of low cost laser diodes, considerable progress in atomic magnetometry has been made in recent years, including the achievement of pG/$\sqrt{Hz}$ sensitivity [59], and m Hz resonance linewidth [23], bringing atomic magnetometry on par with superconducting quantum interference devices (SQUID). The new records have renewed interest in atomic magnetometers for applications to geomagnetism, to biomagnetism [30, 144, 56], to space-based measurements of planetary and of deep-space magnetic fields, to low field NMR [98], and to fundamental physics [106, 29, 148, 119, 18, 79]. With the advent of laser-cooled atoms (Chapter 2), a new "magneto-optical" method of containing the atoms was achieved; the method extended the range of applications in atomic magnetometry. The technology driven-renewed interest, and new application prospects, motivate the work described in this dissertation.

Chapter 2

Laser-cooling ($\sim$100μK) a Cloud of Atoms to: - Preserve Atomic Polarization - Observe Linear & Nonlinear Faraday Effects

Related publication
Title:“Nonlinear Faraday Rotation and Detection of Superposition States in Cold Atoms”
Journal: Phys. Rev. A 81, 053420 (2010)

Authors: A. Wojciechowski [1,2], E. Corsini[2,3] , J. Zachorowski[1,2], and W. Gawlik[1,2].
Affiliations:
[1]Institute of Physics, Jagiellonian University, Reymonta 4, PL-30-059 Krakow, Poland
[2]Joint Kraków-Berkeley Atomic Physics and Photonics Laboratory, Reymonta 4, PL-30-059 Kraków, Poland
[3]Department of Physics, University of California, Berkeley, California 94720-7300, USA

pacs: 33.57.+c, 42.50.Dv, 42.50.Gy, 32.80.Xx
Keywords: magneto optical trap, nonlinear faraday rotation, atomic magnetometer, quantum computing.

Abstract

Nonlinear Faraday rotation (NLFR) in a cloud of atoms laser-cooled with the magneto optical trapping (MOT) technique[1], in a cloud of $\sim 10^7$ rubidium 87 (^{87}Rb) atoms at $\sim$100 μK, was first observed by Wojciechowski, Corsini, Zachorowski, and Gawlik in 2010 [142]. The technique makes possible precision magnetometry with μG sensitivity, large dynamic range (from zero field up to 10 G), and sub-mm spatial resolution. Magnetic field sensing in cold atoms measuring the Larmor precession has been discussed in the context of: MOT [87], Bose Einstein Condensate [121, 140], and optical dipole trap [135]. However, NLFR measures the rotation of a polarization plane which is suitable for measurements of very weak magnetic fields. The polarization rotation is caused by the medium birefringence and dichroism resulting from the light-induced Zeeman coherences [129, 55] (a nonlinear and diamagnetic effect). In this Chapter we focus on the dramatic visualization of both linear and nonlinear Faraday rotations (discussed in Secs. 1.4 & 1.5) made possible with laser-cooled atoms; we also touch on precision magnetometry and diagnostic applications of NLFR. The theoretical development and quantum information applications of this first observation are part of Adam Wojciechowski's Ph.D. dissertation.

2.1 Introduction

The linear Faraday rotation of the polarization plane of light propagating in a medium is caused by the splitting of the Zeeman sub-levels (anisotropy of the medium) by the longitudinal magnetic field (Ch. 1). At room temperature, to observe the complete profile of the linear Faraday effect in an alkali vapor, the Doppler broadening necessitates sweeping the magnetic over a range of $\sim$500 G, centered at zero field (equivalent to a width of $\sim$500 MHz). In contrast the nonlinear effect (also at room temperature) is observed with a $\sim$10-100 μG sweep of the magnetic field (in a shielded environment), making the observation of the linear and nonlinear effects in one sweep of the magnetic field, technically challenging.

The situation differs at 100 μK, at which Doppler broadening is reduced to less than the optical transition natural linewidth (of the order of 10 MHz). A $\sim$10 G sweep of the magnetic field is sufficient to observe the full profile of the linear Faraday effect, making technically easier the observation of the linear and nonlinear effects (of the order of mG, or less) in one sweep of the magnetic field.

The linear effect has been observed in laser-cooled atoms with the MOT technique by Labeyrie [96], Franke-Arnold [70], and Narducci [107], and with the optical dipole trap technique by [134] in the early 2000s. In this Chapter we will show the time-resolved realization of non linear faraday rotation (at zero magnetic field and up to several Gauss) in a cloud of atoms laser-cooled atoms to $\sim$100μK.

Nonlinear effects are the result of creating coherent superposition of Zeeman sub-levels in one (or both) of the atomic hyperfine ground states. The ground state coherences

---

[1] The Magneto Optical Trapping (MOT) technique is extensively described in several works including Ref.[104]

form a variety of nonlinear phenomena such as coherent population trapping [19], electromagnetically induced transparency [69], nonlinear magneto-optical rotation [39] (NMOR - or equivalently nonlinear Faraday rotation [NLFR]), and combinations of these nonlinear effects [65]. The formation of ground state coherences necessitate optical pumping with near-resonant (or resonant) light which mechanically perturbs the laser-cooled atom cloud. In this work we minimize the adverse effect with a retro-reflected beam and with the use of minimum light power.

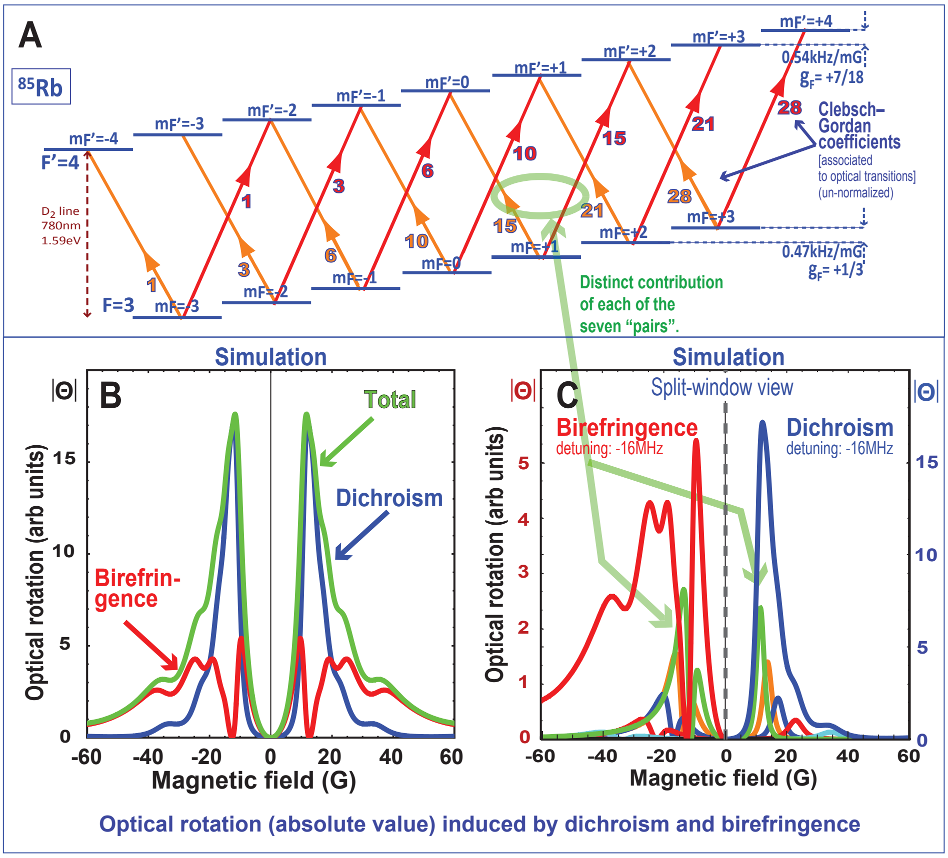

Figure 2.1: A: F=3→F'=4 optical transitions in ^{85}Rb . The transitions are proportional to the square of the ClebschGordan coefficients which, "un-squared" values are shown un-normalized. The splitting of the Zeeman sublevels in a magnetic field causes both dichroism (absorption) and birefringence (dispersion).
B: simulation of the optical rotation (absolute value) caused by the combined effect of dichroism and birefringence for a -16 MHz detuning of the pump/probe light [note: a cross-polarizer would measure the rotation squared]. The contribution of each Zeeman sublevel and the total contribution of Zeeman sublevels, for birefringence (C-left) and for dichroism (C-right) are shown ion the "split" window-view. [Simulation: J. Zachorowski - Collaboration: A. Wojciechowski, E. Corsini - Project management: A. Wojciechowski - PI: W. Gawlik].

2.2 Linear Faraday rotation in a complex Zeeman structure Combined effects of magnetic field and light detuning

In contrast to the three-Zeeman level system, F=1→F'=0 transition, with two electric dipole transitions, shown in figure 1.3, the F=3→F'=4 transition in ^{85}Rb has a 16-Zeeman sublevel system with fourteen electric dipole transitions, each weighed by the square of its respective ClebschGordan coefficient. The absolute value of the simulated linear Faraday rotation profile caused by the combined effect of dichroism and birefringence (different absorption and indices of refraction for left/right circular polarizations) is shown in figure (2.1).

2.3 Experimental setup

Figure (2.2A) shows the optical frequency control scheme to form the necessary laser beams for optimum optical detuning of the MOT and the Faraday pump/probe beams. A master laser is locked to the rubidium D2 line (780 nm), 160 MHz above the F'=2→F'=4 "cross-over" (saturation spectroscopy) and serves to lock two slave lasers by injection locking. One slave laser provides the MOT light beams and the other provides the pump/probe "Faraday" light beam. Acousto-optic Modulators (AOM) are used to shift the optical frequency as shown. A separate laser tuned to the F=2 hyperfine ground state provides the repump beam.

Figure 2.2B shows the schematic of the MOT chamber area with the MOT's three pairs of opposite-helicity, counter-propagating laser beams (the MOT quadrupole magnetic field coils are not shown), the magnetic field coils for the "Faraday" field, the "Faraday" pump/probe beam, and the cross-polarizer setup (which measures the optical rotation squared [Θ^2]).

The Faraday beam is ~2 mm in diameter, 5-200 μW in power, is linearly polarized, and is retro-reflected to partially balance the light pressure on the atom cloud. The retro-reflection was made possible due to low resonant optical density (~0.5). The double pass through the atom cloud approximately doubles the Faraday rotation. An AOM serves to detune the Faraday beam optical frequency up to ~20 MHz above or below the F=3→F'=4 transition. The set up allows (with minor re-configuration) the measurement of optical rotation in two ways; with a cross polarizer (measuring rotation angle squared - shown in Fig. 2.2B), or with a balanced polarimeter (measuring the rotation angle directly - not shown).

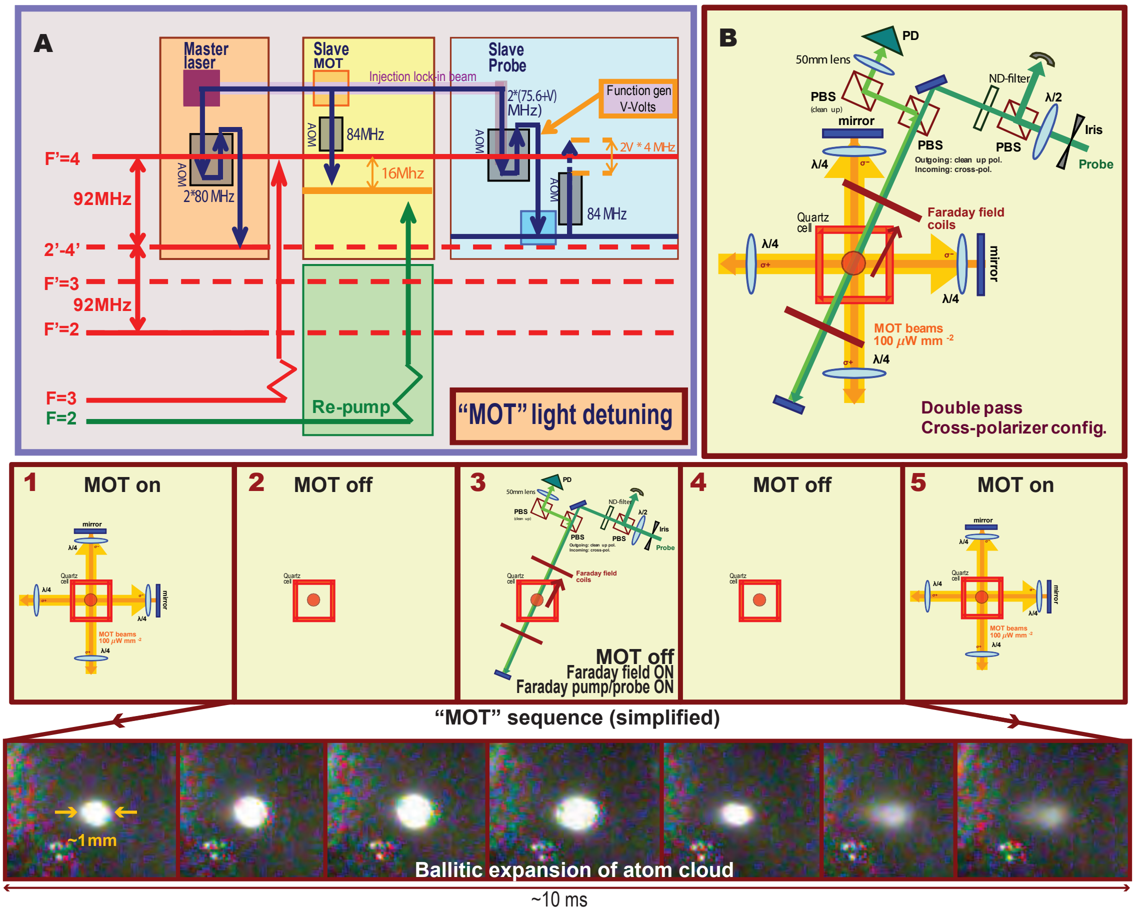

Figure 2.2: A: MOT beams optical frequency detuning scheme. A master laser is locked to the F'=2→F'=3 crossover and locks the optical frequency of two slave lasers (injection locking technique). One slave laser provides the light for the three retro-reflected MOT beams; the other provides light for the Faraday pump/probe beam. B: schematic of MOT beams (yellow), quartz cell (red square), atom cloud, Faraday magnetic field coils, retro-reflected prump/probe beam (green), and cross-polarizer set up to detect optical rotation squared (Θ^2). 1-5: simplified Faraday rotation measurement sequence. Lower: CCD camera photographs of the expanding cloud of atoms during the ~10 ms Faraday rotation measurement. [Schematics: E. Corsini - Collaboration: A. Wojciechowski, J. Zachorowski - Project management: A. Wojciechowski - PI: W. Gawlik].

2.4 Measurement technique

Fig. 2.2 1-5 series shows a simplified measurement time sequence. The sequence starts with a cloud of $\sim 10^7$ atoms, laser-cooled to $\sim 100\mu$K with the magneto-optical trapping technique, the MOT's beams and quadrupole field are then switched off. A homogeneous magnetic field ("Faraday" field) along the pump/probe beam is turned on. The Faraday rotation measurement starts 2 ms after the MOT quadrupole field is switched off to allow decay of the induced eddy currents (and associated transient magnetic field). The optical rotation measurement time is 5-10 ms during which the cloud of atoms expands ballistically. The measurement is terminated when the density of the cloud of atoms has become dilute. The ballistic expansion of the cloud of atoms is depicted in the photograph-series taken with a CCD camera (Fig. 2.2-lower). Upon termination of the measurement, the MOT beams and quadrupole magnetic field are switched on for ~50-200 ms during which the cloud of laser-cooled atom is re-formed. Each measurement is averaged ~20 times; the Faraday field is then incremented and the same measurement steps followed and averaged at the new field value. This procedure measures optical rotation as a function of time for each value of the Faraday magnetic field.

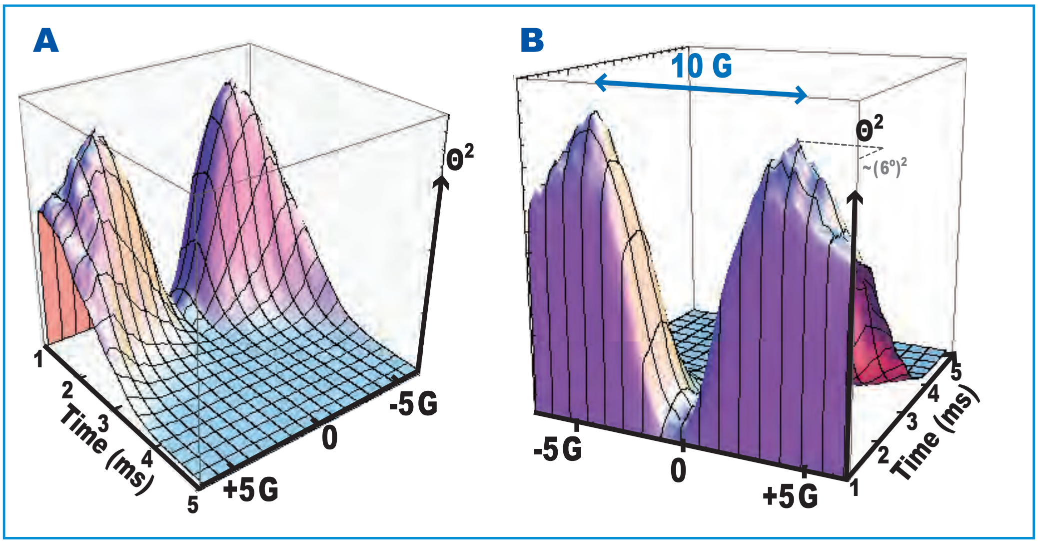

Figure 2.3: Linear Faraday Rotation in a cloud of atoms at a temperature of $\sim 100\,\mu$K. The ~10 ms measurement of optical rotation is repeated for discrete values of the Faraday magnetic field ranging ~±10 G. The 1 ms starting time of the measurement is with reference to the Faraday field being turned on, itself 1 ms after the MOT light and magnetic field were turned off (Fig. 2.2B). The 2 ms total delay-time was the optimum one for a sufficient decay of the MOT quadrupole field (Fig. 2.4) and a minimum expansion of the cloud of atoms. The nearly "vertical" rise of the linear effect at 1 ms (B) is the time constant of the photodiode (Fig. 2.2B). [Data: A. Wojciechowski, E. Corsini - Collaboration: J. Zachorowski - Project management: A. Wojciechowski - PI: W. Gawlik].

2.5 Observation of the time-resolved linear Faraday rotation in a $\sim$1 mm diameter cloud of atoms cooled to $\sim 100\,\mu$K

Figure (2.3) shows the linear Faraday rotation (squared) made manifest with a 10 G sweep of the magnetic field ($\cong$10 MHz). The width of the resonance corresponds to the natural linewidth of the transition, and is in sharp contrast to the one observed in vapor cells where the linear effect is two orders of magnitude broader. It also depends, to a lesser extent, on the pump/probe light detuning and on the initial Zeeman sub-level populations (as was shown by Labeyrie *et al* [96]). The optical rotation squared is measured, which results in an "absorptive" shaped resonance (centered at zero magnetic field - with a balanced polarimeter the shape would be "dispersive"). During the $\sim$10 ms measurement time the observed maximum optical rotation in the linear Faraday effect was $\sim 6^\circ$. In this measurement a magnetic field gradient (within the atom cloud volume) had not yet been sufficiently canceled with the external compensation coils and suppressed the nonlinear Faraday effect. The linear Faraday rotation in a cloud of laser-cooled atoms was first observed in 2001 by Labeyrie *et al* and by Franke-Arnold *et al* [96, 70].

2.6 The time-resolved linear Faraday effect as a diagnostic tool for transient magnetic fields

The linear effect can be used as a diagnostic tool to reveal transient magnetic fields within the volume of the cloud of atoms. In the examples shown in figure (2.4), the transient decay of the MOT quadrupole magnetic field was captured by the shift of the zero of the linear Faraday rotation as a function of time (during the cloud of atoms ballistic expansion). After the MOT quadrupole field has decayed, the zero of the linear Faraday rotation is centered at zero, as expected. The measurements in figure (2.4A) were realized at two pump/probe light detunings (10.4MHz blue detuned [Fig. 2.4A] and 5.2MHz red detuned [Fig. 2.4B]).

In addition to the transient magnetic field, a double "hump" was observed in the red-detuned measurement (Fig. 2.4B). If that effect was indeed a linear effect than only two reasons are possible: 1) the net Faraday field goes through zero at $\sim$1.6 ms, 2) the cloud density undergoes a partial re-collapse at $\sim$1.6 ms. The first is highly unlikely because the effect was not observed at other light detunings and the effect would have had to occur on every single measurements in the series of measurements that make up the 3D figure (an unlikely coincidence). The second may involve the combination of the Faraday field gradient and the light blue-detuning, conspiring to act as a blue-detuned "transient magneto optical trap". More measurements are necessary to explain the observation.

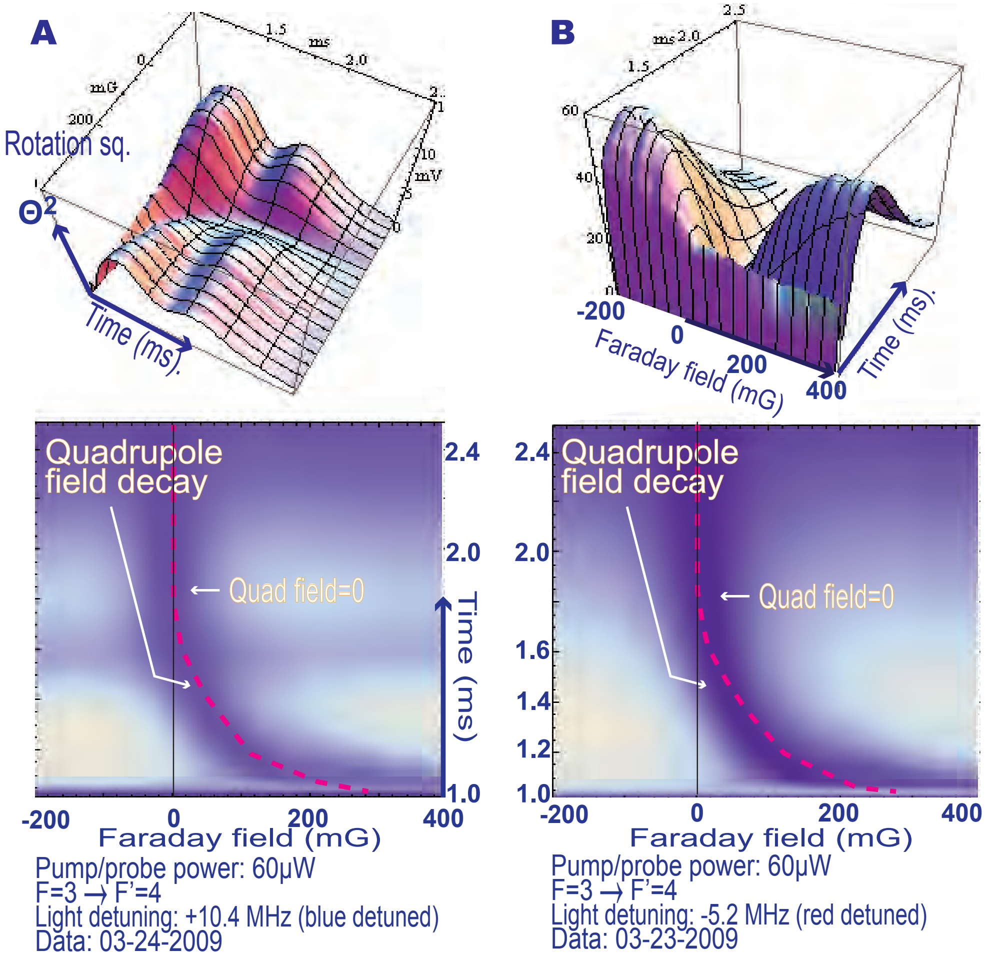

Figure 2.4: Linear Faraday rotation in a cloud of cold atoms was used as a diagnostic tool to detect the decaying MOT quadrupole magnetic field within the volume of the cloud of atoms. The measurement was made at two light detunings (+10.4MHz (A) and -5.2MHz (B), relative to the F=3→F'=4 optical transition). A "double-hump" is observed in the blue-detuned measurement. In this figure the time axis is with reference to the MOT light and quadrupole field being turned off. [Data: A. Wojciechowski, E. Corsini - Collaboration: J. Zachorowski - Project management: A. Wojciechowski - PI: W. Gawlik].

2.7 Simultaneous time-resolved observation of the linear, and the zero-magnetic field nonlinear Faraday rotations, in a ~1 mm diameter cloud of atoms cooled to ~100μK

The nonlinear Faraday rotation at zero magnetic field is shown in Fig. 2.5. The narrow ~50-100 mG width of the nonlinear effect dramatically contrasts the ~10 G-wide linear Faraday effect. The resonance amplitude is of the same order of magnitude as the magnitude observed with the linear effect (~6°) which is up to 10 times larger than what is observed in vapor cells. The nonlinear effect narrow resonance width is due to the long-lived light-induced Zeeman coherences between Zeeman sub-levels differing by —Δm—=2. The buildup time of these coherences depends on light power (see below) in contrast to the linear effect which depends only on number of atoms, the distribution of Zeeman populations, which makes the onset of the linear effect quasi-instantaneous (limited by the time constant of the photo detector). On the decay side of the resonances, both linear and nonlinear effects have a similar rate of decay indicating that the escape of the atoms is the primary mechanism for the signal decay.

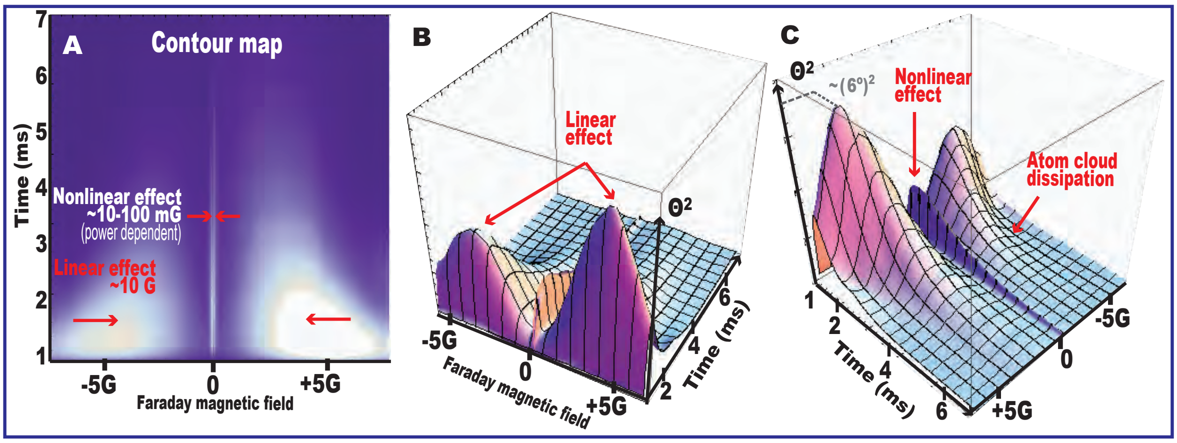

Figure 2.5: Nonlinear Faraday rotation in a cloud of cold atoms. The narrow width of the central nonlinear resonance contrasts sharply with the broader ∼10 G-wide width of linear Faraday rotation. Note the slower rise of the nonlinear effect which depends on a build up of atomic spin polarization, which is the result of optical pumping. [Data: A. Wojciechowski, E. Corsini - Collaboration: J. Zachorowski - Project management: A. Wojciechowski - PI: W. Gawlik].

2.8 The dependence on power of the linear and nonlinear Faraday effects

The dependence on light power and light detuning of the linear and nonlinear effects is plotted in figure 2.6. The linear effect (Fig. 2.6A) does not depend on light power (to first order) whereas the nonlinear effect (2.6B) exhibits the expected linear dependence (for low light power). In the measurements shown in figure 2.6, the resonance width of the nonlinear effect, asymptotically tend to $\simeq$35 mG at zero light power, due to a power broadening and a fixed offset. A later measurement (not shown), with improved cancelation of the magnetic field gradient within the cloud of atoms, at the optimum pump/probe light detuning, had an extrapolated width of $\simeq$10 mG.

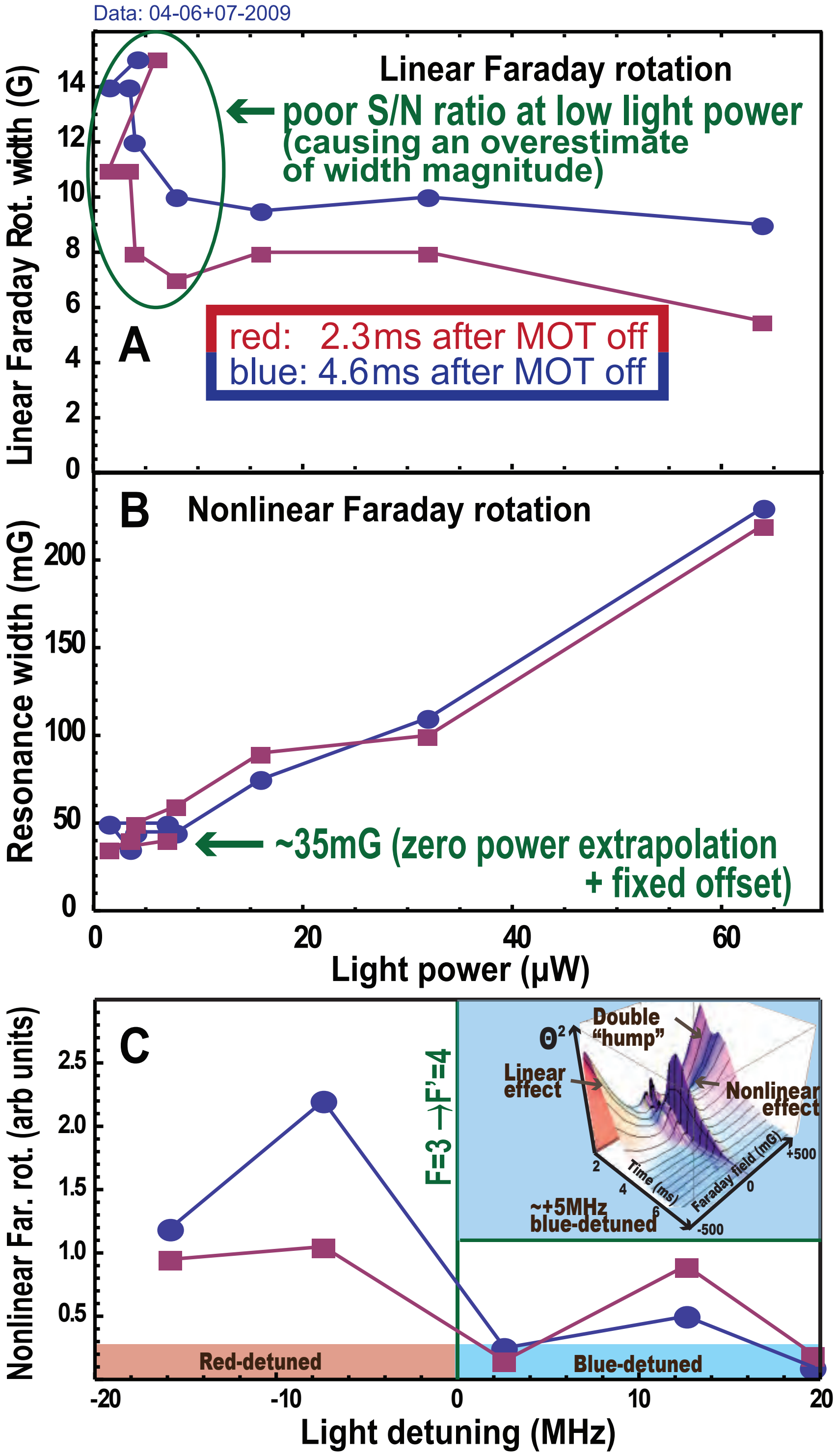

Data: 04-06+07-2009

Figure 2.6: Measurements in A,B,C are made at 2.3 ms and 4.3 ms after the MOT beams and quadrupole field are switched off. A: the linear effect does not depend on light power. The divergence at low light power was due to poor signal to noise ration and an over-estimation of the width of the resonance. B: the nonlinear effect is the result of optical pumping which is light power dependent. In these measurements the width is broadened by light power and a ∼fixed offset; the minimum width ∼asymptotically tends to ≃35 mG. We speculate that the fixed offset contribution to the resonance width is due to the magnetic field gradients within the volume of the atomic cloud. (note: the relative difference between the linear (A) and the nonlinear (B) effects at 2.3 ms and 4.3 ms - see text) [caption cont. next page].

[Caption - Fig. 2.6 - cont.]

C: the maximum nonlinear rotation is a function of the optical detuning of the Faraday pump/probe beam. We observe an opposite relative difference (between the 2.3 and 4.3 ms measurements) for the red-detuned and blue-detuned pump/probe light; The larger optical rotation for a blue de-tuned corroborates the hypothesis (Sec. 2.6) of a re-collapse of the cloud - (see text). [Data: A. Wojciechowski, E. Corsini - Collaboration: J. Zachorowski - Project management: A. Wojciechowski - PI: W. Gawlik].

Three orders of magnitude narrower widths are achieved with alkali vapors at room temperature in a magnetic shield and optimized magnetic field homogeneity. Improving the homogeneity of the Faraday field within the laser-cooled cloud of atoms is expected to narrow the resonance [111]. Another factor broadening the resonance width is the limited 5-10 ms observation time caused by 1) the cloud of atoms becoming dilute through ballistic expansion; 2) the atoms gravitational fall; 3) the light-induced pressure from the pump/probe "Faraday" beam. Causes 1) and 3) can be minimized with a red-detuned and low power pump-probe beam (see below).

Another way to increase the observation time is with an optical dipole trap, which confines the atom cloud to a smaller volume for a longer time, and in which magnetic field gradients are less important.

The amplitude of the nonlinear Faraday rotation is also a function of the optical detuning of the Faraday pump/probe beam. We hypothesize that the maximum rotation observed for red-detuned light is due to additional laser-cooling by the Faraday pump/probe beam (optical-molasses effect), which slows the ballistic expansion of the cloud of atoms. Slowing the expansion implies slowing the dilution of the cloud, and retaining a larger optical depth for a longer period of time; a larger optical depth in turn implies a larger nonlinear Faraday rotation. Indeed the minimum rotation was observed close to the optical resonance, which corresponds to maximum heating of the cloud, which in turn increases the rate expansion/dilution of the cloud and reduces the optical depth.

We also observed that the relative difference (between the 2.3 and 4.3 ms measurements) at the red and blue detuned probe/pump beam optical frequencies was reversed. With a red-detuned beam, from 2.3 to 4.3 ms, the cloud of atoms expands and becomes more dilute whereas with a blue-detuned beam the cloud seems to recollapse (we assume that the larger optical rotation at 4.3 ms is due to a larger optical depth). The observation corroborates the observation captured in the 3D insert in figure 2.6C, in which we observe a double-hump with a $\sim$5 MHz blue-detuned beam; it also corroborates the observation made with the linear effect and a blue detuned beam (Fig. 2.4B) in which a double hump was also observed. The double-hump is indicative of a possible re-collapse of the atom cloud. These observations are based on limited data (are qualitative only) but seem to infer that the cloud of atoms was significantly affected by the Faraday pump/probe beam cooling effect (off-resonance) or heating effect (on resonance) and correspondingly affected the observed amplitude of the nonlinear Faraday effect.

2.9 The time-resolved nonlinear Faraday effect as a diagnostic tool for transient magnetic fields (attempt)

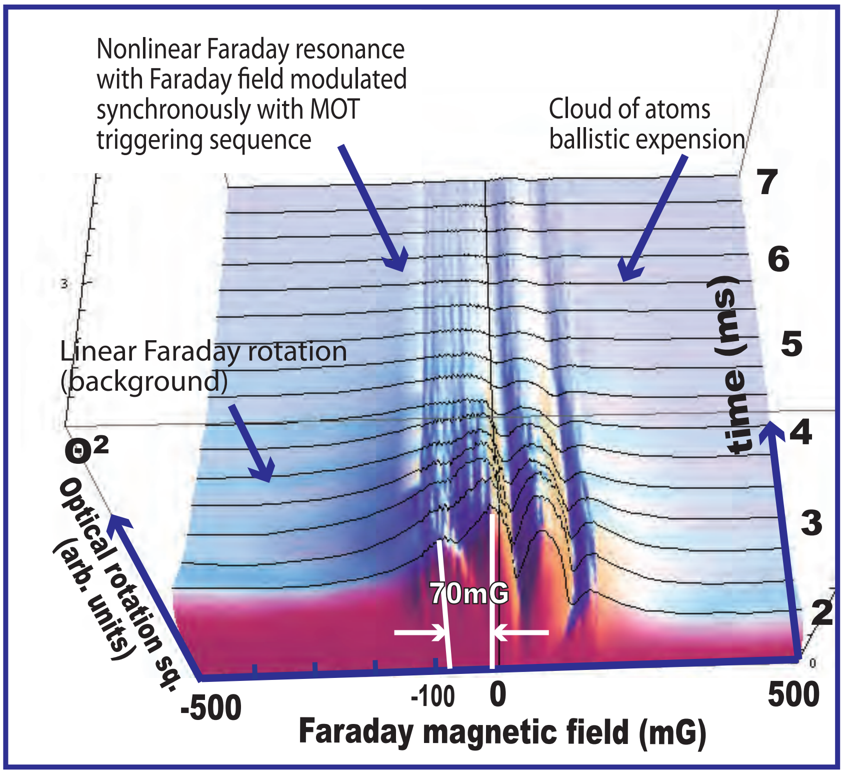

Figure 2.7: Nonlinear Faraday Rotation in a cloud of cold atoms: the Faraday field is “slowly” modulated with the goal of using the central nonlinear resonance as a diagnostic tool to measure transient magnetic fields within the volume of the atomic cloud. The sinusoidal modulation was made synchronous with the triggering of the Faraday field, with a period ∼half the observation time (∼10 ms). However sidebands were observed instead of the anticipated “curving” of the zero-field resonance (as was observed for the linear effect central resonance under the effect of the decaying MOT quadrupole field [Fig. 2.4]). [Data: A. Wojciechowski, E. Corsini - Collaboration: J. Zachorowski - Project management: A. Wojciechowski - PI: W. Gawlik].

As was achieved with the linear Faraday effect (Sec. 2.6 - Fig. 2.4) the nonlinear Faraday effect can be used as a diagnostic tool to measure transient magnetic fields during the expansion of the cloud of atoms. A modulation of the Faraday magnetic field was added to the bias Faraday field, synchronously with the timing of the “MOT” triggering sequence (Fig. 2.2 sequence 1:5), and with a period ≃observation time of the Faraday rotation (∼10 ms). A corresponding time-resolved modulation of the zero magnetic field nonlinear Faraday rotation was expected. However sidebands were observed (Fig. 2.7). Further investigation is needed to explain the observation.

2.10 Simultaneous time-resolved visualization of linear and nonlinear Faraday rotation with a cloud of atoms cooled to $\sim 100\,\mu$K at zero and finite magnetic fields

When the Larmor precession rate becomes larger then the ground state coherence relaxation rate, one possibility to form long-lived ground state coherences, is to modulate the pump light (Ch. 1, Sec. 1.5). Modulation is realized with amplitude modulation (AM-NMOR or AMOR [41]) or with frequency modulation (FM-NMOR [74]. With strobed pumping, in addition to the zero field resonance, two other resonances appear in the demodulated rotation signal. The additional resonances occur at a magnetic field at which the Larmor precession frequency is equal to half the modulation frequency (two-fold symmetry of linearly polarized light). With strobed pumping we observed the nonlinear effect at ±1 G, ±2 G, and ±3 G (Fig. 2.8). The width of these nonzero field nonlinear resonances is similarly determined by the coherence lifetime and were observed to be as narrow as the zero field resonance, similarly contrasting the wider width of the linear effect. The nonlinear effect was observed with a modulation frequency up to 9 MHz ($\cong \pm 9$ G - not shown), which is one order of magnitude larger than that observed in vapor cells, demonstrating the potential for sensitive measurements in a wide dynamic range.

A square amplitude modulation of the pump/probe light was used. The square modulation is the Fourier sum of sine waves which includes the base frequency and all higher harmonics, with an amplitude decreasing with the rank of the harmonic and with the depth of the modulation.

Accordingly we observed multiple sideband pairs at ∼200 kHz modulation frequency (Fig. 2.8A), and only one additional sideband pair at ∼1 MHz modulation frequency (Fig. 2.8B). At higher modulation frequencies the nonlinear Faraday effect increasingly blends with the linear Faraday effect, which compounds the suppression of visible additional sideband pairs (Fig. 2.8C: 2 MHz modulation frequency [$\cong \pm 2$ G], Fig. 2.8D: 3 MHz modulation frequency [$\cong \pm 3$ G]).

2.11 Conclusion

In this chapter we presented the first observation of nonlinear Faraday rotation in a cloud of atoms laser-cooled to $\sim 100\,\mu$K with unmodulated light (zero magnetic field), and with modulated light (magnetic fields up to several G). The technical challenge in the mechanical perturbation by the pump/probe beam was addressed with a retro-reflected beam. In contrast to work in alkali vapor, the nonlinear measurement of Faraday rotation in cold atoms allows the observation of the time-evolution (build-up) of long-lived superposition states (Zeeman coherences in a given F ground-state) both at zero magnetic field and up to several gauss. The technique can be used to measure transient and static magnetic fields with $10\,\mu$s time resolution, mm spatial-resolution, with sub-mG sensitivity, within the volume of intersection between the atom cloud and the laser beam waist size.

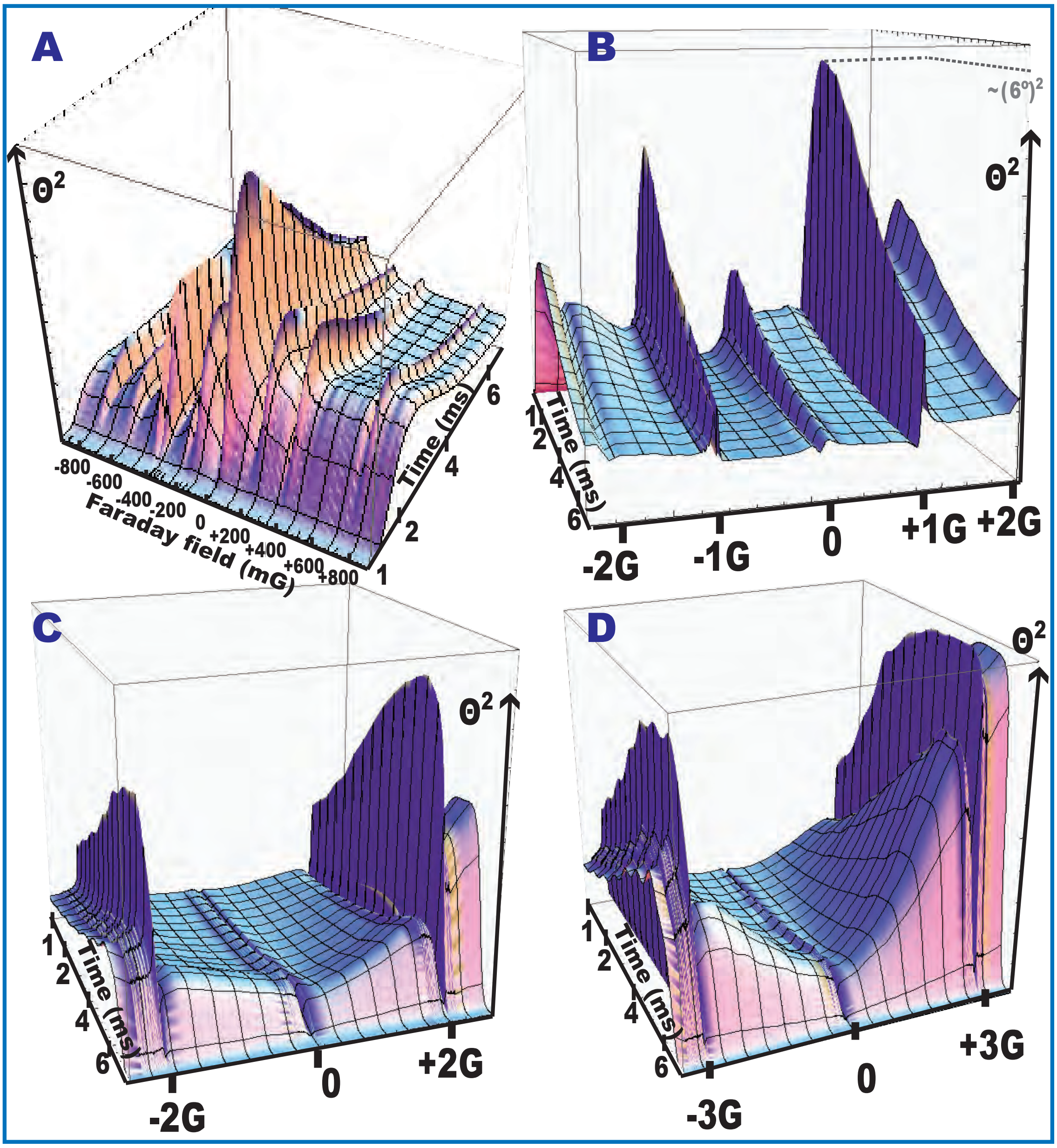

Figure 2.8: Nonlinear Faraday rotation in a cloud of cold atoms at non-zero magnetic field. The AM NMOR (AMOR) resonances are formed when the pump light is modulated at twice the Larmor frequency due to the two-fold symmetry of linearly polarized light. The pump light was modulated at a range of discrete frequencies to be resonant with Faraday magnetic fields of A:±200 mG, B:±1 G, C:±2 G, and D:±3 G. A square modulation of the pump beam was used, which generated higher order sidebands at the lower 200 kHz and 1 MHz modulation frequencies (see text). At higher stroboscopic-pumping frequencies, the nonlinear effect increasingly blends into the linear one (C, D). [Data: A. Wojciechowski, E. Corsini - Collaboration: J. Zachorowski - Project management: A. Wojciechowski - PI: W. Gawlik]

The technique's primary limitation stems from the limited measurement time, inhomogeneous magnetic field, and power broadening. Power broadening can be addressed with the use of separate pump and probe beams (as opposed to a single pump/probe beam); transferring the laser-cooled atom cloud to an optical dipole trap would increase the measurement time to ∼1 s, which would also increase the light-atom coupling (which creates the Zeeman coherences).

2.12 Acknowledgements

In this Chapter we acknowledge valuable discussions with D. Budker, W. Chalupczak, R. Kaiser, M. Kubasik, and S. Pustelny and the funding support by the Polish Ministry of Science (Grant No. N N505 092033 and N N202 046337), by the Foundation for Polish Science Team Program, and by the National Science Foundation Global Scientists Program.

2.13 Historical perspective of the observation of nonlinear Faraday rotation with laser-cooled atoms

The present observation of nonlinear Faraday rotation with laser-cooled atoms is an additional milestone along the path started in 1845 with the discovery of linear magneto-optical effects by Faraday in 1845 [68]. The discovery of resonant effects by Macaluso and Corbino followed in 1898 [100]. Ensuing discoveries of a host of nonlinear effects followed and continue through today [38, 42] (Fig. 2.9). Nonlinear effects ushered in the era of narrow resonances (∼1Hz - and more recently 1 mHz [23]) with corresponding high resolution of the magnetic field measurement, and provided a sharp tool to probe atomic structures and properties. Extensive work has been done to characterize these resonances in glass cells filled with an alkali vapor with and without a buffer gas.

Laser-cooled atoms provided a new way of containing the atomic medium with Doppler broadening less than the natural linewidth and provided new opportunities to experiment with Faraday rotation. The challenge of having limited measurement time due to the expansion of the atom cloud, and/or the nature of the trap, was overcome by Labeyrie who was first to report the presence of linear Faraday rotation in cold atoms in 2001 [96]. In 2010 Wojciechowski, Gawlik, *et al* reported the first observation of nonlinear Faraday rotation with laser-cooled atoms, as described in this Chapter and in Ref. [142].

Nonlinear effects in laser-cooled atoms entail ground state coherences formed by addressing one single, hyperfine excited state. The ability to address one single excited state opened a new door through which it may be possible to resolve unanswered experimental and theoretical questions that were raised over the last several decades in the extensive work done with alkali atoms in glass cells, in which the Doppler broadening had blurred the experimentalist's view [38, 42]. In addition the technique allows in situ observation (with sub-ms time resolution) of the formation and evolution of the ground state coherence for applications to quantum information [142, 14].

Additional historical details of the path followed by discoveries and applications of magneto-optical effects are given in figure (Fig. 2.9).

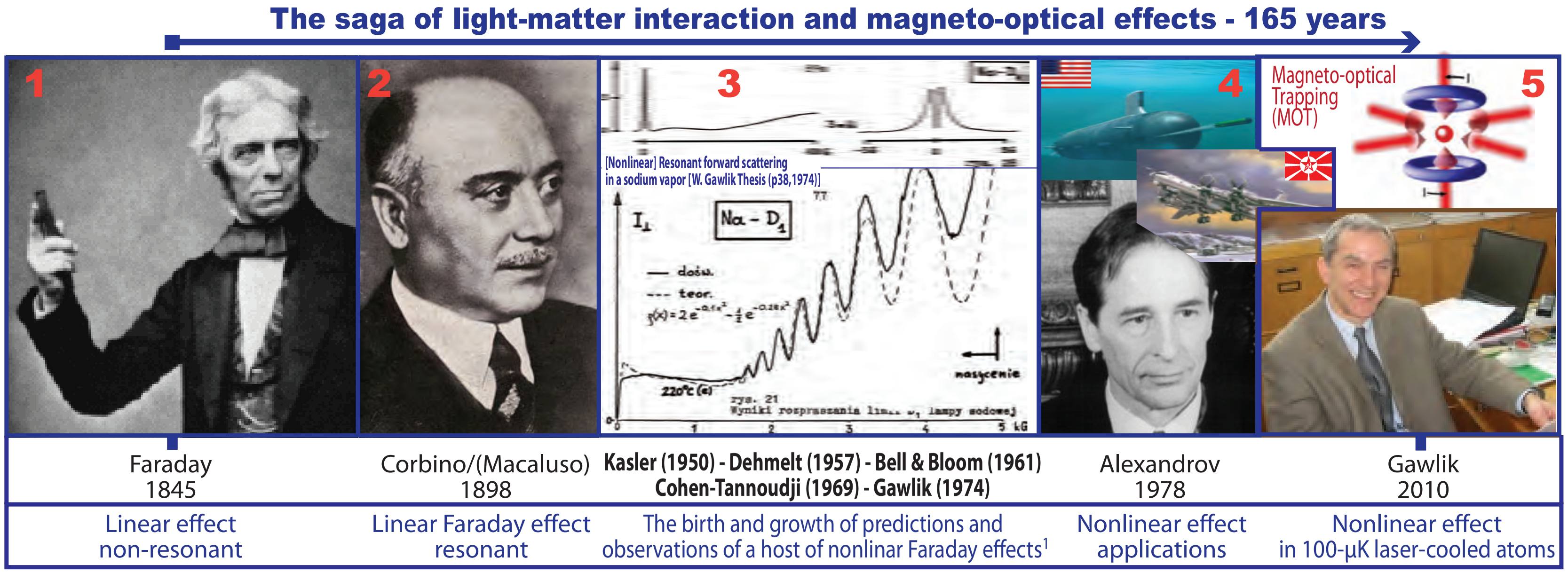

Figure 2.9: The saga of light-matter interaction and magneto-optical effects: 1: M. Faraday (1845) first observed the non-resonant linear effect in a slab of glass [68] (in his hand is the type of glass he used to show that magnetism can affect light in a dielectric material), 2: O. M. Corbino (with D. Macaluso), observed the resonant linear Faraday effect [100], 3: among others (Partial list of participants), A. Kasler [137], H. Dehmelt [62, 61, 117], W. Bell & A. Bloom [28, 27, 31], Bouchiat *et al* [34], C. Cohen-Tanoudji [67], W. Gawlik [73, 75], and D. Budker [38] performed experiments and/or theoretical calculations that were precursor and/or took part in the development of a host of nonlinear magneto-optical effects (including nonlinear Faraday effects), which continues through to the present time. 3: Gawlik *et al* at the turning point from the linear to nonlinear effects. 3-lower: plot of linear Faraday effects in a vapor of sodium atoms at 220°in a forward scattering experiment. [W. Gawlik Ph.D. Thesis p77 [75] (1974) & Gawlik *al* [73], contrasting sharply with the narrower nonlinear effect [3-upper] in a forward scattering experiment with lasers in a sodium vapor [first observation by W. Gawlik Ph.D. Thesis, p89 [75] (1974) & Gawlik *et al* [73])]. 4: an example (among others) of direct application of non linear effects: Y. B. *(or E. B.)* Alexandrov testified during his concluding remarks at the MURI meeting at the United States Navy "Naval Support Activity (NSA)", Panama City, Florida, on June 9th, 2006: "We were recruited [in the 1960s] by [the] Soviet Navy to take part in [a] big collective project to develop extremely super sensitive airborne magnetometers [based on nonlinear magneto-optical effects] for searching for American submarines" (reflecting the Soviet Union Navy's [4-upper] alarm at the decreasing acoustic signature of the United States' submarines); 4-middle: Tupolev 142MZ Bear-G Soviet Anti-Submarine Aircraft; 5: A group led by W. Gawlik was first (2010) to observe the nonlinear resonant Faraday rotation in a cloud of atoms laser-cooled to ~100 μK (with the Magneto-optical trapping technique).

Chapter 3

A Self-Oscillating, All-Optical, Atomic Magnetometer With High Dynamic Range and Large Bandwidth

Related publication
Title:“Robust, High Speed, all Optical Magnetometer”
Journal:Rev. Sci. Inst. 77, 11 (2006)
Authors: J. V. Higbie[1], E. Corsini[1], and D. Budker[1,2].
Affiliations:
[1]Department of Physics, University of California, Berkeley, CA 94720-7300
[2]Nuclear Science Division, Lawrence Berkeley National Laboratory, Berkeley CA 94720
pacs: 06.20.fb,06.30.Ft,32.10.Fn, 3230.Bv
Keywords: self-oscillating, atomic spin, atomic magnetometer.

Abstract

In this chapter we show, in a magnetically shielded laboratory environment, the principle and realization of a self-oscillating all-optical magnetometer based on nonlinear magneto-optical rotation (NMOR) [a subset of the nonlinear Faraday rotation effect]. The magnetometer has separate modulated pump and unmodulated probe beams; the principle of operation falls in the category of amplitude modulated nonlinear magneto-optical rotation (AM-NMOR or AMOR). The magnetometer has been operated both with vertical-cavity surface-emitting lasers (VCSEL [Chapter 3, Appendix 3.12, Fig. 3.8]) and with conventional edge-emitting diode lasers. Pump and probe beams originate from the same laser and are delivered by optical fiber. It is also possible to capture the magnetometer signal (the oscillation of the outgoing probe beam polarization) with optical fibers, providing an all-fiberized connection between the optics/signal-processing and the sensor. The scheme lends

itself to a modular design, to miniaturization, and to sensitive field measurements with a non-metallic sensor. The device achieves a bandwidth exceeding 1 kHz and a sensitivity of approximately 3 nG$\sqrt{Hz}$.

3.1 Introduction to the self-oscillating configuration

The advent of narrow linewidth, low cost laser diodes and the growing availability of fiberized optical components has renewed an interest in atomic magnetometers for geomagnetism, biomagnetism, [30, 144, 56] and for space-based applications [106, 29, 148, 119, 18, 79]. But moving from the laboratory to applications in the field and in space, places significant new demands on the robustness, size, weight, and power consumption of magnetometers. The self-oscillating magnetometer configuration, originally proposed by Bloom [31] is an attractive approach that addresses many of these demands.

In self-oscillation, the detected optical signal, modulated at the Larmor frequency (or a harmonic), is used to drive the magnetic resonance, either with radio-frequency coils or, as in the present work, by optical excitation of the resonance. When the signal is sufficiently amplified, the oscillation builds up spontaneously (seeded by noise) at the resonant frequency. Figure 3.1 shows the laser's optical frequency swept successively through the D1 transitions of ^{87}Rb F=2, ^{85}Rb F=3, ^{85}Rb F=2, and ^{87}Rb F=1. Through the optical frequency sweep we observe spontaneous self-oscillations at the respective AM NMOR resonant frequencies (twice the Larmor frequencies for the applied bias field), of the rubidium species (in this measurement an anti-relaxation coated cell containing a vapor of natural abundance rubidium is used). In this example the self-oscillation frequencies for ^{87}Rb and for ^{85}Rb are approximately 10.8 kHz and 7.6 kHz respectively due to the different gyromagnetic ratios of the species (3:2 in relative magnitude). In addition we observe multiple resonances within each of the optical transition Doppler broadened linewidths, due to the hyperfine structure of the first excited state, which leads to AM NMOR resonances involving either a dark or bright (cycling) state or a combination thereof (additional details are given in Chapter 3). The spontaneous nature of the self-oscillation replaces the necessity of slow scan to search for the resonance, and the need of a lock-in amplifier, resulting in light, compact, low power and simple electronics.

3.2 A new twist in self-oscillation technique

Among other recent works with self-oscillating schemes, a self-oscillating all-optical magnetometer based on electromagnetically induced transparency (EIT) was demonstrated by Matsko et al. [102], and a self-oscillating magnetometer based on NMOR was reported by Schwindt *et al*, [126]. In the work of Schwindt *et al*, the functions of pumping and probing were fulfilled by a single frequency-modulated laser beam. As a result the detected signal was a product of the rotating atomic alignment and of the modulated detuning, resulting in a complicated wave form that required significant electronic processing before being suitable for feeding back to the laser modulation, as required in the self-oscillating scheme.

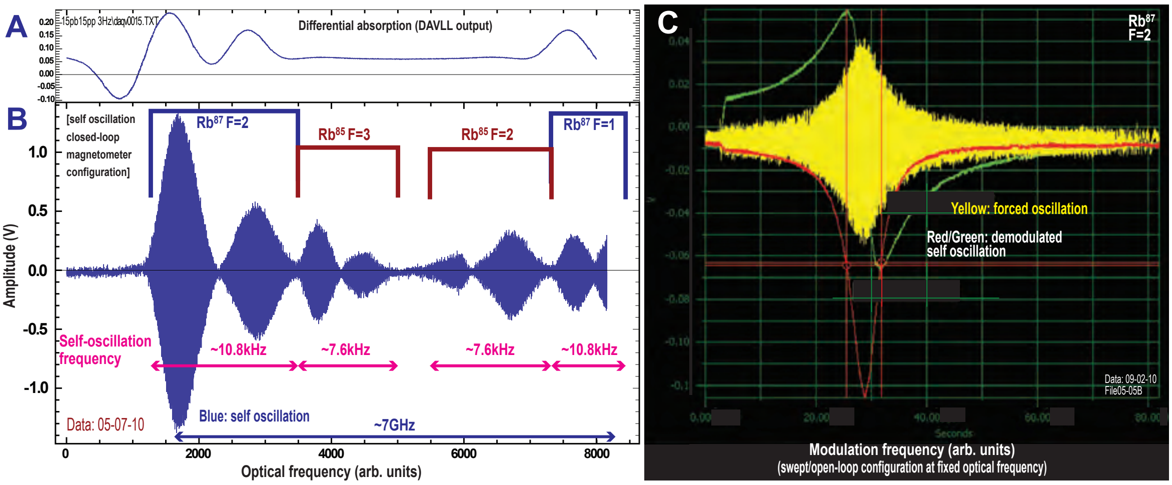

Figure 3.1: A,B: The optical frequency is swept in succession through the four rubidium D1 optical transitions of a natural-abundance rubidium vapor [^{87}Rb (F=2,1) & ^{85}Rb (F=3,2)]. A: Differential absorption (DAVLL output, or linear Faraday rotation). B: self-oscillation in 4×1-in, cylindrical, natural abundance rubidium, alkali vapor cell, with an anti-relaxation alkene-coating. With the proper gain and relative phase shift between the probe signal output and the pump modulation input, in a closed-loop configuration [Sec. 3.4.3]), self-oscillation occurs spontaneously at twice the respective rubidium species Larmor frequencies (due to the two-fold degeneracy of linearly polarized light) for the applied bias magnetic field. Two self-oscillation maxima are observed in each hyperfine optical transition (see text).
C: in this measurement the magnetometer is in swept (or open-loop) configuration (Sec. 3.4.2), a ^{87}Rb-enriched vapor in a 2×1-in cylindrical cell is used, and the modulation frequency of the pump light is swept through the NMOR resonance (with the laser light locked on the D1, F=2, optical transition). The AM-NMOR resonance is shown with the demodulated outputs of a lock-in (blue/red traces). The self-oscillation similarly occurs spontaneously (yellow) at twice the Larmor frequency [data/project manager: E. Corsini (2009-12) - Collaboration: T. Karaulanov - PI: D. Budker - Apparatus: Ch:5: “after” version in Fig.5.1B].

In this Chapter, we present a simple alternative that avoids many of the difficulties encountered in the single-beam self-oscillating NMOR experiment. The use of two laser beams, of a modulated pump and an unmodulated probe, make the optical-rotation signal accurately sinusoidal, avoiding the complexity of digital or other variable-frequency filters in the feedback loop.

Another advantage of the two-beam configuration is the ability to optically adjust the relative phase of the detected signal and the driving modulation by changing the angle between the probe and pump linear polarization axes (Sec. 3.5.2). For magnetometry with a large bias field and/or requiring a wide range of fields, the simple optical tuning of the phase in the feedback-loop promises near-uniformity and long-term stability with respect to frequency, on par with sophisticated electronic phase shift control systems.

3.3 AM-NMOR (AMOR)
Analogy to the driven damped harmonic oscillator

For the NMOR resonances considered in this chapter, both pump and probe are linearly polarized. The pump prepares a state whose alignment symmetry axis is parallel to the pump polarization (atomic alignment), the probe detects the atomic alignment, and the balanced polarimeter measures the optical rotation.

Assuming the in-going probe and pump polarizations to be parallel, the amplitude and phase of the observed optical-rotation signal are described by the complex Lorentzian $(\delta - i\gamma/2)^{-1}$, where $\delta \equiv 2\pi(\nu - 2\nu_L)$ is the detuning from resonance, γ is the full width (in modulation frequency) at half maximum of the resonance, and ν_L is the Larmor frequency. The phase shift relative to the pump modulation as a function of δ is the argument of this complex Lorentzian,

$$\Phi = \frac{\pi}{2} + tan^{-1}\left(\frac{2\delta}{\gamma}\right). \tag{3.1}$$

Consequently the relation of optical pumping to the modulated probe beam polarization is the same as that of a driven damped harmonic oscillator.

3.4 Effects of relative phase-shift between the optical signal and the pump beam amplitude modulation.

(in self-oscillation and forced oscillation configurations)

3.4.1 Phase-shift between signal and pump modulation

At the center of the NMOR resonance there is no phase lag between pumping and precession of the ensemble of polarized alkali atoms. Equivalently, in the limit of short pump pulses, the precessing axis of atomic alignment is parallel to the pump polarization at the optical pumping instant. If the probe polarization is parallel to the pump polarization, the probe polarization-rotation signal will pass through zero (for a “dark state” coherence) at that instant (Eq. 3.1), so that the optical rotation signal is 90°out of phase with the pump modulation. The effect of phase shift is considered below in the two magnetometer configurations (open and closed loop).

3.4.2 Swept (open-loop - or forced oscillation) magnetometer configuration

Swept or open-loop configuration was used in most previous NMOR experiments. In this configuration the modulation of the pump is applied from a stable reference oscillator; there is no feed-back of the optical-rotation signal. The rotation signal is demodulated with a lock-in amplifier at the same reference frequency (or one of its harmonics). A typical optical-rotation response (measured with a lock-in) to a swept modulation frequency is shown in Fig. 3.1C (red and green traces). In this configuration the width and amplitude of the resonance, together with the noise floor, determine how well the center frequency is measured, and consequently determine the magnetometer's sensitivity. With a slowly changing magnetic field, in order to maintain the resonance condition, the reference frequency can be updated from the output of the lock-in; the rate, and ultimately the magnetometer's bandwidth, is governed by the update-rate.

3.4.3 Self-oscillation (closed-loop) magnetometer configuration

By contrast to the open loop configuration, in the self-oscillating configuration the rotation signal is measured and fed back to the pump modulation input in place of the oscillator reference frequency (Fig. 3.5). The signal must first be shifted by 90°(Sec. 3.4.1) in order for coherent buildup at the central resonant frequency to occur. Deviations from this phase shift will result in oscillation away from the resonance line center to maintain a total 2π-phase around the loop. Self-oscillation will continue so long as the magnitude of the gain (which decreases as the oscillation moves away from line-center) is sufficient to sustain oscillation at the shifted frequency. As a result, precise control of the phase shift as a function of Larmor frequency must be implemented to avoid (or compensate for) systematic deviations of the oscillation frequency when the magnetic field varies (Sec. 3.4.1). Precise control of the phase shift also insures maximum gain in the self-oscillation loop. In this configuration the sensitivity of the magnetometer depends on the precision with which the self-oscillating frequency is measured.

3.4.4 Further effect of phase shift in the self-oscillation configuration

The effects of changing the phase shift in the feedback network of the closed-loop magnetometer are shown in Fig. (3.3). The magnetometer adjusts its oscillation frequency so that the phase shift of the NMOR resonance (Fig. 3.3B) cancels that of the feedback network. Since the phase shift of the NMOR resonance is an arctangent function of the detuning from resonance (similar to a damped harmonic oscillator), this results in a change in oscillation frequency which is proportional to the tangent of the applied phase shift.

As seen in Eq. (3.1) the relation between phase shift Φ and modulation frequency detuning λ also depends on the width of the resonance γ, which in turns depends on light power. Precise control of the phase shift cancels the light power dependent deviation of the self-oscillating frequency (Fig. 3.2).

3.5 Two advantages of separate pump and probe beams

3.5.1 Undistorted optical rotation signal

The modulation of the optical-rotation is, to a good approximation, sinusoidal, and at twice the Larmor frequency (since atomic alignment is described by a rank 2 spherical tensor, and the corresponding spin probability distribution is twofold symmetric [118]). In the case of a single-beam experiment (as in most past NMOR experiments), the signal modulation is the product of the optical-rotation (which would be observed with an unmodulated probe) and of a function describing the modulation of the pump (a square, sinusoidal, or other modulation). Consequently, with a single beam experiment, the detected signal is highly non sinusoidal. For self-oscillation such a signal would require filtering (which introduces undesirable phase shifts) so as to closely resemble the reference frequency of Sec. 3.4.2 (as in the work of Ref. [126]). In contrast, when using a separate pump and an unmodulated probe, the detected optical-rotation signal is a near-perfect sinusoid; such a

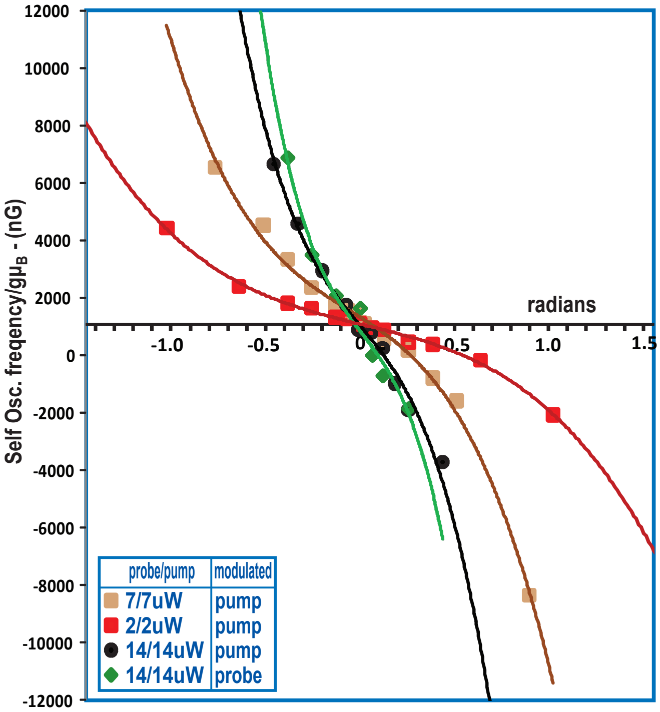

Figure 3.2: Dependence of detuning from AM-NMOR resonant frequency
1) On the relative phase shift between the probe optical signal output and the pump modulation input (shown in radians)
2) On the width of the NMOR resonance (power dependence).
In this measurement the power of the probe or pump beam was modulated by a fixed fractional quantity for four discrete mean power settings (shown in four colors - pump and probe powers are equal at each setting). The frequency shift was recorded in Hz/(gμ_B) [≡nG] units as a function of phase shift from center line resonance. We observed the expected self-oscillation frequency shift arctangent dependence on the phase shift (δ dependence in Eq.3.1). We also observed the dependence of the arctangent slope on power (which is the dependence on Γ in Eq.3.1 [width of resonance], or the dependence on the "Q" of the resonance). Each curve is the frequency shift arctangent function of the phase shift for a given light power. The vertical offset reveals the sub-optimum electronic phase shift which had been thought to be set at the optimum value. Future iterations of the self-oscillation configuration will add a phase modulation to generate an error signal to maintain optimum phase shift [data: E. Corsini, Project manager: J. Higbie, PI: D. Budker (2006) -Apparatus: Ch:5: "before" version in Fig.5.1A].].

signal requires only amplification to make it mimic the reference oscillator od Sec. 3.4.2.

3.5.2 A novel idea: an all-optical control of the phase shift [patent application WO2009/073256]

Analog filter networks capable of generating accurate and stable 90 phase shifts over a broad range of frequencies are difficult to construct. Digital phase shifters add complexity, power consumption, and degradation of the signal. The use of separate pump and probe beams offers a natural and all-optical means of shifting the relative phase between modulation and optical rotation. Indeed, since the rotation of the probe polarization is determined by the angle of the incident polarization with respect to the axis of atomic alignment, which itself rotates uniformly in time, a fixed rotation of the incoming probe polarization is equivalent to a translation in time of the output signal (i.e., a phase shift). Since this phase shift is purely geometrical, it has no frequency dependence and possesses the long-term stability of the mechanical mounting of the polarizers.

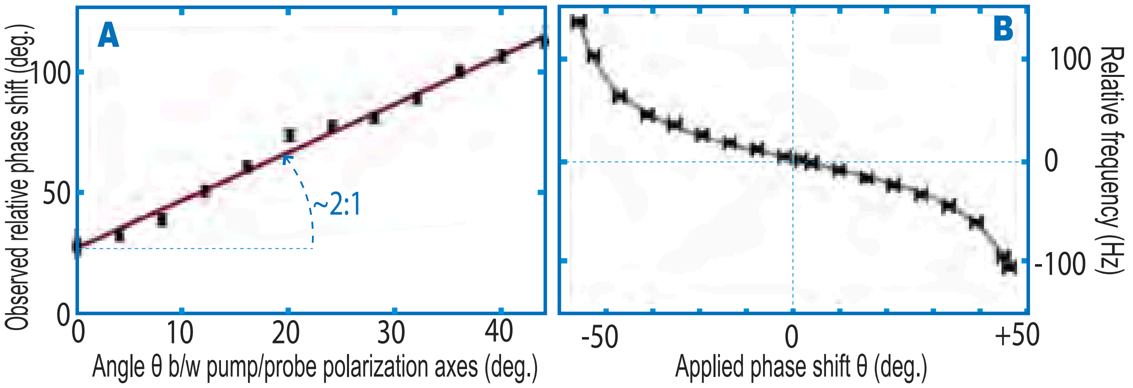

Figure 3.3: A: in driven oscillation, at the resonant AM NMOR modulation frequency, the relative phase of the optical rotation signal and the reference oscillator is a compound phase-shift which is of the sum of the 90° phase-shift between pump and probe modulations (for an angle Θ=0 between pump and probe polarizations [parallel polarization axes]) and of the electronic phase-shift. As the angle Θ between the pump and probe polarization increases the compound relative phase-shift increases by an amount 2Θ due to the two-fold degeneracy of linearly polarized light.
B: in self-oscillation, the frequency is a function of phase detuning from the resonant condition (Eq. 3.1). In B is shown the frequency shift from resonant frequency as a function of phase detuning (dialed by manually rotating the relative optical phase between pump and probe polarization axes). In contrast to electronic phase shifters, the "all-optical" phase shift control is purely geometrical, long-term stable, and has no frequency dependence [data/project manager: J. Higbie, collaboration: E. Corsini, PI: D. Budker (2006) - Apparatus: Ch:5: "before" version in Fig.5.1A].

To demonstrate the optical phase shift of the polarization-rotation signal, in the open-loop configuration, we performed a measurement of the relative phase shift (between the driving reference sine wave and the amplified signal output) as a function of the pump polarizer angle. The resulting curve reveals the expected linear dependence (Fig. 3.3A) with a slope reflecting the expected "two-to-one" ratio of phase-shift to polarizer angle (the optical-rotation signal undergoes two cycles as the atomic alignment rotates by 360°).

The present self-oscillating magnetometer scheme with the all-optical phase shift control, is under PCT Patent Application number WO2009/073256, and under the Lawrence National Berkeley Lab Technology Transfer and Intellectual Property Management entitled "Robust All-Optical Atomic Magnetometer" reference number IB-2353.

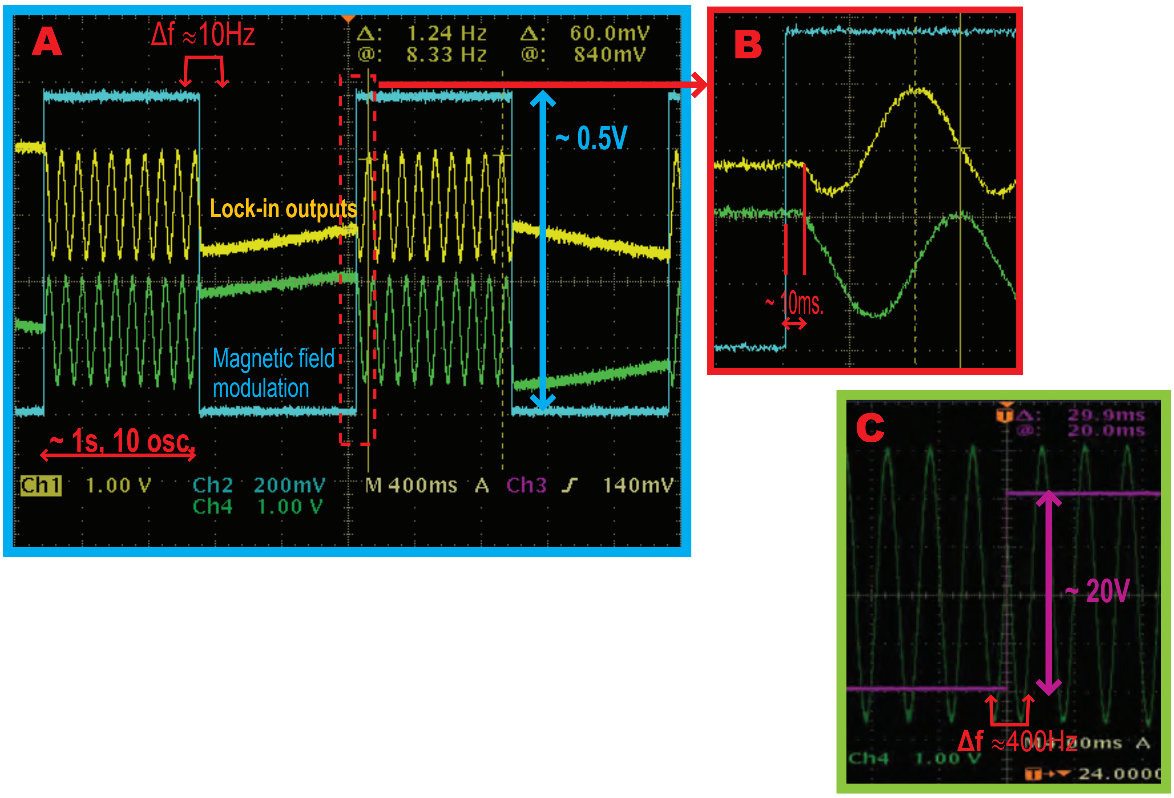

Figure 3.4: A,B: the bias magnetic field is modulated with an auxiliary coil so that the self-oscillation frequency toggles between values differing by ~10 Hz ($\simeq 10\mu$G). The self-oscillation frequency signal is heterodyned with a lock-in fixed reference frequency equal to the self-oscillation frequency when the ~0.5 V negative voltage of the square modulation is applied to the coil. When that voltage toggles to ~0.5 V positive voltage, the Larmor frequency changes instantaneously as shown on the green and yellow traces of the lock-in outputs. B: the 10ms time delay corresponds to the lock-in time constant.
C: A larger ~20 V square modulation is applied to the auxiliary coil. The modulation causes the self-oscillation frequency to toggle by ~ ±200 Hz. The lock-in oscillator reference frequency is set at the average of the two self-oscillation frequencies. No ringing or delay is observed [Data: E. Corsini - Project manager: J. Higbie - PI: D. Budker (2006) - Apparatus: Ch:5: "before" version in Fig.5.1A].

3.6 High bandwidth

A self-oscillating magnetometer combines the properties of atomic spins (which have no inertia) with a feedback-mechanism; the combination achieves near-instantaneous response to changes in the magnetic field. The bandwidth of the magnetometer was assessed by applying a small modulation to the bias magnetic field. In one measurement, a slow square-wave modulation was superimposed on the bias field via a separate Helmholtz coil inside the magnetic shield. Tracking of the field step was quasi-instantaneous, without apparent overshoot or ringing. The magnetometer response was monitored by heterodyning the oscillation frequency with a fixed reference frequency on a lock-in amplifier, with the lock-in time constant set to approximately the oscillation period ($\simeq$10 ms - to remove the conjugate [sum] frequency component). The resulting low-frequency beat signal was recorded on an oscilloscope. Inspection of the wave forms so obtained revealed the sudden shift in the oscillation frequency as the magnetic field toggled between the two values set by the square modulation (Fig. 3.4A-B). The measurements were repeated for a larger square modulation amplitude (Fig. 3.4C) and with a lock-in time constant set to ($\simeq$10 μs). In a related experiment, a small sinusoidal modulation was added to the bias field received, and the power spectrum of the self-oscillation waveform was observed on a spectrum analyzer (data not shown). The sidebands were observed, offset from the oscillation (carrier) frequency by an amount equal to this bias-modulation frequency; their relative power was equal to that expected if the oscillator tracked the changing magnetic field with no delay or diminution of amplitude, with a modulation frequency in excess of 1 kHz.

3.7 Experimental setup and procedure

The experimental apparatus (Fig. 3.5) reveals the simplicity of the self-oscillating scheme. It consists of a cylindrical paraffin-coated ^{87}Rb cylindrical vapor cell (2×2 cm), traversed by linearly polarized pump and probe laser beams. The beams were from a single external-cavity diode laser on the rubidium D2 line. The optical frequency was stabilized $\sim$ 300 MHz below the center of the D2, F=2, Doppler-broadened, optical transition line with a dichroic atomic vapor laser lock [58, 146]. The probe beam was unmodulated. The pump was amplitude modulated with an acousto-optic modulator (AOM). Pump and probe were delivered to the cell by separate polarization-maintaining fibers. After exiting the cell, the pump beam was blocked and the probe analyzed with a balanced polarimeter consisting of a Rochon polarizing beam splitter and a pair of photodiodes. The difference photocurrent was amplified with a low-noise transimpedance amplifier (Stanford Research Model SR570) and passed through a resonant LC filter centered at 20 kHz with a bandwidth of 11 kHz, much wider than either the NMOR resonance ($\sim$80 Hz) or the desired magnetometer bandwidth ($\sim$1 kHz). This filter reduced jitter in the frequency-counter readings, but was not necessary, in principle. The pump modulation was derived from this amplified signal by triggering a pulse generator on the negative-slope zero crossings of the signal; the derived pulse-train switched on and off the radio frequency power delivered to the AOM with a duty cycle chosen to be approximately 15%. The modulation of the pump closed the feedback loop.

For characterization of the magnetometer in the laboratory, the vapor cell was placed in a three-layer cylindrical magnetic shield (Fig. 5.1A) with internal coils for the generation of a stable, well-defined magnetic bias field and gradients. The ^{87}Rb density in the cell was maintained at an elevated value ($\simeq 5 \times 10^{10}/\text{cm}^3$, measured by absorption) by heating the interior of the magnetic shields to around 40°C with a forced-air heat exchanger.

The photodiode signal was monitored with an oscilloscope and a frequency counter (Stanford Research Model SR620). Provided that the trigger threshold of the pulse generator was close to zero (i.e., within a few times the noise level of the signal), oscillation

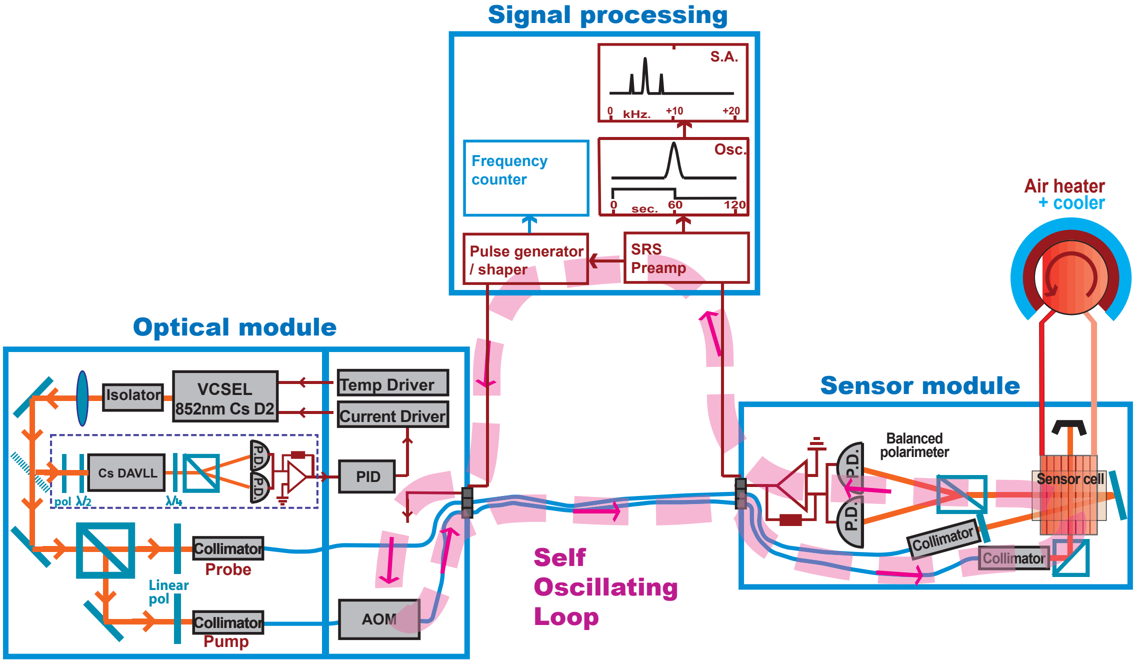

Figure 3.5: The apparatus is divided into three distinct modules: the optical, the sensor, and the signal processing modules. The optical module consists of a VCSEL (or other diode laser), a dichroic atomic vapor laser lock (DAVLL) for optical frequency stabilization, laser current and temperature controller; the optical module lends itself to miniaturization with an optical cage system (Thorlabs). The sensor module consists of an alkali anti-relaxation coated vapor cell (shown), enclosed in a 3-layer shield (not shown). Probe and pump beam are channeled to the sensor cell with optical fibers. The signal processing module functions can be miniaturized by means of custom-made electronics.

occurred spontaneously when the loop was closed, at a frequency set by the magnetic field. Optimum settings for the magnetometer sensitivity were found to be approximately 7 μW mean incident pump power, 7 μW continuous incident probe power, and optical absorption of around 60% at the optical frequency lock-point. A sensitivity of 3 nG was achieved for a measurement time of 1 s at these settings, as discussed in detail in Sec. 3.8.

Several alternative configurations were also implemented. In place of the balanced polarimeter described above, a configuration consisting of a polarizer nearly orthogonal to the unrotated probe polarization (cross-polarizer) followed by a large-area avalanche photodiode (APD) module was employed. This configuration had high detection bandwidth, but suffered from lower common-mode noise rejection and greater sensitivity to stray light. Moreover, the excess noise factor of the APD module prevented attaining shot-noise-limited operation. With the APD module, self-oscillation at frequencies up to ~ 1 MHz was achieved.

In another configuration, frequency modulation of the pump laser was employed. This configuration worked well, but the laser frequency lock point was found to depend subtly on the state of self-oscillation of the magnetometer. For this reason, it was found preferable to employ amplitude modulation of the pump laser with an external modulator (positioned after the light pick off for laser frequency stabilization).

The magnetometer was moreover operated with two separate vertical-cavity surface-emitting diode lasers (VCSELs) as pump and probe beams, on the D1 line of rubidium. The low power requirements, small size, and reliable tuning of VCSELs render them appealing for use in miniaturized and portable magnetometers. Amplitude modulation was also performed with an inline fiber-optic Mach-Zehnder interferometric modulator, which permits further miniaturization and considerably reduced power consumption relative to the acousto-optic modulator (AOM).

3.8 Results - measured sensitivity

The magnetometer sensitivity was measured by the Allan deviation (a time and frequency standard of measurement) as a function of sampling time T and is shown in Fig. 3.6. The data shows the expected $1/T$ dependence for times below ~0.1 s. For measurement times in excess of ~0.1 s, additional sources of noise and drift become dominant. The two main additional sources are external magnetic field fluctuations and noise in the bias field current. We measured fluctuations of ambient magnetic fields with a fluxgate magnetometer external to the shields at approximately $20\,\mu\mathrm{G}/\sqrt{Hz}$ above a $1/f$ corner frequency of ~0.3 Hz. With a measured shielding factor of 3×10^5, this implies a white magnetic field noise of $70\,\mathrm{pG}/\sqrt{Hz}$ averaged over the volume of the vapor cell. The expected average noise on the supplied bias field inside the shield is better than $6\,\mathrm{nG}/\sqrt{Hz}$ between 0.1 and 100 Hz. This value is of the same order of magnitude as the observed Allan deviation floor, although direct and reliable measurements of this bias current have not been achieved. Noise on the bias-field current could be distinguished from other sources by use of a magnetic gradiometer (see, for example, a description of a gradiometer based on a pair of FM NMOR sensors in Ref. [145]), though the small size of our magnetic shield has so far precluded such a measurement.

Other noise sources include sensitivities of the oscillation frequency to laser power and detuning. In addition, and as described in Section 3.4.4, a sensitivity to pump or probe power arises when the feedback-network phase shift deviates from the value which produces maximal oscillation amplitude. The NMOR self-oscillation frequency depends on the linewidth (Eq. 3.1), while the linewidth depends on optical power through the effect of power broadening. Changes in pump or probe power produce changes in phase shift which in turn produce deviations of the self-oscillation frequency. This effect vanishes to first order precisely on the NMOR resonance (optimum feedback-network phase shift). Additional mechanisms for translating power and detuning fluctuations into oscillation-frequency fluctuations are currently being investigated.

3.9 Retro-reflection and remote sensing

One measurement was performed with a retro-reflector consisting of a glass sphere silver-coated on one hemisphere (Fig. 3.7A-B - set up not shown). The sphere was po-

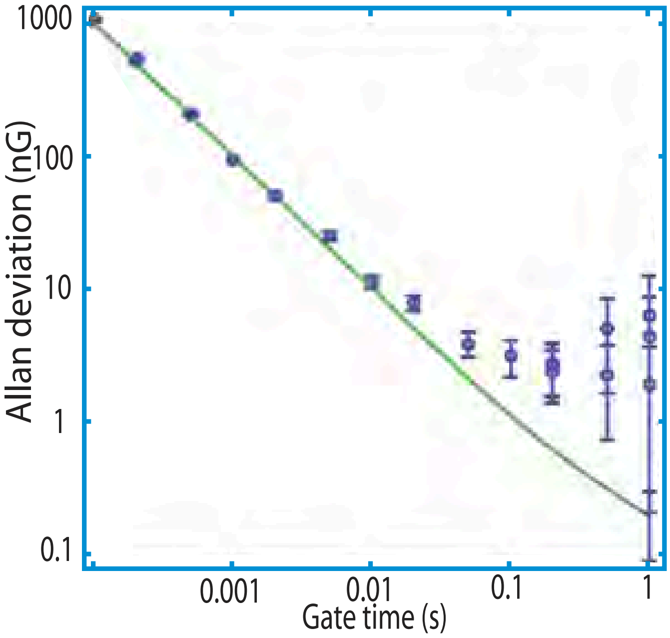

Figure 3.6: We observe the expected $1/T$ dependence for gate times below ∼0.1 s and a drift for longer gate times (see text). [Data/Project manager: J. Higbie - Collaboration: E. Corsini - PI: D. Budker (2006) - Apparatus: Ch:5: "before" version in Fig.5.1A].

sitioned ∼1 m from the shield exit-optical port. No appreciable loss of performance was observed (data not available). The measurement was an in-lab proof-of-principle of remote sensing in a magnetometer in self-oscillating and swept configurations, and was the forerunner of a planned remote sensing field measurement and made possible with the field-able magnetometer device which construction is described in Chapter 4, Part I. A possible future remote sensing application is depicted in figure 4.13; the application uses a graduated index GRIN-sphere lens such as the one described by Handerek *et al* in 2005 [81] (Fig. 3.7C-F).

3.10 Conclusion

We have demonstrated a self-oscillating two-beam magnetometer based on amplitude modulated nonlinear magneto-optical rotation (AM NMOR [AMOR]) and have shown that the independent adjustment of pump and probe polarizations provides a frequency-independent means of supplying the phase shift necessary for self-oscillation. Moreover, the use of an unmodulated probe eliminates the necessity of elaborate filtering procedures, producing instead a clean sine wave suitable for a feedback/self-modulation signal. The resulting device possesses a high bandwidth and a measured sensitivity of 3 nG with 1 s measurement time. Considerable improvement, approaching the fundamental atomic and optical shot-noise limit of ≤30 pG in 1 s measurement time for a ∼6 cm^3 cell, is expected through the use of quieter amplifiers and a more thorough control of the electronic phase shifts (incorrect phase shift cause light-power-dependent and laser-frequency-dependent ef-

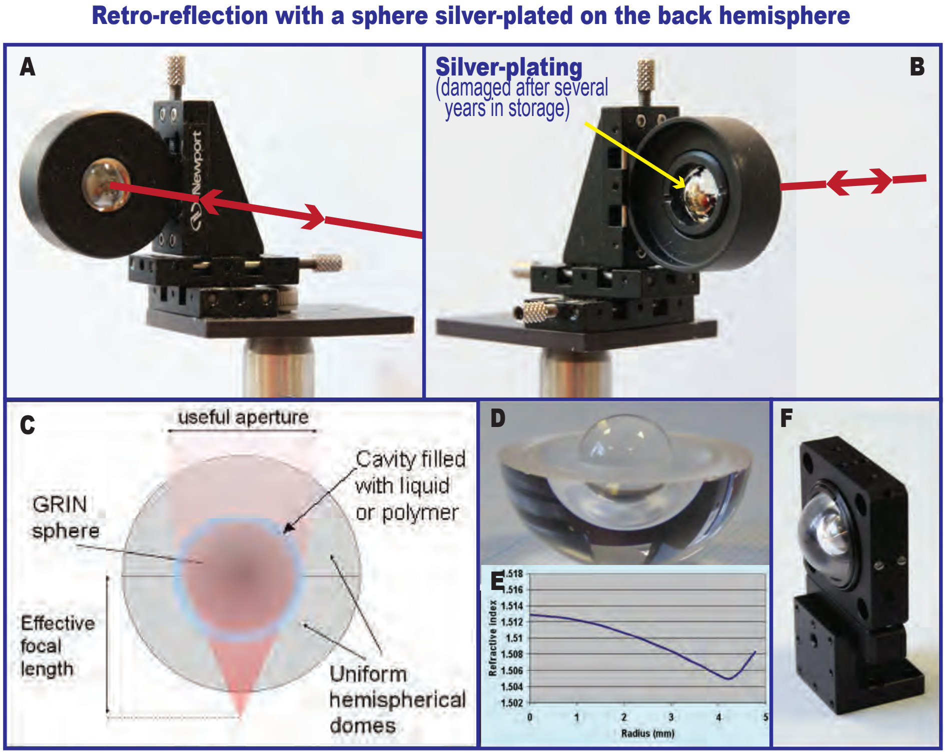

Figure 3.7: A,B: semi silver-coated glass sphere (courtesy of Joseph Tringe, Lawrence Livermore, National Laboratory). C-F: graduated index (GRIN) sphere-lens as devised by Handerek *et al* in 2005 [81].
[Data/Project manager: J. Higbie - Collaboration: E. Corsini - PI: D. Budker (2006) - Apparatus: Ch:5: “before” version in Fig.5.1A - Photographs (A,B -2012): E. Corsini].

fects). The fundamental constituents of this magnetometer are small and lightweight, lending themselves to compact and low power designs for the field and for space-borne applications. Operation in the geomagnetic range of fields has been achieved. In Chapter 4, Part II, the robustness of the self-oscillation configuration in an unshielded environment and an arbitrarily directed geomagnetic field will be investigated. Performance in the presence of splitting of the NMOR resonance line by the quadratic Zeeman shift, in the self-oscillation configuration, will also be shown.

3.11 Acknowledgments

In this chapter we acknowledge the project management by J. Higbie, discussions with E. B. Alexandrov, S. M. Rochester, and J. Kitching, and contributions of V. V. Yashchuk and J. E. Stalnaker to the design and construction of the magnetic shields, coils, and the vapor-cell heating system. This work was supported by DOD MURI Grant No. N-00014-05-1-0406, by an ONR STTR grant through Southwest Sciences, Inc., and by an SSL Technology Development grant.

3.12 Appendix (Chapter 3) Vertical Cavity Surface Emitting Laser Diodes (VCSEL)

Vertical Cavity Edge-emitting Lasers (VCSEL) are inexpensive (∼\$100 in 2006), are available pigtailed to a fiber, and have output powers of several hundreds of μW [10, 12] (Fig. 3.8). VCSELs are also available in ∼1 cm^3 package complete with a Peltier element and a thermistor for temperature stabilization. The VCSEL presented in this appendix requires a separate temperature and thermal control (Thorlabs).

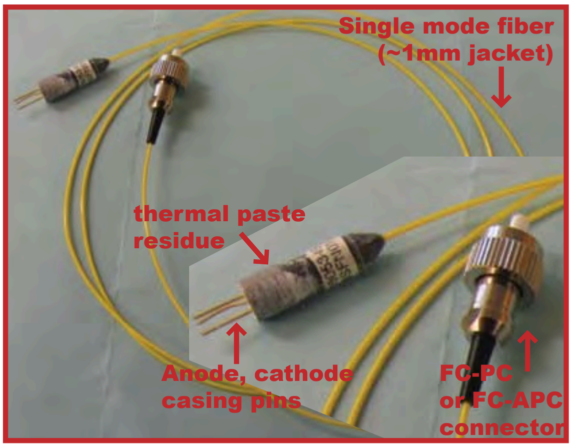

Figure 3.8: The diode is pigtailed (with an intermediate gradient-optics [GRIN] lens) to a single-mode fiber with FC-PC connector. To operate, the diode is mounted on a Peltier-temperature regulated thermal mount (Thorlabs Temperature Controlled Laser Diode Mount). A feedback loop from the temperature sensor to the laser temperature controller maintains the desired temperature.

VCSELs have been used successfully in the work by Affolderbach *et al* [15] on coherent population trapping and in the work by Schwindt *et al* [126] on a self-oscillating magnetometer using NMOR. The large modulation bandwidth capability of VCSELs leads to applications to time and frequency standards and to atomic magnetometry [143].

3.12.1 Conclusion (Appendix - Chapter 3)

In this appendix we have shown that although VCSELs are cheaper and simpler alternatives to other laser diodes for experiments pertaining to NMOR and time and frequency standards [126, 15, 143], off-the-shelf ∼ \$100-VCSELs, when operated at room temperature, may come with center lasing-wavelengths up to 1 nm detuned from the desired resonant alkali optical transition, and may come with a second orthogonal mode. The “luck of the draw”, compromises, and/or substantial heating or cooling of the diode may be required to bring the lasing optical frequency at the desired optical frequency.

v

From figures 3.9 & 3.10 we observe on-resonance lasing on the D1 rubidium and D2 cesium lines, at ~50°C and 4°C respectively. Compromises need to be made to reach the desired optical frequency, at a power sufficient for the experiment, with the second orthogonal mode sufficiently suppressed, and within the limits of the laser temperature controller.

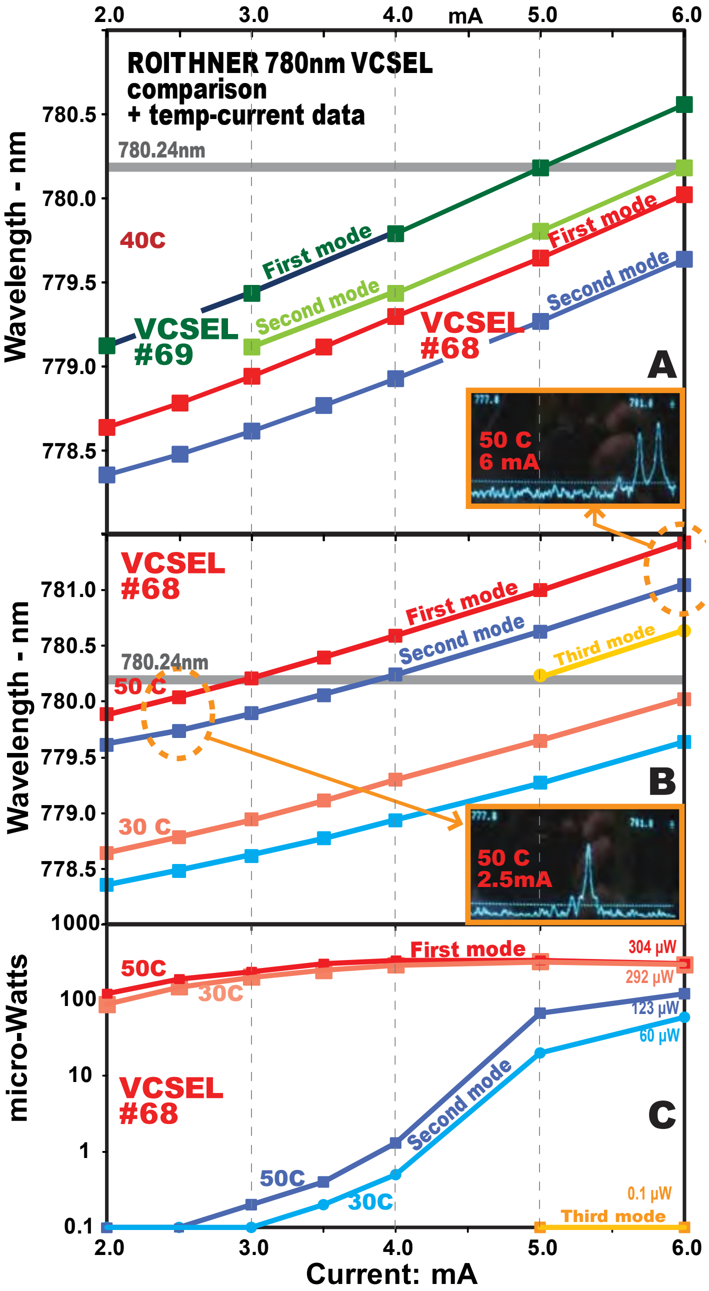

Figure 3.9: The grey horizontal line in A&B is the wavelength in vacuum of the rubidium D2 line. A: comparison of wavelength outputs, at 40°C, of two rubidium (D2-line; 780nm) VCSELs from the same vendor (Roithner). B: comparison of wavelength outputs of one VCSEL at 30° and at 50°C for the two orthogonal modes. C At 50°C and at a current of 6 mA the amplitude of the second mode is 123 μW compared to 304 μW for the first mode. A third mode is observed at 50°near the limiting continuous laser current. [data/project manager: E. Corsini, PI: D. Budker (2005)].

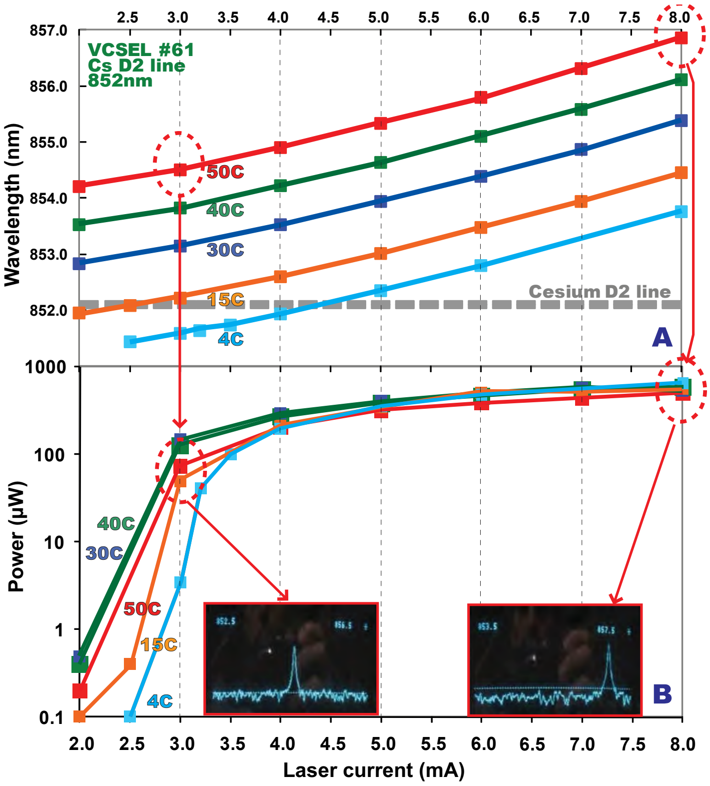

Figure 3.10: A: the cesium (Cs) D2 line VCSEL diode's wavelength is shown at discrete temperature settings. The grey horizontal line is the cesium D2 line's wavelength in vacuum. To achieve sufficient output power and to lase on the Cs D2 line, the VCSEL is cooled to 4°C or below (A & B) which presents a challenge with respect to condensation. There was no indication of a second orthogonal mode in the Cs diode at 50°C or at 4°C (not shown) in contrast to the rubidium VCSEL in Fig. 3.9 [data/project manager: E. Corsini, PI: D. Budker (2005)].

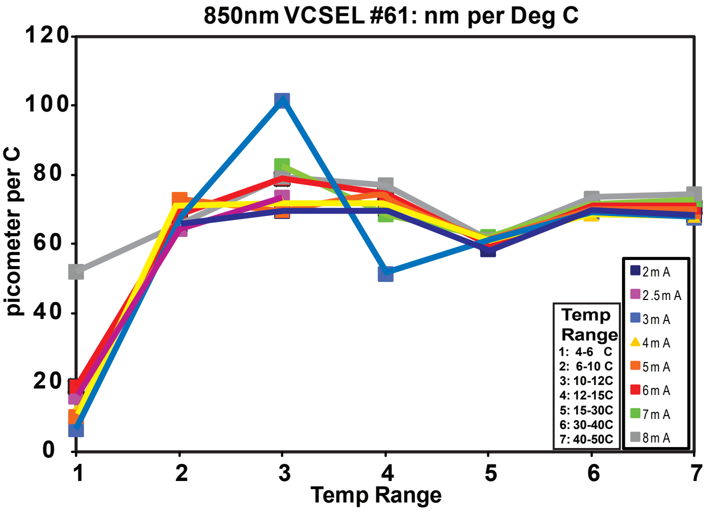

Figure 3.11: The dependence on temperature of the cesium D2 line VCSEL (#61) is shown in a range of discrete temperatures [data/project manager: E. Corsini, PI: D. Budker (2005)].

Chapter 4

Earth's Field Magnetometry (Parts I and II)

Related publication:
Title: "Design and realization of a multi-configurable, non-magnetic, field-able, and transportable optical platform, to investigate and optimize atomic magnetometry at Earth's magnetic field".
Journal: Part I → in preparation (RSI)

Collaboration (2006-2008):
Part I: E. Corsini[1]
Part II: E. Corsini[1], J. H. Higbie[1], C. Hovde[2], T. Karaulanov[1], and B. Patton[1] (from spring 2008).
PI: D. Budker[1,3]
Affiliations:
[1]Department of Physics, University of California, Berkeley, CA 94720-7300
[2]Southwest Sciences, Inc., 1570 Pacheco St., Suite E-11, Santa Fe, NM 87505
[3]Nuclear Science Division, Lawrence Berkeley National Laboratory, Berkeley CA 94720

pacs:32.10Dk, 32.30Dx, 93.85Jk, 93.85Pq, 93.90+y, 91.10Fc, 91.25Dx, 91.25Fd, 91.60Pn, 93.85Jk, 94.30Lr
keywords: atomic magnetometer, multi-configurable, fiber connection, geomagnetism, heading error, amplitude modulation, all-optical.

Abstract

Atomic vapor cell magnetometers are today's most sensitive magnetic field sensors on par with superconducting quantum interference devices (SQUID) [59, 42]; however the performance is achieved near zero magnetic field. At Earth's field commercial portable atomic magnetometers available today have a sensitivity approximately three orders worse [5, 7]. Higbie, Corsini, and Budker previously reported a promising, lab-tested, all-optical, self-oscillating atomic magnetometer configuration for operation at Earth's magnetic field [83] (Ch. 3). To investigate the self-oscillating configuration as well as other configurations and optimization methods at Earth's field we report in Parts I of Chapters 4 and 5 on the designs of two complementary magnetometer platforms. The first one, described in this Chapter, is a portable and field-able optical platform. The second one, described in the next Chapter, is a laboratory-based design, is a complement to the field-able one, and serves to systematically investigate the parameter space pertaining to Earth's field magnetometry, in a well-controlled and magnetically shielded environment. Both designs have rapid and multi re-configurability for an effective evaluation and optimization of several magnetometer schemes suitable for geophysical applications.

The field-able optical platform design embodies multi-configurability within a relatively compact and transportable volume. Mechanical stability of the device (magnetometer sensor-head) is achieved with a tubular-ring design. We present, in Part II, several preliminary measurements to exemplify the robustness of the optical platform design and to reveal several facets of the science of atomic magnetometry at Earth's field. Uses of the device after the work described in this Chapter led to subsequent published (and soon to be published) results which validate the motivations of investigating Earth's field magnetometry, validate a subset of the preliminary measurements shown in Part II, and testify to the capability and to the use of the device.

Chapter 4 - PART I
Design and realization of a multi-configurable, non-magnetic, field-able, and transportable optical platform, to investigate atomic magnetomer/gradiometer configurations at Earth's magnetic field

4.1.2 Introduction

Sensitive detection of magnetic fields in an un-shielded environment has applications encompassing non invasive diagnostic of heart and brain activities [30, 144], plant biomagnetism [56], land-mine detection, geomagnetism, and space exploration. The most sensitive magnetometers are atomic magnetometers, which have achieved sensitivities on the order of pG/$\sqrt{Hz}$ near zero-field, on par with superconducting quantum interference devices (SQUIDs)(a record of 1.6 pG/$\sqrt{Hz}$ was achieved by the Romalis group at Princeton in 2010 with a S.E.R.F atomic magnetometer [59]). However, to our knowledge, most currently available commercial field-portable atomic magnetometers for geophysical applications have sensitivities on the order of 1 nG/$\sqrt{Hz}$ and operate on discharge lamps [6].

The advent of inexpensive and reliable laser diodes, of fiberized and stable amplitude and phase optical-modulators, of new techniques in the manufacture of polarization maintaining optical-fiber, and of other fiberized optical components (attenuators, splitters,...), has spurred a renewed interest in integrating these emerging technologies to field-able and/or miniaturized magnetometer designs [78, 133]. To compete with several decades of engineering which have perfected commercial discharge-lamp atomic magnetometers, one needs to show that an atomic magnetometer, incorporating these new technologies, are reliable, has better sensitivity, and can be built in a compact, field-able, and portable device. Showing these desirable characteristics motivates the work described in this Chapter.

Commercial atomic magnetometers are optimized in a fixed configuration. To our knowledge there is currently no available optical platform allowing multi- and in-the-field re-configurability. In this article we demonstrate a field-able magnetometer design with multi- and rapid re-configurability options to investigate configurations and optimization of atomic magnetometer based on nonlinear magneto optical rotation (NMOR) [38, 42]. The field-able design provides the ability to replicate the stability and multiple options one would expect from in-lab standard optical components mounted on a laser table. The multiple options are made possible within a 6.5×24 in. cylinder, which is only one order of magnitude larger than a commercial sensor head (an example is the G858 from Geometrics Inc. [6]). The device is non-metallic and unshielded for optimum sensitive field-measurements. The design evolved over a period of two years. Design features for transportability, mechanical stability, beam alignments, and ease of in-the-field reconfigurability are shown.

In particular, the device can be configured and investigate the all-optical self-oscillating, or swept modes configurations described by Higbie, Corsini, and Budker [83]. Self-oscillation allows a wide dynamic range, benefits from having a large bandwidth, does not necessitate a lock-in, and lends itself to lightweight and compact designs. The principle and advantages of this self-oscillating all-optical scheme are described in Ref [83] and all references therein.

To exemplify the versatility and capabilities of the field-device, and of the self-oscillating scheme, in Part II we show preliminary field-measurements of the Earth's magnetic field near an urban area, featuring rapid magnetic field fluctuations (of the order of 1 mG) from the San Francisco bat Area electric trains system; we show bandwidth of several kHz in gradiometer mode, self-oscillation stability in the presence of large magnetic field fluctuations induced by a near-by moving vehicle. The preliminary measurements described in PART II also serve to motivate further investigation of the all-optical self-oscillating magnetometer described in Ref. [83].

Subsequent published results by Hovde *et al* ([85, 86, 84] and results recently and soon to be submitted by Patton *et al* [109, 110] include deployments of the device at magnetometer test fields at the Geometrics Inc. testing location at NASA Moffett Airfield, California, and at the Naval Surface Warfare Center in Panama City, Florida. The latter works by Hovde *et al* and Patton *et al* demonstrate the design's robust qualities and a subset of the device's multi-capabilities. The results also confirm the multi-faceted physics pertaining to atomic magnetometry at Earth' magnetic field, and further motivate the construction of a fieldable and reliable re-configurable optical platform.

4.1.3 Overview

The field-able magnetometer consists of two separate modules: the sensor-head and the optical-signal processing modules (Fig. 4.1). In gradiometer mode, the two sensor heads are mounted on a fibreglass frame-rail system (Fig. 4.1-Upper). The optical-signal processing module sub-divides into the "optical cage" system and two "pulser" boxes and one common power supply (Fig. 4.1-Upper-Left [inside dashed-oval]). Two umbilical cords (one per sensor) channel the optical, the electrical signals, and the electrical power between the two modules. The magnetometer configuration shown in the schematic (Fig. 4.1-lower) shows the all-optical self-oscillating configuration described in Ref. [83].

4.1.4 Field-able design: sensor head

The field-able sensor (Figs. 4.2-4.5) has configuration options including single or separate pump and probe beams, single or double (retro-reflected) probe beam pass, options for two additional laser beams (for example: re-pump and an AC stark shift-canceling beams [89]), optical-rotation detection within or removed from the sensor volume (Sec. 4.1.6), cell temperature stabilization, and in-the-field re-configurability. The design consists of two-sensor heads allowing single-sensor or gradiometer operation. When used as a gradiometer the rail-mounted sensors can be independently orientated (to test for heading-error effects), and can be positioned such that the sensor-to-sensor distance (measured at the alkali cells) range from approximately 24 in. to a minimum of 1.5 in. (Fig. 4.1). For sensitive magnetic field measurements of a small external physical object, the construction allows the alkali vapor cell inside the sensor to be positioned as close as 0.75 in. to the sensor outer end-cap surface area.

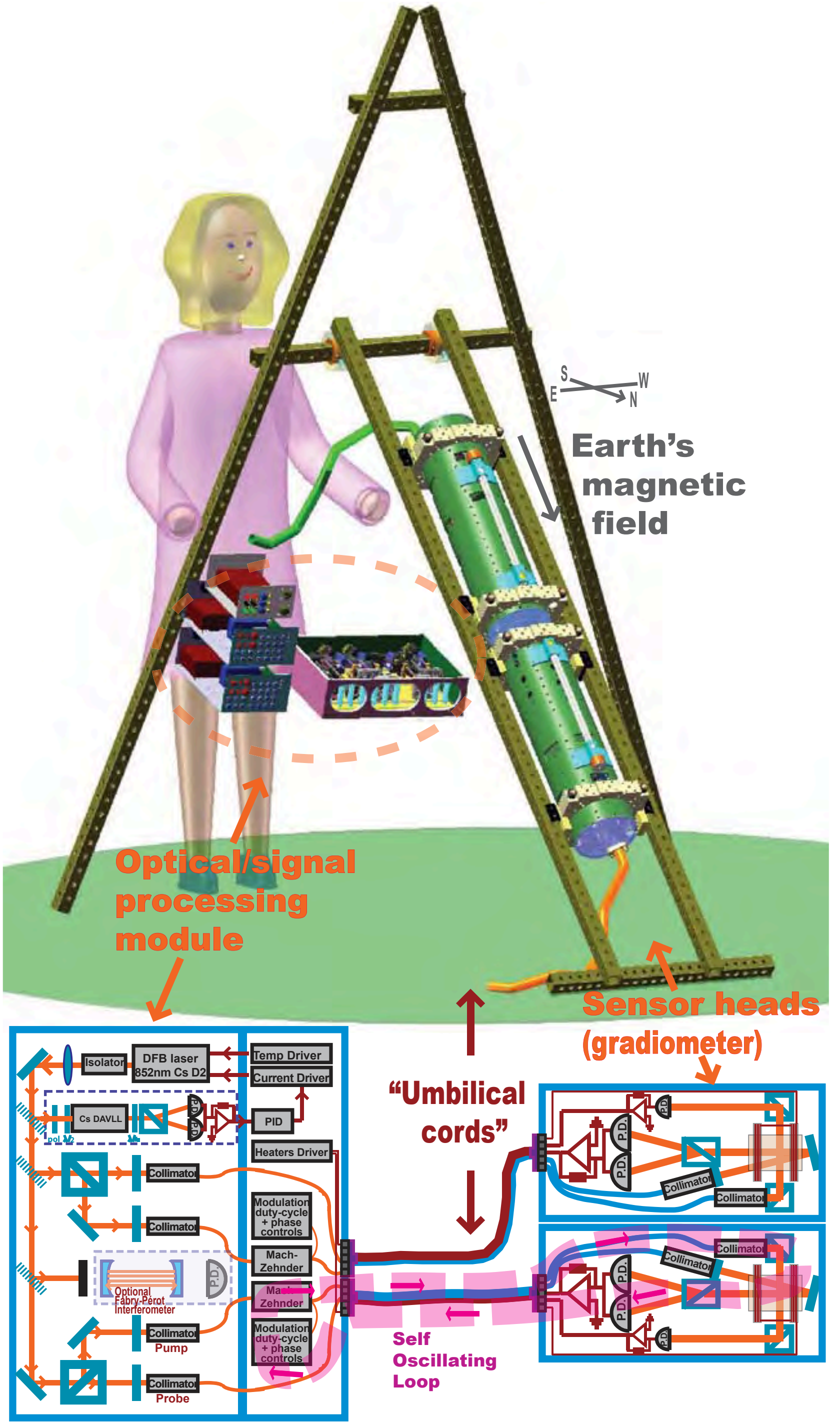

Figure 4.1: Gradiometer configuration. Upper-right: two-sensor (non-metallic) and frame field-able module, is shown in gradiometer mode. Upper-dashed oval: optical/signal-processing module. Lower: schematic of the 2-channel gradiometer based on the all-optical self-oscillation described in Ref. [83]. The self-oscillation configuration lends itself to a modular design with the sensors and the optical/signal processing modules linked with an "umbilical cord" housing the optical fibers and electrical cables. The self-oscillating optical/electronic loop (dashed pink line) consists of a modulated pump beam, stroboscopically pumping the alkali atoms in the vapor cell. The induced atomic polarization modulates the polarization axis of a weak probe beam at twice the Larmor frequency. A balanced polarimeter (consisting of a polarizing beam splitter, matched photodiodes and a difference amplifier) converts the modulation of the probe beam light into a sinusoidal signal. The amplified signal is amplified and directed back to the pump beam modulator to close the feedback loop. [Conception/design/construction (2006-08): E. Corsini - P.I.: D. Budker]

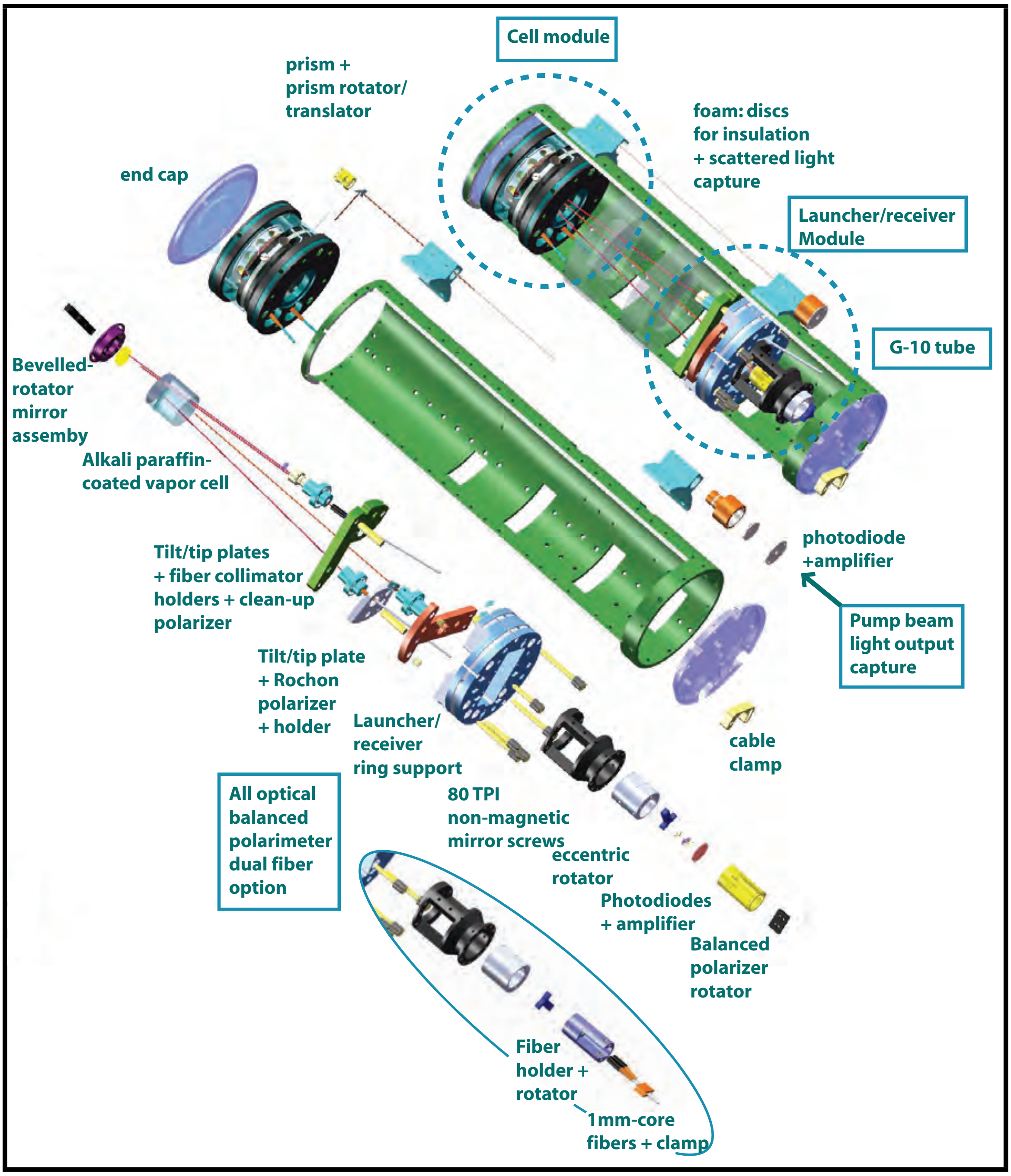

Figure 4.2: Sensor-head exploded-view. lower-left: the all-optical balanced polarimeter option consists of a pair of 1-mm core fibers with pig-tailed collimators in lieu of the two photodiodes. Additional detailed description in text. [Conception/design/construction (2006-08): E. Corsini - P.I.: D. Budker]

Mechanical stability of each sensor head is realized with a (G-10) fiberglass 6.5 in. in diameter and 24 in. long cylinder supporting modular ring-mounted optical components (see fig.4.2-4.5). The ring-mounted components are inserted from the G-10 tube ends and are positioned and locked within the tube in one-inch or half-inch increment intervals.

The tube features cut-out windows to allow some manual access for optical alignment and trouble shooting. The last-generation sensor's main components are the launcher-receiver module and the cell module; each module can be quickly removed for in-depth trouble-shooting and put back into place with minimum re-alignment necessary.

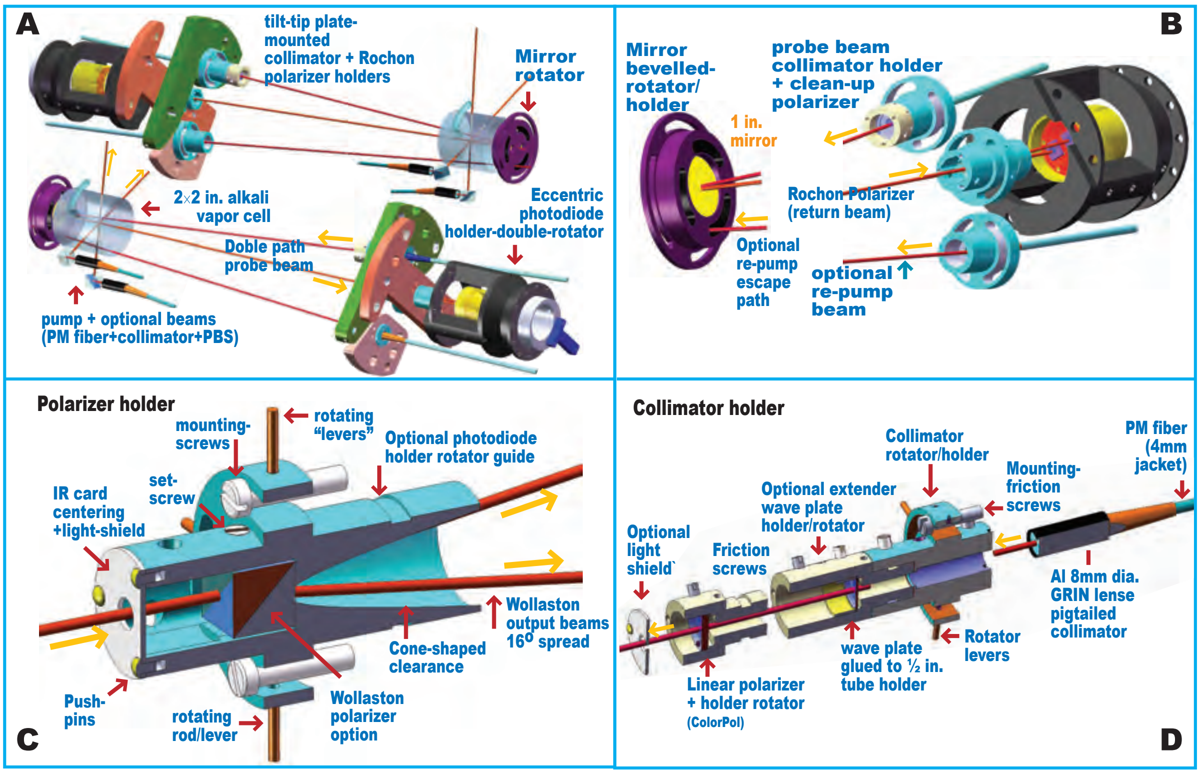

Figure 4.3:
Upper-left: optical components and beam paths.
A: coarse adjustment is achieved with a beveled mirror rotator and fine adjustment with tilt/tip plates.
B: details of fiber collimator and Rochon polarizer holders.
C: Section-view of polarizer holder with Wollaston polarizer option.
D: Section-view of collimator holder with clean-up polarizer, optional wave plate, and optional light-shield.
[Conception/design/construction (2006-08): E. Corsini - P.I.: D. Budker].

Laser light for the pump, probe, and optional beams is channeled to the sensor-head via polarization maintaining fibers terminated by non-magnetic output collimators mounted on the launcher-module and on the cell module. Precise alignment and polarization-control of the probe and the optional beams (witch output collimators are mounted on the launch-module) are accomplished with precision tilting and tipping plates and rotatable/lockable clean-up polarizers (Color-Pol), respectively. The clean-up polarizers have an extinction ratio better than $1:10^6$.

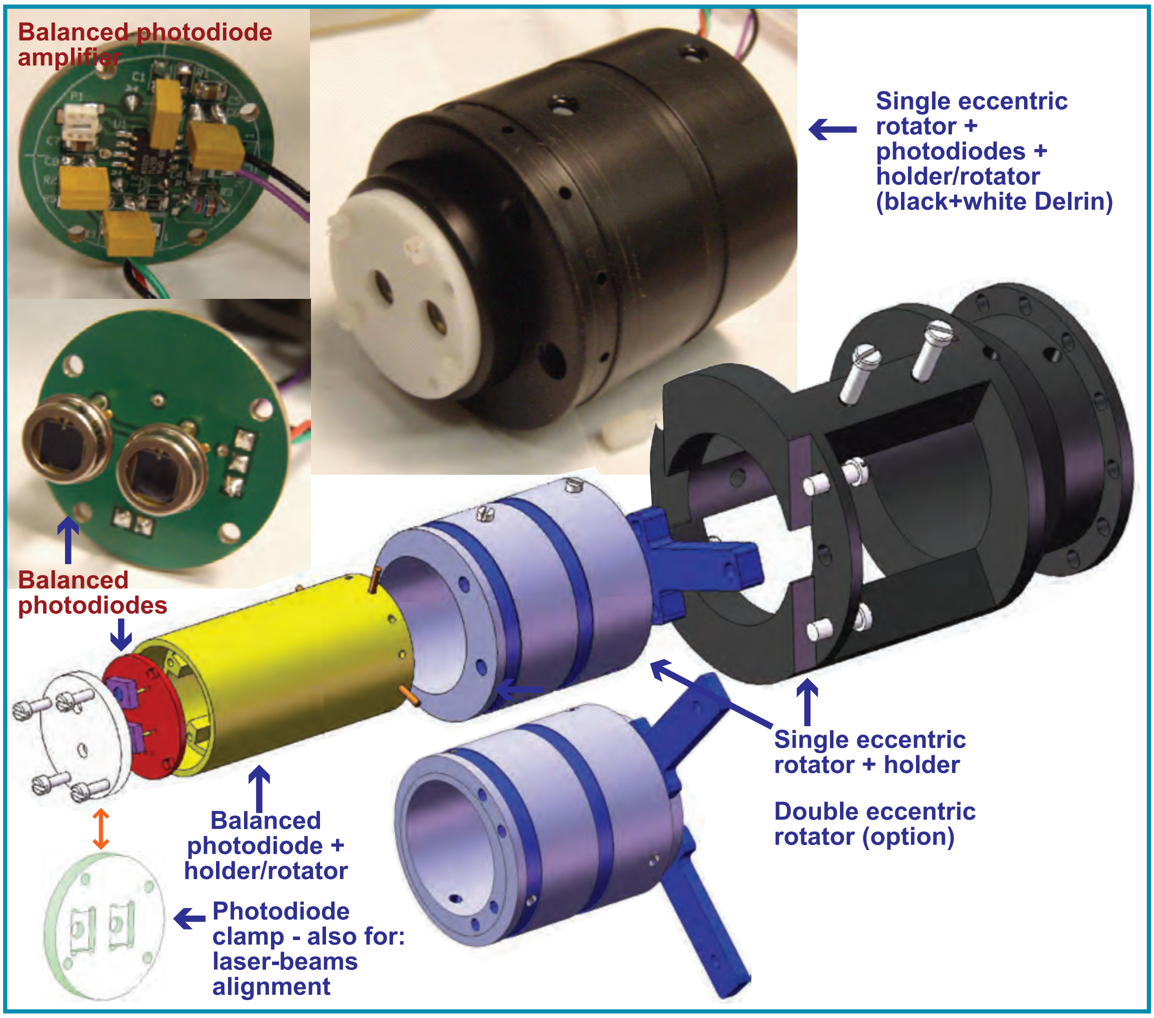

Figure 4.4: Sensor's balanced polarimeter: photodiodes and transimpedance amplifier. The photodiode holder/rotator is mounted inside an eccentric rotator in turn mounted inside the assembly support (itself attached to the launch module). Two versions of the eccentric rotator are shown. [Acknowledgment: the difference amplifier electronic design on the 1-in. disc PCB is a modification of the first (1.5×1.5 in.) iteration completed by J. Higbie. (shown in Fig. 4.7E & F]. [Conception/design/construction (2006-08): E. Corsini - P.I.: D. Budker].

The pump and optional beams, which output collimators are mounted on the cell module, pass through a polarizing beam splitter, redirecting the beams paths at right angle to the main sensor axis. In double-pass configuration (to increase the cell's effective optical depth) the probe beam is retro-reflected with a mirror mounted on a beveled rotator to provide coarse beam alignment; the mirror reflects the return probe beam to the balanced polarimeter (mounted on the launcher-module); The balanced polarimeter consists of a Rochon polarizer mounted on a precision tilting and tipping plate for control of the incident return light beam incidence on the polarizer surface. The Rochon polarizer's two-beam output is captured on two photodiodes mounted on the front of a 1-in diameter electronic board; a surface-mount transimpedance amplifier is mounted on the back of the board (Fig. 4.4).

The launcher/receiver and cell modules can be separated by a distance ranging from ∼3 in to 12 in, to investigate the effect of residual magnetism from the launcher/receiver module.

4.1.4.1 Cell module

The cell module houses the alkali vapor cell. Two light beams are channeled to the cell module via polarization maintaining fibers terminated by non-magnetic rotatable and lockable collimators. Two polarizing beam splitters serve to clean-up the beams polarization axes and to re-direct the beams at right angle to the sensor's axis. Down-stream of the polarizing beam splitter an optional $\lambda/2$ or $\lambda/4$ wave plate rotates the beam polarization or adds circular polarization to the beam. The outgoing beams can be captured for monitoring by either a photodiode inserted in the 1/2 in dia. output beam channel (not shown) or by a prism reflecting the beam back to a photodiode mounted externally on the sensor (Fig. 4.2). The cell module is temperature controlled with two heaters, each consisting of a coiled quad-twisted non-magnetic heater wire, and capable of delivering up to a total of ∼4 W. The heater coils are positioned by the cell fore and aft walls to keep the cell walls warmer than the cell stem to avoid condensation of alkali vapor on the cell-walls. Approximate temperature homogeneity is achieved with removable custom shaped foam discs and walls mounted inside the cell module. The cell temperature is monitored with non-magnetic K-type thermocouples.

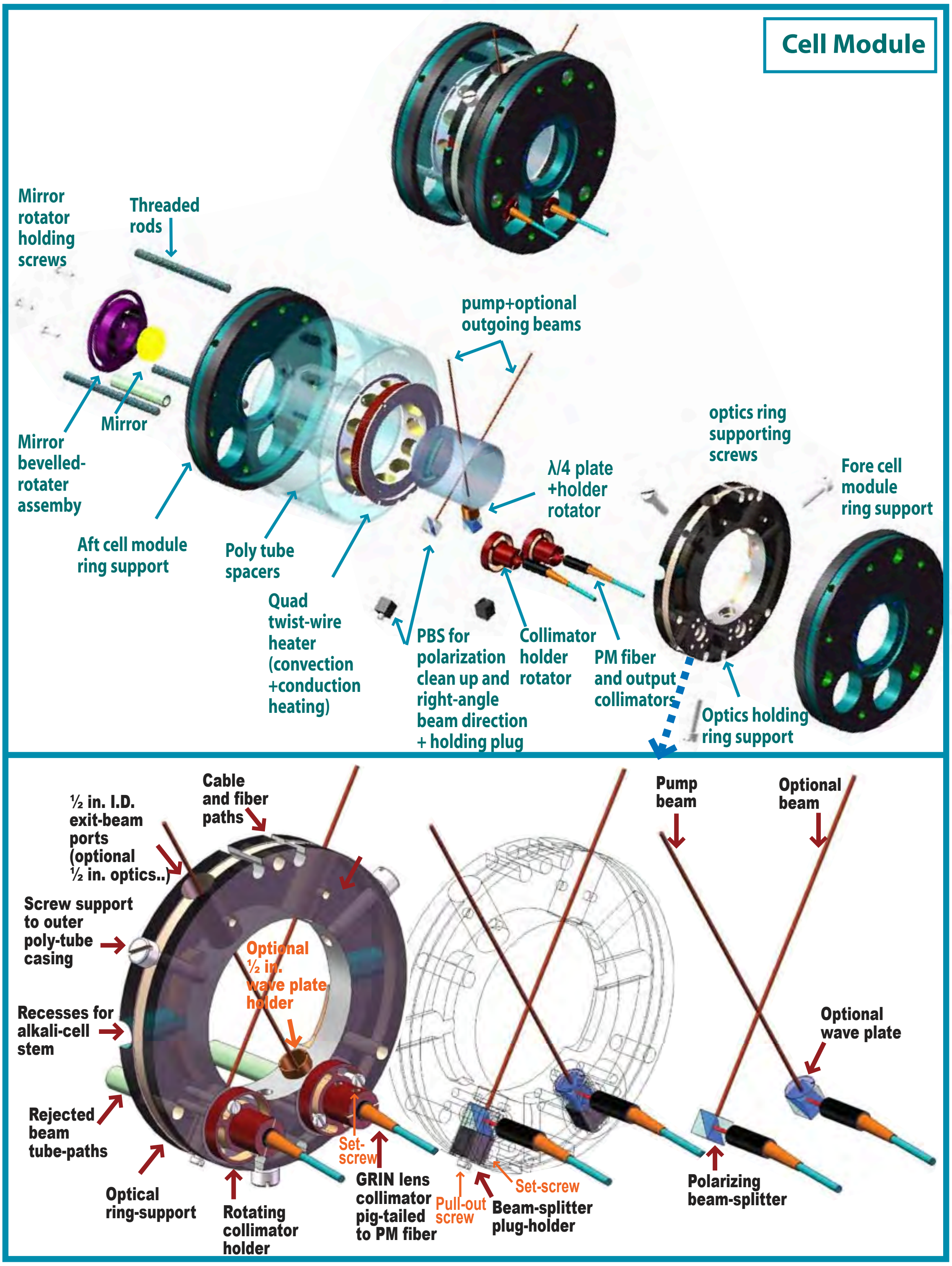

Figure 4.5: Cell module (upper) + exploded-view (middle). Insulation not shown (Fig. 4.11). The mirror is mounted on a beveled-face rotator for coarse beam adjustment. The rotator has arc-shaped clearances to allow optional beam to be captured by light absorbing foam behind the mirror assembly. Lower: Optical ring within the cell module with pump and optional beams channeled via polarization maintaining (PM) fibers. [Conception/design/construction (2006-08): E. Corsini - P.I.: D. Budker]

4.1.4.2 Balanced polarimeter - options

The two photodiodes can be replaced by an optional pair of collimators channeling the modulated probe beam signal back to the processing center via a pair of 1 mm core fibers (fiber-return) 4.6. With this option the AM NMOR magnetometer signal (the alkali atoms-induced nonlinear magneto-optical rotation) is encoded in the two beams' intensity difference, which is modulated at twice the Larmor frequency.

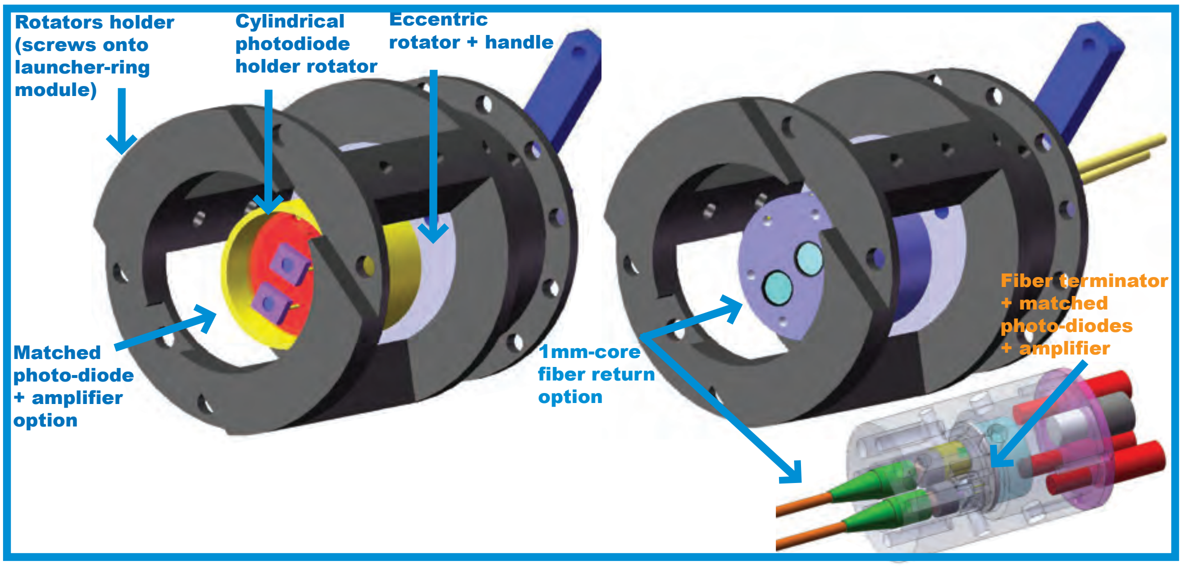

Figure 4.6: Balanced polarimeter options
Left: Matched photodiode + transimpedance amplifier + electrical signal return via non-magnetic coax cable.
Right: 1-mm core fiber signal-return with (lower) fiber terminator + transimpedance amplifier.
[Conception/design/construction (2006-08): E. Corsini - P.I.: D. Budker].

4.1.4.3 Tube/ring design material and additional options

Delrin acetal is used for the ring supports and the optics-holding parts. Delrin acetal has good intrinsic frictional qualities and is the preferred plastic material for gears [3]. Delrin's thermal coefficient of expansion is comparable to that of G-10 fiberglass which, combined with Delrin's low friction, makes it an ideal material for the ring supports and optical parts.

Ring-mounted optics can be added as needed for other in-the-field applications. Figures 4.7, 4.9 & 4.8 show examples of ring-mounted mirror mounts, polarizer, balanced polarimeter, and 1-in lens holder (sensor-head earlier generation components - can be used with later generation sensor-head).

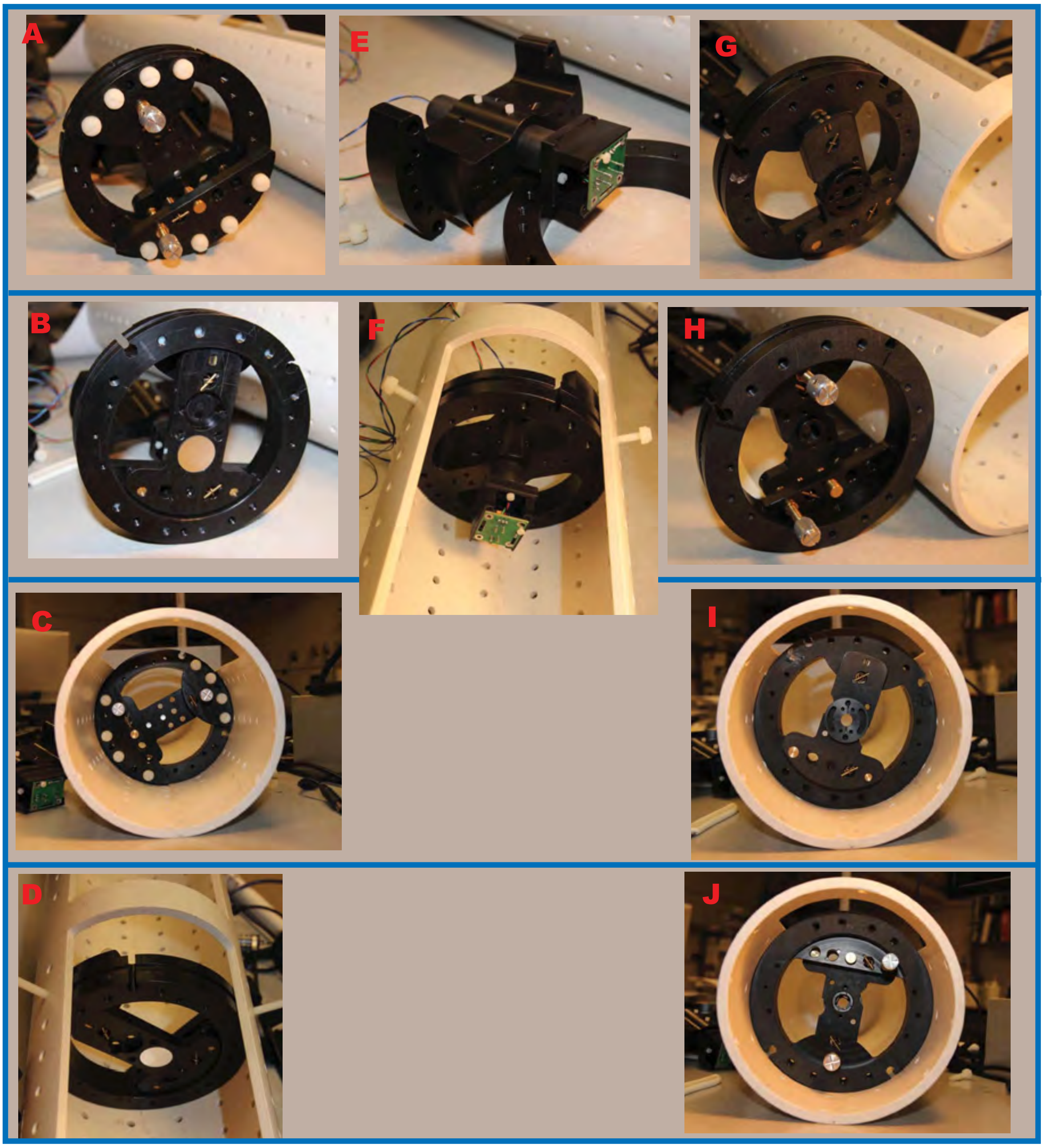

Figure 4.7: Optional ring components (part-A): components are shown disassembled from the ring support, assembled on the ring support and inserted inside the six-in. I.D. PVC test-tube.
A,B,C,E: tilt/tip mirror mount, with non-magnetic 80-TPI screws. The non-magnetic springs and pivot points can be replaced with polycarbonate (non-metallic) substitutes.
E,F: Balanced photodiode + amplifier with longitudinal and lateral adjustments.
G-H,I,J: tilt/tip mount, with non-magnetic 80-TPI screws, for the polarizing beam splitter (Rochon polarizer) holder. The non-magnetic springs and pivot points can be replaced with polycarbonate (non-metallic) substitutes.
[Conception/design/construction (2006-08): E. Corsini - P.I.: D. Budker].

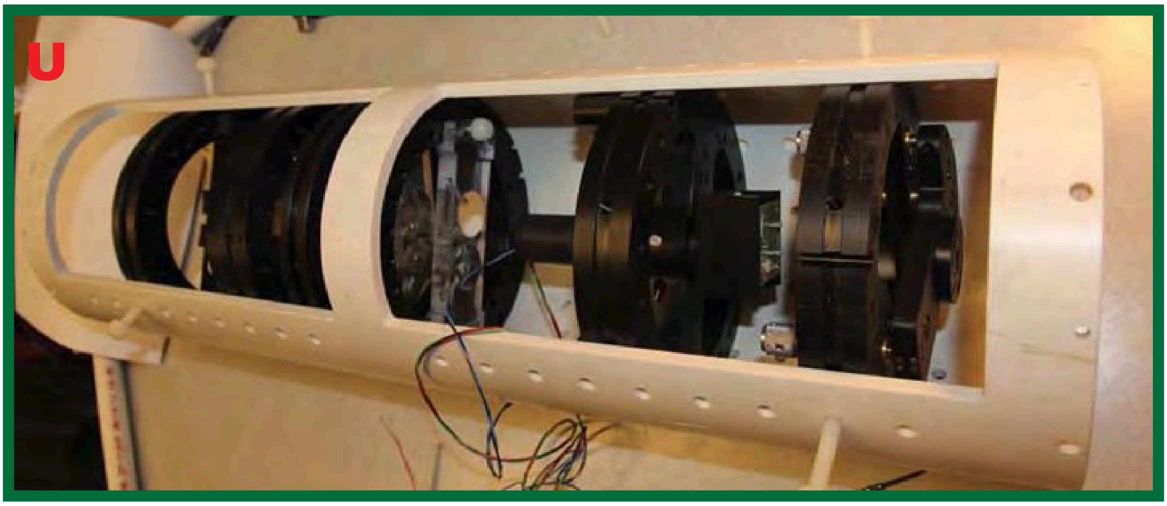

Figure 4.8: Optional ring components of Figs 4.7 &4.9 mounted in alignment PVC-plastic test-tube. [Conception/design/construction (2006-08): E. Corsini - P.I.: D. Budker]

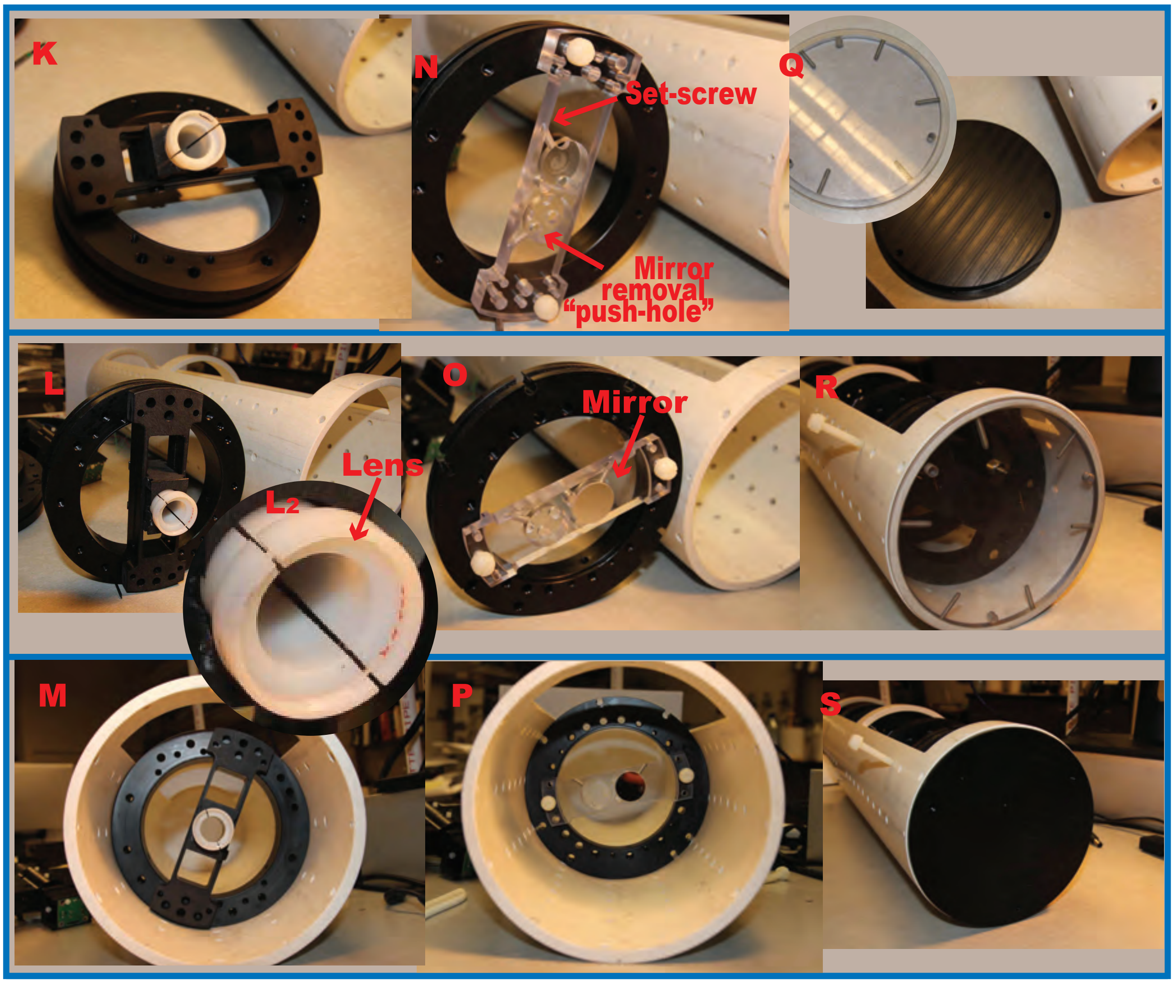

Figure 4.9: Optional ring components (part-B): components are shown disassembled from the ring support, assembled on the ring support and inserted inside the six-in. I.D. PVC test-tube.
K,L,M: All Delrin-plastic 1-in. lens mount with longitudinal and lateral slider-adjustments
N,O,P: Fixed 2-position mirror mounts.
Q,R,S: Tube end caps: black Delrin and clear poly.
[Conception/design/construction (2006-08): E. Corsini - P.I.: D. Budker].

4.1.4.4 Heading error ($\sim$1 nG/°) caused by induced paramagnetism and diamagnetism near the sensor cell

The sensor's cylindrical construction provides a stable and multi-configurable field-design, but the cylindrical shape is not optimum near the sensor cell. The diamagnetism of the cell's supporting material and the paramagnetism of displaced oxygen (vacuum cell), induce a longitudinal magnetic field offset and gradients (Fig. 4.10). Vapor cells benefit from motional averaging (the polarized atoms sample the magnetic field in the entire volume of the cell, as opposed to buffer gas cells), but the NMOR resonance nonetheless broadens in the presence of field gradients (broadening characterization was performed in the work by Pustelny *et al* [111]). the dia- and para-magnetism from a cylindrical shape (a distribution of offset and gradient) changes as the sensor is tilted away from the direction of the main bias field, and causes heading error.

The D & E section of Fig. 4.10 show the magnetic field offset and gradient distribution in the longitudinal and radial directions within the vapor cell in a 500 mG bias magnetic field along the longitudinal direction. The magnetic longitudinal and radial components of the magnetic field at the cell's center are $\sim$-0.15 μG & 0.0 μG, respectively. However due to motional averaging, the average magnetic field in the cell's volume is the relevant quantity. A coarse visual inspection, using the color scaling in figure 4.10 indicates that the difference of the volume-average magnetic fields (shift) is on the order of 0.05-0.1μG. A similar inspection indicates that the longitudinal and radial volume-average magnetic field gradients are in a 2:1 ratio. Consequently rotating the sensor away from the Earth's magnetic field direction will cause a change in sensitivity (gradient-induced) and a heading error (shift-induced). We approximate the heading error to be the same 0.05-0.1 μG order of magnitude (for a 90°rotation), equivalent to $\sim$5-10 nG for a rotation of the sensor's axis 6°away from the Earth's field direction. In contrast cylindrical constructions cause a constant magnetic field shift and have no gradient [88]. Future design improvements will incorporate a cylindrical cell and cell module sandwiched between two support rings.

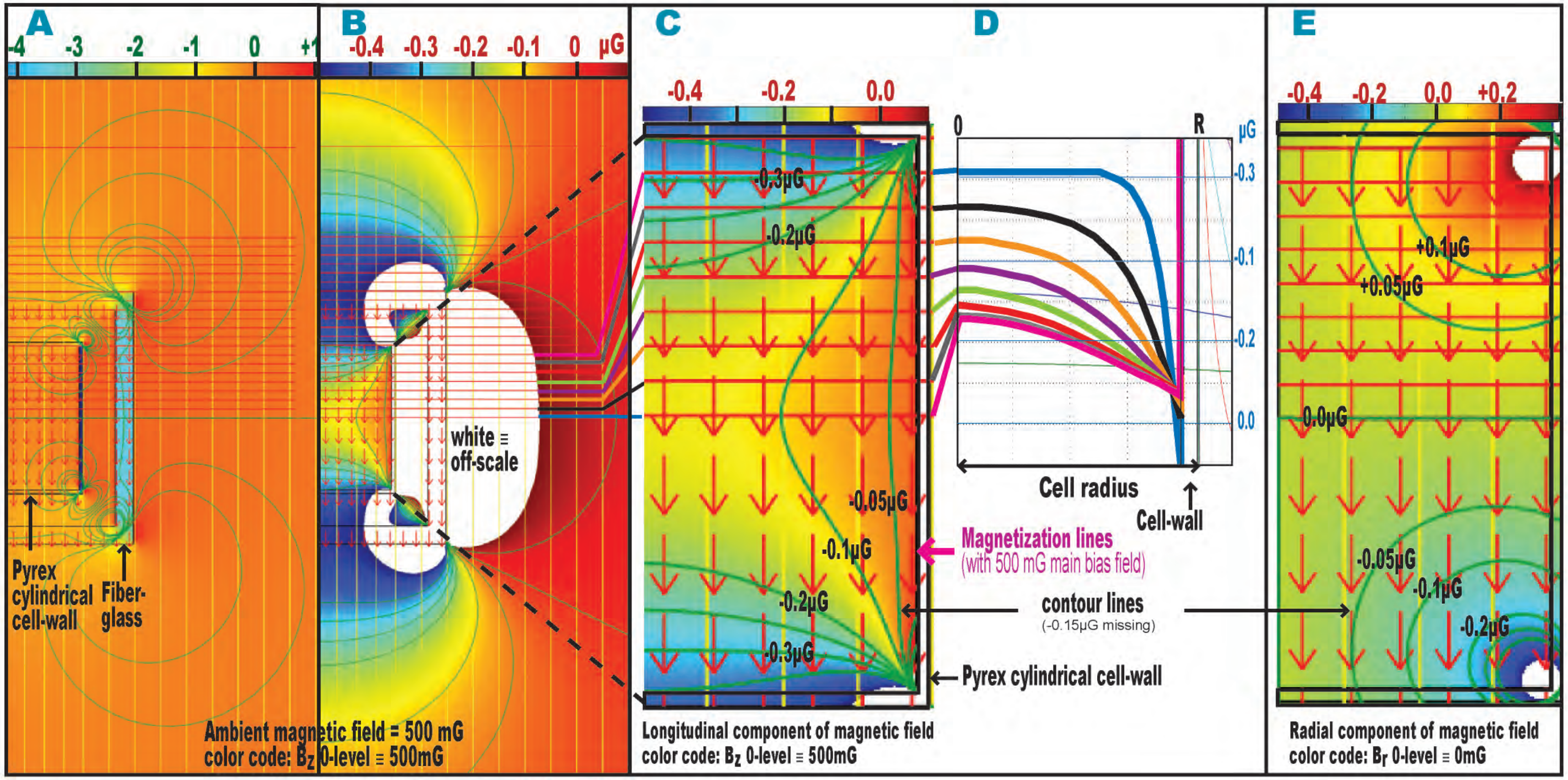

Figure 4.10: The simulation of diamagnetism and paramagnetism from a cylindrical Pyrex cell, a fiber-glass cylinder enclosing the cell, and the absence of oxygen, induced by a 500 mG bias magnetic field (parallel to the cell's axis), is shown. A-D: shows the longitudinal component, B_z; E shows the radial direction, B_r. The color scales of the magnetic field are in μG. In A the scale extends over a range of 5 μG. In B,C,D, the scale extends over a range of 0.6 μG. In E the scale extends over a range of 0.9 μG. The white-colored areas are off-scale. The enlarged cylindrical vapor cell region is shown in C & E. B_z as a function of radial distance from the cell's axis is shown in D for 8 z coordinates. The contour lines in C & E show that the magnetic field inside the cell spans a range of approximately 0.3 nG. The physical dimensions are in arbitrary units. [Conception/design/simulation (2009-12): E. Corsini - P.I.: D. Budker]

4.1.4.5 Insulation

The 6-in. internal diameter and the availability of pre-cut 6-in foam disks ease the task of insulating the cell module and minimize inner-tube air convection (Fig. 4.11). Similarly the availability of foam tubes (not shown), which can be slipped over the G-10 tube, allows sufficient thermal insulation.

4.1.5 Support frame

The two sensor heads are mounted on a rail-system which is part of a fiber-glass frame (Figs. 4.1 & 4.12). The two rails can be angled outward for easy mounting of the sensor heads and can be inclined from a horizontal to a near-vertical position. For most applications the sensors' axes are positioned parallel to the Earth's magnetic field which is approximately 60° where this work took place. The rail system also allows one sensor to be inclined with respect to the other sensor for heading error measurements (Fig. 4.12D).

4.1.6 Remote sensing capability

The modular character of the design allows configuration of the sensors as shown in Fig. 4.13 for remote detection of the magnetic field. The proof-of-principle remote sensing was realized in Chapter 3 in a shielded in-lab apparatus and a retro-reflector. Remote sensing was realized in the field, with the present field-able device, by Patton *et al* [109] during a 2011 deployment at the magnetometer testing site of the United States Navy base in Panama City, Florida [109] (Sec. 4.1.9). Remote sensing has applications as the one depicted in the cartoon shown in the lower part of figure 4.13.

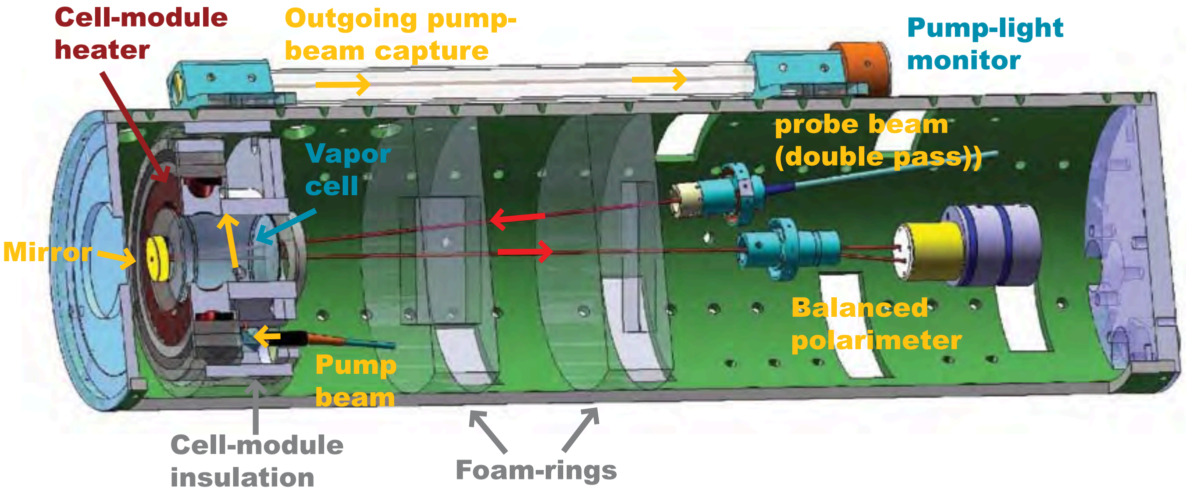

Figure 4.11: The ring design eases the task of insulating the cell module, and of minimizing convection that would cause power and polarization fluctuations. [Conception/design/construction (2006-08): E. Corsini - P.I.: D. Budker]

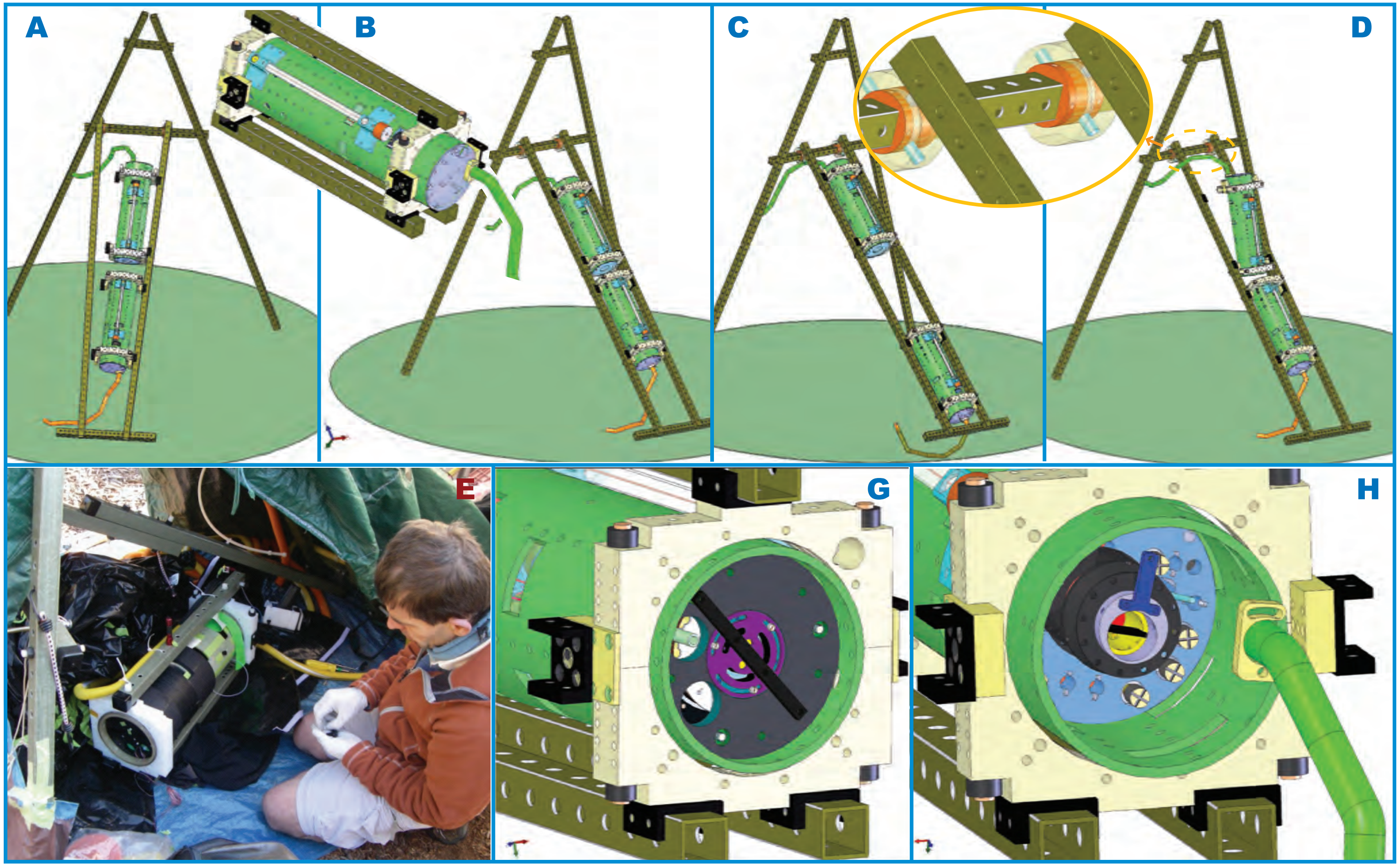

Figure 4.12: Fiberglass frame system + In-the-field trouble-shooting, re-configuring, and optical alignment. A & oval insert: the PVC-plastic joints and the frame design make for easy insertion and removal of the sensors on the rails. B,C: the sensors can slide and be locked in position on the rails with a variable sensor to sensor distance for gradient measurements. G,H: access to the beveled mirror-rotator (G) and to the launcher module (Fig. 4.2) precision adjusting screws (H) is achieved by removing with the tube end caps. E: performing in the field trouble-shooting, re-configuring, and optical alignment.[Conception/design/construction (2006-08): E. Corsini - P.I.: D. Budker]

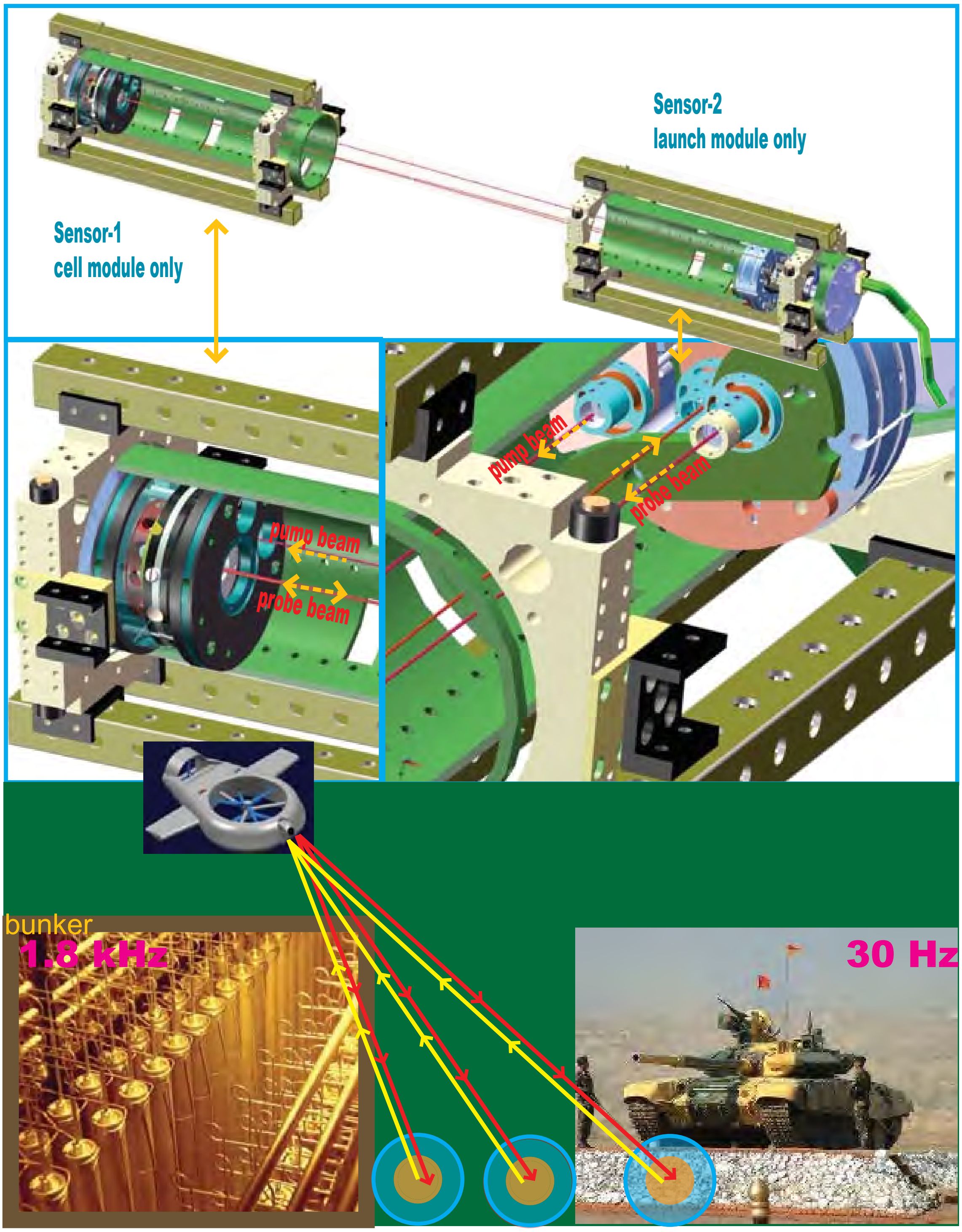

Figure 4.13: Remote detection capability: the modular and ring-mounted optical components allows re-configuration using one sensor as a "launcher" and the other as the "cell module" for "remote" sensing of the magnetic field. In the scenario depicted on the lower part of the figure, each sensor alkali vapor cell has, suspended at its center, a spherical retro-reflector (glass sphere with radially dependent index of refraction - Ch. 3) which returns a single pump/probe laser beam. A pilotless drone scans the area where sensors have been scattered on the desert floor and registers the AM-NMOR or free induction decay (FID) resonance which provides the magnitude of the Earth's magnetic field, and superimposed AC modulations of the field (up to several kHz - Sec. 4.2.15). [Caption cont. next page]

[Caption - Fig. 4.13, cont.] Acknowledgment: the idea of remote detection was mentioned by V. Yashchuk early 2006 (no written reference available). The detection of in-lab AC magnetic fields was realized by Higbie *et al* [83] later in 2006. The idea of more distant remote sensing scenarios such as the one shown on the lower part of this figure were presented by Corsini *et al* at oral presentations at MURI meetings in 2007 and 2008 and at the DAMOP-2009 conference. Remote detection in the field with AC magnetic fields, using the present field-able platform (in a slightly different configuration), was realized by Patton *et al* in 2011 [109].

UNIVERSITY OF CALIFORNIA AT BERKELEY

BERKELEY • DAVIS • IRVINE • LOS ANGELES • MERCED • RIVERSIDE • SAN DIEGO   SAN FRANCISCO • SA

COMMITTEE FOR PROTECTION OF HUMAN SUBJECTS
OFFICE FOR THE PROTECTION OF HUMAN SUBJECTS
University of California, Berkeley
2150 Shattuck Avenue, Suite 313
Berkeley, CA 94704 -5940

NOTICE OF APPROVAL FOR HUMAN RESEARCH

DATE: *June 07, 2011*
TO: *Dmitry BUDKER, Physics*
Eric P. Corsini, Physics, Brian R. Patton, Physics
CPHS PROTOCOL NUMBER: *2010-03-1050*
CPHS PROTOCOL TITLE: *Heart Magnetism*

Effective Date: June 16, 2011
Expiration Date: June 15, 2012

This approval is issued under University of California, Berkeley Federalwide Assurance #00006252.

Thank you for your cooperation and your commitment to the protection of human subjects in research.
Sincerely,

Sensor cell's nearest wall can be positioned 3/4in. from the sensor's outer cap surface

Figure 4.14: Another possible configuration to measure the magnetic field from the heart. In the above configuration the alkali cell's wall is positioned 3/4 in from the human subject's skin surface. Human research approval was obtained from the Office for the Protection of Human Subjects; the approval is renewed yearly. A measurement has not yet been realized. [Conception/design/construction (2006-08): E. Corsini - P.I.: D. Budker]

4.1.7 Heart magnetism in the field - another possible device's configuration

Reversing the orientation of the top sensor, the device's construction allows the alkali cell to be positioned with the cell wall 3/4 in from the sensor cap outer surface (details not shown - Fig. 4.14). Magnetocardiography has been achieved with an atomic magnetometer with some magnetic shielding ([30] & Ch.7, Sec. 7.1). To the best of our knowledge a magnetic field mapping of the heartbeat as is shown in figure 7.2A has not been achieved in an unshielded environment. A measurement of the magnetic field of the heart beat with the present field-able device, is pending, and has not yet been realized.

4.1.8 Cabling, signal processing, and optical modules

The field-able design consists of two main modules, the sensor heads and the signal processing/optical module joined by two ∼10 m "umbilical" cords (Fig. 4.1).

Figure 4.15: Signal and power electrical cables and polarization maintaining optical fibers are housed in two split woven wrap-around sleeves (black and white, respectively) and are further protected inside a split corrugated flexible polyethylene tubing (red) which coils around the sensor when boxed (yellow in Fig. 4.20-lower left). The polyethylene tubing was replaced every ∼ two years due to sunlight U.V. damage. The optical fibers did not suffer noticeable deterioration except at connector end joining the fiber to the optical/signal processing module. [Conception/design/construction (2006-08): E. Corsini - Photographs (Feb. 2012): E Corsini - P.I.: D. Budker]

4.1.8.1 Cabling system - "umbilical cord"

The cabling and optical fibers are protected by a 1 in-diameter split corrugated flexible polyethylene tubing (Wire Loom). The "umbilical cord" houses the polarization maintaining optical-fibers (further protected by a woven wrap-around sleeve [Roundit 2000]), two doubly-shielded non-magnetic co-ax cables for the optical-rotation and pump monitor signals, shielded power lines for the balanced polarimeter and pump light monitor amplifiers, and optional thermocouple K-type wires (Fig. 4.15). The "umbilical cord" may also include the optional 1-mm core optical-fiber pair for the balanced-polarimeter optical return (an option making an optical-fiber-only “umbilical cord”). An insertion tool (not shown) allows rapid insertion and removal of cables and fibers, in the wrap-around sleeve and in the split tubing, for in-the-field trouble-shooting and replacement when necessary.

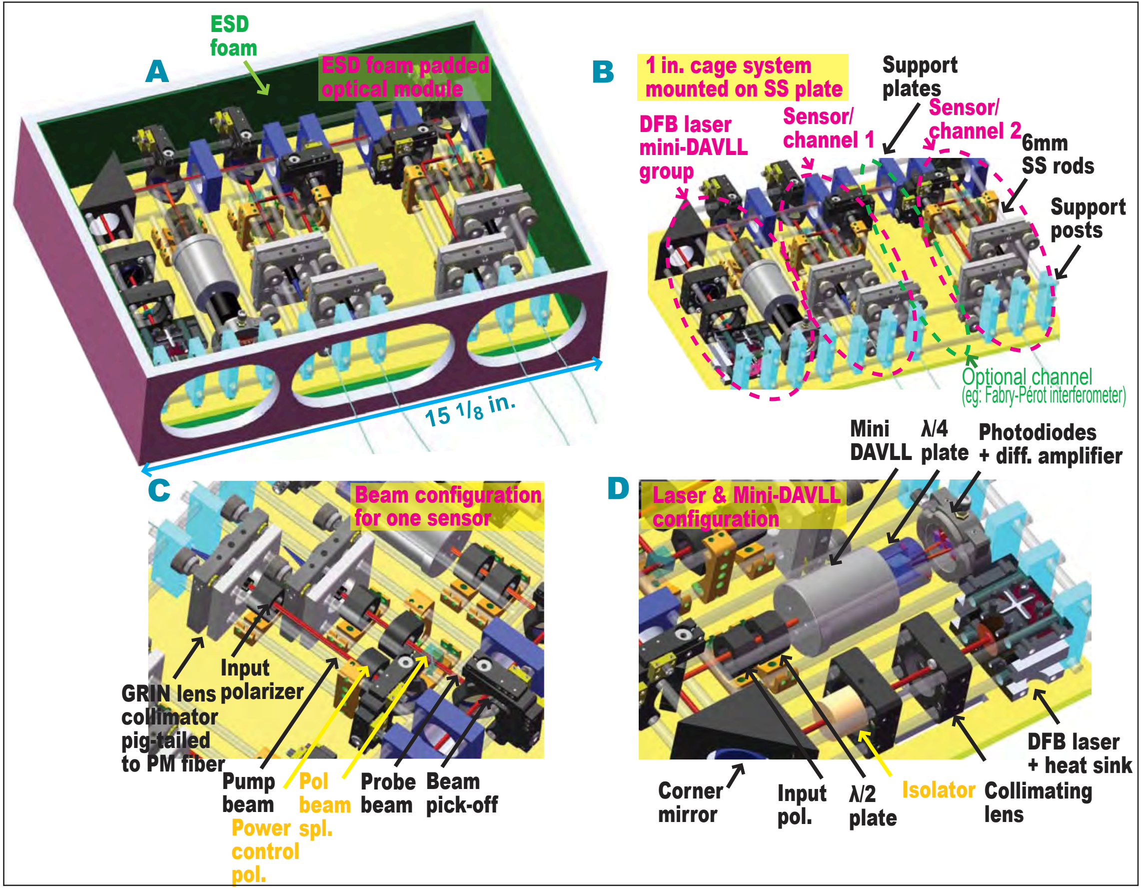

Figure 4.16: Optical cage system. The optical path starts with the distributed feed back (DFB) laser (lower left in A & B and mid-right in D), and follows with (fig. B) the optical isolator, a branch-off to mini-DAVLL (dichroic atomic laser lock) system (Sec. 4.1.8.4), a branch-off to sensor/channel 1 optical group, followed by a polarizing beam splitter (PBS); the two beams (pump and probe) pass through linear polarizers and couple through collimators to single mode fibers. A MachZehnder interferometer (not shown) modulates the pump light (Sec. 4.1.8.2). The second branch-off is for sensor/channel 2 optical group which comprises the same optical components as for channel 1.
A The cage ESD foam padded module is in a Thorlabs 19-in. drawer (not shown). A future iteration will incorporate all laser, temperature, and amplitude modulators drivers in an outer shielded casing.
B: Cage is mounted on a stainless steel support plate serving as a temperature equalizer connected to a Peltier element. In the first iteration the optical module construction was stable enough to be deployed without the support plate.
C: Close-up of laser/collimation lens/isolator group. D: Close-up of channel 1 optical group. [First iteration (Thorlabs cage system components - not shown): J. Higbie - Collaboration: E Corsini - PI D. Budker / This version: conception/design/construction (2006-08): E. Corsini - P.I.: D. Budker]

4.1.8.2 Optical cage

The optical sub-module (Fig. 4.16 consists a custom-modified 1 in-optics cage system (Thorlabs) mounted on a stainless steel base-plate which serves to maintain an even temperature. The cage-system can be operated without the base plate. The distributed feed back (DFB) laser is mounted in a custom-made combination heat-sink/support or a commercial one (Thorlabs). The laser beam is collimated with an aspherical lens and the laser diode is isolated with an optical isolator (Thorlabs). A “corner” mirror directs the beam to three optical “pick-offs”, one goes to the mini-DAVLL (dichroic atomic vapor laser lock) [99] described in Sec. 4.1.8.4, and two go to the gradiometer two channels.

The beam for each channel is further divided into pump and probe beams, which are collimated into polarization maintaining fibers. The pump beams are modulated with fiberized Mach-Zehnder interferometer amplitude modulators. The two modulated pump and two unmodulated probe beam fibers are terminated by fiber-to-fiber precision ground angle polished connectors (APC) to which connects the optical-fibers of the “umbilical cords” (Sec. 4.1.8.1).

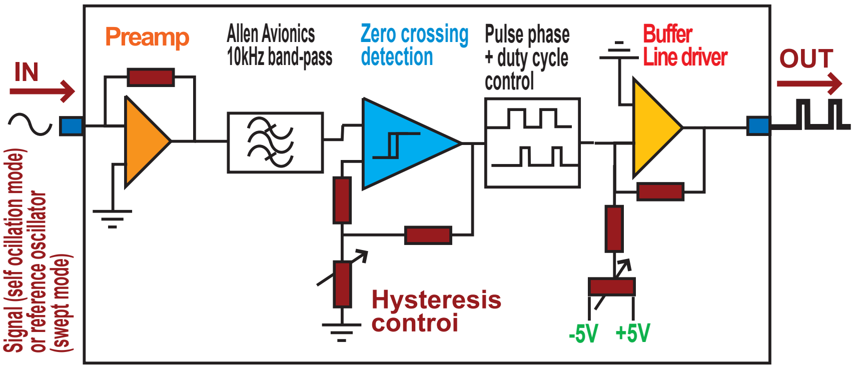

Figure 4.17: Electronics sequence: amplification, 5 kHz or 10 kHz bandpass filter, zero-crossing detection, control of phase and duty cycle, buffering. The sequence was initially realized with a cascade of home-made and commercial devices. In this work it was later consolidated into one PCB board (Sec. 4.4) [Conception/design/construction/caharacterization (2006-08): E. Corsini - P.I.: D. Budker]

4.1.8.3 Signal processing

The electronic signal processing module functions are amplification, bandpass-filtering, conversion of the amplified signal to a square pulse, adjusting the pulse’s phase and duty cycle for optimum self-oscillation gain, and adding buffering to drive the optical modulator 50 Ω load. The electronic sequence is depicted in the schematic of Fig. 4.26 (top). In early deployments, the functions of that sequence were realized with a cascade of simple home-made and commercial amplifiers, and function generators. In the last deployment described in this work, these functions were consolidated into one PCB board with separate power and split ground planes, and shielding of the pre-amp function.

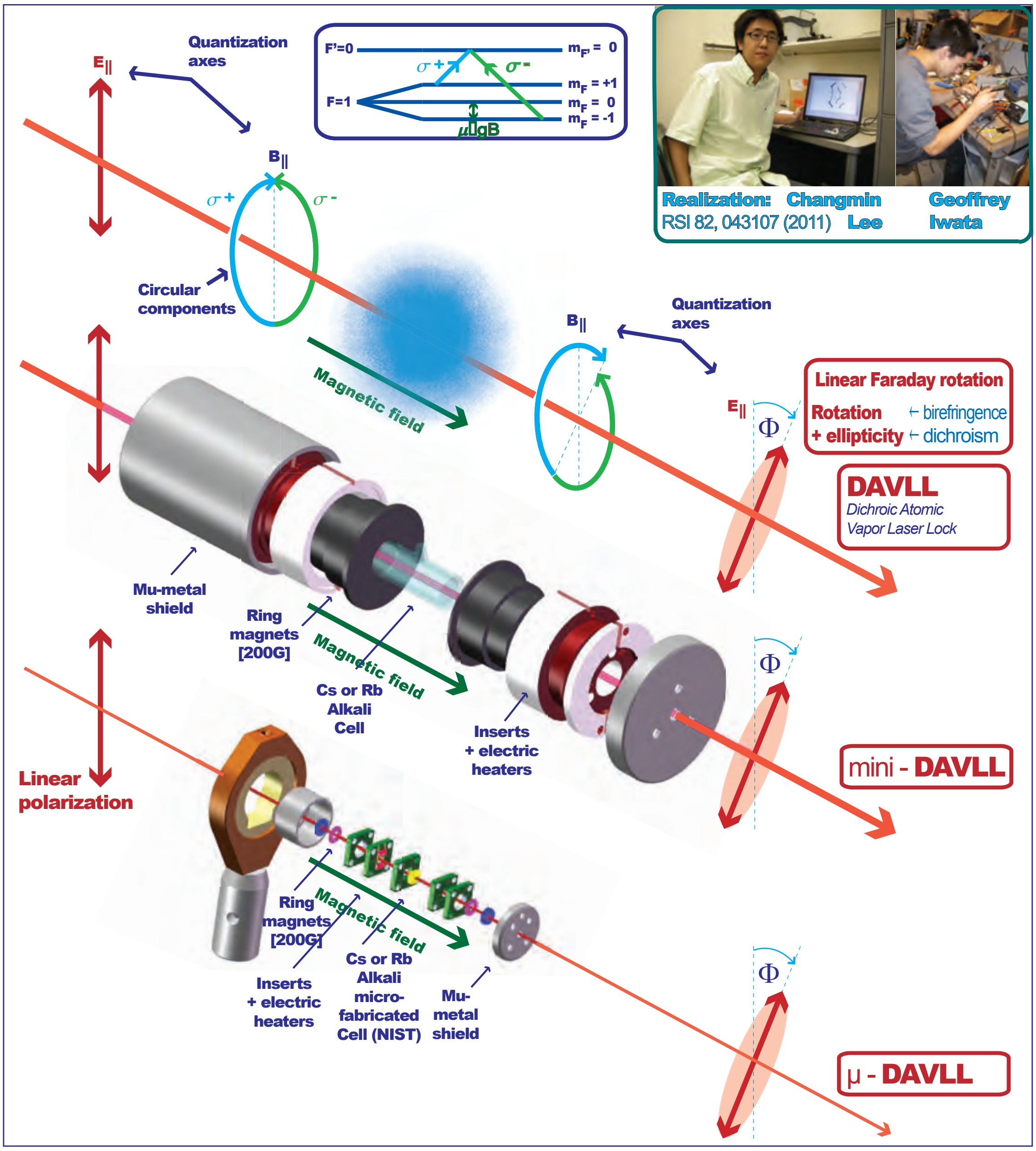

Figure 4.18: Top: Linear Faraday rotation in an alkali vapor. Ring magnets are used to make a homogenous magnetic field of approximately 200 G within the volume of the alkali vapor cell. The mini DAVLL is a ∼ 2×1.5 in. and the micro-DAVLL is ∼1/2×1/2 in. In this figure an optional inner-resistive heater was added to the mini-DAVLL (Middle). The micro-DAVLL (Lower) has a micro-fabricated alkali vapor cell fabricated by S. Knappe (Kitching group) at N.I.S.T. and requires continuous heating for operation. The mu-metal shielding allows the mini and micro-DAVLLs to be used in sensitive measurements.
[Conception/design/construction of mini-DAVLL inner-electric heater: E Corsini]
[Conception/design/construction of mini- and micro-DAVLL: Changmin Lee and Geoffrey Z. Iwata (UC Berkeley undergraduate students) - work published in RSI [99]. Poster presented by E. Corsini on behalf of Iwata *et al* at ICAP 2010 (Cairns-Australia)]

The “pulser-box”, although of simple electronics design, resulted in a significant reduction in electronic noise and low jitter (∼nG-equivalent in magnetic field noise). The electronic “pulser-box” construction (described in App. 4.4) bears no significant merit but indicates that simple, fast and well shielded/grounded electronics (which can be made compact and with low power consumption), are well suited for Earth’s field atomic magnetometry, including the detection of AC magnetic fields superimposed on the Earth’s field (Sec. 4.2.15).

A later iteration of the signal processing module, not described in this work (and realized by B. Patton - Sec. 4.3), consists of dynamic stabilization of the optical modulator DC-bias input (as suggested in Sec. 4.1.9) and was included in the deployments described in Refs. [85, 86, 109, 110].

4.1.8.4 Mini- and micro-DAVLL (Dichroic Atomic Vapor Laser Lock)

Optical frequency stabilization is realized with a mini-DAVLL. The DAVLL is based on linear Faraday rotation and is described in Refs. [146, 58]. Future iterations of the optical cage will incorporate a micro-DAVLL (Fig. 4.18). The mini and micro-DAVLL were realized by two U.C. Berkeley undergraduate students, Changmin Lee and Geoffrey Iwata [99].

4.1.9 Future design directions

Improvements and upgrades of the field-able device not yet realized at the conclusion of this work are listed or commented below.

- Multi-configurability makes the device larger (6×24 in. cylinder) then would a fixed single-configuration. We also propose a glued-in-place single-configuration design, with optimum configuration parameters determined from the multi-configurable design. the one-configuration sensor is over one order of magnitude smaller (3×2 in), while using the same optical-components. The reduced-size model is shown in Fig. 4.19 in gradiometer configuration. The rejected light from the pump beam is split three-ways to provide external positioning capability, to subtract magnetic field fluctuations caused by mechanical vibrations (the magnetic field gradient in the field was measured at 1-10 μG/cm (Sec. 4.2.13), or equivalently 10-100 nG for mechanical vibrations of the order of 0.1 mm).

- The phase in the self-oscillation loop has instability caused by the Mach-Zehnder interferometer/modulator’s static electrical charge built-up (inherent problem to this type of modulators). The static charge alters the value of V_π. A home made double-demodulation scheme was proposed as a feed-back loop to the D.C. input of the interferometer (the D.C. input sets the modulator’s $V\pi$). Alternatively an optical pick-off at the output of the modulator can be fed to a commercial modulator bias controller.

- Temperature stabilizing the optical cage, with Peltier elements mounted on the base plate (to evenly distribute the heat), would add stability to the laser power, DAVLL signal, and to the free-space to fiber-coupling (Sec. 4.1.8.2).

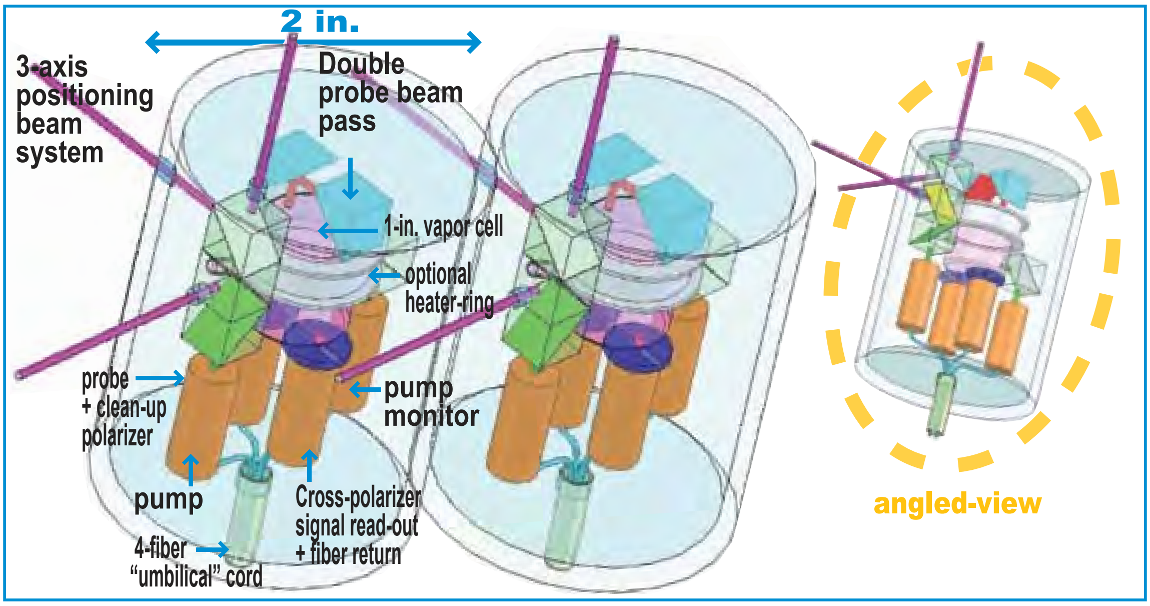

Figure 4.19: Proposed fixed-configuration sensor design shown in gradiometer configuration (left/right: two angled-views). The design has the same optical components as in the multi-configuration platform described in this Chapter. The cell is a 1 in×1 in. cylinder (in contrast to the 2×2 in. cylindrical cell in the multi-configuration platform). The optical-rotation signal is captured with a cross-polarizer configuration (in contrast to the balanced polarimeter used in the multi-configuration platform). The three-axis laser positioning allows some cancelation of the magnetic field fluctuations caused by mechanical vibrations (capture of the positioning beams not shown). The single-sensor size is approximately 2.×3 in. [drawing by E. Corsini and presented by Corsini *et al* at MURI meetings in 2007 & 2008 and at Geometrics, Inc. in 2008].

- The effective thermal expansion of the green G-10 and black Delrin were mismatched in the field; the reason may be that although the two materials have comparable thermal expansion coefficient they may have different emissivity coefficients. That design flaw made the ring-supports expand faster than the tube-support and made difficult to perform in-the-field reconfigurability on hot days. Replacing black Delrin with white Delrin may better match the effective thermal expansion coefficient of the ring support to that of G-10.
- The use of spherical vapor cells and of spherical support structures geometry near the vapor cell (as opposed to cylindrical), would near-eliminate heading errors induced by para- and dia-magnetism (Sec: 4.1.4.4.

4.1.10 Conclusion

We have shown the design of an optical platform with optomechanical components mounted on a ring/tube support in a package-size that lends itself to transportation. The next part of this chapter will show the device in use in the field and several aspects and challenges of atomic magnetometry at Earth's field. Except for the thermal expansion mismatch between G-10 and black Delrin (Sec: 4.1.9), the design proved to be mechanically stable throughout large temperature and humidity variations and buffeting by strong winds, after shipping coast to cost and multiple transports when packed as shown in figure 4.20D & E. The tubular shape made simple the shielding of the inner optical elements from light, wind, water, morning dew, and dust.

Subsequent to the preliminary measurements presented in PART II the sensor heads were subsequently and successfully deployed at the magnetometer test centers at Moffett Air base, California (Fig. 4.20A-C), and at the United States Navy "Naval Support Activity (NSA)", Panama City, Florida, in 2009 and 2010, respectively. The work by Patton *et al* and Hovde *et al* accomplished during these deployments, is described in references [85, 86, 109, 110]. The field-able design showed to be comparable in mechanical stability and reliability (except for the thermal issue mentioned above) to what would be expected from in-lab sheltered and climatized optomechanical components mounted on a laser table.

4.1.11 Acknowledgments

Acknowledgment is given to James Higbie for suggesting the idea that a tube/ring design would provide long-term stability, and for the first iteration of the optical cage system which is the seed-idea of the present optical cage. Credit is also given to Mike Brown, at the U.C. Berkeley physics department machine shop, for machining the parts and providing valuable guidance in the area of "feasibility" of the design.

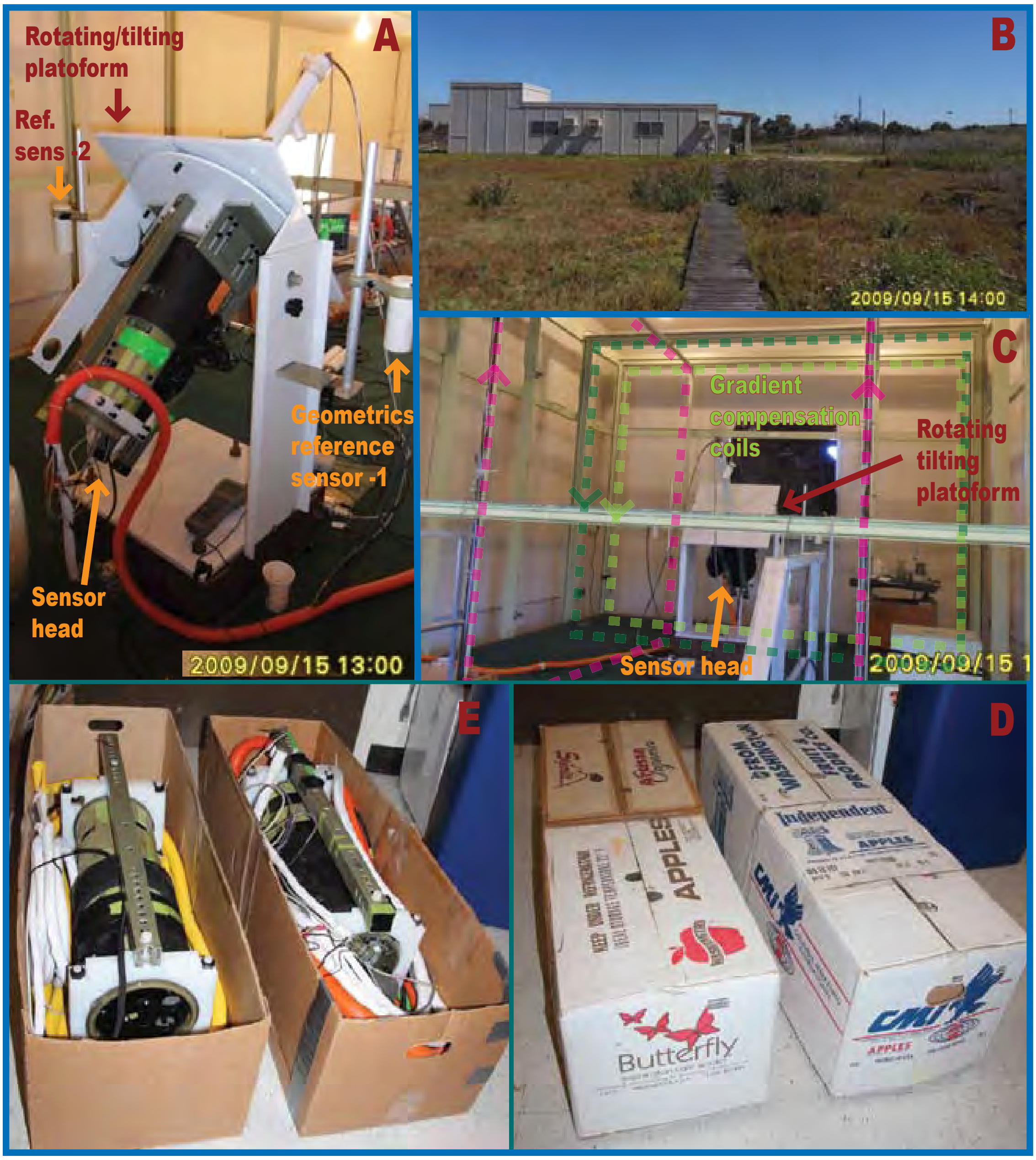

Figure 4.20: A: Field-testing the magnetometer on a rotating/tilting platform at the Geometrics Inc. magnetometer test-bed at NASA Moffett Air Base (B). C: platform gradient compensation coils D,E: The two 24-in. sensors and "umbilical cords" fit in two taped back-to-back 20-lbs apple boxes (courtesy of Berkeley Bowl). The sensors, as shown, have sustained round-trip shipping between West and East coasts, multiple truck/car transportation, and have weathered many continuous months in the field including strong rain, wind and up to 25°C temperature fluctuations . [Upper: photographs: E. Corsini, 2009 Moffett deployment managed by B. Patton) / Lower: photographs and packaging: E. Corsini (Feb. 2012)]

Chapter 4 - PART II
Preliminary field measurements to show and exemplify:
-The device's multi-configurability
-The multi-facets of Earth's field magnetometry

4.2.12 Introduction

The large magnetic field gradients in the laboratory suppress the NMOR resonance [111]. Optimum locations for sensitive unshielded magnetic field measurements are removed from urban environment, and are generally difficult to access for experimental field-work, during deployments lasting up to several months. One sub-optimal but convenient location is the U.C. Berkeley Botanical Garden $\sim$ two miles from downtown Berkeley, a 10 minute free bus-ride from the U.C. Berkeley campus, and open from 9 AM to 5 PM (Fig. 4.21-upper). Paul Licht, the UC Berkeley garden director, granted us the use of the garden's research plateau, which is removed from the garden's main public paths and shown in Fig. 4.21 (upper and insert). The project involved several collaborators; acknowledgement of specific contributions are given in the figure captions.

4.2.13 Outdoor/unshielded location

The location is pristine, with a stunning view of the San Francisco Bay and of the Golden Gate Bridge. We set up an open-air laboratory, starting in summer 2006, which was captured by Google map in 2007 (Fig. 4.21-insert). The map in the same figure shows the location of the plateau in relation to the garden's entrance, to the university campus, and to Berkeley downtown's station of the Bay Area Rapid Transit (BART) electric train system.

The location was not so pristine with respect to magnetic field noise from urban activities. A 24-hour ambient-magnetic field recording (Fig. 4.22) at the research plateau location reveals the magnetic field fluctuations induced by the BART electric train system. The fluctuations are of the order of 1/2 mG (0.1% of the Earth's magnetic field) and are over one order of magnitude smaller when BART suspends operations at night between $\sim$1:am and $\sim$5:am (longer down-time on weekends).

Self-oscillation with AM NMOR occurs at twice the Larmor frequency [83] which is $\sim$ 350kHz for cesium and $\sim$ 680 kHz for rubidium 87, which are frequencies falling within the frequency bands of amplitude modulated (AM) radio stations and aviation non-directional beacons. Radio broadcasts near the self-oscillation frequency decrease the AM NMOR signal/noise ratio by increasing the noise floor (Fig. 4.22 - insert).

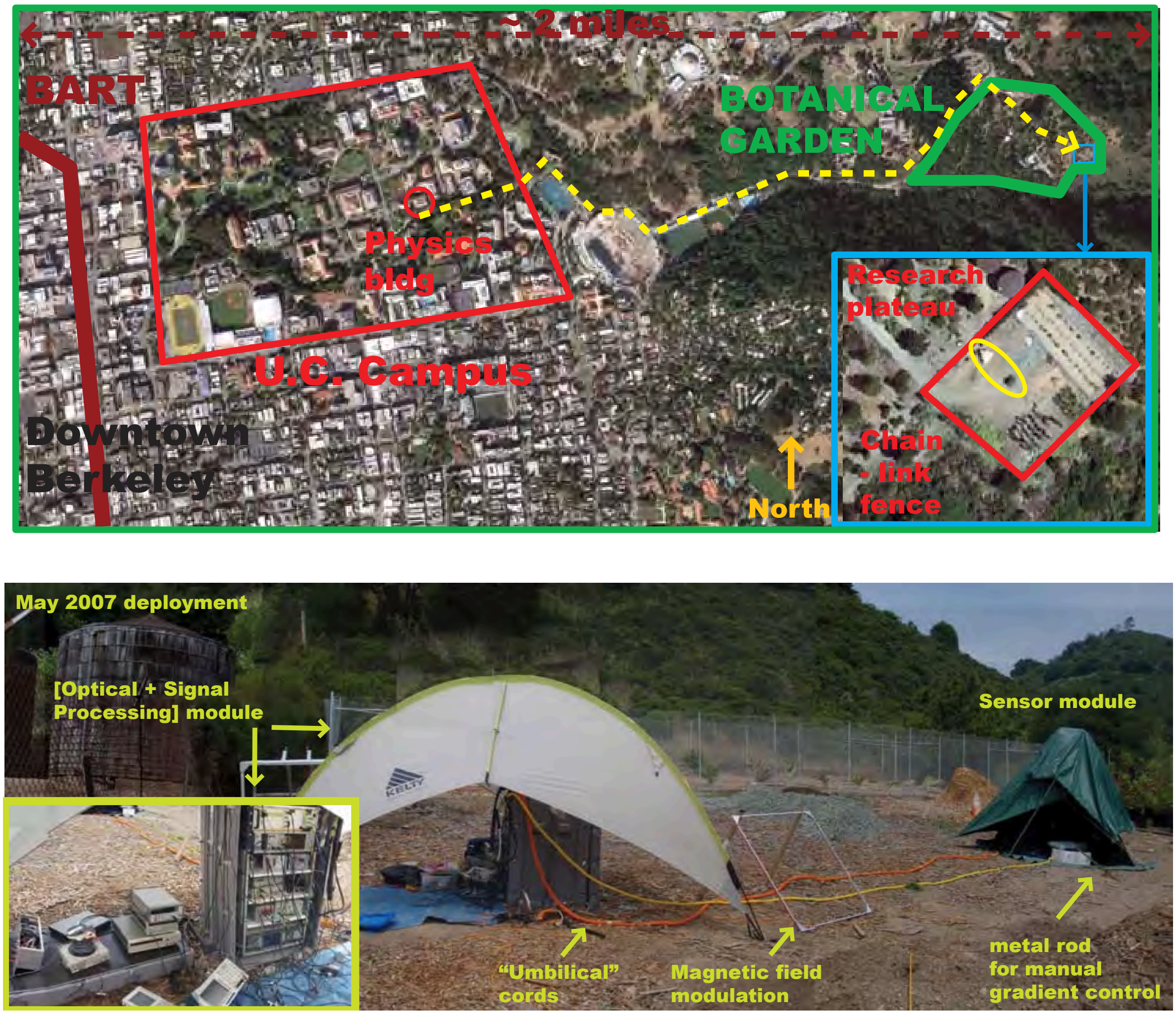

Figure 4.21: Upper: The University of California Botanical Garden, located approximately two miles from downtown Berkeley, has a research plateau which is a non-optimal location (in terms of magnetic field gradients) for testing and optimizing the sensitivity of a field-able atomic magnetometer. Insert: Aerial view (Google map) of the research plateau and view of the apparatus (yellow oval) with optical/signal-processing and sensor-head modules separated by $\sim$ 10 m . On the plateau the magnetic field gradient was measured at approximately 1-10 μG/cm (up to 5 orders of magnitude better than in the lab). The plateau is closed with a chain-link fence, has conductive wet-ground, and residual ferromagnetism in the gravel ground cover. The Bay Area Rapid Transit (BART) electric trains, although $\sim$ 2 miles distant, causes up to mG-size magnetic field fluctuations (Fig: 4.22) - deployment: 2007.

Lower: The gradiometer/magnetometer's two modules are connected by two flexible "umbilical cords" (one for each of the two sensor heads) channeling optical fibers, signal and power cables. An iron bar near the sensor module serves to set a non-zero gradient to minimize electronic cross-talk between the two sensor channels. The optical/signal-processing module is sheltered and enclosed in a weatherproof 19-in. rack [Deployment: 2007 - Project manager: J. Higbie - Collaborators: J. Higbie, E. Corsini, C. Hovde, T. Karaulanov - Photographs: E. Corsini - PI: D. Budker].

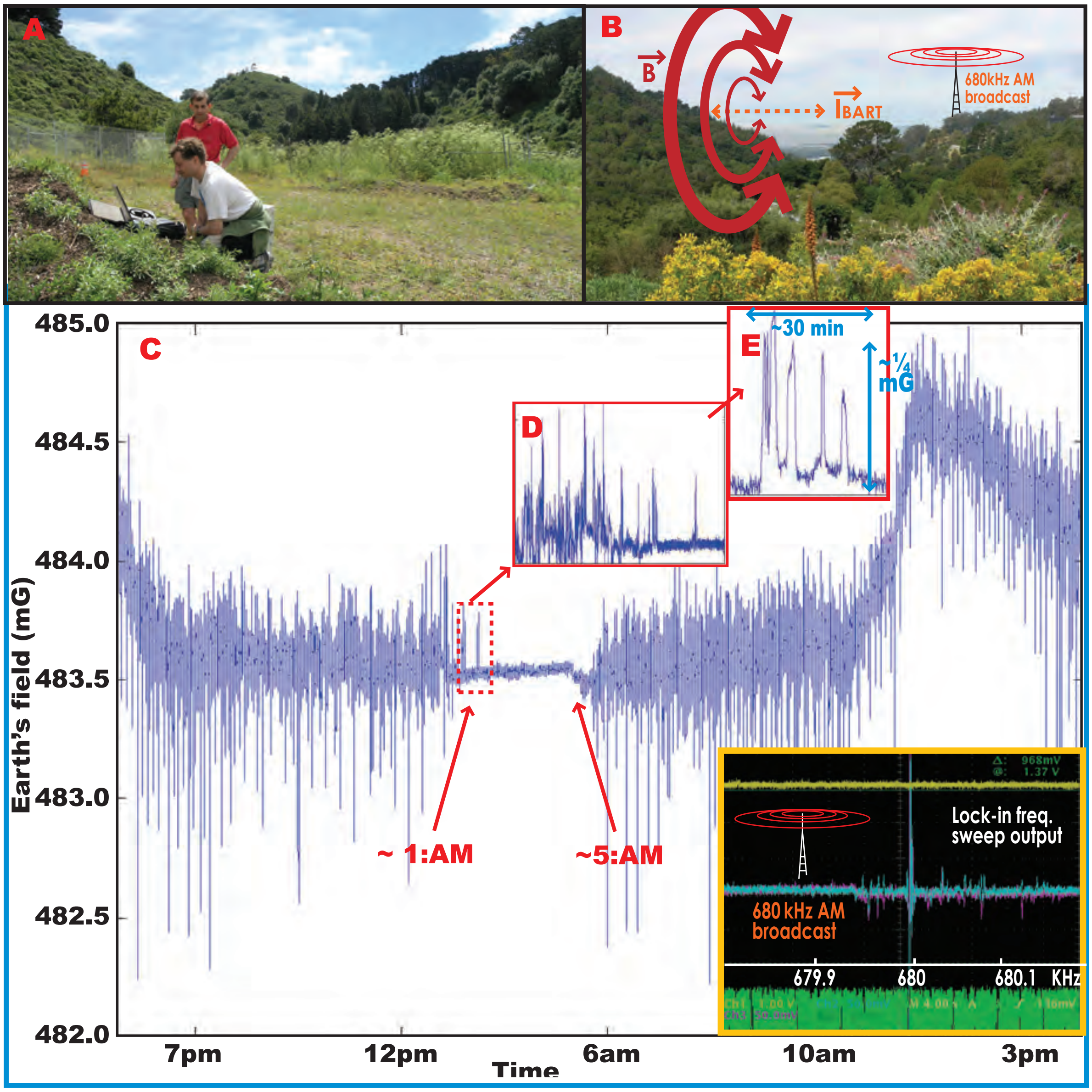

Figure 4.22: Earth's magnetic field at the University of California botanical garden research plateau (A): - 24 hour measurement (C,D,E) with a triaxial fluxgate magnetometer (Walker Scientific FGM-5DTAA). Although approximately two miles from the nearest station (B) the Bay Area Rapid Transit (BART) electric train system, fluctuations are recorded on the order of up to 1/2 mG superimposed on a mean Earth's magnetic field of ~500 mG. BART suspends operation between approximately 1-5 AM, and longer during the week ends during which we observe a dramatic reduction in the magnetic field fluctuations (three consecutive 24-hour periods are shown in Fig. 7.7 and in Ref. [56]). Lower-right insert: KNBR is a 50 kW AM sport-radio station broadcasting non-directionally at 680 kHz. The signal can be heard in most of the western United States and as far as the Hawaii at night. The output of a lock-in with the onboard oscillator sweeping through 680 kHz shows a noise floor over one order of magnitude larger at that frequency. [deployment: 2006 (J. Higbie and E. Corsini are shown in A) - data collection: J. Higbie, E. Corsini, P.I.: D. Budker - project manager: J. Higbie - Data presented by Higbie *et al* (meetings info not available) and by Corsini *et al* at MURI meetings in 2007 & 2008 / Insert data (2008 deployment): E Corsini, C. Hovde - project manager: E Corsini - PI: D. Budker].

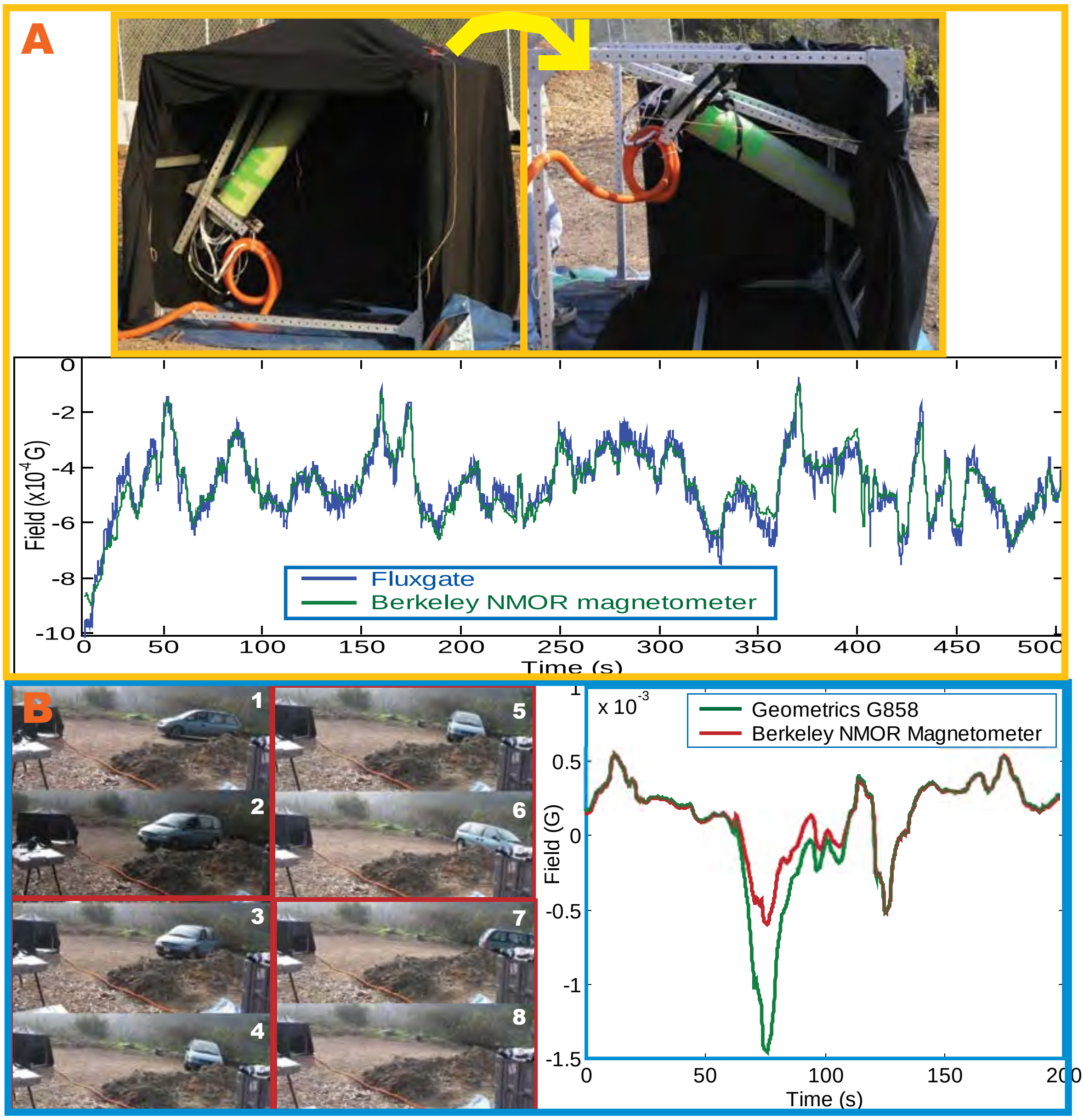

Figure 4.23: Stability and robustness of mechanical construction and self-oscillation A: Self-oscillation (one channel with Cs vapor cell ≃350 kHz) and optical alignment is maintained through translation (not shown) and rolling of the optical sensor/platform. The first iteration of the magnetometer sensor is shown; the one-sensor's G-10 fiberglass tube-support is 48 in long and the supporting frame is made of aluminum. In the lower part of figure A the sensor self-oscillation signal (green) is shown tracking the output of a G858 commercial atomic magnetometer from Geometrics Inc.(blue) [deployment: Feb 2007]
B: Robust self-oscillation in the presence of a large magnetic field fluctuation. The first iteration of the sensor self-oscillation signal is shown tracking a G858 commercial atomic magnetometer from Geometrics Inc. The sensors are approximately 1 m apart [deployment: 2007 - data collection by J. Higbie, E. Corsini, and C. Hovde - PI: D. Budker - project manager: J. Higbie - Photographs: E. Corsini - Data presented by Higbie *et al* (meetings info not available), by Hovde *et al* (meetings info not available), and by Corsini *et al* at MURI meetings in 2007 & 2008].

4.2.14 Mechanical stability and robustness of self-oscillation

Optomechanical designs currently available for laser table experiments have benefited from several decades of cumulative engineering experience. The ring/tube design showed robust beam-alignment stability when the platform was transported (not shown) or rolled as shown in Fig. 4.23A. The platform showed long term stability (several months at a time) in the presence of temperature fluctuations ranging from 10-30°C, buffeting by high winds, and with humidity ranging from relatively dry to one associated with a downpour (data not shown). We observed negligible wear and tear after several months of deployment in the field.

Self-oscillation with AM NMOR can sustain non-optimum alignment of the magnetic field (Fig. 4.23A) and large magnetic field fluctuations in the presence of a moving vehicle (Figs 4.23B). However the amplitude of the self-oscillation signal is reduced when the self-oscillation frequency shifts beyond the fixed band-pass filter frequency range (the filter stage comes after electronic amplification and before digitizing). Fig. 4.24D shows an example of signal amplitude reduced when the modulated magnetic field shifts the self-oscillation frequency outside the range of the bandpass filter.

4.2.15 Self-oscillation with modulated gradient. High bandwidth demonstration

In figure 4.24, the gradiometer's capability to detect AC magnetic fields is shown. A square-modulated AC magnetic field is added to the Earth's field, producing a modulation of the total magnetic field (Fig. 4.24A) and a modulation of the field gradient (Fig. 4.24B). The gradient is measured by referencing a lock-in to one of the gradiometer channels while the other channel goes to the lock-in input (Fig. 4.24B,D). In figure 4.24E we observed a reduced amplitude of the self-oscillation signal due to the range of the bandpass filter. With the spectral analyzer function of the oscilloscope we observed a DC gradient at 125 Hz (the gradient between the two channels was deliberately set at ∼100 Hz to avoid cross-talk in the two channels electronics). In addition to the DC gradient, a side band corresponding to the applied modulated gradient is observed separated from the DC gradient by the modulation frequency. In this preliminary result the AC magnetic field signal was observed up to ∼ 2 kHz (Fig. 4.24).

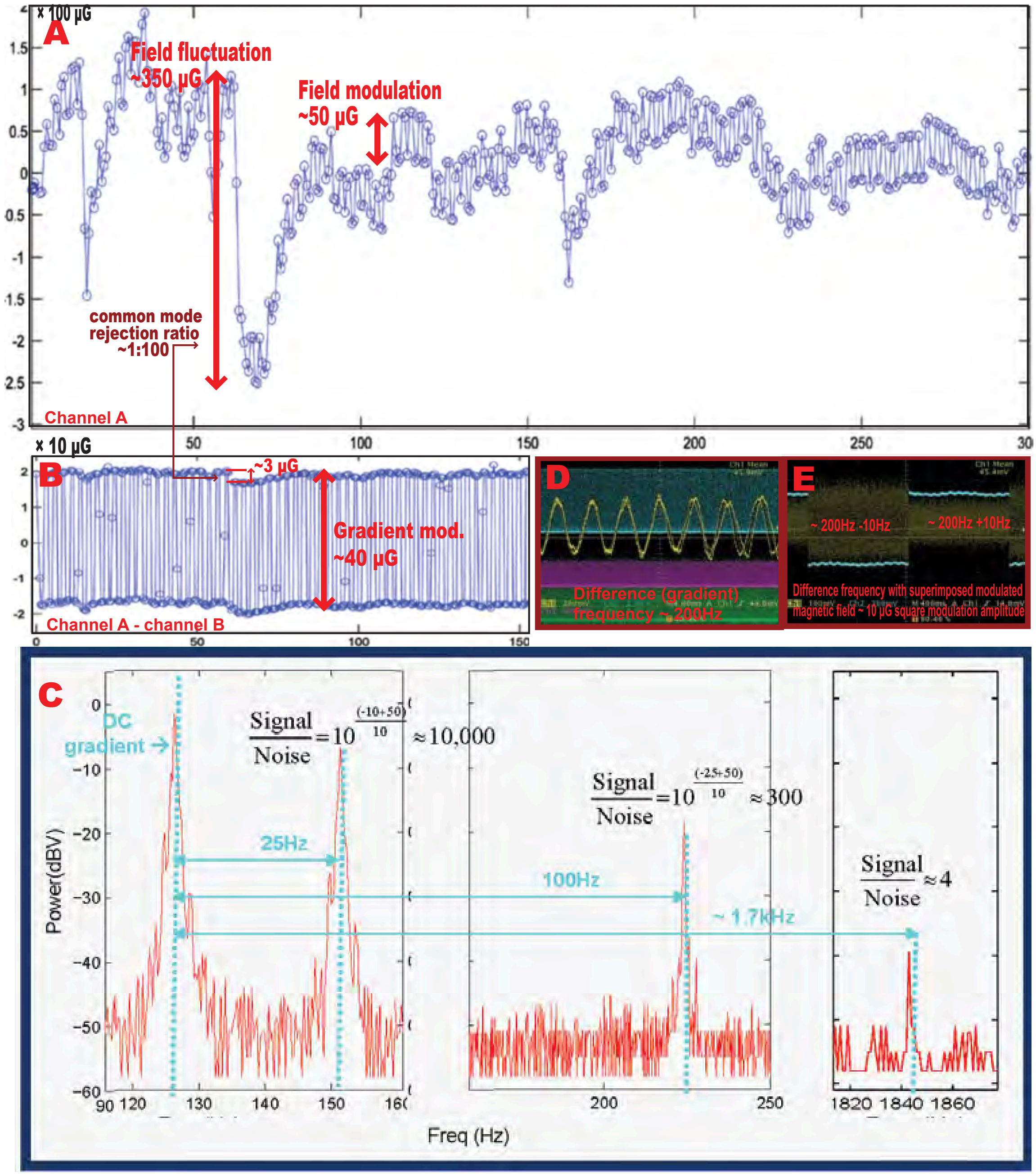

Figure 4.24: High bandwidth demonstration: self-oscillation on two channels with cesium vapor cells (≃350 kHz). The field (A) and gradient (B) are modulated up to 1.8 kHz (C: difference frequency FFT) demonstrating the bandwidth capability of a self-oscillating magnetometer. Field technique: to obtain the difference frequency, the self-oscillation of one channel is demodulated using the other channel as the reference frequency (insert D). The difference frequency is seen alternating (insert E) by ±200 Hz when the ∼1 μG square magnetic field modulation is superimposed to the Earth's field. [deployment: Oct 2007 (D & E inserts: 2008) - data collection by E. Corsini and T. Karaulanov - PI: D. Budker - project manager: J. Higbie - Data presented by Corsini *et al* at MURI meetings in 2007 & 2008]

4.2.16 AM NMOR in the presence of nonlinear Zeeman effect with ^{87}Rb

In this section we report on a field deployment of 2008 with anti-relaxation coated cells filled with a ^{87}Rb vapor (Fig. 4.25. At Earth's field the self-oscillation frequency for ^{87}Rb is ∼680 kHz. The amplitude of the self-oscillation signal was larger with the laser frequency locked on the F=2 hyperfine ground state. There are three NMOR resonances on the F=2 ground state. The three resonances are nearly degenerate (not "resolved") at low magnetic field and are separated by ∼70 Hz at Earth's field. The three resonances are shown "resolved" in figure 4.25A_1 & A_2. Resolved resonances makes possible to self-oscillate on one narrow resonance rather than a wider overlap of the three. The a Hz separation offers the advantage of resolving and self-oscillating on either one of the three narrow resonances. In sections 4.2.14 & 4.2.15 cesium cells were used resulting in a the self-oscillation frequency of ∼350 kHz. At earth's field the NMOR resonance are separated by ∼15 Hz and are not resolved, therefore broadening the NMOR resonance width and reducing the magnetometer sensitivity.

4.2.17 Conclusion

We have shown that an optical platform, based on a tube/ring design, replicates in the field, the re-configurability and stability one finds in the lab with standard optical elements mounted on a laser table. We have shown that the tube/ring design conception is well suited for rapid in-the-field alignment, reconfigurability, and trouble shooting. The design was shown to be optically stable while physically rolled through $\sim 90°$, and lends itself to airborne test-flights such as balloon flights.

The electronics presented in Appendix B show that a simple, fast, compact, well grounded and shielded design is well suited for a self-oscillating, high-bandwidth atomic magnetometer.

The field-tests allowed us to determine improvement that may be made to the platform. In particular temperature stabilization to the entire optical/signal-processing module, a feedback loop to optimize the contrast of the Mach-Zehnder amplitude modulator, and a feedback to the electronic phase-shift control to optimize the self-oscillating loop, are three areas of needed improvement.

We have also shown that the physics pertaining to atomic magnetometry at Earth's field in a non-shielded environment is many-faceted and offers challenging research directions. In particular the all-optical self-oscillation magnetometer scheme introduced by Higbie *et al* was shown to have a robust in-the-field self-oscillation in the presence of fast and large magnetic field fluctuations, and was shown to detect AC magnetic field up to several kHz.

We have also shown that, to effectively investigate the physics of Earth's field magnetometry and the self-oscillation configuration in Earth's field, a multi- and rapid reconfigurable non-magnetic optical platform is necessary. We have shown that the optical platform, which construction was shown in Part I, fulfils that necessity. To the best of our knowledge, field-able commercial or test-magnetometers have so far been constructed in a glued-in-place single-configuration, such as the ones manufactured and/or tested by Geometrics Inc. and Twinleaf LLC. The fixed configuration is suitable for marketing but is

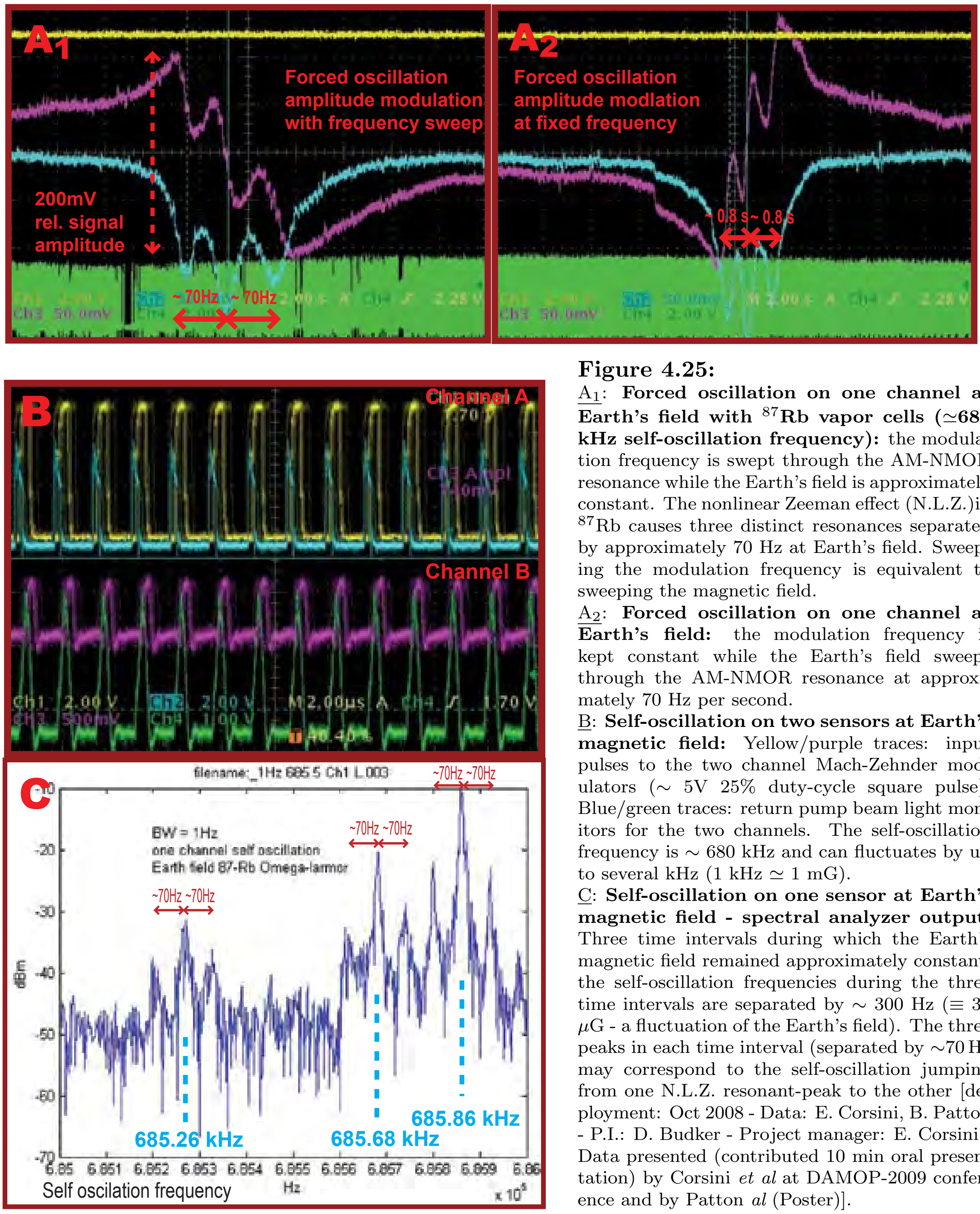

Figure 4.25:
A$_1$: **Forced oscillation on one channel at Earth's field with ^{87}Rb vapor cells ($\simeq$680 kHz self-oscillation frequency):** the modulation frequency is swept through the AM-NMOR resonance while the Earth's field is approximately constant. The nonlinear Zeeman effect (N.L.Z.)in ^{87}Rb causes three distinct resonances separated by approximately 70 Hz at Earth's field. Sweeping the modulation frequency is equivalent to sweeping the magnetic field.
A$_2$: **Forced oscillation on one channel at Earth's field:** the modulation frequency is kept constant while the Earth's field sweeps through the AM-NMOR resonance at approximately 70 Hz per second.
B: **Self-oscillation on two sensors at Earth's magnetic field:** Yellow/purple traces: input pulses to the two channel Mach-Zehnder modulators ($\sim$ 5V 25% duty-cycle square pulse). Blue/green traces: return pump beam light monitors for the two channels. The self-oscillation frequency is $\sim$ 680 kHz and can fluctuates by up to several kHz (1 kHz $\simeq$ 1 mG).
C: **Self-oscillation on one sensor at Earth's magnetic field - spectral analyzer output.** Three time intervals during which the Earth's magnetic field remained approximately constant; the self-oscillation frequencies during the three time intervals are separated by $\sim$ 300 Hz ($\equiv$ 30 μG - a fluctuation of the Earth's field). The three peaks in each time interval (separated by $\sim$70 Hz) may correspond to the self-oscillation jumping from one N.L.Z. resonant-peak to the other [deployment: Oct 2008 - Data: E. Corsini, B. Patton - P.I.: D. Budker - Project manager: E. Corsini - Data presented (contributed 10 min oral presentation) by Corsini *et al* at DAMOP-2009 conference and by Patton *al* (Poster)].

not optimum for the work realized in this chapter and the one completed afterwards (Sec. 4.3).

4.2.18 Acknowledgements

Acknowledgement is given to the U.C. Berkeley Botanical Garden staff for the use of the “research plateau”. In particular we thank Paul Licht and Holly Forbes for their warm welcome and interest in our research. We also thank Mark Prouty, C.O.O. and director of Geometrics Inc., for the loan of a G858 magnetometer, which we used to perform reference measurements.

4.3 Appendix to PART II: Later design improvement and deployments

After the conclusion of this work, Brian Patton took management of the apparatus and realized some of the future improvements suggested in Sec 4.1.9. In particular he added feed-back loops to stabilize the Mach-Zehnder amplitude modulator’s contrast and phase, and to the phase-shift in the self-oscillation loop. He also added temperature stabilization to the mini-DAVLL and to the laser diode. The improvements made the self-oscillation long-term stable. Brian Patton and Chris Hovde (Southwest Science) realized test deployments at magnetic field testing areas at the NASA. Moffett Air Base (Fig. 4.20), and at the United States Navy base in Panama City, Florida. In these deployments Patton and Hovde quantified heading error in both swept and self-oscillation modes, and realized remote detection described in Sec. (4.1.6). Description and results of this work are in Refs. by Patton *et al* and by Hovde *et al* [85, 86, 109, 110]. These results confirm the stability, multi-configurability, and practical use of the field-able design described in this Chapter, and confirm the rich and multi-facetted physics surrounding atomic magnetometry in the geophysical magnetic field range.

4.4 Appendix to PART I: "The Pulser Box"

The function of the electronic signal processing module is to amplify, to apply a bandpass-filter, to convert the amplified sinusoidal signal to a pulse, to control the pulse's phase and duty cycle for optimum self-oscillation gain, and to add an output buffer capable of driving the optical modulator 50Ω load. The electronic sequence is depicted in the schematic of Fig. 4.26 (Upper).

In early deployments the above functions were realized with a cascade of home-made and commercial amplifiers, and function generators. Later a "pulser box" consolidated these functions into one PCB board. The board had separate power and split ground planes and shielding of the pre-amp function . Other improvements of the "pulser box" was a filtered power supply, a variable DC output for manual tuning of the optical modulator DC-bias input, a copy of the amplified signal for monitoring purposes, and in-phase and out-of-phase copies of the square pulse for frequency counting and other optional uses.

The "pulser-box" electronics (although simple), significantly reduced the electronic noise and jitter (the pulse jitter was measured to be nG-equivalent in magnetic field noise).

4.4.1 Conclusion of Appendix

The "pulser" construction indicates that simple, fast and well shielded/grounded electronics, which can be made compact and with low power consumption are well suited for Earth's field atomic magnetometry, including detection of AC magnetic fields (Sec.4.2.15). The "pulser box" was used in the last deployment described in section 4.2.16.

4.4.2 Acknowledgements of Appendix

James Higbie, together with Todor Karaulanov, provided the first iterations of the commercial and home-made electronic components which became the seed-ideas for the "pulser-box". Construction of both "pulser boxes" and the testing and characterization of one box were completed by E. Corsini during 2007-2008.

Brian Patton (provided help in the final deployment described in Part II [summer 2008]) fixed soldering shorts in one of the two pulser-boxes, suggested reducing the number of amplification stages from four to two, and adding AC coupling between amplification stages.

the amplifications stages. Chris Hovde (Southwest sciences) took part in some additional characterization of the ”pulser box”

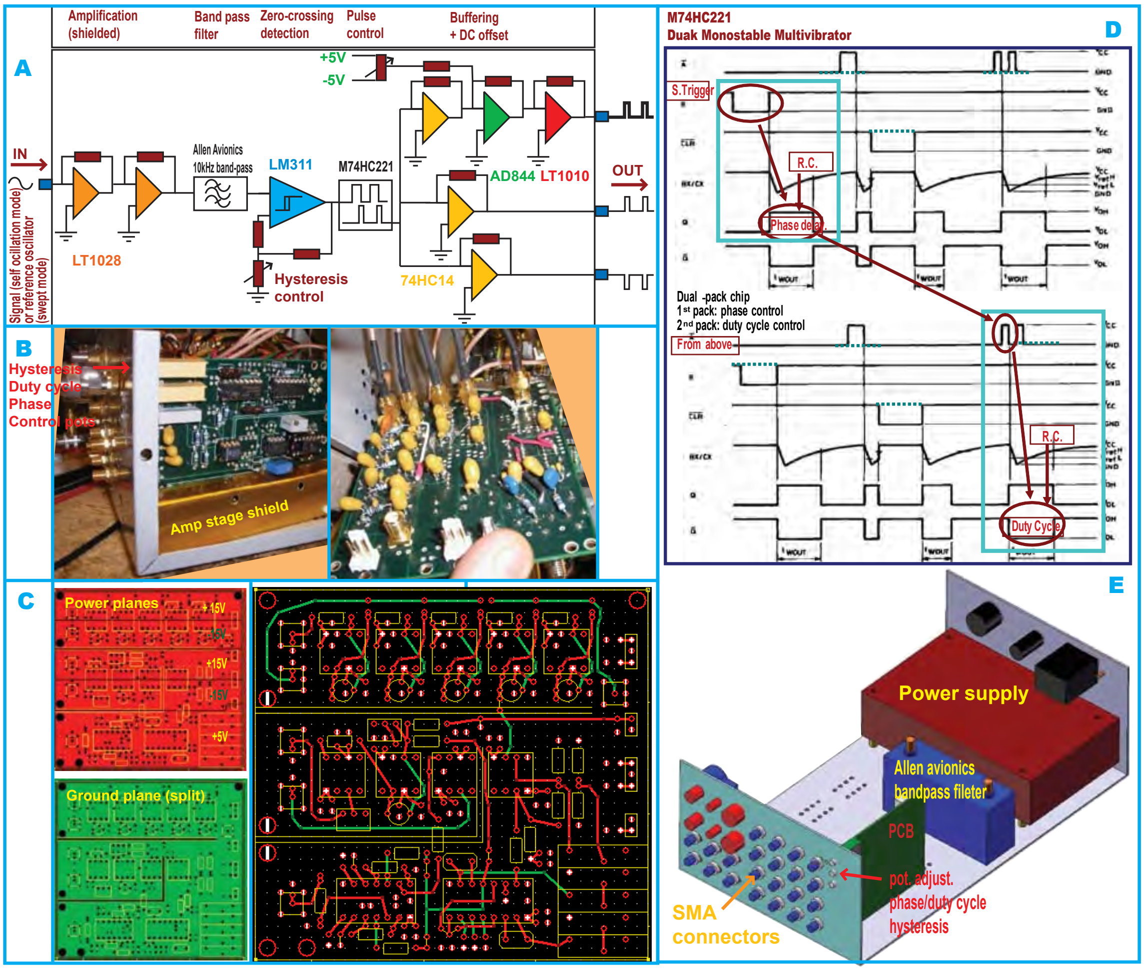

Figure 4.26: Left: power supply, amplification, filtering, and pulse shaping electronics (“pulser box”).
Right: The electronics sequence is a 4-stage 10 kΩ input amplification (LT1028 - later reduced to a 2-stage), a 5 kHz or 10 kHz bandpass filter, a zero-crossing detection (LM311 Schmitt trigger) with adjustable hysteresis-control, a dual monostable multivibrator (M74HC221) to adjust phase and duty cycle, a digital buffer (74HC14 - 6 inverting outputs), branching into three outputs, one in-phase, one out-of-phase, and one in-phase with a DC bias added to it (AD844) and 150mA or 250mA high speed buffer (LT1010 or BUF634, respectively) [The “pulser box” seed ideas: J. Higbie & T. Karaulanov. Construction, testing and characterization: E. Corsini, added modifications mentioned above: B. Patton (Sec. 4.4.2)].

Chapter 5

A Multi-functional, Shielded (in-lab) Magnetometer Platform, to Investigate Atomic Magnetometer's Configurations at Magnetic Fields Ranging up to, and Beyond, Geomagnetic Range Parts I and II

Related publication
Title: "Multi-functional and rapidly re-configurable magnetometer platform to efficiently investigate and optimize atomic magnetometer configurations at magnetic fields ranging from zero magnetic field to geomagnetic range and beyond".
Journal: in preparation (RSI)

Collaboration (2009-2012):
Part I: E. Corsini[1],
Part II: E. Corsini[1], T. Karaulanov[1], M. Balabas[2], [limited collaboration: J. H. Higbie[1], C. Hovde[3]].
PI: D. Budker[1,4]
Affiliations:
[1]Department of Physics, University of California, Berkeley, CA 94720-7300
[2]the S. I. Vavilov State Optical Institute, St. Petersburg, 199034 Russia
[3]Southwest Sciences, Inc., 1570 Pacheco St., Suite E-11, Santa Fe, NM 87505
[4]Nuclear Science Division, Lawrence Berkeley National Laboratory, Berkeley CA 94720

pacs: 07.90.+c, 07.55.Db, 07.55.Nk, 07.60.-j, 32.10.Dk, 32.70.Jz, 33.15.K,r 42.82.Bq, 44.15.+a, 93.85.-q, 93.85.Jk
Keywords: multi-functional, re-configurable, geomagnetism, optimization, self-oscillation, all-optical, transfer of polarization, magnetometer, noise floor, sensitivity, coil-system.

Abstract

Atomic vapor cell magnetometers are today's most sensitive magnetic field sensors on par with superconducting quantum interference devices (SQUID)[59, 42]. However atomic magnetometers highest sensitivity is achieved near zero magnetic field and decreases by approximately three orders of magnitude at Earth's field [7, 5]. Higbie, Corsini, and Budker, have reported a promising, lab-tested, all-optical, high bandwidth, self-oscillating atomic magnetometer configuration (Ref. [83] and Ch. 3). To investigate magnetometer configurations (in particular the one described in Ref. [83]), as well as optimization methods, we report on the construction of two complementary magnetometer designs. The first one was described in Chapter 4) and is a portable/field-able design. The second one, described in this chapter, is a laboratory-based design. Both designs embody multi-functionality, and rapid re-configurability, for an effective evaluation and optimization of several magnetometer configurations.

The in-lab magnetometer device complements the fieldable one by allowing a systematic investigation of the parameter space in a well controlled and magnetically shielded environment. In part I of this Chapter (Ch. 5) we show design techniques to realize multi- and rapid re-configurability in a compact design with a footprint 43×42 in., (∼48×48 in. including instrumentation [∼1/2 a standard laser table] - Fig. 5.1B,C,D). In part II of this Chapter we present some preliminary measurements touching on the magnetometer's stability and noise floor when operated as a magnetometer in a self-oscillation configuration, on techniques in measuring sensitivity, on self-oscillation as a diagnostic tool, on transfer of polarization through the excited state, and on a tip on magnetic shield "de-Gaussing". These measurements and techniques serve to exemplify the capability and versatility of the device and the many facets of atomic magnetometry at non-zero field. Subsequent results (soon-to-be published - Ref. [57]) are presented in chapter 6 and demonstrate one particular use of the device. Additional results using some of the other capabilities of the device are forthcoming.

Chapter 5 - PART I

Design and realization of multi-functionality and rapid reconfigurability with a small footprint

5.1.3 Introduction

Testing magnetometer characteristics (such as sensitivity, bandwidth, noise floor, and stability of feedback mechanisms) and investigating areas of optimization, are more easily accomplished in a well controlled and shielded environment, one parameter at a time. The key to these goals is to enable rapid changes in the magnetometer configurations (changing alkali cells, pumping and probing schemes, temperature, magnetic field and gradients, for example). Changing configurations in the original in-lab testing platform, shown in Fig. 5.1A, took several hours, and provided the motivation to build a quickly reconfigurable and multi-functional platform.

The platform shown in Fig. 5.1B,C,D (and all subsequent figures in this Part I) show the realization of that goal. The platform has a footprint of 43×42 in., fits on two-third of a 4×10 ft. laser table (including instrumentation and room for future functionalities). It is supplemented with a compact but fully operational work-station, including soldering station, tools, spare optical and electronic components, miscellaneous supplies, and storage space for organization. The platform is fully enclosed by light blocking velcro-removable curtains to perform sensitive optical measurements while work is on-going in other sections of the lab-room. The platform/workstation combination occupies ∼1/2 of a 15×21 ft. laboratory room and can be used as a semi-permanent and sustainable magnetometer testing tool.

5.1.4 Schematics of apparatus

The apparatus (schematic shown in Fig. 5.2 and partial 3D drawing shown in Fig. 5.3) consists of: two lasers with optical frequency stabilization; optical elements to control the laser beams polarizations; powers, beam-merging, and beam alignment to traverse the vapor cell on three axes; optical amplitude modulation for the pump beams on three axes; a four-layer mu-metal shield enclosing an anti-relaxation coated alkali vapor cell (^{85}Rb, ^{87}Rb, or Cs); a magnetic shield temperature stabilizing mechanism; a coils-system to provide a homogeneous bias magnetic field, and photo sensors to measure optical rotation or absorption on three perpendicular axes.

The pump and probe beams are selected from one of two distributed feedback (DFB) laser (Toptica LD-0795) resonant with the Rubidium (Rb) $5\text{s}^2S_{1/2} - 5s^2P_{1/2}$ D1 line (λ=795 nm); or from a DFB laser (Toptica LD-085) resonant with the Cesium (Cs) $6\text{s}^2S_{1/2} - 6s^2P_{3/2}$ D2 line (λ=852 nm). Lasers current drivers (Thorlabs LD-205) and temperature controllers (ILX LDT6412 & Wavelength Electronics MPT5000) maintain the laser optical frequency on resonance.

Two Dichroic Vapor Laser Locks (DAVLLs) [146] and two P.I.D. (SRS SIM960) are used to lock the lasers' optical frequencies within the width of the Doppler broadened optical resonance. Two reference vapor-cells and a Fabry-Pérot interferometer provide additional monitoring of the optical frequencies stability.

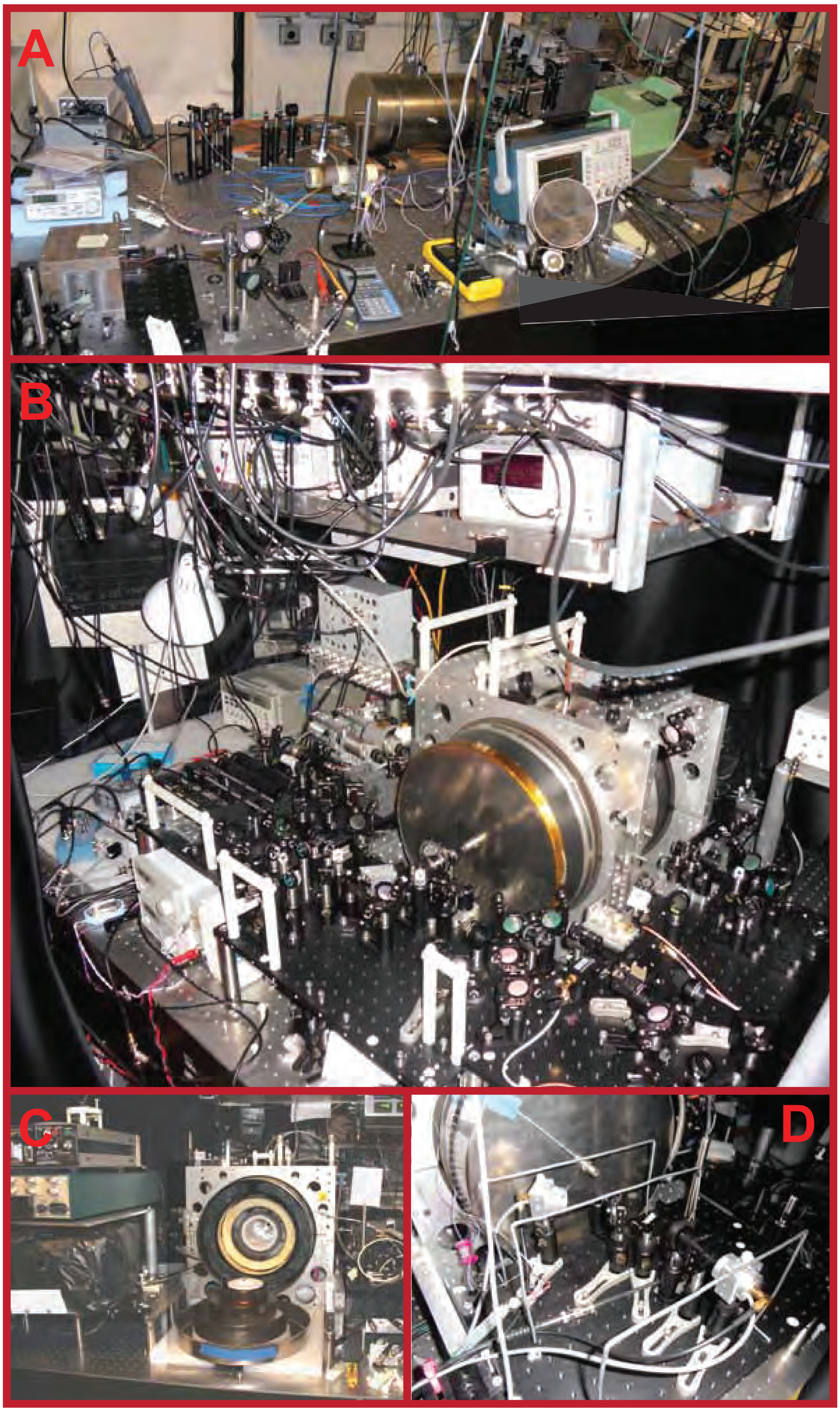

Figure 5.1: A: the "before" version sparsely covered a 10×4 ft laser table and allowed one magnetometer configuration at a time; changing the alkali cell or the configuration took several hours. The magnetic three-layer shield is the work of Valeriy Yashchuk.
[Construction/project-management (2006-07): J. Higbie - Collaboration E. Corsini - PI D. Budker].
B,C,D: the "after" version has a footprint: ∼48×48 in., occupies a 6×4 ft. area on the same laser table (with ample space for additional components and functionalities - and leaves room for two additional undergrad projects on the same laser table), and incorporates several configurations at any one time, as well as rapid-reconfigurability for additional ones (for example, changing the alkali cell takes 5-10 min).
[Conception/design/construction/project-management (2009-2012): E. Corsini - Collaboration: T. Karaulanov - PI: D. Budker].

The 3 mm diameter collimated laser beams pass through optical isolators to minimize retro-reflection to the laser diode. For intensity and polarization control, each beam passes through a variable neutral density filter, a polarizer, and a quarter wave-plate. The beams traverse the alkali cell on either of or any combination of the three axes. Optical rotation (or absorption) is measured with a balanced polarimeter (or a photodiode) on each of the three axes. The optical rotation (or absorption) signal is amplified (SRS SR570 [or SR560]) and digitized with a DAQ (IOtech P-Daq/3001).

The magnetic field is applied with a set of three orthogonal coils, three gradient coils along the same directions, and one longitudinal second-order gradient coil, positioned within the inner-most layer of a four-layer mu-metal shield (manufactured by Amuneal). There are three main longitudinal bias coils, one is made of 1500 turns (36 gauge wire) and generates ∼4 mG with two AA batteries for several weeks, or ∼2 G with 20 mA and a ∼12 V compliance voltage. COMSOL modeling was used to optimize the geometry of the coils and to achieve better than 1% magnetic-field homogeneity within a 2 in-diameter, 4 in-long cylindrical volume (Fig. 5.8).

The pump light polarization and the relative orientations of the pump light, and magnetic field, are optimized for the desired resonance by controlling the axis of the bias magnetic field and the light intensity and polarization.

The self-oscillating loop feedback mechanism consists of a balanced polarimeter analyzer (Rochon polarizer + transimpedance differential amplifier [220kΩ feedback resistor + OP27 low noise amplifier]), a low noise voltage preamplifier (model: SRS SR560), a custom-made zero crossing detector (based on the single comparator LM311), and a function generator (model: BNC 675 in triger/burst mode), or a pulse generator (BNC 575), are used to adjust the phase and duty cycle of the pulse-train sent to the R.F. generator driving the AOM (Isomet). The AOM, in turn, modulates the pump-laser beam, which stroboscopically pumps the alkali atoms (Ch. 1). The Larmor precession of the atoms is detected by the balanced polarimeter, which closes the loop.

A temperature controller (Omega CN77353-PV) regulates the DC current (on/off with a user-set dead-zone - analog regulation is under construction) to two electric heaters consisting of quad-twisted non-magnetic heater wire (LakeShore QT36), which coils are positioned fore and aft of the cell, on the main shield axis. The residual magnetic field produced by the heaters is on the order of 2 μG with a ∼60 mA current in each strand (Sec. 5.2.8). In each heater coil the two twisted pairs (quad-twist - each twisted-pair having an Ohmic resistance $\simeq$180 Ω) are connected in parallel to a fixed 10.5V power supply. The electric heaters are supplemented with a water heater/cooler system. The innermost shield serves to conduct and distribute the heat so as to achieve a temperature which is approximatively uniform within the cell's volume, over a range spanning 15°C to 50°C, and with an outside air temperature of ∼20-25°C .

A second temperature controller (Omega CNI3252) regulates the DC current to the Rb DAVLL inner-shield heater and maintains a ∼constant cell (natural abundance Rb mixture or enriched ^{87}Rb) temperature (∼50°C) to increase the electronic error signal to noise ratio. The error signal to noise ration for the Cs DAVLL is sufficient at room temperature and no cell heater is used.

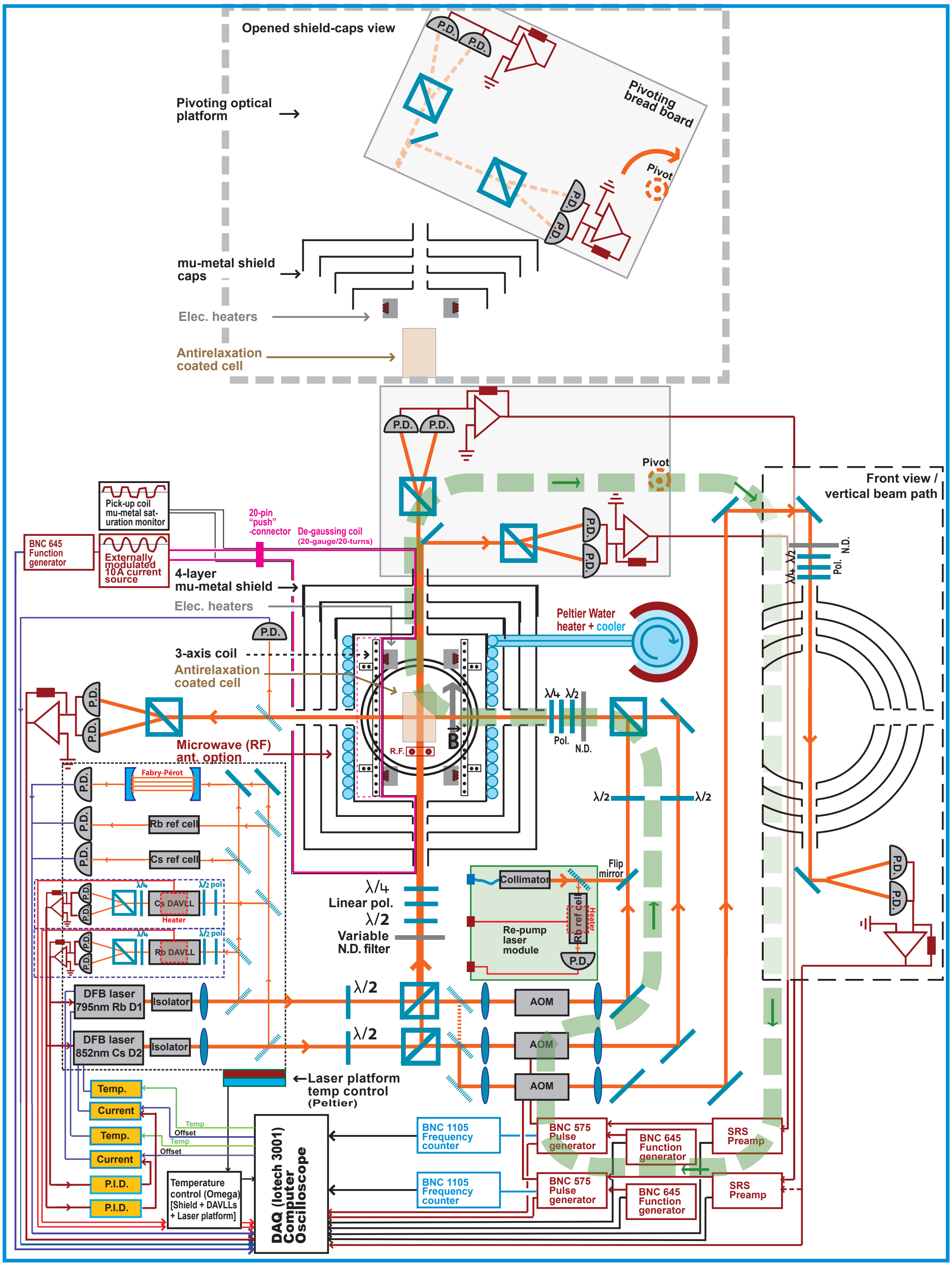

Figure 5.2: Multi-functional magnetometer platform (top view).Dashed box- top: shield caps and pivoting optical breadboard are shown in open position. Dashed box - right: front view - vertical beam path. Dashed green path: self-oscillation loops. [figure caption continued on next page].

Figure 5.2 caption continued:

Linearly polarized probe and circularly polarized pump beams are selected from either one of the two DFB lasers [Cs D2 and Rb D1]. An acousto-optic modulator (AOM) modulates the amplitude of each pump. A four-layer mu-metal shield encloses an alkali vapor cell. The inner shield temperature stabilization is realized with two electric heaters consisting of quad-twisted non-magnetic wire coiled in two solenoids parallel to the main axial symmetry. The Peltier heater/cooler was under construction at the time of publication (pressurize water [from a pump or tap water] and a hot/cold heat exchanger were temporarily used). The orthogonal three-axis coils generate the bias magnetic field. Balanced polarimeters measures optical rotation on three axes. The optical rotation signals are amplified and recorded with a DAQ. In self-oscillation configuration mode each signal is digitized, the phase shift and duty cycle are optimized, to drive the AOM. [Design/construction/project-management (2009-12): E Corsini - Collaboration: T Karaulanov - PI: D. Budker]. [Components under construction at time of publication: partial computer control only, shield's water coller/heater was built and tested but with a water heat exchanger (Peltier element under construction), the temperature control of the laser platform temperature was under construction, one balanced polarimeter (horizontal path perpendicular to the shield's axis) under construction, other three balanced polarimeters tested, two were used in the measurements of Part II. All other parts/components hereby described have been constructed, used, and tested.] [Conception/design/construction/project-management (2009-12): E. Corsini - Collaboration: T. Karaulanov - P.I.: D. Budker].

A removable "de-Gaussing" coil (20 turns of 20-gauge [HML-coated, NEMA MW 16-C, MWS Wire Industries, magnet wire]) is routed through the shield axial ports with a "push"-connect connector for easy insertion and removal. The coil has a capacity of up to 40 A for up to ~30 s (Sec. 5.1.6). In the planning stage is a permanent de-Gaussing coil to operate while making measurements (an effect, which has been shown to increase the shielding factor, and which has been investigated by V. Yashchuk [147]).

The option of adding microwave antennae to generate and "pick-up" microwave magnetic fields is available (Ch. 6).

5.1.5 Design and construction techniques

The magnetometer platform design incorporates a modular custom-made optical "rail-platform", "pivoting platforms", laser module, and fully integrated DAVLL module.

5.1.5.1 Modular optical "rail" and pivoting optical sub-platforms (or modular "optical groups")

The "rail" sub-platforms are for rapid removal and easy access to the shield's horizontal optical ports (Fig. 5.3E); after re-positioning the rail, optical re-alignment is greatly minimized. A top-rail (Fig. 5.3B) is for partial access (lateral displacement) or for complete access (longitudinal displacement) of the shield's vertical optical ports.

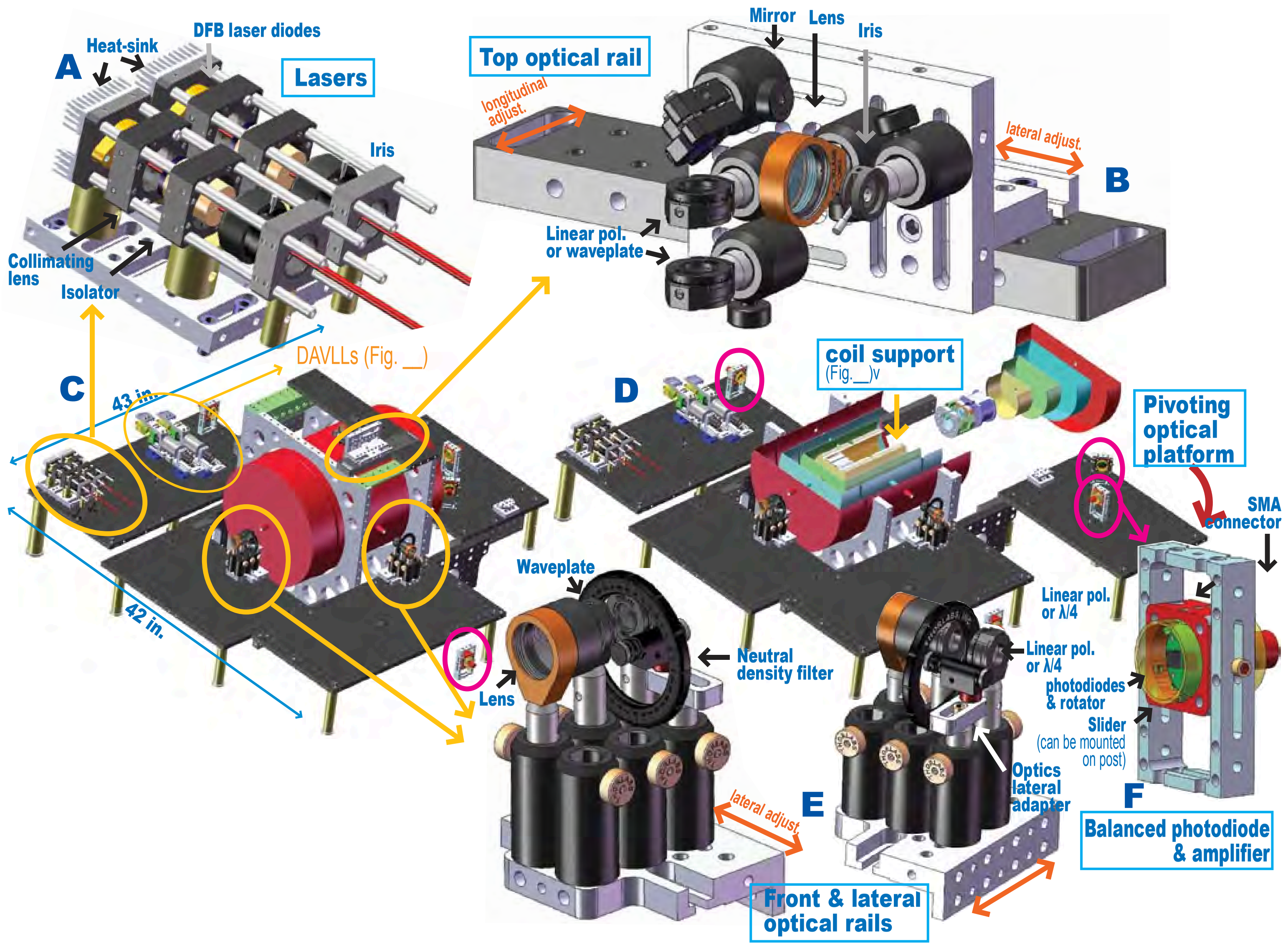

Figure 5.3: Multi-functional magnetometer platform and custom-made components (only the custom-made or rail mounted optical elements are show). C,D: pivoting optical platform (shown in the “closed” and “opened” positions) for rapid opening of the shields end-caps, access and switching vapor cells (10 minute turn around time) [Caption cont. next page].

[Caption - Fig. 5.3, cont.]

The scaled-up inserts show the two lasers (rubidium D1 line and cesium D2 line) and the rail-mounted optical components which mount at the shield's front, side and top entry-ports (the two dichroic vapor laser locks [DAVLL] platforms are shown in figure 5.4). The four-layer mu-metal shield achieves a shielding factor of 1:10^6. The sizes of the inner- and outer-most shields are 4.5×8.5 in. and 13×18 in., respectively. The multiple (shielded) electric cable connections and routings are not shown. The devices' multiple functions are realized within a footprint size of ∼48×48 in. not including instrumentation. [Conception/design/construction/project-management (2009-12): E. Corsini - Collaboration: T. Karaulanov - P.I.: D. Budker - (the three inner shields are the work of Valeriy Yashchuk)].

A pivoting optical sub-platform (5.1C & D) supports the optical-rotation (or absorption) photo-detection module; the platform pivots (and stores under another instrument-platform) for access and removal of the magnetic shield caps (to access the alkali vapor cell and electric heaters). The optical elements on the sub-platform are chosen so as to require minimum re-alignment when the pivoting platform is re-positioned. Details of the rail and pivoting sub-platforms, the DAVLL platform and other construction techniques are shown and described in figures 5.3,5.4, & 5.5.

5.1.5.2 Laser module

A distributed feed back laser is mounted on a modified Thorlabs cage system on a platform incorporating diode isolation and beam collimation (Fig. 5.3A). Laser temperature and current drivers are external to the module.

5.1.5.3 Balanced photodiode and amplifier module

Measuring optical rotation (performed at the shield's three outputs and at the two DAVLL's outputs) is realized with a balanced photodiodes and amplifier electronics. A common design and PCB board is used; however the speed of the Opamp and the value of the Opamp feedback resistor chosen for the appropriate bandwidth. The PCB board has the same 1 in.circular size and approximate layout as the one shown in Fig. 4.6, is mounted inside a custom made cylindrical mount, with one end closed with an SMA connector. It can mounted on the DAVLL module (Fig. 5.4 or on the custom made "pivoting optical mount" (Fig. 5.3F) for angle and height adjustments or on a standard 1/2 in.or 1 in.post (not shown).

5.1.5.4 Integrated DAVLL module

The DAVLL (optical frequency stabilization) necessary (and optional) optical components, balanced polarimeter, and amplifier, are mounted a DAVLL-platform and form the DAVLL module (Fig. 5.4). The DAVLL ring-magnet holders[99] were modified to incorporate an electric heater wound on the outer part of the holder (Figs. 5.4 & 4.18). Similarly the DAVLL module can be removed and replaced with almost no optical re-alignment necessary once repositioned, facilitating switching DAVLL vapor cells (for example, switching a cell with enriched ^{87}Rb for one with Rb in natural abundance, or one with potassium).

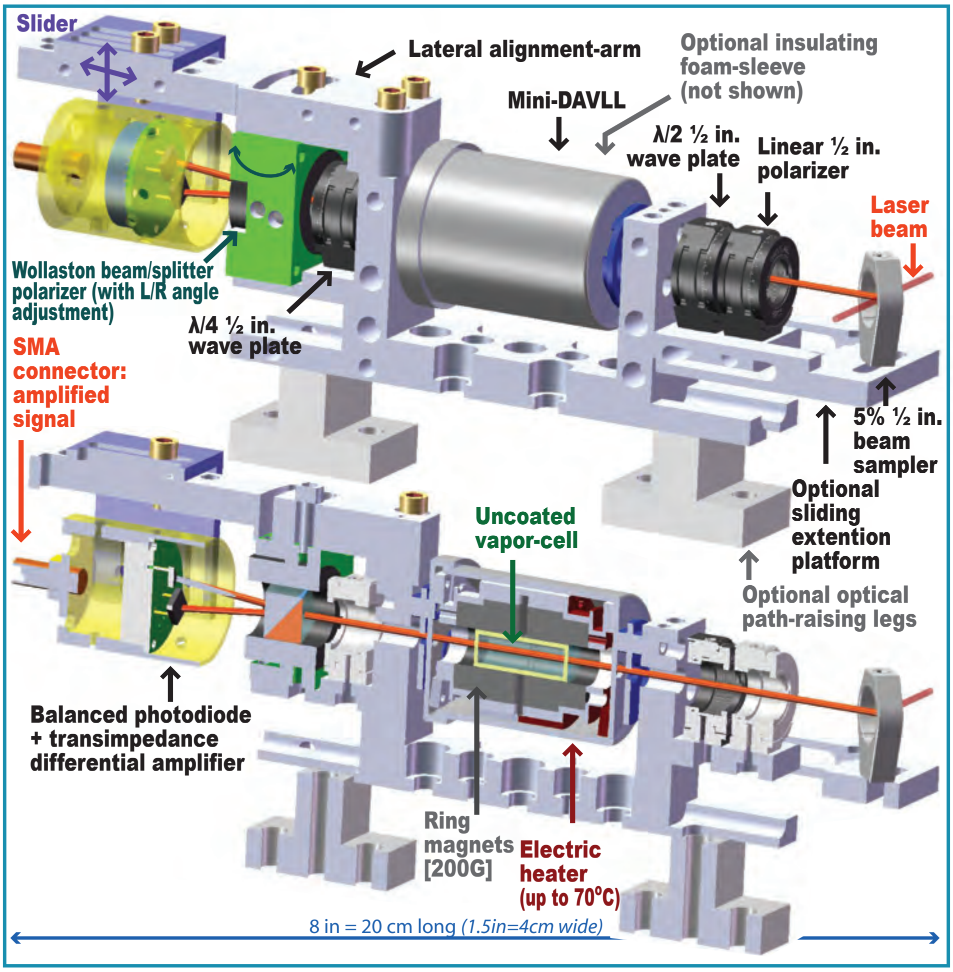

Figure 5.4: The mini-DAVLL (Dichroic Atomic Vapor Laser Lock - Ch. 4), is integrated into one DAVLL-platform. The platform includes an internal heater and all necessary optical elements (as shown). The DAVLL-platform can be easily removed and repositioned with almost no re-alignment necessary, allowing rapid changes of DAVLL alkali cells or interchange of DAVLL-platforms. DAVLL vapor cells temperatures up to 70 C can be achieved with the inner electric heater when supplemented with an optional foam sleeve (not shown) covering the mu-metal DAVLL mini-shield, and with ∼100 mA DC current. [Conception/Design/construction/project-management (DAVLL platform and inner heater (2009-12): E. Corsini - Collaboration: T Karaulanov - PI: D. Budker] [Conception/Design/construction/management of mini-DAVLL (2006-2011): Changmin Lee, G. Iwata - Collaboration: E. Corsini, J. Higbie, S. Knappe, M. Ledbetter - PI: D. Budker].

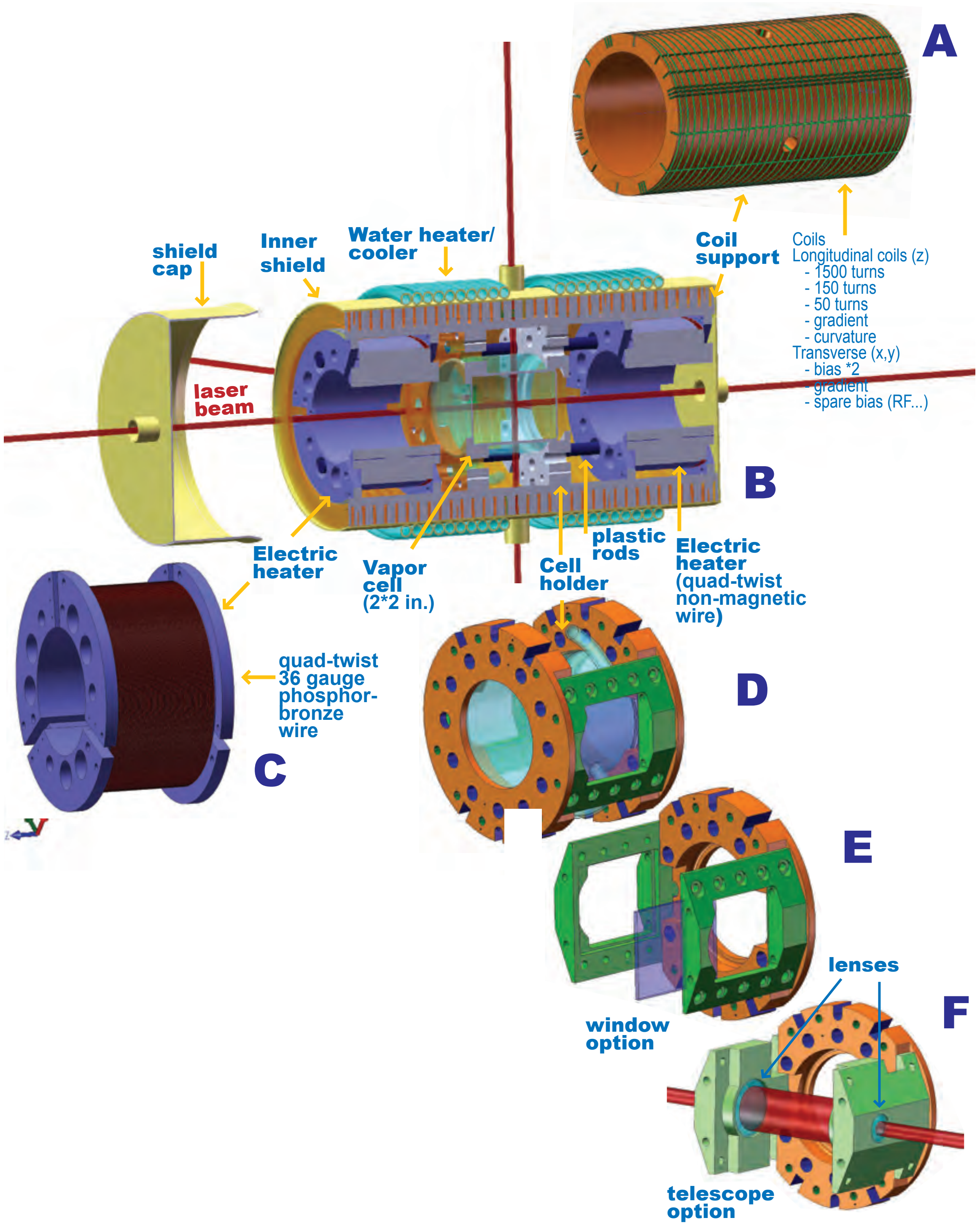

Figure 5.5: Inner shield; Teflon cylinder supporting the magnetic field bias, gradient, and curvature coil system; cell holder; electric heaters; water heater/cooler (see text). The cell-holder with optical-telescope was under construction at the time of publication. [Design/construction/project-management (2009-12): E. Corsini - Collaboration: T. Karaulanov - PI: D. Budker].

5.1.5.5 Inner shield cell holder and electric heaters

An inner-shield 5.5 in.diameter Teflon cylinder (Fig. 5.5A) supports the coil system described in Sec: 5.1.4. Within the Teflon cylinder an inner-shield cell holder (Fig. 5.5D,E,F) accommodates a variety of cell sizes and shapes, in particular alkene coated cells with a longer two-part stem to accommodate the alkali reservoir and a precision ground lock (Fig. 5.6 & 5.7) sealing the reservoir from the cell. One of the cells used in the experiment described in Chapter 6 was the spherical alkene coated cell (Fig. 5.7Rb3) made by M. Balabas (5.6 - lower left insert) and with which Balabas *et al* achieved a record (at the time) 77 s Zeeman relaxation time [59]. Another cell in the same experiment was a 4×1 in cylindrical alkene coated cell (Fig. 5.6 & 5.7Rb1 & Rb2). The precision-ground lock necessitates an axial rotation of the cell to open and close the lock (Fig. 5.6-right), which has to be performed every 4-5 hours, and can be achieved in a short time with the pivoting optical platform described in Sec: 5.1.5.1. The seal of the lock is crucial for long Zeeman relaxation times; two lock geometries are shown in figure 5.7. The cell holder can also support side windows (Fig. 5.5E) to minimize air currents, and an optional telescope to make the size of the beam larger than the shields' optical ports (Fig. 5.5F).

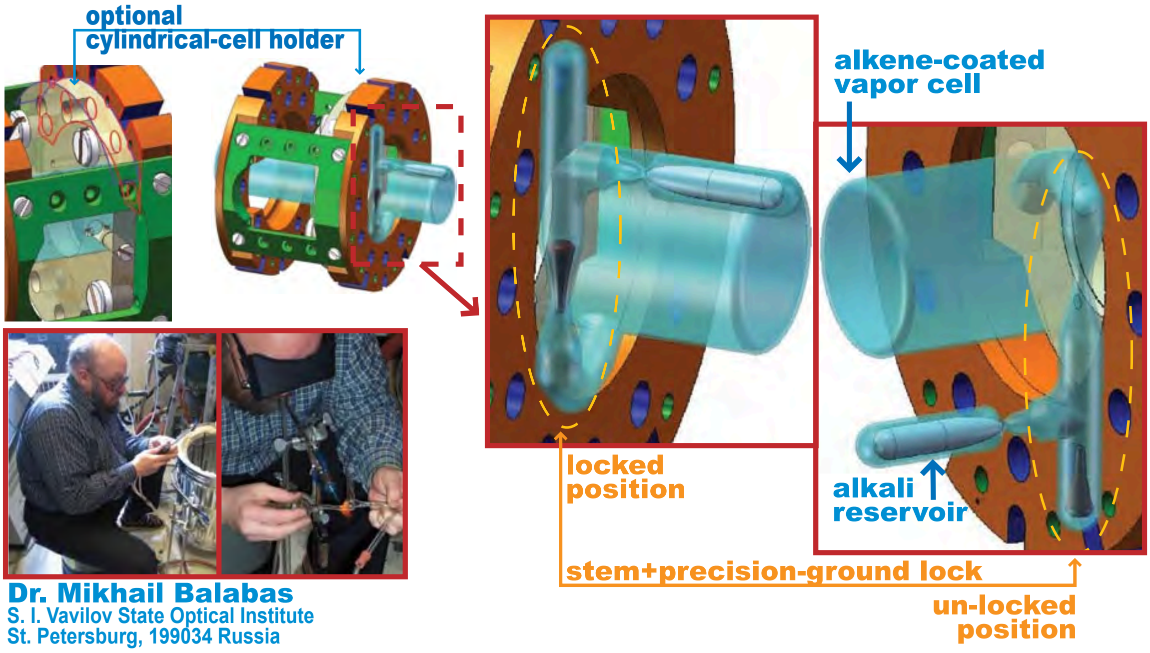

Figure 5.6: Alkene-coated cell with precision-ground lock + cell-holder adapter. Up to 77 sec Zeeman relaxation time was achieved with the anti-relaxation cell-wall alkene coating [23]. Coating and cell making (2009-10): Mikhail Balabas (insert), S. I. Vavilov State Optical Institute, St. Petersburg, 199034 Russia.[Design/construction/project-management (2009-12): E. Corsini - Collaboration: T. Karaulanov - PI: D. Budker].

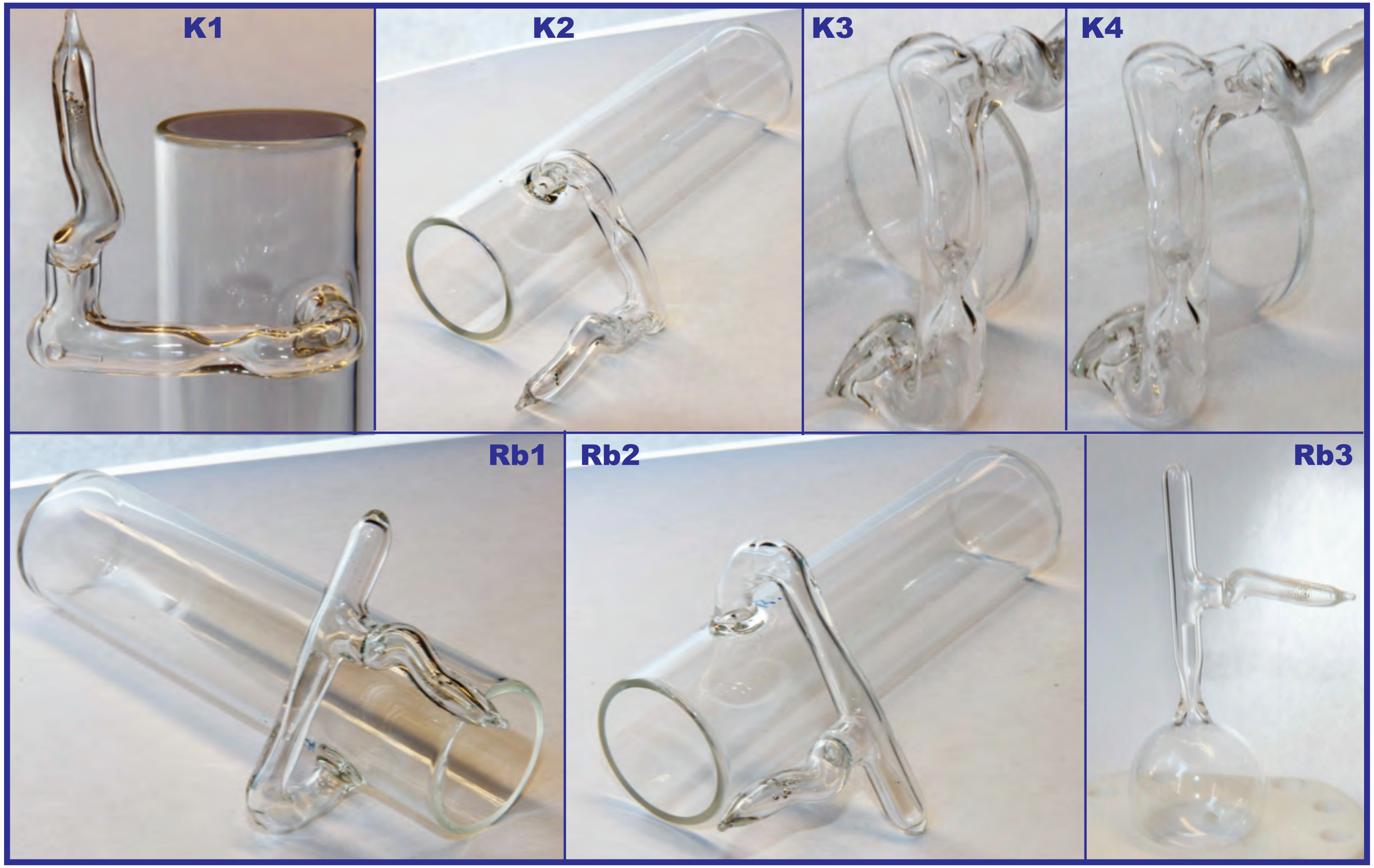

Figure 5.7: Alkene-coated cells with precision-ground locks. Different lock geometries were made. K1-4: potassium vapor cell (4 in long ×1 in diameter) with new ball-pin lock (3,4: the lock-pin can be positioned pointing up or down). underlineRb1-2: Natural rubidium vapor cell (that cell is one of the cells used in Chapter 6) with "traditional" lock. Rb3: the "legendary" 1 in. diameter spherical cell used which exhibited a Zeeman relaxation time of 77 s, as observed by Balabas *et al* [23]. [Coating and cell making (2009-10): Mikhail Balabas (insert), S. I. Vavilov State Optical Institute, St. Petersburg, 199034 Russia].

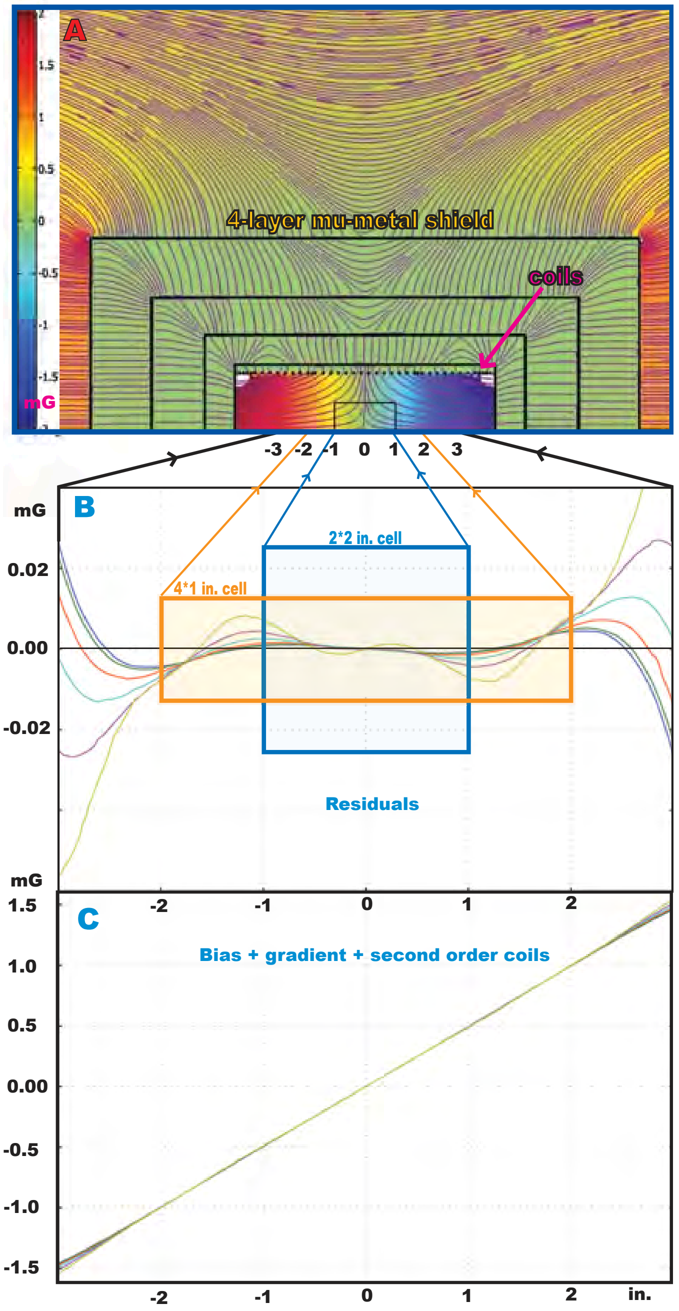

Figure 5.8: Simulation of the bias magnetic field in the four-layer mu-metal shield. The magnetic field is homogeneous to better than 1% in the axial direction within a 4×1 in cylindrical volume (see text). The [Simulation/project-management (2009-12): E. Corsini - Collaboration: T. Karaulanov, M. Balabas - PI: D. Budker].

There are two electric heater rings (Fig. 5.5B). The electric heater ring (Fig. 5.5C) has options for attaching additional optical elements (not shown) in the longitudinal beam path. Quad twisted phosphor-bronze wire is used. One ring generates up to 2.5 W. A complementary water heating/cooling teflon tube is wound on the outer surface of the inner-shield (Fig. 5.5B).

5.1.5.6 Inner shield magnetic field modeling and coil system

COMSOL modeling was used to simulate the magnetic field inside the mu-metal four layers in both the longitudinal and transverse directions (Fig. 5.8). A cylindrical-symmetry COMSOL model was used for the longitudinal coils, and included all four mu-metal shields. For the transverse (x & y) magnetic fields directions a 3D model was used with one shield layer due to the computer RAM limitation. A magnetic field gradient is added to a DC bias magnetic field applied; the second order gradient correction is applied. The gradient with the mean DC bias field subtracted is shown in A,B,C. A: magnetic field lines and color coded magnetic field magnitude. C: the magnetic field is shown in the longitudinal direction for six equally spaced radial positions, starting at the axis and extending 1 in.from it. B: the magnetic field residual from an exact linear gradient is shown for the axis and the five radial positions; better than 1% field homogeneity was achieved in the longitudinal direction within the volume of a 2×2 in.and of a 4×1 in.cylindrical cells (which profiles are shown by the blue and orange shaded rectangles, respectively).

5.1.6 Tips on magnetic shield de-Gaussing

Enamel, 18 gauge wire (MWS 20HML) and a 20-pin connector were used to make a 20-turn loop routed through the shield's axial ports (Fig. 5.2). "Saturation" of the shield's mu-metal was measured with a secondary pick-up coil, and seemed to be more easily achieved with A.C. currents at lower frequencies than the traditional 60 Hz available with a Variac (which seems to be confirmed by Amuneal Manufacturing Corp data - Fig. 5.9-lower/right). No data was recorded but notes were taken indicating that a ~5 A current (in the main de-Gaussing coil) sinusoidally modulated at ~15 Hz, induced a clipped sinusoidal signal in the secondary coil . Similar indications of saturation were observed at 60 Hz with the Variac with a ~30-40 A current. The current was measured with a clamp-on ammeter.

To claim a conclusion with respect to saturation from the above observations, one would need to take into account the effect of skin-depth,

$$\delta \propto \sqrt{\frac{\rho}{\mu_{\mathrm{rel}} f}}, \tag{5.1}$$

where ρ is the resistivity, μ_{rel} is the relative permeability, and f is the frequency [44]). The μ_{rel} of non ferromagnetic material $\simeq$1 [44]; Amuneal recommends using a conservative" $\mu_{\mathrm{rel}}\simeq$10,000 for their proprietary mu-metal (Stuart Koch, Director, Technical Products, Amuneal Manufacturing Corp.); the skin depth of common conductors at 60 Hz $\simeq$1 cm [44]. From Eq. 5.1 we get that skin depth of Amuneal-mu-metal $\simeq 100\mu$m $\simeq 1/10$ the thickness of the magnetic shield wall (=40/1000 in.$\simeq 1000\mu$m). In conclusion, the above observation of "saturation" does not include sufficient information and no conclusion is inferred as to the relationship between observed "saturation", actual saturation of the mu-metal in the bulk (not measured), and Amuneal's data of μ_{rel} vs. frequency.

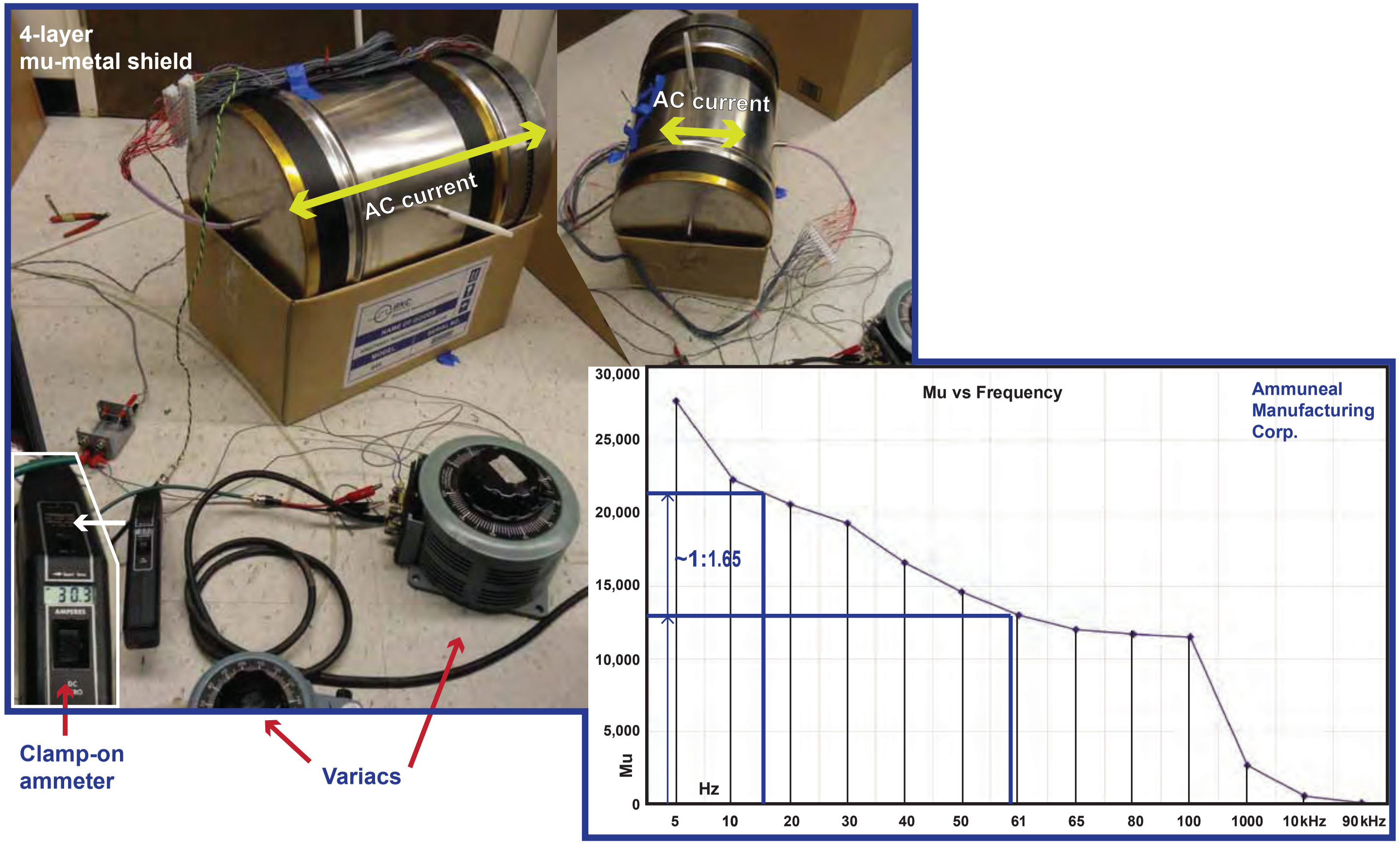

Figure 5.9: Upper & Left: deGaussing the four-layer mu-metal shield of (Fig. 5.1B,C & D) using two Variacs in series and a 20-turn 18 gauge wire coil. One Variac serves to limit and the other to manually modulate the current amplitude. The current is monitored with a clamp-on ammeter. Right: relative permeability μ_r as a function of frequency (courtesy: Stuart Koch, Director, Technical Products, Amuneal Manufacturing Corp. - email dated May 10, 2011 - undated data) shows a decrease in the shielding factor of 1.65 from 15 Hz to 60 Hz. The data implies an attenuation of $1.65^4 \simeq 7.4$ for a four-layer shield. Not shown: an externally modulated current supply was also used with current frequencies ranging 5-100Hz. Saturation (monitored with a pick up coil) of the mu metal was achieved at 15 Hz and $\sim$5 A whereas $\sim$35 A were required at 60 Hz, a ratio of 7 in the currents, which happens to be close to the 7.4 factor pertaining to the decrease in the shielding. However, the close value of these two factors has no obvious explanation at this time; skin effect has to be taken into account. [Project-management (2009-12): E. Corsini - Collaboration: T. Karaulanov - P.I.: D. Budker]

PART II
Preliminary measurements to show and exemplify: - The device's multi-configurability - Optimizations and sensitivity measurement techniques

5.2.7 Introduction - (Part II)

To exemplify the capability of the device and to investigate a few of the many optimizations pertaining to magnetic field in the geophysical range, we present the five following topics (a-e), which show preliminary measurements and partial results; we comment on the results' implications.

a) Self-oscillation as a tool to characterizing the long term drift of the DC bias magnetic field and to characterize the magnetometer noise floor; self oscillation to characterize the shield's residual magnetic field within the cell volume (Sec. 5.2.8).

b) Transfer of atomic polarization through the excited state and effects on self-oscillation (Sec. 107).

c) Magnetometer sensitivity: measurement techniques and preliminary results (Sec. 116).

d) Self-oscillation (a coherence between Zeeman sub-levels in one hyperfine ground state - ~kHz energy splitting) to measure the absorption profile of the F=i→F=i+1 microwave transition (a coherence between Zeeman sub-levels in two hyperfine ground states - ~GHz energy splitting - Sec. 112).

e) A tip on de-Gaussing a magnetic shield (Sec. 94).

5.2.8 Self-oscillation as a characterizing tool

5.2.8.1 Long term drift of the self-oscillation frequency - interpretation

We investigated the long-term stability of the magnetometer in self-oscillation configuration. One of the motivations for this investigation was for future synchronous measurements with another atomic magnetometer located in Kraków, Poland [1] (for a search of a possible coupling of exotic matter to the electron spin - a preliminary cross-correlation of the time-signal, broadcast from Fort Collins, Colorado, USA [broadcast on Am radio at 5, 10, 15, & 20 kHz (WWV), and of the counterpart broadcast from Moscow, Russia [broadcast on 4,996 kHz, 9,996 kHz, 14,996 kHz (RWM)], was made in May 2010 to test the data-taking and cross-correlation analysis software - Section-appendix 5.5). A fixed-bias magnetic field of a few mG was applied in the longitudinal direction, and the phase and duty cycle were optimized for self-oscillation with a 4×1 in. ^{85}Rb alkene-coated vapor cell. The NMOR resonance driving the self-oscillation was set in alignment configuration (linearly polarized pump and probe beams) [38] causing a self-oscillation frequency at twice

---

[1] The other magnetometer is located at the Jagiellonian University, in the group of Dr Gawlik, Head of the Photonics-Institute of Physics A.2, where the project is managed by Dr Szymon Pustelny.

the Larmor frequency at ∼3.6 kHz. The inner-shield heater control (Omega CN77353-PV) was set at 29.5°C with a 1°C dead-zone (which turned the heater on/off at 29.5∓0.5 °C); when turned on, the heater was powered with a 10.5 V supply which generated ∼60 mA current in each of the strands of the heater quad-twist wire.

The magnetometer self-oscillated for a 13-hour period during which we observed a ∼1.5 Hz stepwise shift in the self-oscillation frequency coincident with the heater turning on/off (Fig. 5.10. We attributed the shift to the heaters' residual magnetic shield. A ∼1.5 Hz shift in the self-oscillation frequency corresponds to ∼3 μG(for ^{85}Rb and alignment-based NMOR). An analog heater control would generate a temperature dependent residual field, which is not desirable; however an AC heater current set at a frequency sufficiently removed from the Larmor frequency (or harmonic), and larger than the low-pass filter in the signal amplification, would be an acceptable alternative (under construction at publication).

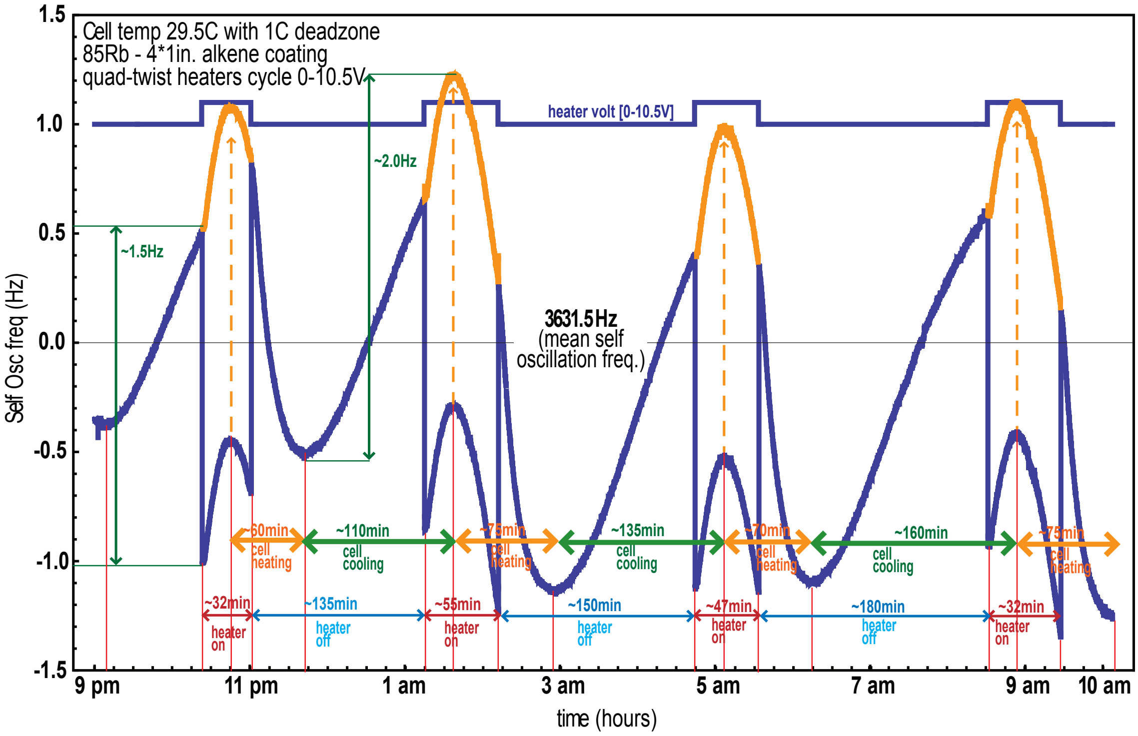

Figure 5.10: Self-oscillation (13-hour period) provides information on the shield's residual magnetic field and thermal conductivity. The two electric heaters (with phospor-bronze non-magnetic quad-twist 36-gauge wire), with ∼ 60 mA (in each wire strand), shift the ∼3.6 kHz self-oscillation frequency by ∼1.5 Hz (≡ 2 μG). In addition a ∼1°C temperature drift in the cell's temperature (= controller dead zone) causes a ∼2 Hz drift in the self-oscillation frequency. The frequency drift infers information about the magnitude of the shield's thermal conductivity and rate of heat loss. It also provides information about the temperature dependence of the residual magnetic field and/or the electronic phase shift in the self-oscillation loop (see text). [Data/project-management (2009-12): E. Corsini - Collaboration: T. Karaulanov - PI: D. Budker].

In addition to the stepwise shift we observed a pattern in the drift of the self-oscillation frequency which shows and infers the following:

5.2.8.1.1 Source of the drift in the self-oscillation frequency. The pattern consisted in a drift in the self-oscillation frequency of ∼2 Hz (≃4 μG). We attribute the drift to a ∼1°C drift of the inner shield temperature (which we assumed to be the same as the ∼1°C dead-zone of the heater control). Since the resistivity of the heater wire's has negligible temperature dependence in a range of 1°C , it suggested that the source of the temperature-dependent frequency drift was due to one or a combination of both:

a) The temperature dependence of the shield's residual magnetic field. The source may be a temperature dependence of a residual stress in the mu-metal shield, or may be a temperature dependence of the support-induced stresses on the mu-metal.

b) A sub-optimum phase shift in the self-oscillation loop causes a light power-dependence (or equivalently: optical depth-dependence) of the shift in the self-oscillation frequency (Ch. 3). In this scenario the cause would be the optical depth, which has large temperature dependence.

In conclusion, a shift in the self-oscillation frequency caused by a temperature dependence of the inner-shield's residual magnetic field limits the absolute accuracy of the magnetometer to the μG order of magnitude. The residual field may be reduced by de-Gaussing and/or re-annealing the shield, which needs to be tested. If the shift in the self-oscillation frequency is caused by a sub-optimum phase shift, a modulation/demodulation feedback to the phase control would remove the temperature dependence.

5.2.8.1.2 Information about the magnetic inner shield's insulation. The thermistor connected to the shield's temperature controller is taped on the outer surface of the inner shield. The inner shield temperature was monitored at several positions during heating and cooling and found to have an evenly distributed temperature. We assume that the airflow through the access ports of the shield is made negligible by the curtains surrounding the shield assembly. The effectiveness of the curtain is confirmed by the temperature of the shield assembly being ∼3-5°C warmer than the laboratory room. A temperature dependent drift in the self-oscillation frequency infers the following thermal properties:

a) With the electric heaters (∼60 mA current per wire strand) generating ∼1.2 W, the inner shield's temperature rises by a 1°C in time τ ≃60-70 min. (with a 1°C temperature control dead-zone; with ∼22-25°C outside air temperature; and with a shield temperature of ∼29°C). With the heaters turned off we the inner shield's temperature decreases by 1°C time ≃4τ. Ignoring the heat loss while the heater in on, the inner shield cooling rate is therefore ≃1/4 W.

b) The time taken for the cell's temperature to rise by ∼1 °C and decrease by the same amount, is in a ratio of 1:2. We conclude that the ratio of radial thermal conductivities from the inner shield to the cell, and from the inner shield to the shield's outer layer is also 1:2.

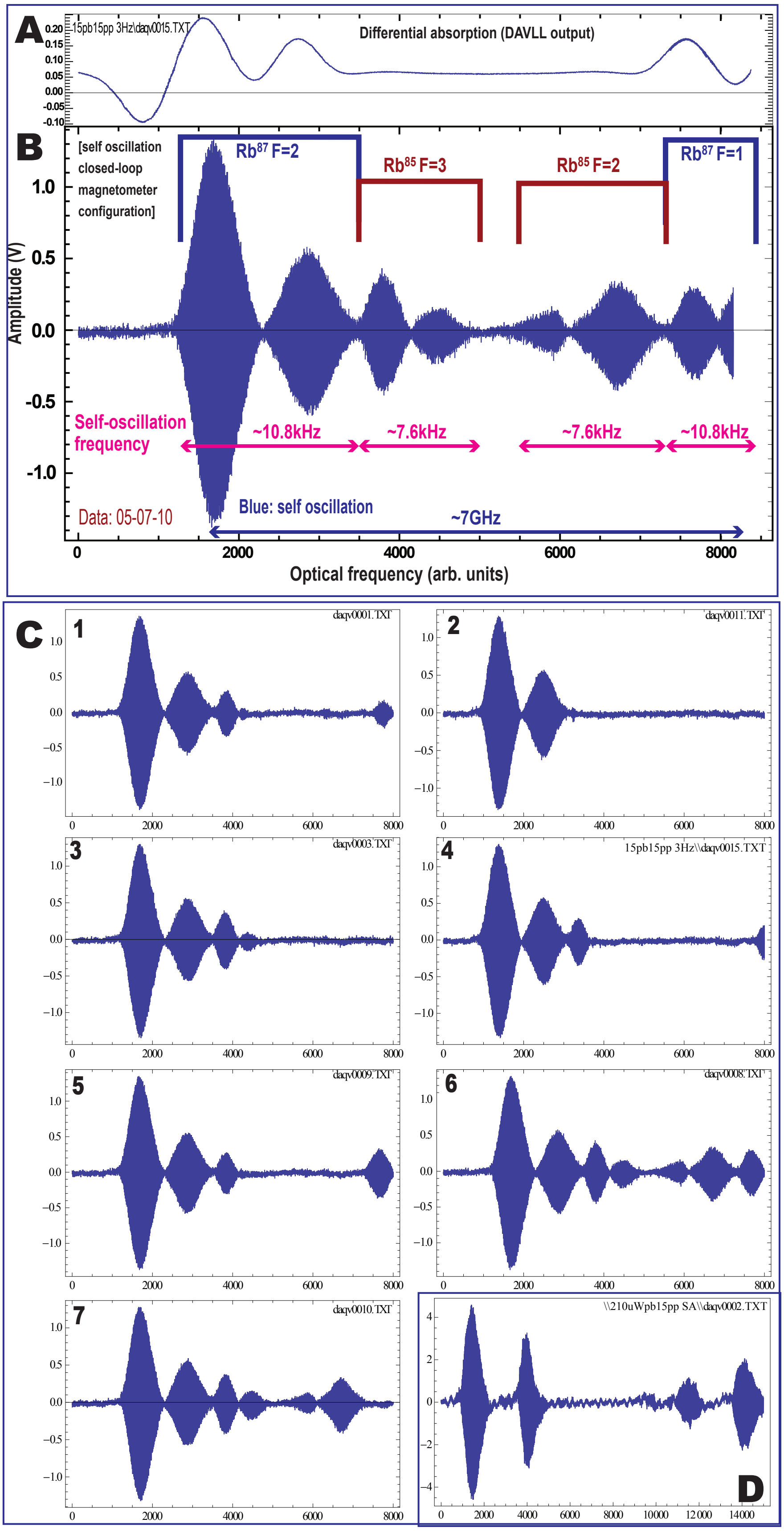

Figure 5.11: Transition of self-oscillation between alkali species at ∼10 mG bias magnetic field. The measurement technique allows the investigation of the factors pertaining to the onset of self-oscillation [caption cont. next page].

[Caption - Fig. 5.11, cont.]

A: Output of DAVLL (differential absorption) spanning ~7 GHz from ^{87}Rb F=2, through ^{85}Rb F=3 & F=2, to ^{87}Rb F=1 (four hyperfine ground-states), on the D1 optical transition. B: response of the magnetometer with a ~10m G bias field, 15 μW light power, in self-oscillation configuration, while scanning the optical frequency through the four hyperfine ground-states. We observed two self-oscillation maxima per species, per hyperfine ground state, spontaneously occurring at two light detunings within each hyperfine ground state of ^{87}Rb and ^{85}Rb , at (twice) the Larmor frequency commensurate with the alkali species and the applied bias field. C: repeating the scan of the same optical frequency range (with a 15 μW light power) did not necessarily trigger all maxima as shown in the sequence 1-7. Increasing the light power to 210 μW (C-7) consistently suppressed one of the maxima within each hyperfine ground state (only one measurement is shown at 210 μW). The cause for the self-oscillation suppression is shown in figure 5.21.

In conclusion, by sub-optimizing the phase in the self-oscillation loop, a cell-temperature dependent drift in the self-oscillation frequency can be imposed. In this fashion the self-oscillation frequency provides direct information about the inner shield's thermal insulation and about the outward and inward radial thermal conductivities from the inner shield.

5.2.9 Spontaneity and triggering of self-oscillation
Smooth self-oscillation transition between alkali species

To the best of our knowledge, the characterization of self-oscillation with an NMOR resonance within the self-oscillation loop has not been yet been realized. Higbie *et al* ([83] presented a theoretical modeling of self-oscillation based on a mechanical driven oscillator; the model is yet to be experimentally confirmed.

A series of measurements shown in figure 5.11 revealed that the spontaneity of self-oscillation varies from one measurement to the next. The alkali cell in the measurement was with natural rubidium abundance, a 4×1 in. cylinder, with an alkene anti-relaxation coating, and with the stem-lock closed (Fig. 5.6). Understanding the parameters pertaining to the onset of self-oscillation is important for self-oscillating magnetometers. One of the mechanisms pertaining to the onset of self-oscillation is described in section 5.2.12 and figure 5.11. The multi-configurability of the device enhances the investigation in as much as it makes possible the dialing of a wide range of parameters: temperature, alkali species, locked and unlocked stem-locks, tilting of the magnetic field, % of polarization ellipticity, two versus one-axis pumping...

5.2.9.1 Self-oscillation to measure noise floor of the magnetometer

5.2.9.1.1 Introduction In this section the self-oscillation configuration is used to measure the magnetometer noise floor. A ~4 mG bias field is applied in the shield's longitudinal direction. The self-oscillation frequency is recorded for 200 s. The data is divided into equal, non overlapping, and consecutive time intervals (data time-series).

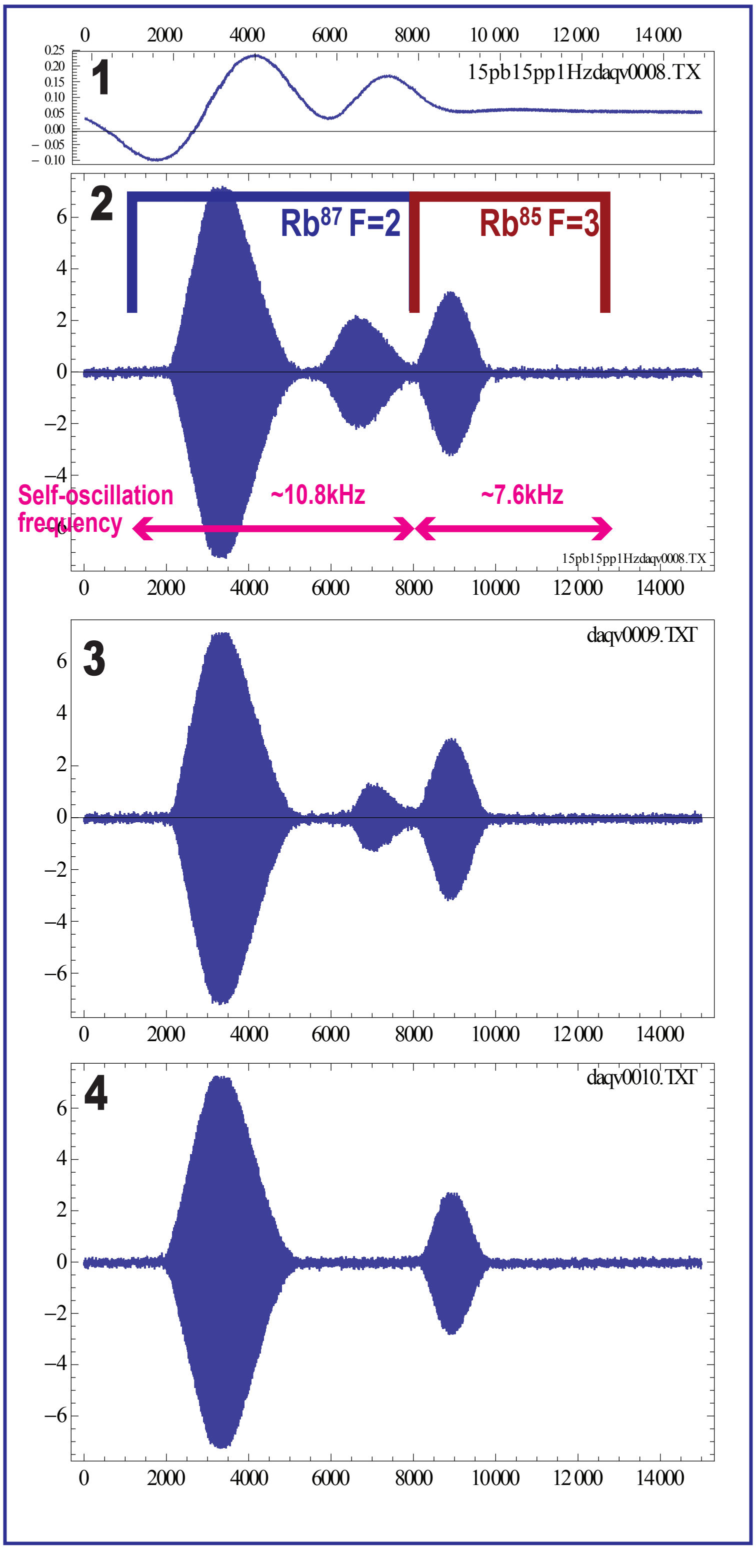

Figure 5.12: 1:DAVLL signal (differential absorption) spanning the hyperfine ground-states ^{87}Rb -F=2, and ^{85}Rb -F=3 2-4: a slower scan rate (three times slower than the one in Fig. 5.11 of the optical frequency through a range encompassing the hyperfine ground states did not improve - and in fact made worse - the onset of self-oscillation.

Each time interval is fit to a sinusoidal function. The extracted frequencies form a frequency time-series. The magnetometer noise floor is the Fourier transform of the frequency time-series. This technique investigates the magnetometer noise as a function of observation time τ and as a function of time t. It is closely related to the Allan Variance which characterizes the stability of clocks. It is in contrast to the Fourier transform of the entire observation period and in contrast to the output of a spectral analyzer.

5.2.9.1.2 Apparatus - Set Up The measurement was made with an alkali vapor cell with a natural mixture of rubidium (1×4 in. pyrex cylinder), with an alkene anti-relaxation wall coating as described in ref.[23]. The self-oscillating configuration, AM NMOR, and perpendicular linearly polarized pump and probe beams were used (Ch. 3 - Ref.[83]). The main 1500-turn bias coil and two AA batteries in parallel were used to generate the $\sim$ 4 mG bias magnetic field.

The distributed feedback laser (DFB,) tuned to the ^{87}Rb D1 line (795nm), provided a $\sim 1\mu$W probe beam and a $\sim 15\mu$W average power pump beam (measured after modulation).

A total of four self-oscillation detunings (with similar amplitude) were observed within the ^{87}Rb F=3 and F=2 hyperfine optical transition Doppler lines. With the laser unlocked, by manually adjusting the laser current and by setting the electronic phase shift in the self-oscillation loop at a suitable (but not optimum) value for all four zones, a smooth transition was made at four self-oscillating optimal detunings. The self-oscillation transition between the ^{87}Rb and ^{85}Rb hyperfine F=2 and F=3 hyperfine optical transition Doppler lines occurred with the self-oscillating frequency switching smoothly between 5.4kHz and 3.6kHz corresponding to the ratio of the respective gyro-magnetic ratios ($^{87}\mathrm{Rb}_{\mathrm{gF}}/^{85}\mathrm{Rb}_{\mathrm{gF}}$) = 3/2. The distinct optical detuning and self-oscillation frequency for each self-oscillation provided the identification of each zone (Fig. 3.1).

5.2.9.1.3 Data collection and processing techniques The laser was locked within the ^{85}Rb hyper-fine F=3 line, at an optical detuning corresponding to the largest amplitude of the two possible self-oscillations within the F=3 line. The magnetometer was in self-oscillation configuration at $\sim$3.6 kHz. A DAQ (model: IOtech P3001) sampled three analog inputs at 50,000 points per sec and recorded: the self-oscillation signal, the modulated pump light intensity, and a TTL pulse synchronized to the pulse modulating the AOM RF amplifier. The data (including a time stamp on each DAQ sampling) was recorded over 200 sec in ASCII format (a total of 10^7 points). In this preliminary analysis, only the time and self-oscillating sine wave data were extracted.

The data were segmented into two interval data sets of non-overlapping equal time intervals. One set with 5 ms time intervals (a total of 40,000 intervals with 250 data points each) and another set with 500 ms time intervals (a total of 400 intervals with 25,000 data points each). An identical analysis was performed on each interval data set.

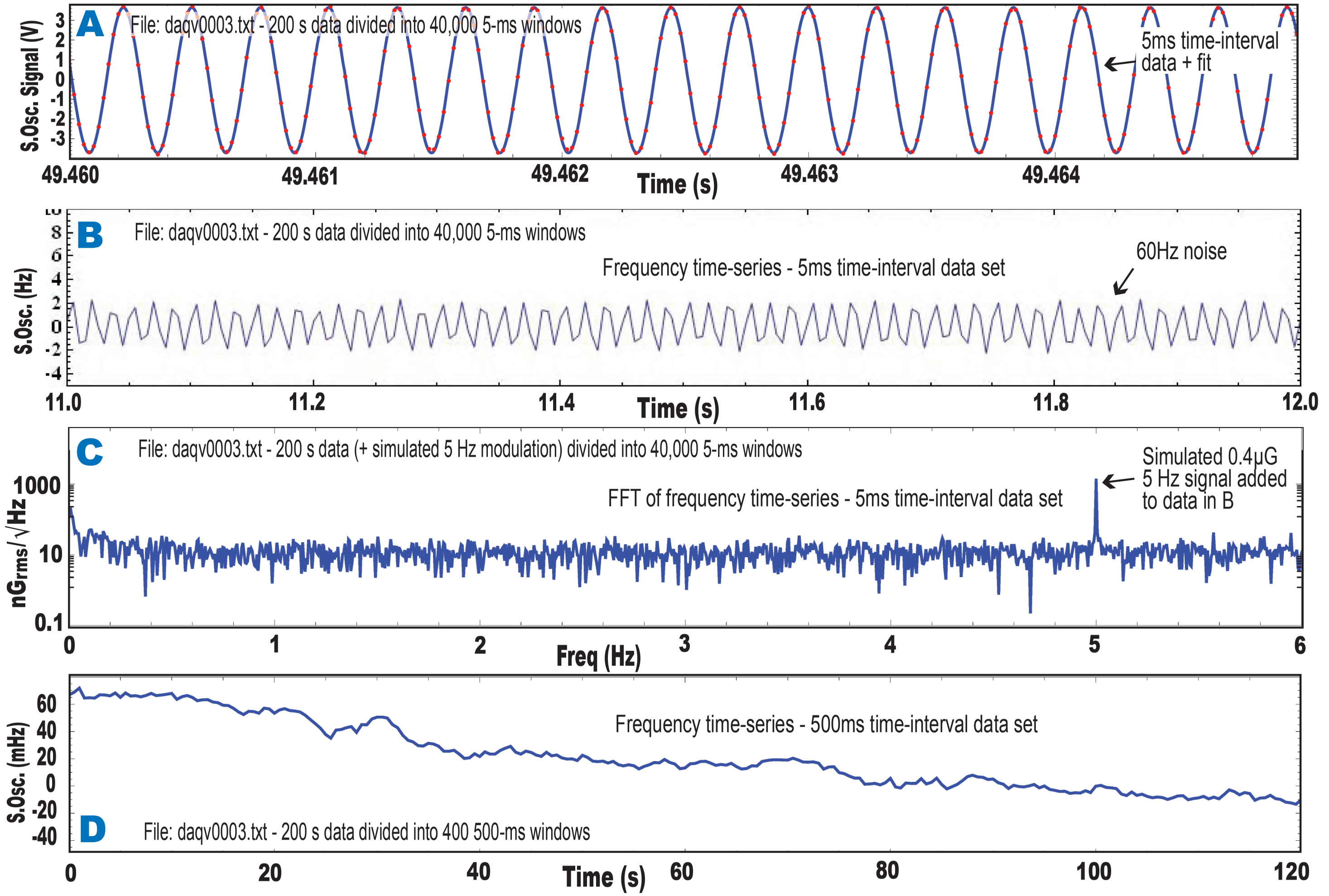

Figure 5.13: A: self-oscillation signal (∼4 kHz) with sinusoidal fitting-function (blue): an example of one 5-ms interval (interval # 9893 out of a total of 39,999) from the 200-s interval data. A 5 ms interval contains 250 data point (red). The DAQ scanning rate is 50,000 points/s.
B: frequency time series: a 1-s segment (out of a total of 200 s) of the 5-ms interval frequency time-series. The sinusoidal modulation is the "60 Hz noise" shown in the Fourier transform of this frequency time-series (Fig. 5.14). The mean, 3599.85Hz, self-oscillation frequency (of the 200 s data) has been subtracted [Caption continued next page].

[Caption - Fig. 5.13, cont.]

C: FFT of frequency time series in B; to verify the calibration of the scaling of the Fourier transform of the "5-ms" frequency times series, a 5 Hz ~0.4 μG modulation was added to the frequency time-series shown in B.

D: frequency time series: a 120-s segment (out of a total of 200 s) of the 500 ms interval frequency time-series. The 60 Hz signal has been averaged out.

[Data/analysis/project-management (2009-12): E. Corsini - Collaboration: T. Karaulanov - P.I.: D. Budker - Valuable discussions with V. Acosta, M. Ledbetter, and B. Patton1].

Each time interval was fit to a sine function using the Mathematica "FindFit" function (the "Findfit" function does not generate statistical data but processes faster than the "NonLinearFit" function - an advantage which will be explained below). Figure 5.13A shows an example of a 5 ms time interval. To check the quality of the fit-function, the standard deviation was computed and the fit was visually inspected for all intervals using standard Mathematica plot display tools. For each time interval the fit parameters (amplitude, offset, frequency and phase), and the time stamp at the beginning of the interval were recorded in a table of parameters time series. One segment for each of the frequency time series (from the 5 ms and 500 ms interval data sets), are shown in figures 5.13B & D, respectively. The (absolute) Fourier transform of the two frequency time series were computed and are shown in figures 5.14 & 5.15. To scale the amplitude, the output of the Fourier transform function was scaled by $2/\sqrt{\mathrm{N}}$, where N was the total number of frequency samplings in each series. To check the validity of the scaling a simulated 5 Hz 0.4 $\mu\mathrm{G}_{\mathrm{PP}}$ AC magnetic field signal was added to the 5 ms frequency time-series data and recovered at that amplitude from the scaled Fourier transform (Fig. 5.13C).

5.2.9.1.4 Results The Fourier transforms of the frequency times series for the 5 ms and 500 ms time interval data sets, are shown in figures 5.14 & 5.15. In figure 5.14 the dominant noise is at 60 Hz. In figure 5.15 the noise floor follows a $1/f$ behavior and the 60Hz noise has been averaged out.

Excluding the 5Hz span about the 60 Hz frequency point, the magnetometer noise floor was:

- From figure 5.14

  0.5 Hz to 100 Hz: ~ mean: 9-10 nG $\sqrt{Hz}$ (white noise)
  (Upper envelope[1]: mean: 18-19 nG/$\sqrt{Hz}$).

- From figure 5.15

At 5.7mHz:		$\simeq$1.7 μG$\sqrt{Hz}$
0.01 Hz to 0.02 Hz:	Mean	$\simeq$900 nG$\sqrt{Hz}$
0.1Hz to 0.2 Hz:	Mean	$\simeq$81 nG $\sqrt{Hz}$
0.6 to 1.0 Hz:	Mean	$\simeq$21 nG $\sqrt{Hz}$

---

[11] The upper envelope of the noise is extracted (black trace in figure 5.14) and the mean of that envelope is computed.

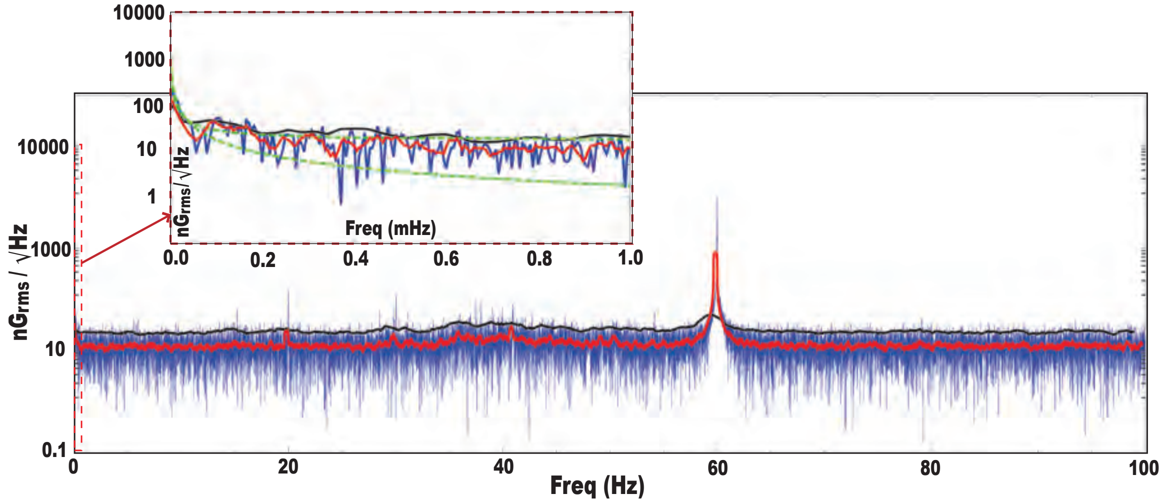

Figure 5.14: Frequency time series from the 5-ms time interval data set. Blue: Fourier transform. Red: mean. Black: top envelope.
The 60Hz peak amplitude is 0.4 μG.
From 0.5Hz to 100Hz (excluding the 5Hz segment about 60Hz):
- noise floor: 9-10 nG/$\sqrt{Hz}$ (mean - bin size: 60 points);
- noise floor top envelope: 19-19 nG/$\sqrt{Hz}$ (mean - bin size: 100 points).
Insert: Blue: expanded 0-1Hz segment. Red: mean. Dashed green fits, upper: $1/f$ + offset, lower: $1/f$. Black: top envelope. In contrast to the Fourier transform of the 500-ms frequency time series (Fig. 5.15) the $1/f$ behavior of the mean of the noise floor levels off at 0.5Hz to 9-10 nG/$\sqrt{Hz}$.
[Data/analysis/project-management (2009-12): E. Corsini - Collaboration: T. Karaulanov - PI: D. Budker - Valuable discussions with V. Acosta, M. Ledbetter, and B. Patton]

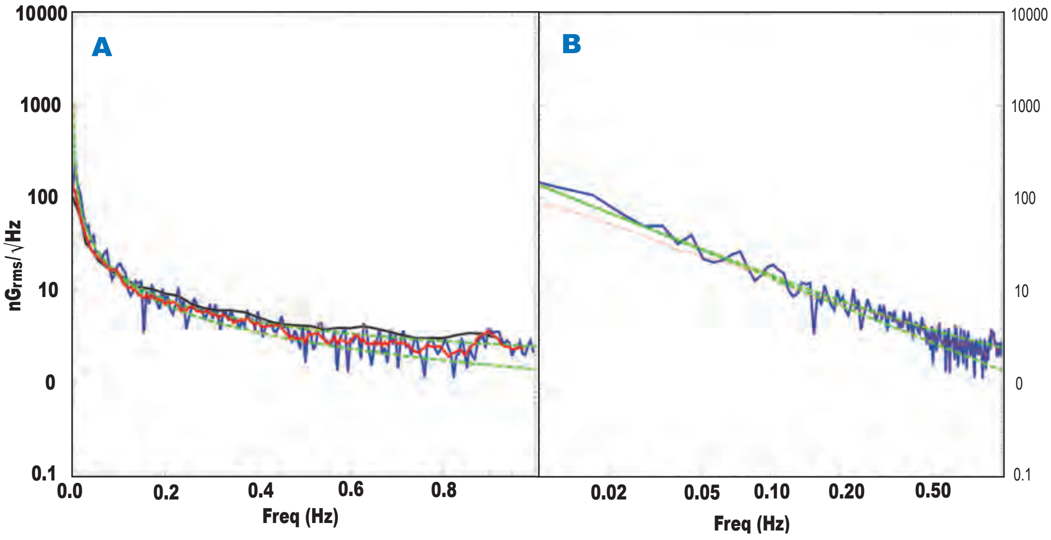

Figure 5.15: 500-ms window frequency time series. Blue: Fourier transform. Red: $1/f$ fit. In contrast to the Fourier transform of the 5 ms frequency time series (Fig. 5.15), the 500 ms frequency time series has an integration time 100-times longer (which averages the white noise) and yields a $1/f$ behavior that does not level off. A: loglinear plot; B: loglogplot.
[Data/analysis/project-management (2009-12): E. Corsini - Collaboration: T. Karaulanov - PI: D. Budker + valuable discussions with V. Acosta, M. Ledbetter, and B. Patton]

5.2.9.1.5 Conclusion - ongoing investigation and analysis Self-oscillation configuration combined with the time-series Fourier transform technique provides a "real-time" picture of the noise floor; with an optimized algorithm the "refresh rate" of the Fourier transform of a frequency time series would be ∼30 s or better. This technique has several applications including three listed below:

1) Investigation of the bandpass-filtering effect of the NMOR resonance width (a function of cell-wall coating) on the self-oscillation phase noise. Two sources are responsible for that effect: 1) The contribution to the signal by the atoms pumped out of phase will be dampened by Lorentzian response of the self-oscillation NMOR resonance; 2) only a small fraction of the atoms are pumped by each light pulse (a function of pump power), therefore decreasing the effect of out-of-phase pumping. To investigate and characterize this effect, phase noise can be added to the phase shift in the self-oscillation loop and the dampening of that noise by the NMOR resonance can be analyzed as a function of noise, pump power, optical depth (temperature), pump pulse duty cycle, and other parameters that do not presently seem to be a factor in the dampening effect. Understanding that effect may yield a better understanding of the NMOR-self-oscillation process involving atomic ground state coherences. One may note that the apparatus' inherent ability to span a large temperature range, ad to allow rapid changes of alkali species and/or alkali cells enhances the scope of the investigation.
2) The technique can work at magnetic fields up to 1-2 G. At high fields the nonlinear Zeeman components of the NMOR resonance are well resolved and would appear as three peaks in the Fourier transform of the frequency time-series . The apparatus' capability to allow tilting of the bias magnetic field direction, varying the self-oscillation phase shift, and vary other parameters, allows the investigation of regimes and settings that would favor self-oscillation on one of the three peaks, with applications to vector-magnetometry and heading error correction [86, 110].
3) The technique allows a "real time" optimization of the magnetometer noise floor. In particular it allows determining whether the source of the 60 Hz peak is from the electronics and/or from an actual modulation of the bias magnetic field.

5.2.10 Polarization transfer through the excited state - effect on a self-oscillating magnetometer

5.2.10.1 Introduction

NMOR resonances are at the heart of atomic magnetometry and are based on ground state polarization of an alkali vapor [38, 42]. One effect of interest is the transfer of atomic polarization from one hyperfine ground state to the other hyperfine ground state. The effect, called repopulation pumping and transfer of atomic polarization through the excited state, is described in the 1972 "Optical Pumping" review article by W. Happer [82]. The effect occurs in optical pumping experiments in which the atomic ground state is populated though the spontaneous decay of a polarized excited state.

In this section we show an example of orientation transfer through the excited state between the F=1 and the F=2 hyperfine ground states of ^{87}Rb. We propose possible applications, and comment on implications to atomic magnetometers operating with the self-oscillation or forced oscillation configurations [83].

5.2.10.2 Theory

Two polarized hyperfine (hf) ground states cause two NMOR resonances offset by the difference between the two hf ground states' gyro-magnetic ratio magnitudes $g_{F=1}$ and $g_{F=2}$ in ^{87}Rb as shown in equation 5.2.
From equation 1.8 (Chapter 1),

$$\begin{aligned} g_F &= g_J\left(\frac{F(F+1)-I(I+1)+3/4}{2F(F+1)}\right) \\ &+ g_I\left(\frac{F(F+1)+I(I+1)-3/4}{2F(F+1)}\right), \end{aligned} \tag{5.2}$$

where g_J is the total angular electron g-factor and g_I is the nuclear g-factor (numerical values are given in Tab. 1.1).
Evaluating equation 5.2:

$$\begin{aligned} g_{F=1} &\equiv -702.37\text{kHz/G} \\ g_{F=2} &\equiv +699.58\text{kHz/G}, \end{aligned} \tag{5.3}$$

the two "mirror" resonances are separated by 2.8Hz per mG of applied bias field which equates to ~30 Hz for a 10 mG bias magnetic field. The two NMOR resonances are detected with the magnetometer in swept configuration (Ch. 6.1, Ref. [83]).

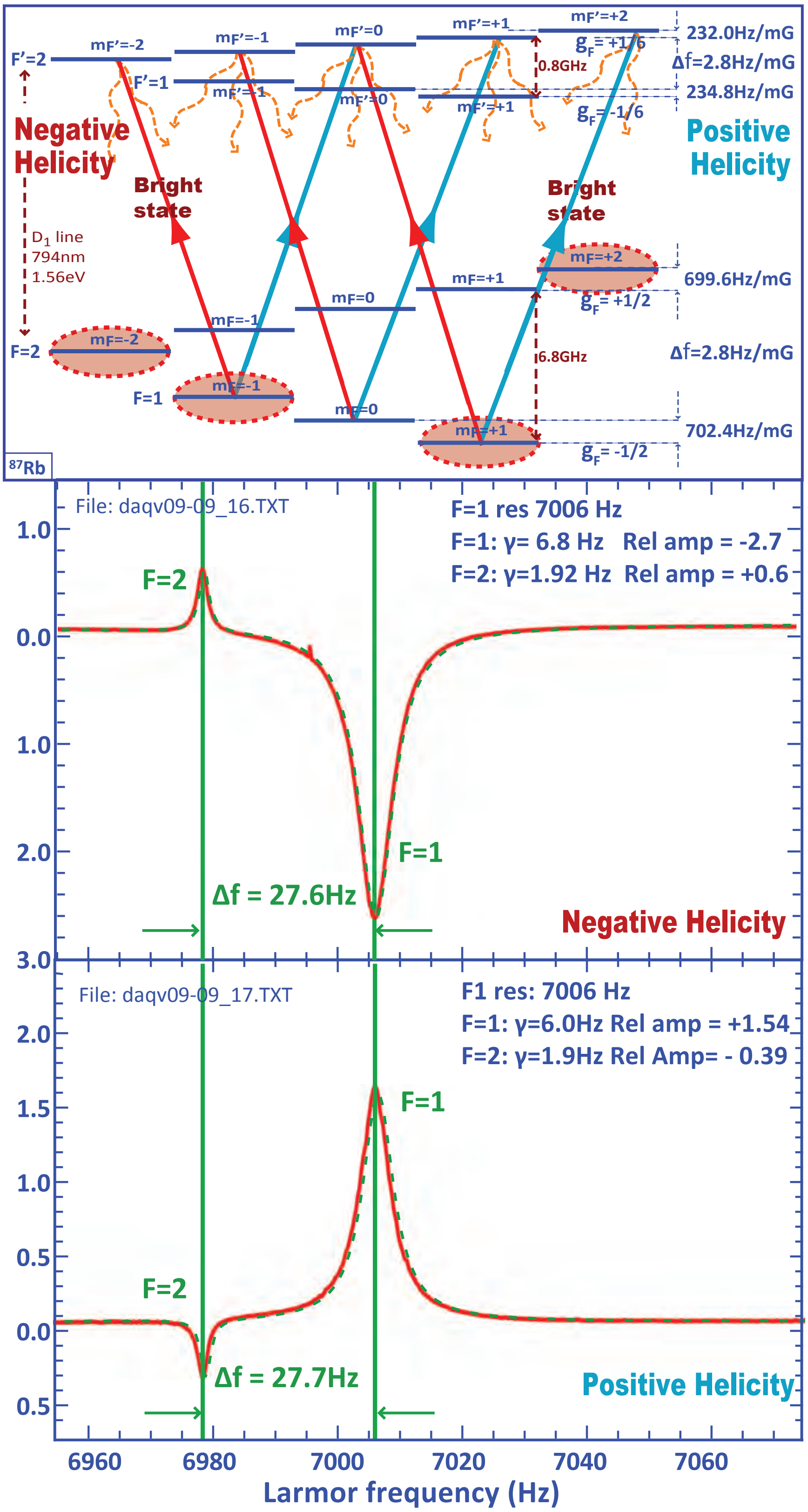

Figure 5.16: Polarization transfer from F=1 through F'=2 to F=2 for left and right circularly polarized lights in ^{87}Rb. Reversing the helicity reverses the AM NMOR resonances phase. The relative phase (opposite in this example) of the two NMOR resonances is explained in figure 5.17. [Data/analysis/project-management (2009-12): E. Corsini - Collaboration: T. Karaulanov - PI: D. Budker - Valuable discussions with V. Acosta, M. Ledbetter, and B. Patton].

5.2.10.3 Measurements and results

The measurements are made with a rubidium-87 vapor cell with an alkene-based anti-relaxation coating, and with a longitudinal Zeeman population relaxation lifetime (T1) of a few seconds as measured using a modification of Franzen's "relaxation in the dark" technique [71], described in Ref. [77][2]. Measurements with ^{85}Rb and cesium (Cs) cells are planned.

We applied a $\sim$4 mG bias magnetic field in the longitudinal direction, and used perpendicular pump and probe beams with linearly polarized probe and circularly polarized pump light. The DFB laser (resonant with the rubidium D1 line) was locked on the F=1→F'=2 optical transition.

In swept configuration the two resonances were detected $\sim$30 Hz apart and with reversed phase (Fig. 5.16). By reversing the circularity of the pump light, the phases of the primary resonance (direct pumping) and of the secondary resonance ("transfer" pumping) were reversed, as shown in figure 5.16. By shifting the optical frequency from the F=1→F'=2 to the F=1→F'=1 transition (Fig. 5.17), the phase of the primary resonance was also reversed indicating a change from a bright to a dark coherent state, but the phase of the secondary resonance was not reversed, indicating that the nature of the coherent state in the secondary resonance remains unchanged (a dark state in both cases).

At low magnetic fields the two resonances overlapped, as shown in figure 5.18. The separation of the two AM NMOR resonances was measured as a function of applied magnetic field ranging from 0 to 50 mG. The separation followed a 2.8 Hz per mG dependence from 0 to 120 Hz as shown in figure 5.19, and corresponds to the one from Eq. 5.3.

We did not observe a transfer of polarization from the F=2 to F=1 hyperfine ground states, possibly due to competing transition strengths.

---

[2] This technique yields two exponential decay constants characterizing the Zeeman population relaxation; the longer time constant is used to define T_1

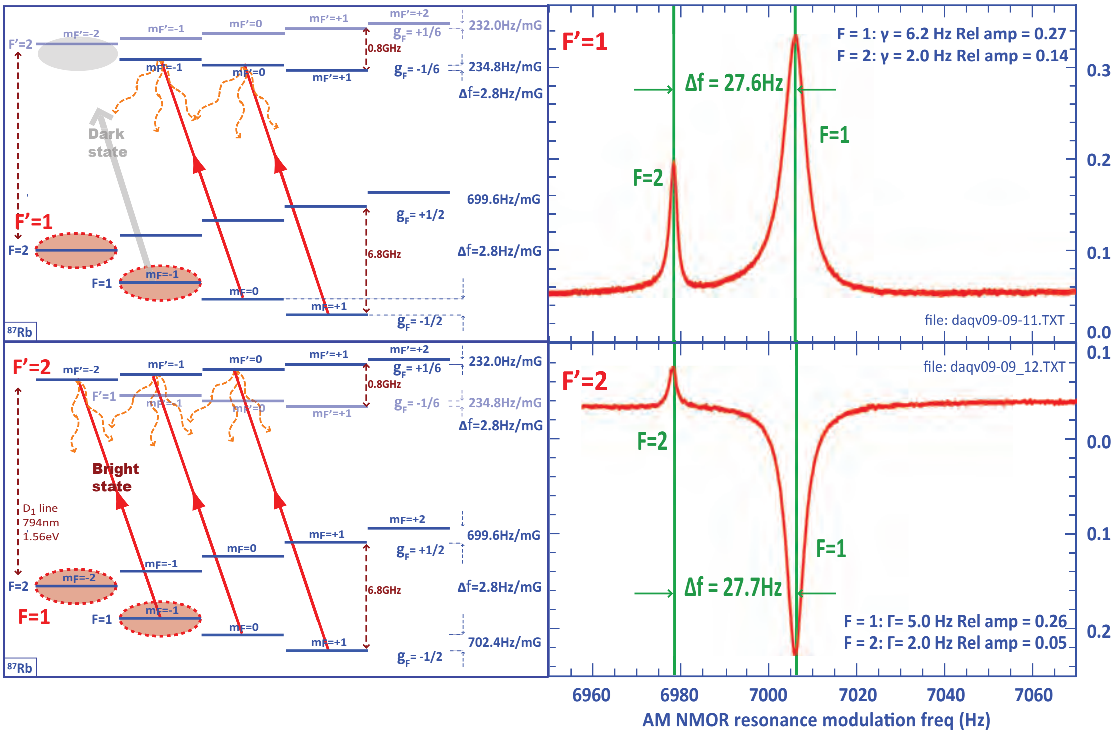

Figure 5.17: Hyperfine ground states F=2 NMOR resonance (with indirect optical pumping), and F=1 NMOR resonance (with direct optical pumping), separated by ~ 30Hz at a mean $\Omega_{\text{Larmor}} \sim 7$ kHz. The NMOR resonance is generated with circular polarized pump and linear polarized probe beams. The resonances are recorded with the laser light tuned to the F=1→F'=1 and F=1→F'=2 optical transitions. The phase reversal occurs when the NMOR resonance switches from a dark (F'=1) to a bright (F'=2) state. There is no phase reversal on the F=2 ground state (the resonance is a dark state for both optical transitions). [Data/analysis/project-management (2009-12): E. Corsini - Collaboration: T. Karaulanov - PI: D. Budker - Valuable discussions with V. Acosta, M. Ledbetter, and B. Patton].

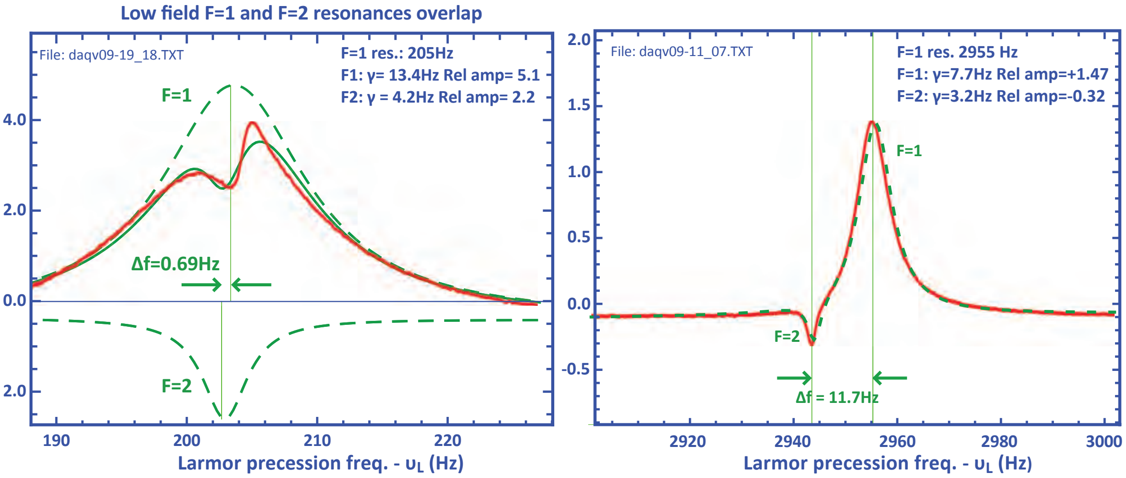

Figure 5.18: Hyperfine ground states F=2 NMOR resonance (with indirect optical pumping), and F=1 NMOR resonance (with direct optical pumping), are partially overlapped (with distortion) at a magnetic field corresponding to $\nu_{\text{Larmor}} \simeq 3$ kHz (left), and are nested at a magnetic field corresponding to $\Omega_{\text{Larmor}} \simeq 200$ Hz (right). [Data/analysis/project-management (2009-12): E. Corsini - Collaboration: T. Karaulanov - PI: D. Budker - Valuable discussions with V. Acosta, M. Ledbetter, and B. Patton].

5.2.10.4 Conclusion (5.2.10))

Earth's field atomic magnetometry measurements are performed in real time and do not benefit from multiple measurement averaging to null systematic errors. In swept configuration the observation of the two resonances enhances the sensitivity and allows calibration of the magnetometer. However, in self-oscillation configuration, the magnetometer is susceptible to nearby resonances shifting the self-oscillation frequency and phase.

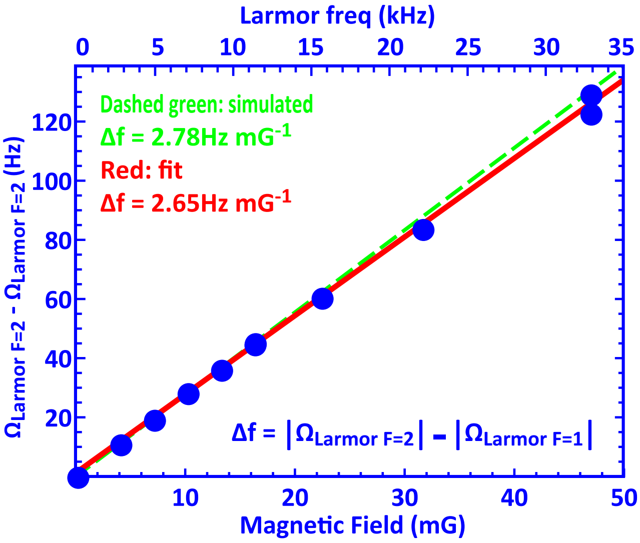

Figure 5.19: Within a range of 0-50mG, the separation between the two hyperfine levels F=1 and F=2 AM NMOR resonances scales with the difference in the Larmor frequencies of the hyperfine ground states (Eq. 5.3). Blue dots: data. Green: Simulated Larmor frequency difference (Δf=2.78Hz/mG). Red: fit, falls within 5% of the simulated value and within the measurement error. [Data/analysis/project-management (2009-12): E. Corsini - Collaboration: T. Karaulanov - PI: D. Budker - Valuable discussions with V. Acosta, M. Ledbetter, and B. Patton].

It may however be possible to extract an advantage from the double resonance even in the self-oscillation configuration. Since in self-oscillation one has to contend with two competing factors to optimize the light power setting, minimizing resonance broadening by reducing light power and maximizing the signal to noise ratio by increasing light power. The "mirror" resonance may circumvent the competition because it is not power broadened; it may provide both a narrow resonance and a good signal to noise ratio[3]. Double self-oscillation on both resonances may provide a source of common mode noise cancelation. Investigation of one or a combination of these schemes may yield an increased sensitivity in magnetometers operating in the self-oscillation configuration.

---

[3] Off-resonance, non-power broadened magnetometer schemes have also been investigated by Guzman *et al*[80] and by Pustelny *et al*[47]

5.2.11 Probing hyperfine resonances with self-oscillation

5.2.11.1 Introduction

Applications of alkali vapor cells to frequency standard has been widely investigated (Refs. [139, 46, 93] and all references therein). Vapor cells' small-size and room-temperature operations are appealing. One major disadvantage of vapor cells is the phase shift accumulated by the atoms during the cell-wall dwelling time . The phase shift results in a hyperfine frequency shift which is cell-wall coating and temperature dependent (Ch. 6 and all references therein). Consequently it is necessary to characterize the hyperfine frequency shift to use alkali vapor-cell in atomic clocks. The prevailing technique is to apply a bias magnetic field (to resolve the Zeeman sub-levels hyperfine resonances), and measure the absorption of a weak probe beam (resonant with one of the two hyperfine ground states) and sweep a microwave-frequency magnetic field through the Zeeman hyperfine resonances (in particular the $\mathrm{m_F{=}0{\rightarrow}m'_F{=}0}$ [0-0 or clock] transition). At the resonant frequencies, an absorption (1-3%) is observed (in our case, and as was observed in Ref. [64]). This (prevailing) technique and a description of the apparatus is presented in chapter 6 and Ref. [57].

5.2.11.2 Self-oscillation to measure microwave spectra - an alternative technique to absorption

We present an alternative technique, yet to be fully characterized, with a co-magnetometer in the self-oscillation configuration. The self-oscillation provides two separate information: 1) it is a direct measure of the applied magnetic field, a quantity of interest, since the magnetic field causes a second-order shift (quadratic) in the clock transition frequency (Ch. 1);

2) the amplitude of the self-oscillation (which is based on Zeeman coherences in the same F-ground state) is used to probe other resonances competing with the Zeeman coherence and resulting in a decrease (or increase) in the self-oscillation amplitude. In particular it can be used to detect hyperfine coherences between two hyperfine F-ground states.

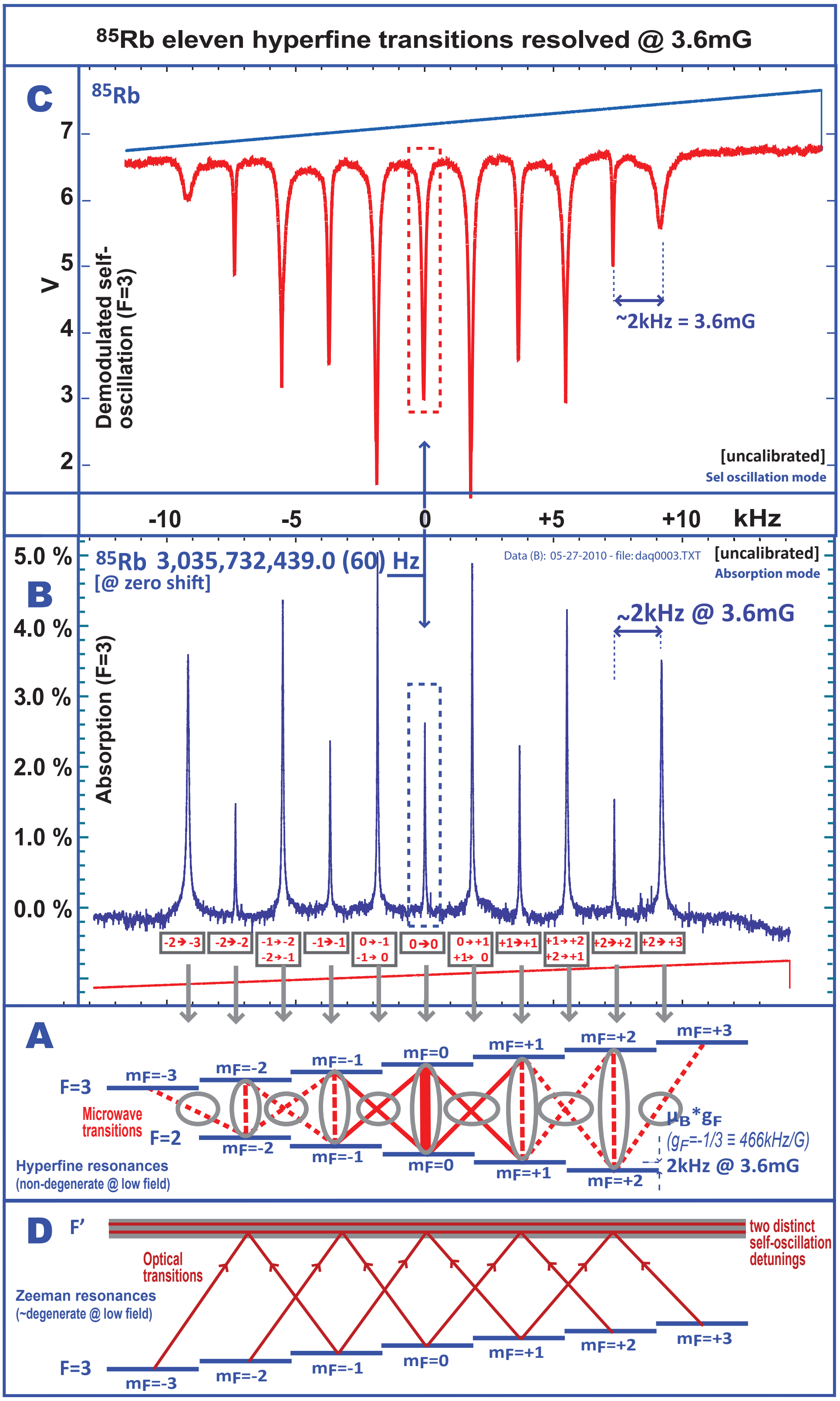

centering

Figure 5.20: A: The 11 hyperfine resonances are shown in rubidium 85. B the resonances are measured with the absorption of a weak probe beam as a function of microwave frequency (the prevailing method). C: with a magnetometer in self-oscillation configuration the hyperfine resonances are measured by demodulating the self-oscillation signal. While the magnetometer is in self-oscillation, and when sweeping through the hyperfine resonances, the Zeeman coherences D responsible for the self-oscillation are suppressed and the amplitude of the self-oscillation signal is reduced. [caption continued on next page]

Figure 5.20 caption continued:

The self-oscillation frequency provides a direct measure, and enables the control of the bias magnetic field which is responsible for the second-order shift in the frequency of the hyperfine clock resonance (there is no first-order shift). The measure and control of the bias field also enable an effective investigation of other possible first-order or second-order magnetic-field dependent effects pertaining to cell-wall coatings. [Data/analysis/project-management (2009-12): E. Corsini - Collaboration: T. Karaulanov - PI: D. Budker + valuable discussions with V. Acosta, M. Ledbetter, B. Patton, K. Tsigutkin, and D. Dounas-Fraser].

With this alternative technique, we similarly apply a bias magnetic field (to resolve the Zeeman hyperfine resonances) and sweep a microwave-frequency magnetic field. However, instead of measuring absorption of a weak probe beam, the magnetometer self-oscillation configuration is used. The self-oscillation signal is the input and the reference to a lock-in. The frequency of a microwave magnetic field is swept through the Zeeman hyperfine resonances (in particular the $m_F=0 \rightarrow m'_F=0$ [0-0 or clock] transition) while the magnetometer is in self-oscillation. At the resonant hyperfine frequencies the Zeeman coherence responsible for the NMOR driving the self-oscillation is suppressed due to the co-existing hyperfine Zeeman resonances competing for the same population of alkali atoms, and the amplitude of the self oscillation is reduced. The demodulated self-oscillation amplitude is recorded as a function of microwave frequency. A comparison of the two methods is shown in figure 5.20.

5.2.11.3 A specific application and Conclusion (Sec. 5.2.11)

The self oscillating magnetometer acts a co-magnetometer. The concept of using a co-magnetometer in sensitive measurements of nonlinear magneto-optical effects has been used in prior works [97, 95]. To our knowledge a self oscillating high bandwidth co-magnetometer has not been investigated. The high bandwidth property of AM-NMOR-driven self-oscillation allows the control of a rapid and effective sweep of the magnetic field. This makes possible an effective investigation of quadratic (second order) effects in the Zeeman sub-levels splitting, in particular AC Stark shift induced by the electric field on the surface of the cell-wall coating. The quadratic effect would cause a nonlinear spread of the hyperfine resonances, for example the ones shown in figure 5.20. A preliminary analysis of the data, which samples are shown in figures 5.20 and 6.2, and in which the bias magnetic field spread the hyperfine resonances over ∼50 kHz, did not reveal any quadratic effect (results not shown). We expect the quadratic effect to be suppressed by the ratio of the energy corresponding to the hyperfine splitting to the energy of the optical transition, and therefore small . With the use of the present self oscillating, large dynamic range and bandwidth, co-magnetometer, we propose (with the appropriate feed back mechanism) locking the microwave frequency on one hyperfine transition and using a combination of ramping and modulation of the magnetic field to amplify (with demodulation) the manifestation of the quadratic effect.

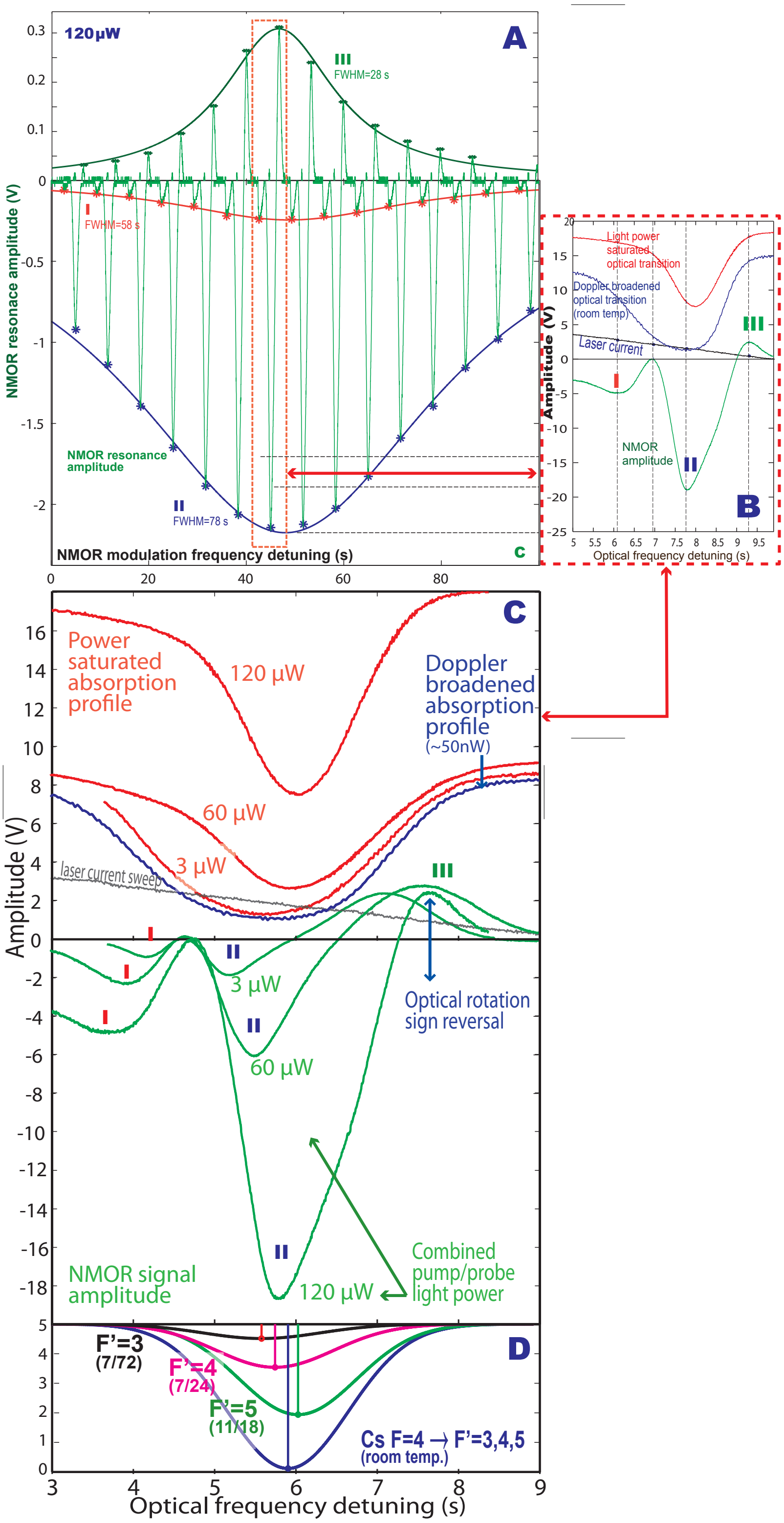

Figure 5.21: A,B: double modulation technique showing the NMOR resonance as a function of light and NMOR modulation detuning. The laser optical frequency is swept through the Doppler width in ∼10 s while the modulation frequency is swept through the NMOR resonance in ∼100 s. The technique makes manifest the NMOR signal maxima at any given light power setting. D: the Doppler broadened line of the F=3 hyperfine ground state optical transition is the sum of three transitions to the F'=3,4,5 hyperfine first excited states. C (the results are qualitative due to un-resolved timing in the scan): light detuning favors in turn one of the three hyperfine excited states causing the Zeeman coherence to change from a bright to a dark state, which correspond to a change in sign in the NMOR optical rotation (reversal in phase). The NMOR-signal is shown as a function of optical detuning for three light power settings (qualitative results). The amplitudes and locations of the maxima shift as a function of light power. [Apparatus: Fig. 5.1A ("before version") - Data/analysis/project-management (2007-08): E. Corsini - Collaboration: J. Higbie, C. Hovde (Southwest Sciences) - PI: D. Budker - Technique developed by J. Higbie, E. Corsini, and C. Hovde]

5.2.12 Magnetometer sensitivity - measurement techniques and preliminary results

5.2.12.1 Introduction

The sensitivity of an atomic magnetometer is measured as a function of several parameters, for example, optical detuning, NMOR modulation detuning, and of light power. In this section we present two techniques to measure sensitivity with a double modulation scheme. The techniques are insensitive to drifts in the bias magnetic field and to the NMOR maxima dependence on optical detuning.

5.2.12.2 Measurement technique: AM-NMOR and optical detuning double modulation

In the first technique, for a given light power, the optical frequency is modulated with a depth spanning the width of the Doppler broadened optical transition in ∼10 s, while the pump modulation frequency is swept through the AM NMOR resonance in ∼100 s (swept magnetometer configuration). The technique reveals optical rotation maxima as a function of optical frequency and NMOR modulation detunings, for any light power setting (Fig. 5.21A,B).

Within one optical sweep at different light power settings (Fig. 5.21C) we observe that the maxima of the NMOR signal amplitude (itself proportional to the optical rotation) are light detuning and light power dependent (green traces in Fig. 5.21C). We observe that with increasing light power one maxima may increase while the other (with an opposite phase) decreases; which provides information about the factors pertaining to the onset of self oscillation described in Sec. 5.2.9.

The light detuning dependence of the NMOR optical rotation is caused by the hyperfine structure of the excited state (Fig. 5.21D). As the optical frequency is swept through the Doppler broadened line, the optical transition favors in turn one of the three hyperfine excited states, which in turn favors a Zeeman coherent “bright” or “dark” state and causes the optical rotation phase reversal (which corresponds to a reversal in the sign of the optical rotation). The NMOR maxima dependence on power is caused by power broadening.

5.2.12.3 Measurement technique: Bias magnetic-field and optical-detuning double modulation

The other sensitivity measurement with double modulation technique is achieved by modulating the magnetic field with a square waveform, with a period of ∼20 s, about a central bias field value, while sweeping the optical frequency through the Doppler broadened optical transition Fig. 5.22. The response of the magnetometer to a fixed modulation of the field is a measure of its sensitivity. As with the first technique, the determination of the NMOR signal maxima is independent of fluctuations in the bias magnetic and in the laser detuning.

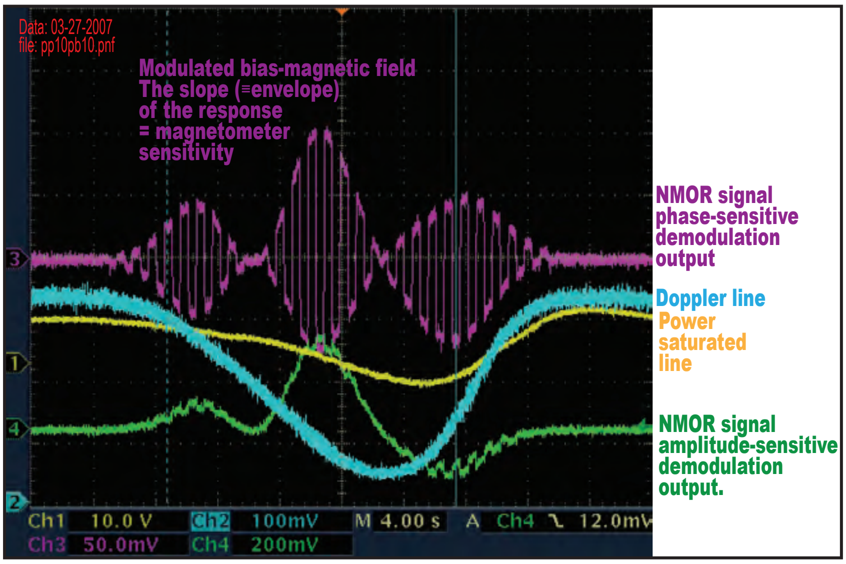

Figure 5.22: The bias magnetic field is modulated with a square waveform with a period ∼1 s. The optical frequency is swept through the Doppler width in ∼40 s. For small changes in the phase, the relative phase between the lock-in outputs is set so as to have one output sensitive to phase (purple) and the other sensitive to amplitude (green). The phase sensitive output (purple) of the demodulated NMOR signal serves to measure the magnetometer's sensitivity. The blue and yellow traces are the unsaturated and saturated Doppler profiles, respectively. [Apparatus: Fig. 5.1A ("before version") - Data/analysis/project-management (2006-07): J. Higbie, Collaboration: E. Corsini, C. Hovde - P.I.: D. Budker]

5.2.12.4 Results

Once the optimum light detuning and light power has been determined, the width of the resonance is measured at fixed optical detuning, light power, and magnetic field (Fig. 5.24A). In figures 5.24B-D (blue data), in an alkene coated ^{87}Rb cell (2×1 in.cylinder) and with the apparatus shown in figure 5.1B ("after version"), the shot-noise limited optical rotation, sensitivity, and the NMOR width is measured as a function of a parameter of interest (in this example light power), while keeping the other parameters fixed (in this example light detuning magnetic field). We observe a peak in optical rotation 80 μW and a maximum sensitivity near 50 μW (the sensitivity is proportional to the optical rotation and inversely proportional to the width of the resonance. The measurement was also performed with a repump light (red data). Due to the limited repump power the validity of the data on the effect of the repump extends up to 100 μW. We speculate that the sensitivity may remain constant over a range of light power. Using larger light power results in a larger signal amplitude and generally in a larger signal to noise ratio.

Results (using the earlier apparatus shown in Fig. 5.1A) in a cesium paraffin coated

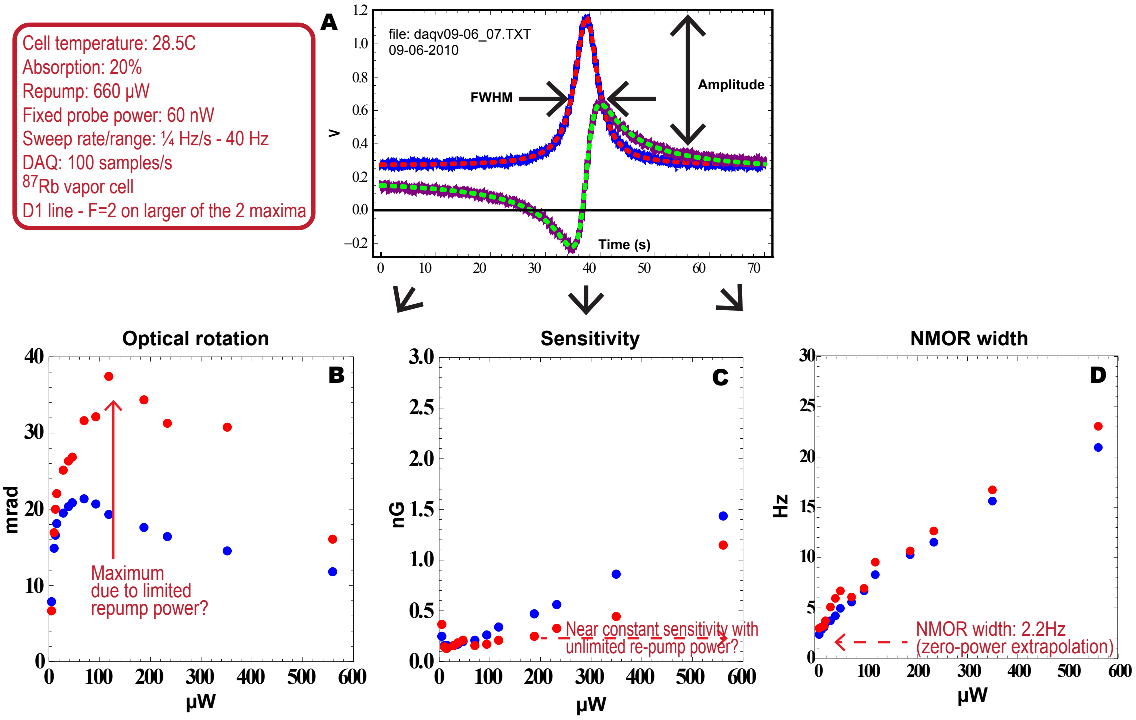

Cell temperature: 28.5C
Absorption: 20%
Repump: 660 μW
Fixed probe power: 60 nW
Sweep rate/range: ¼ Hz/s - 40 Hz
DAQ: 100 samples/s
^{87}Rb vapor cell
D1 line - F=2 on larger of the 2 maxima

file: daqv09-06_07.TXT
09-06-2010

Maximum due to limited repump power?

Near constant sensitivity with unlimited re-pump power?

NMOR width: 2.2Hz (zero-power extrapolation)

Figure 5.23: Once the global maxima have been found, the sensitivity at the maxima points is more accurately measured with the optical frequency and the magnetic field locked at a fixed setting. The modulation frequency is swept through the NMOR resonance (A) at different light power settings. From the data the optical rotation (B), the sensitivity (C), and the NMOR resonance width are extracted. [Apparatus: Fig. 5.1B ("after version") - Data/analysis/project-management (2009-12): E. Corsini - Collaboration: T. Karaulanov - P.I. Dr. Budker - Valuable discussions with V. Acosta, M. Ledbetter, B. Patton, K. Tsigutkin, and D. Dounas-Fraser].

vapor cell, similarly show a peak sensitivity near ~10-20μW (Fig. 5.24). No repump light was used in these earlier measurements.

5.2.12.5 Conclusion (Section 5.2.12)

The preliminary measurements presented in this section indicates a peak sensitivity of a fraction of a nG/$\sqrt{Hz}$, two orders of magnitude away from the record sensitivity achieved by the Romalis group in 2010 [59]. Several parameters (listed below) have yet to be (or further) investigated.

1) Using repump light seemed to indicate that the present peak sensitivity may be maintained with sufficient repump light power. The advantage of a large pump light power is the increased signal to noise ratio which is necessary to drive the self-oscillation.
2) At this time, optimization of the magnetic field gradients has not been concluded.

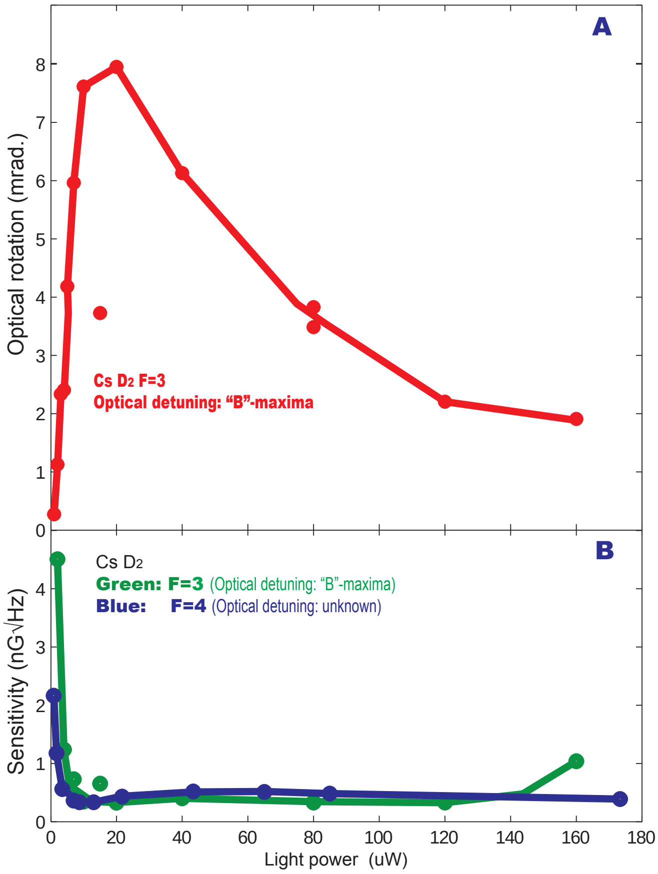

Figure 5.24: The shot-noise projected sensitivity B and the NMOR optical rotation A data, as a function of light power, are extracted from the data represented in figures 5.21 & 5.22. [Apparatus: Fig. 5.1A ("before version") - Data (red and green)/analysis/project-management (2007-08): E. Corsini, collaboration: J. Higbie - PI: D. Budker - The sensitivity data in blue is from earlier work (2006-07) by J. Higbie in collaboration with E. Corsini, C. Hovde - P.I. D. Budker].

3) One parameter not yet investigated is the cell's optical depth. We speculate[4] that higher sensitivity may be achieved at a low optical depth. The present apparatus cell-cooling capability makes that investigation possible.

---

[4] Speculation based on S. Rochester's simulation.

5.3 Conclusion (Chapter 5)

We have shown the design and construction of a multi-and rapid re-configurable optical platform to test, optimize, and trouble-shoot, configurations of atomic magnetometers. We have investigated several directions in the optimization-parameter space. In particular we have shown that self-oscillation can be used as a tool to optimize the phase in the self-oscillation loop, to monitor heat transfer within the shied, and to act as a co-magnetometer in hyperfine frequency measurements. We have observed a transfer of polarization in the orientation configuration; the transfer causes a nearby resonance which can potentially shift the self-oscillation frequency. We have measured the magnetometer sensitivity using a double modulation technique which directly shows the global maxima with respect to three variables: the NMOR frequency detuning, the light detuning, and the light power.

The magnetometer platform described in this chapter provides the capability to have several concurrent configurations and to rapidly re-configure the platform. This capability was essential to make the systematic, and effective scanning of the optimization parameter space and magnetometer configurations we have investigated. We conclude that the multi-configurable and rapidly re-configurable platform, whose construction was described in Part I of this Chapter, is necessary for effectively determining an optimum magnetometer configuration and operating parameters.

5.4 Acknowledgements (Chapter 5)

Acknowledgement is given to Todor Karaulanov for his knowledgeable guidance and mentorship, to James Higbie who assembled the “before” version shown in Fig. 5.1-A, to Valeriy Yashchuk who designed the magnetic shield three inner-layers (after which the fourth one was designed), and to Larry Maltin, President Technical Products, Stuart Koch, Director Technical Support, and to Dave Lafferty, at Amuneal Manufacturing Corp., for their guidance in the design of the fourth layer of the magnetic shield. This work was supported by NSF (grant PHY-0855552) and by LBNL-NSD.

Figure 5.25: Kraków-Berkeley synchronous magnetic field measurements.
7: time signal broadcast by Moscow, Russia (RWM) and (1,2) by Fort Collins in Boulder, CO, USA (WWV - operated by NIST) were simultaneously recorded in Kraków and Berkeley, respectively. [caption continued next page].

[Caption - Fig. 5.25, cont.]: A shortwave radio receiver (Degen DE H1103 - underline3,7), a GPS receiver (Novotech, Ontario, Canada; antenna: 57860-10 [5,6]; resolution T embedded timing board: 52664-05 [3]), custom made electronics, and a custom made LabVIEW software package, were used to simultaneously record the time AM broadcast time signal and the GPS time signal at each site. The recording hardware (3) and software, and the file transfer between the two sites, were tested in April 2010, during several consecutive hours. The signal-correlation was performed by the team in Kraków. 4,5: a makeshift antenna was strung between pine trees in Berkeley for lacking access permission to the physics' building rooftop. After a few throws, the pine cone led the wire as desired [the throw was performed by Pzemek Wlodarczyk during his several-month long visit in Berkeley]; the antenna remained in place for ∼2 years until natural causes brought it down. Another ∼30 m long antenna was strung (by E. Corsini) along the length of the first floor west-facing balcony of the Birge building, between two lengths of vertical PVC tubing attached to the balcony. The reception of that antenna was qualitatively the same; the location necessitated the use of a ∼40 m long coax cable from the west to the east sides of the building; for that reason the "pine-tree" antenna was preferred. 10: Kraków-Berkeley lunch at the UC Berkeley Faculty Club to brainstorm ideas including the one on exotic matter coupling to the atomic spin. A search for exotic coupling with the electron spin will involve simultaneously recording the NMOR signal with a bias magnetic field applied in the innermost shield, and the GPS time stamp-signal.

5.5 Appendix - Chapter 5

5.5.1 Appendix - A
Search for exotic-matter coupling to the atomic spin Preliminary/calibration measurement

A collaborative effort is underway between the Berkeley and Karków groups of Dr Budker and Dr Gawlik (Fig. 5.25) to search for a yet-unknown source (dark matter for example) of coupling to electron spin and/or the nucleus spin (atomic spin). The current members and participation in the collaboration are as follows:

Kraków site

Project management: Dr Gawlik, Szymon Pustelny - Collaboration: Pzemek Wlodarczyk, Piotr Jan Wcisło - Conception/design/construction of electronics, GPS hardware, and composition of operation manual (7:) Pzemek Wlodarczyk - Data recording: S. Pustelny, Przemyslaw Wlodarczyk, Piotr Jan Wcisło. LabVIEW routine: Piotr Jan Wcisło

Berkeley site

Project management: Dr Budker - Collaboration: E Corsini, M Ledbetter, Mohammed Sheikh - Data recording: E Corsini - Center photograph (10): E Corsini - Other photographs: Google image-search.

5.5.2 Appendix - B
Lab footprint and space-organization for the apparatus of Fig. 5.1

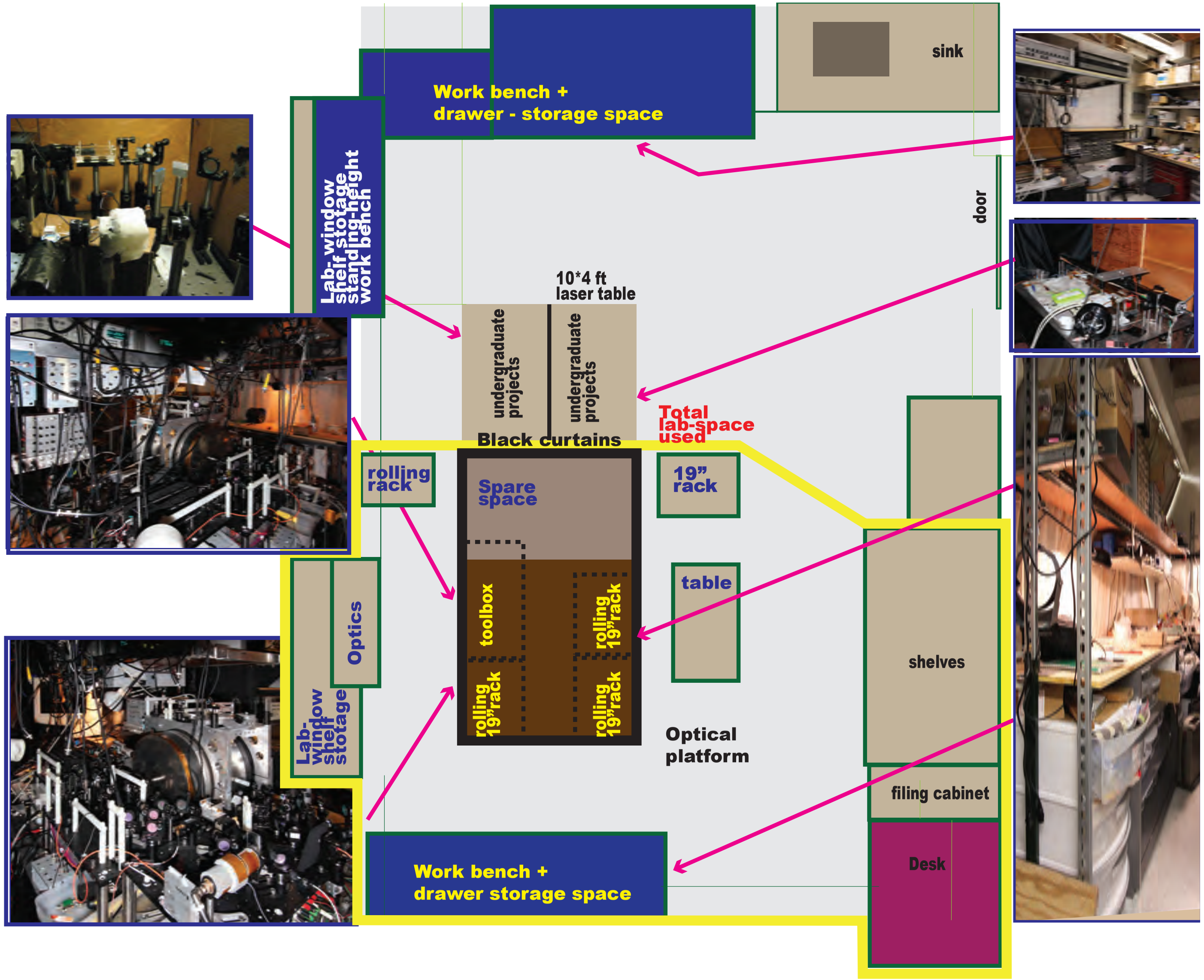

Figure 5.26: A compact and multi-configurable design occupying 2/3 of a 10×4 ft laser table and 1/2 15×21 feet laboratory room. Two undergraduate projects occupy the remaining 1/3 of the laser table. The upper-left project was managed by undergraduate student Geoffrey Iwata [Supervision: E. Corsini] and is shown in Fig. (4.18) [Conception/design/project management: E Corsini - Collaboration: T Karaulanov - Work-space construction: M. Solarz - PI: D. Budker].

Chapter 6

Dependence of Hyperfine Frequency Shift on Zeeman Relaxation in Alkali Vapor Cells with Anti-relaxation Alkene Coating. Comparison with Anti-relaxation Alkane (Paraffin) Coating

Related publication
Journal:Phys. Rev. A Jan 2012 - Submitted
Note: Reviewer objected to speculations of Sec. 6.8 - Re-submission: planned May 2012.
Title: Hyperfine frequency shift and Zeeman relaxation in alkali vapor cells with anti-relaxation alkene coating.

Authors: E. Corsini[1], M. Balabas[2], T. Karaulanov[1], and D. Budker[3]
Affiliations:
[1]Department of Physics, University of California, Berkeley, CA 94720-7300
[2]S. I. Vavilov State Optical Institute, St. Petersburg, 199034 Russia
[3]Nuclear Science Division, Lawrence Berkeley National Laboratory, Berkeley CA 94720

pacs: 06.20.fb,06.30.Ft,32.10.Fn, 3230.Bv
keywords: anti-relaxation, Zeeman relaxation, alkali vapor cell, alkene, alkane, adsorption, absorption, wall dwelling time.

Abstract

An alkene based anti-relaxation coating for alkali vapor cells exhibiting Zeeman relaxation times in excess of 60 s was recently identified by Balabas *et al.* The long relaxation times, two orders of magnitude longer than in paraffin (alkane) coated cells, motivate revisiting the question of what the mechanism is underlying wall-collision induced relaxation, and renew interest in applications of alkali vapor cells to secondary frequency standards. We measure the width and frequency shift of the ground state hyperfine $m_\mathrm{F}{=}0{\rightarrow}m'_\mathrm{F} = 0$ transition (clock resonance) in vapor cells with ^{85}Rb and ^{87}Rb atoms, with an alkene based anti-relaxation coating. We find that the frequency shift is slightly larger than for paraffin coated cells. The Zeeman relaxation rate appears to be a linear function of the hyperfine frequency shift. We propose a model describing the different Zeeman relaxation mechanisms of alkene and alkane cell-wall coatings.

6.1 Introduction

Important experiments in fundamental physics, and applications in metrology, such as magnetometry and time (frequency) standards, rely on long-lived ground-state polarization of alkali vapors [38, 42]. The major technical difficulty is to preserve atomic polarization while containing the vapor. Buffer gas or anti-relaxation coated glass cells, and laser cooling and trapping are the current leading techniques. Glass cells filled with an alkali vapor at near-room temperature are easier to implement than laser trapping. For applications to magnetometry and secondary time standards, anti-relaxation coated cells have the additional benefit of lower laser power requirements; they also benefit from motional averaging which reduces the magnetic-field-gradient resonance broadening [111].

Coating the cell walls with paraffin was proposed by Ramsey in 1950 [114], first realized by Robinson and Dehmelt in 1958 [117], and extensively characterized by Bouchiat and Brossel [34, 33]. The coating consists of a thin film of long chains of nominally saturated C-C bond alkane molecules ($\mathrm{C_nH_{2n+2}}$) [127]. Octadecyltrichlorosilane (OTS), which allows approximately 2000 polarization maintaining wall bounces at temperature up to 170°C, and paraffin, with up to 10,000 bounces (but limited to below 60-80°C), have been the leading anti-relaxation coatings in the last several decades [128, 127]. There is limited understanding about the interaction of paraffin with alkali atoms and why only certain procedures by which the coating is applied work, which up to now has made the production of high quality cells more an art than a science.

Alkene ($\mathrm{C_nH_{2n+1}}$) coatings [22] with one unsaturated C=C bond were recently demonstrated [23]. They allow 10^5 to 10^6 bounces with atoms in the ground state and enable Zeeman coherence lifetimes (in a $\sim$1-in spherical cell) to reach from several seconds to over one minute (up to two orders of magnitude improvement over paraffin) . This discovery renewed the interest in understanding the underlying mechanism in wall-collision induced decoherence, and prompted the question: "Is a long relaxation time due to a short cell-wall adsorption (dwelling) time?" A short wall dwelling time would imply a small hyperfine frequency shift (Sec. 6.3). It would re-ignite interest in vapor coated cells for use in applications to secondary frequency standards, an application that has been limited by the large, temperature dependent, hyperfine $m_{\rm F}{=}0{\rightarrow}m'_{\rm F} = 0$ transition (clock resonance) frequency shift [112].

To answer the above question we measure the width and frequency shift of the clock resonance in alkali vapor cells with alkene-based anti-relaxation coatings. We compare our results to those with alkane coated vapor cells [64], and propose an explanation for the result and the source of wall-collision induced relaxation.

6.2 Anti-relaxation coated cells in the context of wall collisions and surface interactions

6.2.1 Background

Atom-wall collision processes, a subset of surface-interaction science, are ubiquitous in nature, and yet are far from being well understood. Upon collision with a surface, an atom (or molecule) undergoes physical adsorption (physisorption) by the wall potential [in contrast to chemical adsorption (chemisorption)], adheres to and desorbs from the surface after an average adsorption time $\bar{t}_{\rm w}$, with an Arrhenius temperature dependence [60, 120]

$$\bar{t}_{\rm w} = \tau_{\rm o} e^{E_{\rm w}/kT}, \tag{6.1}$$

where $\tau_{\rm o}$ is the period of vibration of the wall potential, $E_{\rm w}$ is the adsorption energy, k is the Boltzmann constant, and T is the temperature.

While on the surface, the adsorbed atom undergoes surface migration [32]. In the limit of a perfectly smooth surface adsorption energy, the adsorbed atoms form a two-dimensional gas governed by the atoms' thermal kinetic energy transverse to the surface. The two-dimensional mean free path is generally smaller, and the density larger, than for the three-dimensional gas [32]. When there are spatial fluctuations in the adsorption energy $E_{\rm w}$, the mean free path becomes even shorter due to the participation of surface atoms (this mechanism is also the one by which energy is exchanged between the adsorbed atoms and the surface [32]). In the limit when the average fluctuation $\varDelta E_{\rm w}$ is of the order of the atoms' kinetic energy, an atom hops from one adsorption site to another with a characteristic time

$$\bar{t}_{\rm hop} = \tau_{\rm o} e^{\Delta E_{\rm w}/kT}. \tag{6.2}$$

The property of a good anti-relaxation coating is thought to come from the absence of free electron spins which could result in alkali spin destruction, and from a low dielectric constant (low polarizability) and consequently a low adsorption energy E_{w}, which reduces the time of adsorption $\bar{t}_{\mathrm{w}}$ (Eq. 6.1). For example paraffin and Pyrex have a wall adsorption energy of the order of 0.1 eV [34] and 0.5 eV [60], respectively.

Additionally a small average spatial fluctuation ΔE_{w} in the coating's adsorption energy may play a central role in determining the anti-relaxation quality of the coating (Sec. 7.5C).

6.2.2 Previous work and techniques in measuring the adsorption energy and adsorption time

Ingenious methods have been realized to measure the time of adsorption $\bar{t}_{\mathrm{w}}$, which is one of the most consequential variables of surface interaction.

In one of the earliest attempts in the 1930s, Clausing [51, 50] directly measured the average propagation time $\bar{t}$ of argon atoms through a glass capillary. Molecular flow (Knudsen flow) transit time through a capillary can be calculated and decoupled from surface interaction (for example, the average propagation time of an atom through a 1 μm diameter, 1 m long capillary, with a 100 μs average adsorption time, is 50 s, compared to 5 ms without adsorption). Clausing derived the time of adsorption $\bar{t}_{\mathrm{w}} = (2d^2/l^2)\bar{t} - d/\bar{v}$, where d and l are the capillary diameter and length, $\bar{v}$ is the average atomic thermal velocity, and found $\bar{t}_{\mathrm{w}} = 31$ μs for a glass surface at 90 K.

In 1964 Bouchiat and Brossel [34, 33] measured the adsorption energy and time of adsorption by measuring the Zeeman relaxation time as a function of magnetic field. When scanning the magnetic field, Bouchiat and Brossel observed steps (Magnetic decoupling) in the Zeeman relaxation time. A step occurs when the frequency corresponding to the adsorbed atoms' Zeeman splitting falls out of resonance with the inverse correlation time of a perturbing wall-magnetic field. Each Zeeman relaxation process reveals itself as a step; one in particular involves the average time $\bar{t}_{\mathrm{w}}$ an atom spends on one adsorption site.

In 1994 Stephens *et al* [32] quantified the adsorption energy by measuring the vapor density in a cell with a fixed number of atoms as a function of temperature. They also detected the time of adsorption by measuring the vapor density as the cell filled with alkali atoms as a function of time. The measurements were realized in the context of atom trapping and interaction between cesium atoms and Pyrex, stainless steel, sapphire and OTS.

In 2004 Brewer *et al* [37] measured the energy and time of adsorption by light induced atomic desorption (LIAD), a technique pioneered by Moi and Gozzini *et al* [105, 76]. This process involves atom desorption through non resonant photon-stimulation. The measurements were made in the context of sodium and rubidium atoms and polydimethylsiloxane (PDMS) coating, and showed that desorption is a multi-step process in which the initial excitation is decoupled from the final desorption. In 2009 Karaulanov *et al* extended the investigation of LIAD into the UV range and found a sharp dependence on wavelength [90]. That investigation was made in the context of alkali vapors and paraffin coatings. The results derived from LIAD underline the complex dynamics governing adsorption.

In 2005 Budker *et al* [64] indirectly measured the time of adsorption by measuring the shift in the clock resonance frequency caused by the cell-wall adsorption energy. The measurements were realized in the context of interaction of alkali atoms with paraffin and paraflint (alkane molecules) coated cells.

In 2009 Zhao, *et al* [149] directly measured the time of adsorption by means of Zeeman light shift of polarized alkali atoms pumped and probed by evanescent waves. The work concerned interaction of alkali atoms with OTS and paraffin [149, 138].

This summary although not exhaustive, outlines the continuing interest and new techniques in adsorption-science research. The ongoing research and the newer techniques of evanescent wave and LIAD are revealing adsorption dynamics far more complex than the one described early on by Eq. 6.1. The more recent works by Zhao *et al* [149, 138] and Freita *et al* [72] and work with LIAD [37, 105, 76, 90] indicate that in addition to the two-dimensional interaction (of the order of 10^{-10} s), adsorption also involves atoms entangled in bulk of the coating for times spanning several orders of magnitude longer (Sec. 3A and Refs. [149, 138])

6.3 Theory

6.3.1 Hyperfine resonance frequency shift

The adsorption energy E_w has two related effects in anti-relaxation coated vapor cells. The first effect is physical adsorption of the alkali atoms, as described in Sec. 6.2.1. The second effect is a shift ΔE_hf in the hyperfine ground state energy levels during physical adsorption. A similar hyperfine energy shift is observed with alkali atoms in the presence of foreign gases [101] and is caused by the potential-energy perturbation of the gas on the alkali atoms. The hyperfine energy shift is a function of the adsorption energy,

$$\Delta E_\mathrm{hf} = f(E_\mathrm{w}), \tag{6.3}$$

is scaled by the average time $\bar{t}_\mathrm{w}$ the atoms spend on the wall relative to the average time between collisions with the walls $\bar{t}_\mathrm{c}$, and leads to an average ground state hyperfine frequency shift,

$$\Delta\nu = \frac{\bar{t}_\mathrm{w}}{\bar{t}_\mathrm{w} + \bar{t}_\mathrm{c}} \frac{\Delta E_\mathrm{hf}}{h}, \tag{6.4}$$

where h is the Planck's constant.

Assuming the trajectories of the atoms have a cosine angular distribution after desorption, the atoms' average collision rate per unit surface is

$$\nu_\mathrm{c} = \frac{1}{4}\frac{N}{V}\bar{v}, \tag{6.5}$$

where N is the number of atoms in a volume V, $\bar{v} = \sqrt{8kT/\pi M}$ is the average atomic thermal velocity, k is the Boltzmann constant, and M the mass of the atom. For one atom, the average collision rate with a wall-surface of area S is

$$\nu_\mathrm{c} = \frac{1}{4}\frac{S}{V}\bar{v}, \tag{6.6}$$

and for a spherical cell the average time between collisions is,

$$\bar{t}_\mathrm{c} = \frac{4R}{3\bar{v}}, \tag{6.7}$$

where R is the radius (for non spherical cells, R can be generalized to be the cell's geometric factor, a function of both size and shape).

In the present work and in the work of Ref. [64] the cell-wall dwelling times of different cells are evaluated by measuring the hyperfine frequency shift and scaling it to a common cell size, temperature and alkali species. The underlying assumption is that the wall dwelling time has the same linear dependence on the hyperfine frequency shift in all cells. One may ask"is this a reasonable assumption?"

For $\bar{t}_\mathrm{w} \ll \bar{t}_\mathrm{c}$ and from Eq. (6.4) we have

$$|\Delta\nu| \propto \Delta E_\mathrm{hf}\frac{\bar{t}_\mathrm{w}}{\bar{t}_\mathrm{c}}, \tag{6.8}$$

which means that to measure hyperfine frequency shifts ($\Delta\nu$), in order to compare cell-wall adsorption energies E_w, between alkane coatings (work in Ref. [64]), between alkane and alkene coatings, and between alkene coatings (present work)by only measuring the hyperfine frequency shift [64], one must assume from Eq. (6.8) that ΔE_hf is nearly constant for all alkane and alkene coated cells. One needs to assess the quality of that assumption for coatings differing in their molecular structure and for coatings with the same molecular structure but with Zeeman relaxation times T_1. ranging from several seconds to over one minute.

Bouchiat and Brossel measured the cell-wall dwelling time $\bar{t}_\mathrm{w} \simeq 10^{-9}$ s in paraffin coated cells using magnetic decoupling ([34], Sec. 6.2.2). This measurement implies that for a hyperfine frequency on the order of $E_\mathrm{hf} \equiv 1$ GHz, for a typical hyperfine frequency shift $\Delta\nu = -100$ Hz, in a cell of radius ~2 cm, at room temperature, we get $\bar{t}_\mathrm{c} \simeq 10^{-4}$ s, and from Eq. (6.4),

$$\frac{\Delta E_\mathrm{hf}}{E_\mathrm{hf}} = \frac{h\Delta\nu}{E_\mathrm{hf}}\frac{\bar{t}_\mathrm{w} + \bar{t}_\mathrm{c}}{\bar{t}_\mathrm{w}} \simeq 1\%. \tag{6.9}$$

Consequently the hyperfine energy shift ΔE_hf caused by the cell-wall adsorption energy E_w is within the limit of applicability of perturbation theory and we may expect Eq. 6.3 to be a linear relationship, $\Delta E_\mathrm{hf} \propto E_\mathrm{w}$. From Eq. (6.1), we have $\Delta\nu \propto e^{E_\mathrm{w}}$, which implies that substantial changes in t_w can be associated with small changes in E_w, a fact substantiated by the perturbative character of the wall effect on the hyperfine splitting (Eq 6.9).

From the above one may infer that indeed ΔE_{hf} is approximately constant in all cells, and that "presuming that the hyperfine energy shift is near-constant, so as to interpret the hyperfine frequency shift as a measure of cell-wall dwelling time, is a reasonable assumption."

A different adsorption mechanism in which the atoms are thought to be trapped inside the tangled web of the long paraffin molecules ($\mathrm{C_nH_{2n+2}}$ where n=40-60) on the cell wall was recently proposed by Ulanski and Wu [138] who measured a dwelling time $\bar{t}_{\mathrm{w}} \simeq 10^{-6}$ s in a paraffin coated cell with 5 torr of nitrogen buffer gas.

The large cell-wall dwelling time difference between Ulanski and Wu's and Bouchiat and Brossel's results (three orders of magnitude difference) may be that the former work pertains to atoms interacting with the bulk of the coating whereas the latter work pertains to atoms interacting with the coating's surface only. The results with LIAD point to a population of atoms which is otherwise permanently trapped in the coating. In fact there may be a continuum of dwelling times ranging from several nanoseconds (Bouchiat's measurements) to semi-permanent. The results from Bouchiat, Wu and the work with LIAD may provide information as to the relative size of each population. In this work we assume that atoms trapped in the coating (even for dwelling times of the order μs) lose all microwave-induced coherence and do not contribute to the hyperfine energy shift ΔE_{hf}; we assume that the atoms dwelling at the surface of the cell-wall, as described by Bouchiat and Brossel, are the population of atoms generating the hyperfine frequency shift.

6.3.2 Hyperfine resonance linewidth

In addition to the hyperfine frequency shift, another measurable and independent quantity is the width of the hyperfine transitions $\mathit{\Gamma}_{\mathrm{hf}}$. The linewidth comes from two main known sources. The first source is spin exchange (between atoms in the vapor and in the two hyperfine ground states)

$$\frac{\mathit{\Gamma}_{\mathrm{se}}}{2\pi} = \frac{\mathcal{R}(I) n \bar{v}_{\mathrm{rel}} \sigma_{\mathrm{se}}}{\pi}, \tag{6.10}$$

where $\mathcal{R}(I) = (6I+1)/(8I+1)$ (Sec. VI of Ref. [82]) is the nuclear slow-down factor in the low polarization limit, I is the nuclear spin, n the atomic density, $\bar{v}_{\mathrm{rel}}$ the average relative velocity of the colliding atoms, and σ_{se} is the spin cross section.

The second source is the adiabatic broadening $\mathit{\Gamma}_{\mathrm{a}}$ which is the result of the statistical nature of $\bar{t}_{\mathrm{w}}$ and $\bar{t}_{\mathrm{c}}$ which leads to a dispersion of the average phase shift $\bar{\mathit{\Phi}}_{\mathrm{w}}$ accumulated by the atoms at each adsorption event [64],

$$\frac{\mathit{\Gamma}_{\mathrm{a}}}{2\pi} = \frac{\bar{\mathit{\Phi}}_{\mathrm{w}}^{\,2}}{\pi \bar{t}_{\mathrm{c}}}. \tag{6.11}$$

Other sources of relaxation (assumed to be small in this work), include the stem-effect, in which atoms are re-adsorbed by the alkali reservoir, and coating absorption-effect, in which the atoms are trapped inside the coating's long molecule chains [64].

For a typical hyperfine frequency shift $\Delta\nu \simeq -100$ Hz, $\mathit{\Gamma}_{\mathrm{a}}$ is the dominating contribution (Fig. 6.4A) giving the total hyperfine linewidth a near-quadratic dependence in the variable $\bar{\mathit{\Phi}}_{\mathrm{w}}$.

In contrast, the hyperfine frequency shift

$$\Delta\nu = \frac{1}{2\pi}\frac{\bar{\mathit{\Phi}}_{\mathrm{w}}}{t_{\mathrm{c}}} = \frac{3}{8\pi}\frac{\bar{\mathit{\Phi}}_{\mathrm{w}}}{R}\bar{v} \tag{6.12}$$

is linear in $\bar{\mathit{\Phi}}_{\mathrm{w}}$ [64].

Measuring $\mathit{\Gamma}_{\mathrm{a}}$ (Eq. 6.11) is an independent measurement of $\bar{\mathit{\Phi}}_{\mathrm{w}}$ which, if inconsistent with the one derived from measuring $\Delta\nu$ (Eq. 6.12), would indicate the presence of additional relaxation mechanisms.

6.3.3 Zeeman linewidth

The Zeeman resonance linewidth $1/T_1$, in contrast to the hyperfine resonance, is not sensitive to adiabatic collisions. T_1 (Sec. 6.5) is sensitive to spin randomization on the wall (non adiabatic collisions) and to uniform sources of relaxation, such as collisions with the alkali metal in the stem reservoir and semi-permanent absorption by the cell-wall coating [77, 124].

6.4 Experimental setup

The apparatus is shown in Fig. 6.1. The components used in this work consist of an alkali vapor cell with an alkene-based anti-relaxation coating, a four-layer mu-metal shield, a temperature stabilizing mechanism, a coil-system to provide a homogeneous bias magnetic field, a microwave loop antenna, a laser, and a photodiode to measure the laser light transmission through the cell.

The pump/probe beam is from a distributed feedback (DFB) laser (Toptica LD-0795) resonant with the rubidium (Rb) $5^2\mathrm{S}_{1/2}$ - $5^2\mathrm{P}_{1/2}$ (D1 line, λ=795 nm).

The 3 mm diameter collimated laser beam passes through an isolator, a variable neutral density filter, a polarizer, a rotatable quarter wave-plate, and the alkali vapor cell. The photodiode signal is amplified (SR-560) and the amplitude digitized with a digital acquisition system (DAQ - IOtech P-Daq/3001).

A dichroic atomic vapor laser lock (DAVLL) [146] is used to lock the laser optical frequency near the peak of F=2→F'=1 for ^{87}Rb and F=3→F'=2 for ^{85}Rb, for maximum hyperfine resonance contrast. A temperature controller (Omega CNI3252) maintains the DAVLL vapor cell temperature ~ 50°C to increase the electronic feedback signal to noise ratio.

A reference cell and a Fabry-Pérot interferometer provide additional monitoring of the optical frequency stability.

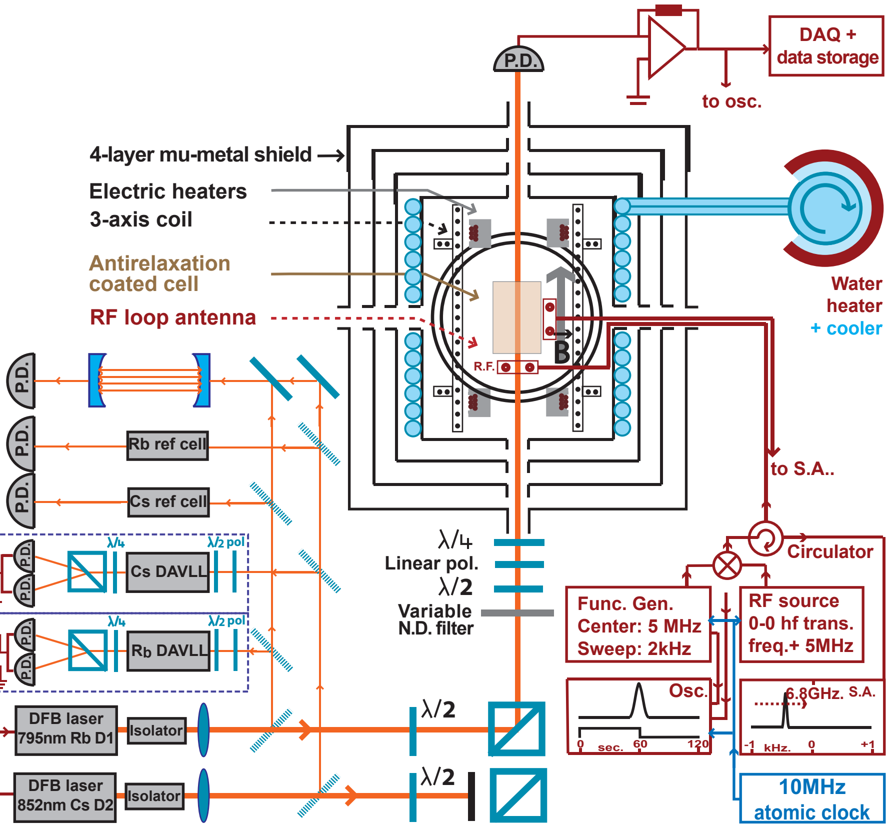

Figure 6.1: Apparatus: the alkene coated cell is placed inside a 4-layer mu-metal shield. A one-loop microwave antenna is positioned next to the cell. The orthogonal 3-axis coils and three gradient coils along the same axes induce a ∼3.6 mG bias magnetic field to resolve the Zeeman components of the hyperfine resonance. The magnetic field axis is slightly tilted with respect to the axial symmetry to achieve optimum clock-resonance contrast. A synthesizer provides a fixed microwave source set 5 MHz above the hyperfine transition, and is mixed with the output of a function generator which frequency is swept through a 2 kHz span about a 5 MHz center frequency. A circulator directs the mixed output to the one-loop microwave antenna and directs the return signal to a spectral analyzer (S.A.). The inner shield temperature stabilization is realized with two electric heaters consisting of quad-twisted non-magnetic wire coiled in two solenoids parallel to the main axial symmetry, and supplemented with a water heater/cooler system. The light beam from a distributed feedback (DFB) laser, is resonant with the rubidium (Rb) D1 line, and is made linear with approximately 5% circularity for optimum resonance contrast. Also for maximum contrast, the optical frequency is locked to the blue detuned side of the peaks of $F = 2 \rightarrow F' = 1$ (^{87}Rb) and $F = 3 \rightarrow F' = 2$ (^{85}Rb), using a dichroic vapor laser lock (DAVLL) [146]. Stability of the laser optical frequency is monitored with a reference (non-coated) cell and a Fabry-Pérot cavity. A photodiode registers the light transmission through the cell, the signal is amplified, sampled, and recorded with a digital acquisition system (DAQ). [Note: the apparatus is a multi-purpose platform (Ch. 5-part I) which, together with a field-able device (Ch. 4-Part I), is designed to investigate areas of magnetometry and secondary time standards.]. [Data/analysis/project-management (2009-12): E. Corsini - Collaboration: T. Karaulanov - P.I. Dr. Budker - Valuable discussions with V. Acosta, M. Ledbetter, B. Patton, K. Tsigutkin, and D. Dounas-Fraser]

The magnetic field is applied with a set of three orthogonal coils, three gradient coils along the same directions, and one longitudinal second-order gradient coil, positioned within the inner-most layer of the four-layer mu-metal shield manufactured by Amuneal. COMSOL modeling was used to optimize the geometry of the coils and achieve better than 1% magnetic field homogeneity within a 2 in-diameter, 4 in-long cylindrical volume.

A 3.6 mG bias magnetic field resolves the $m_{\mathrm{F}}{=}0{\rightarrow}m_{\mathrm{F'}}{=}0$ (0-0) rubidium clock resonance from the other Zeeman components of the hyperfine resonance (Fig.6.2). The clock resonance is only sensitive to second order magnetic field-induced hyperfine frequency shift, which is negligible in this work. There are seven Zeeman components for ^{87}Rb and eleven for ^{85}Rb.

The pump light polarization and the relative orientations of the pump light, magnetic and microwave fields are optimized for optimum hyperfine resonance contrast. Maximum contrast is achieved with axis of the antenna oriented approximately parallel to the shield's axis, with the magnetic field orientation tilted approximately 10° upward, and with the pump light polarization made approximately linear.

The microwave magnetic field is generated by mixing the output of a synthesizer (HP8673B), set at a fixed frequency, and the output of a function generator (BNC625), which frequency is swept through the desired measurement range. The function generator also outputs a marker step as an additional frequency reference. The mixer (Mini-Circuits ZX05-153) feeds a circulator (DiTom D3C6012). One port of the circulator is directed to a one-loop 2 cm diameter antenna positioned next to the cell; the other port directs the return signal to a spectral analyzer (Agilent 8562F) to monitor the microwave frequency and power. A second microwave antenna serves as a receiver and provides an additional microwave power monitor. The HP synthesizer, BNC function generator and Agilent spectral analyzer are referenced to a 10 MHz signal from a commercial wireless-network-referenced rubidium atomic clock (Symmetricom TS2700B).

A temperature controller (Omega CN77353-PV) regulates the DC current to two electric heaters consisting of quad-twisted non magnetic heater wire (LakeShore QT36), positioned fore and aft of the cell, and coiled along the main shield axis. The residual magnetic field produced by the heaters is on the order of 1 μG and can be neglected. The electric heaters are supplemented with a water heater/cooler system. The innermost shield serves to conduct and distribute the heat so as to achieve a temperature which is approximatively uniform within the cell's volume within a range of 15°C to 50°C.

6.5 Measurement procedures

Measurements were made on six rubidium (Rb) vapor cells. Four cells are coated with alkene Alpha Olefin Fraction C20-24 from Chevron Phillips (CAS Number 93924-10-8) with a light fraction removed by partial vacuum evaporation at 80°C. One cell is coated with alkene AlphaPlus C30+ from Chevron Phillips (CAS Number 131459-42-2), and one cell is coated with deuterated paraffin. The melting temperature for C20-24 is 35°C and 73°C for C-30. The cells are of different sizes, have cylindrical or spherical shapes, and are filled with enriched ^{87}Rb or with rubidium in natural isotopic abundance. They are prepared according to the technique described in Ref. [16]. The alkene coated cells are fitted with a precision ground stem lock [23, 90] which near-eliminates Zeeman relaxation caused by the atoms being re-absorbed by the stem reservoir (stem-effect [34]). The Zeeman population lifetimes of the four C20-24 alkene coated cells T_1 were measured with the stem-lock closed and were found to range from approximately 2 s to 60 s. T_1 was measured using a modification of Franzen's "relaxation in the dark" technique [71], described in Ref. [77]. That technique yields two exponential decay constants characterizing the Zeeman population relaxation; the longer time constant is used to define T_1.

The microwave synthesizer was set 5 MHz above the rubidium hyperfine transition frequency, and the function generator frequency was centered at ∼5 MHz, such that the center of the sweep was approximately 100 Hz below the hyperfine transition to help in the data fit. The mixer output frequency, resonant with the hyperfine transition, was the difference frequency, was separated from the conjugate (sum) frequency by 10 MHz, and was not low-pass filtered. At saturation power the microwave magnetic field induced a 0-0 hyperfine transition AC Stark shift of approximately 10^{-5} Hz, which was neglected.

We measured the ground state hyperfine $m_{\mathrm{F}}{=}0{\to}m'_{\mathrm{F}} = 0$ transition (clock resonance) width and frequency shift by sweeping the function generator frequency through a span of 2 kHz, in a time of 120 s. The measurements were made for a range of microwave powers spanning 30 dB such that at maximum microwave power the width of the resonance was broadened by a factor of ∼5, and for optical powers ranging from ∼100 nW to ∼30 μW. For the cell filled with Rb with natural abundance we performed the measurements for each species.

For each microwave and optical power setting, we fit the light transmission data to a Lorentzian, and averaged the results from approximately five measurements. To mitigate frequency calibration errors the center frequency was measured and averaged from the start of the scan and from the falling edge of the frequency marker (Fig. 6.3A). The clock resonance width and frequency shift for each cell was extracted from a zero microwave power extrapolation followed by a zero optical power extrapolation (an example of light power extrapolation is shown in Figs. 6.3 B1 & B2).

We measured the temperature dependence of the clock resonance width and frequency shift in one of the alkene coated cells and we found no significant dependence in a range

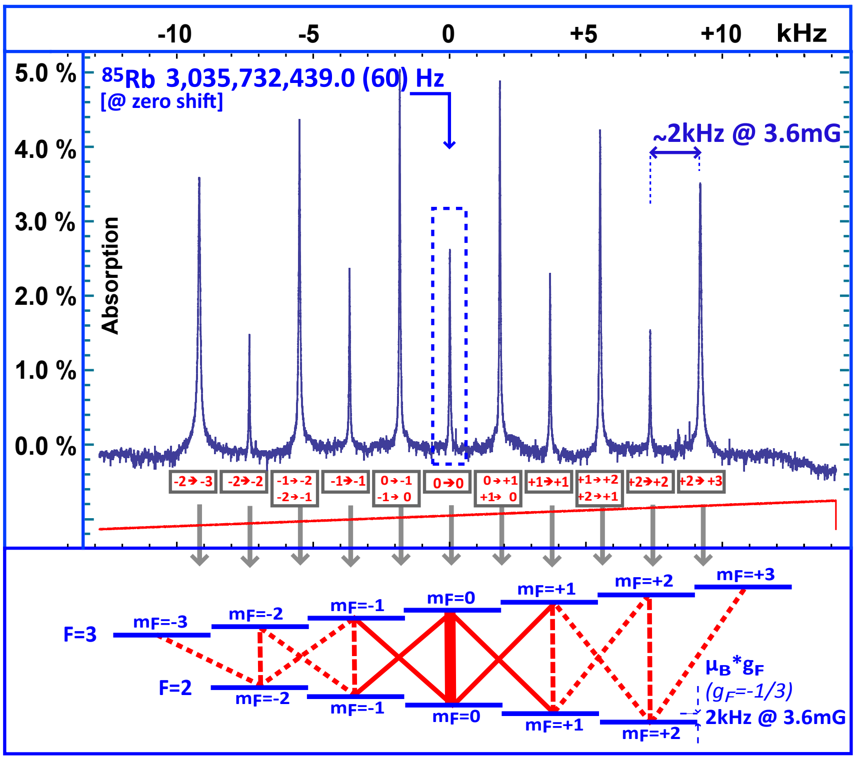

Figure 6.2: Upper: The eleven Zeeman components of the hyperfine resonance in ^{85}Rb are resolved with a ~3.6 mG bias magnetic field. The relative intensities of the peaks depend on the relative orientation of the pump light beam, the bias magnetic and microwave fields, the pump light detuning, and the polarization. Under typical conditions the optical resonant absorption through the alkali vapor is ~ 25% and increases by 1-5 percent on the hyperfine resonances.
Lower: F=2 and F=3 hyperfine ground states Zeeman sublevels for ^{85}Rb, and corresponding Zeeman components of the hyperfine transition.
[Data/analysis/project-management (2009-12): E. Corsini - Collaboration: T. Karaulanov - P.I. Dr. Budker - Valuable discussions with V. Acosta, M. Ledbetter, B. Patton, K. Tsigutkin, and D. Dounas-Fraser]

of 24-31°C. The range was limited by the alkene anti-relaxation coating properties which was shown to deteriorate above 33 °C [23] and by the poor signal to noise ratio below 24°C.

For consistency and comparison with the results from Ref. [64], we repeated the clock resonance frequency shift and width measurements in one of the paraffin coated cells measured in that work (cell labeled H2 in Tables 6.1, and found equivalent results.

In all alkene coated cells we found no significant dependence of the clock resonance width and frequency shift on whether the stem lock was open or closed. With the lock closed the vapor density was found to decrease over several hours (depending on the lock fit) due to the semi-permanent absorption of alkali atoms by the wall-coating [23] (which could potentially be desorbed using the LIAD technique [90].

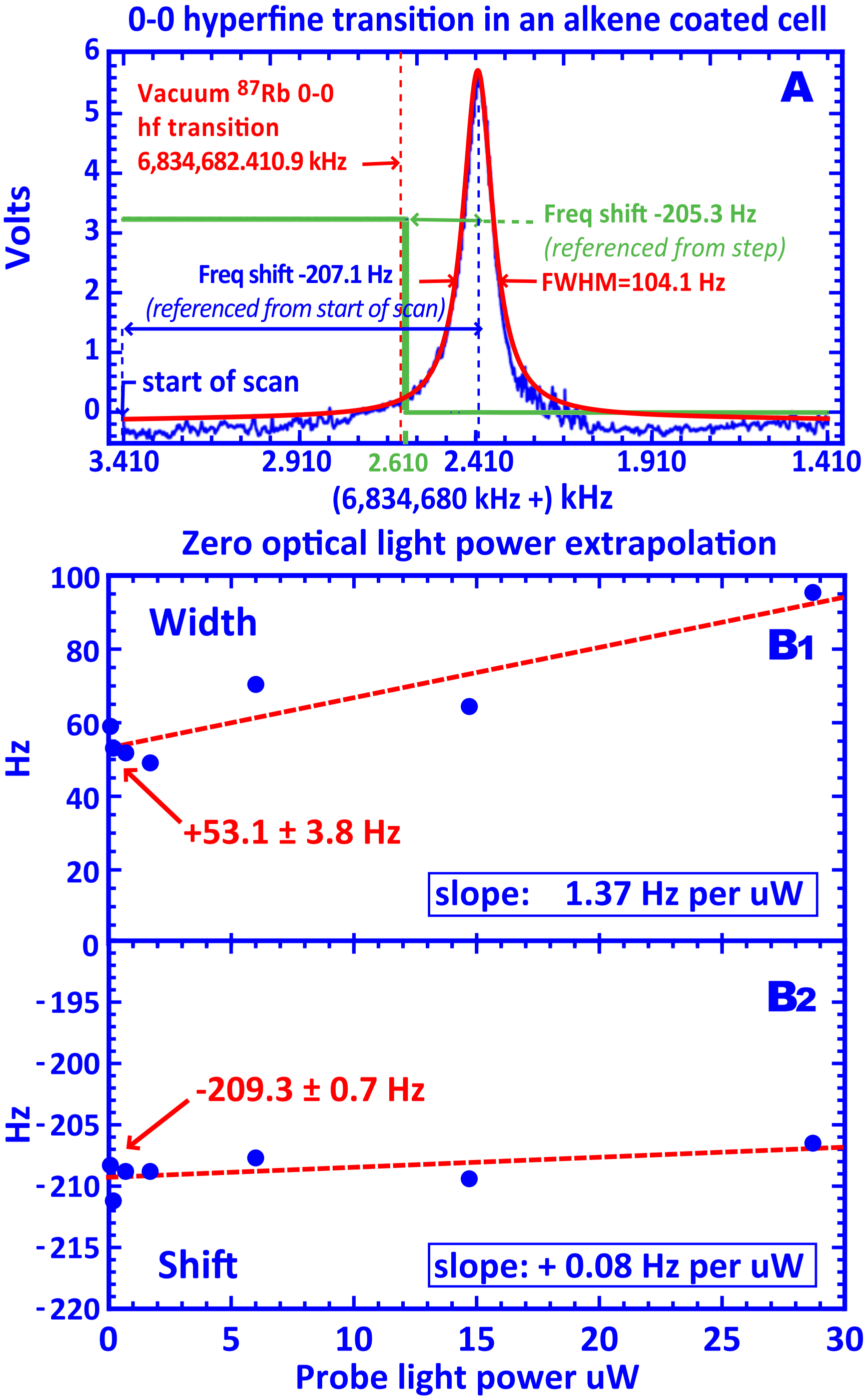

Figure 6.3: Extracting the $m_{\rm F}=0\rightarrow m'_{\rm F}=0$ (0-0) hyperfine transition (clock resonance) width and frequency shift (example).
Fig. A: Scan of a ^{87}Rb clock resonance at large optical (10.7 μW) and microwave powers. The data are fit to a Lorentzian. The difference between the data and the wings of the fit may be attributed to the relatively fast scan rate (17 Hz/s). The induced error in determining the resonance center frequency is within the margin of measurement error. To mitigate timing jitter the center frequency is measured from both the step-edge and from the beginning of the scan. In this example the clock-resonance un-scaled (Sec. 6.5) FWHM and un-scaled frequency shift, relative to the hyperfine frequency for atoms in free space, are 104Hz and -206.2 Hz, respectively.
Fig. B1 & B2: Extraction of the clock-resonance width and frequency shift by extrapolation to zero light power (each data point represents an extrapolation to zero microwave power). The example shown is for the 2-in. long, 1-in. diameter cylindrical cell filled with isotopically enriched ^{87}Rb. [Data/analysis/project-management (2009-12): E. Corsini - Collaboration: T. Karaulanov - P.I. Dr. Budker - Valuable discussions with V. Acosta, M. Ledbetter, B. Patton, K. Tsigutkin, and D. Dounas-Fraser] .

To improve and to maintain a constant signal to noise ratio, all final measurements were made with the stem-lock open. We note that the alkane coated cells in Ref. [64] were not fitted with stem-locks.

The clock resonance width and frequency shift measurements were scaled to the ^{85}Rb hyperfine transition frequency in a 1 in. diameter spherical cell at 25 C. The scaling factors were derived from the equations in Sec. 6.3.

6.6 Results

We observed a dispersive and wing residual in the hyperfine resonance fitted to a Lorentzian (Fig. 6.3A). A better fitting function would take into account the broader profile below the "clock" resonance's Lorentzian profile.[64]. The Lorentzian profile originates from Dicke narrowing due to the cell size being comparable to the microwave frequency wavelength. Another source for the residual may come from atoms entangled in the bulk of the coating. Such atoms would have a hyperfine frequency shift much larger than the one from atoms adsorbed on the coating's 2D surface. However the corrections to the hyperfine frequency shift that would be derived from these factors are of the order of a few % of the total frequency shift (itself of the order of 100 Hz) and fall within the measurement uncertainty.

The scaled (Sec. 6.5) width and shift data, and the data from Ref. [64] on paraffin coated cells, are summarized in Table (6.1). The scaled hyperfine linewidth data as a function of scaled frequency shift are plotted in Fig. 6.4A. The Zeeman linewidth as a function of scaled hyperfine frequency shift data are plotted in Figs. 6.4 B1 and B2.

There is good agreement between the data on Fig. 6.4A, for the alkene coated cells filled with ^{87}Rb, with the value predicted by the sum-contribution (dotted line) of the spin exchange and adiabatic broadening mechanisms (Sec. 6.3); however we observe a near 50% discrepancy for ^{85}Rb.

Comparing the results to those on alkane coatings [64], we find that the range of hyperfine frequency shifts is comparable (sightly larger) for cells coated with alkene than for cells coated with alkane. The Zeeman relaxation rate $1/T_1$ of the C20-24 alkene coated cells exhibit a linear dependence on the scaled frequency shift with a -66 Hz frequency offset (Fig. 6.4B2). The alkene C-30 and deuterated paraffin coated cells data do not follow the same linear dependence, are not included in the fitting function (Fig. 6.4B2), and are shown for comparison only.

The Zeeman linewidths $1/T_2$ (which was measured for three of the four alkane coated cells [64]) does not seem to exhibit such linear dependence (Fig. 6.4B1). We note that the C-30 alkene and deuterated paraffin coated cells $1/T_1$ data points (Fig. 6.4B1) which are also shown in Fig. 6.4B2, are within the same distribution as the paraffin coated cells $1/T_2$ data.

Rb Species	Cell shape	Cell size [in.]	Temp. [C]	Density [$10^9/\mathrm{cm}^3$]	$\bar{t}_c$ $\frac{timeb/w}{coll.}$ [μs]	Cell label [64] and/or coating type	T_1 [s]	T_2 [s]	Linewidth $\left(\frac{\Gamma}{2\pi}\right)^{\mathrm{expt}}$ [Hz]	Shift $\Delta\nu^{\mathrm{expt}}$ [Hz]	Phase shift $\bar{\Phi}^{\mathrm{expt}}$ [mrad]	Linewidth $\left(\frac{\Gamma}{2\pi}\right)^{\mathrm{scaled}}_{\mathrm{expt}}$ [Hz]	Shift $\Delta\nu^{\mathrm{scaled}}_{\mathrm{expt}}$ [Hz]
85	Sph.	4	25	8	249	Par. (Ale-10)	-	1.2	8.7	-24	0.037	35	-96
85	Sph.	4	25	8	249	Paraffin (Gib)	-	2.9	11	-14	0.021	44	-56
87				8	252				16	-42	0.066	28	-74
87	Sph.	1.4	21	7	249	Paraffin (H2)	-	3.5	22	-93	0.051	14	-57
87			30	7		(H2, meas. by E.C.)	-	-	22	-90	0.049	13	-56
87	Sph.	1.4	22	6.4	250	Paraffin (TTll)	-	-	23	-80	0.043	14	-4
85	Sph.	1.2	33	0.23	73	Deuterated	0.8	-	42	-88	0.04	50	-106
87	Cyl.	2×1	29	0.14	99	Alkene C20-24	3.0	-	53	-209	0.13	37	-146
87	Cyl.	4×1	29	0.14	109	Alkene C20-24	4.2	-	42	-180	0.124	33	-140
85			29	0.14	110				20	-75	0.051	35	-132
87	Sph.	1.2	28	0.12	75	Alkene C20-24	17.7	-	32	-158	0.074	17	-83
85	Sph.	1.2	29	0.12	74	Alkene C20-24	60	-	11	-57	0.026	13	-68
85	Sph.	1.2	30	0.12	74	Alkene C30	1.6	-	16	-70	0.032	19	-84

Table 6.1: [Tables 6.1 & 6.2] Upper: paraffin coated cells data from Ref. [64]. Middle and lower: Deuterated paraffin coated cell and alkene coated cells data, respectively (this work). The work in Ref [64] included the measurement of the NMOR coherence relaxation time T_2 in three of the four cells used in that work. In the present work we measured the Zeeman relaxation time T_1 using the technique described in Sec. 6.5. The hyperfine resonance linewidth $\Gamma/2\pi^{\mathrm{expt}}$ and frequency shift $\Delta\nu$ are shown both un-scaled and scaled to the ^{85}Rb species, in a 1-in. diameter spherical cell, at 25° C (Sec. 6.5). The alkane coated cell labeled “Gib”, and the alkene coated 4-in cylindrical cell, are filled with natural-abundance rubidium vapor.

Rb Species	Cell shape	Cell size [in.]	Geometric factor	Cell label [64] or coating type	Nuclear factor	Slow-down spin	Linewidth $\left(\frac{\Gamma}{2\pi}\right)^{\text{expt}}$ [Hz]	Linewidth $\left(\frac{\gamma}{2\pi}\right)^{\text{a+se}}_{\text{theory}}$ [Hz]	Linewidth $\left(\frac{\Gamma}{2\pi}\right)^{\text{Scaled}}$ [Hz]
85	Sph.	4	4	Par. (Ale-10)	$\frac{5}{2}$	$\frac{16}{2}$	8.7	9.0	35
85	Sph.	4	4	Paraffin (Gib)	$\frac{5}{2}$	$\frac{16}{2}$	11	4.3	44
87					$\frac{3}{2}$	$\frac{10}{2}$	16	6.3	28
87	Sph.	1.4	1.4	Paraffin (H2)	$\frac{3}{2}$	$\frac{10}{2}$	22	4.5	14
87			1.4	(H2: measured by E.C.)	$\frac{3}{2}$	$\frac{10}{2}$	22		13
87	Sph.	1.4	1.36	Paraffin (TTll)	$\frac{3}{2}$	$\frac{10}{2}$	23	3.7	14
85	Sph.	1.2	1.2	Deuterated	$\frac{5}{2}$	$\frac{16}{2}$	42	11.3	50
87	Cyl.	2×1	1.58	Alkene C20-24	$\frac{3}{2}$	$\frac{10}{2}$	53	57.1	37
87	Cyl.	4×1	1.76	Alkene C20-24	$\frac{3}{2}$	$\frac{10}{2}$	42	47.7	33
85					$\frac{5}{2}$	$\frac{16}{2}$	20	10.5	35
87	Sph.	1.2	1.2	Alkene C20-24	$\frac{3}{2}$	$\frac{10}{2}$	32	26.1	17
85	Sph.	1.2	1.2	Alkene C20-24	$\frac{5}{2}$	$\frac{16}{2}$	11	5.8	13
85	Sph.	1.2	1.2	Alkene C30	$\frac{5}{2}$	$\frac{16}{2}$	16	7.6	19

Table 6.2: Table 6.1 part 2 - See caption in Table 6.1

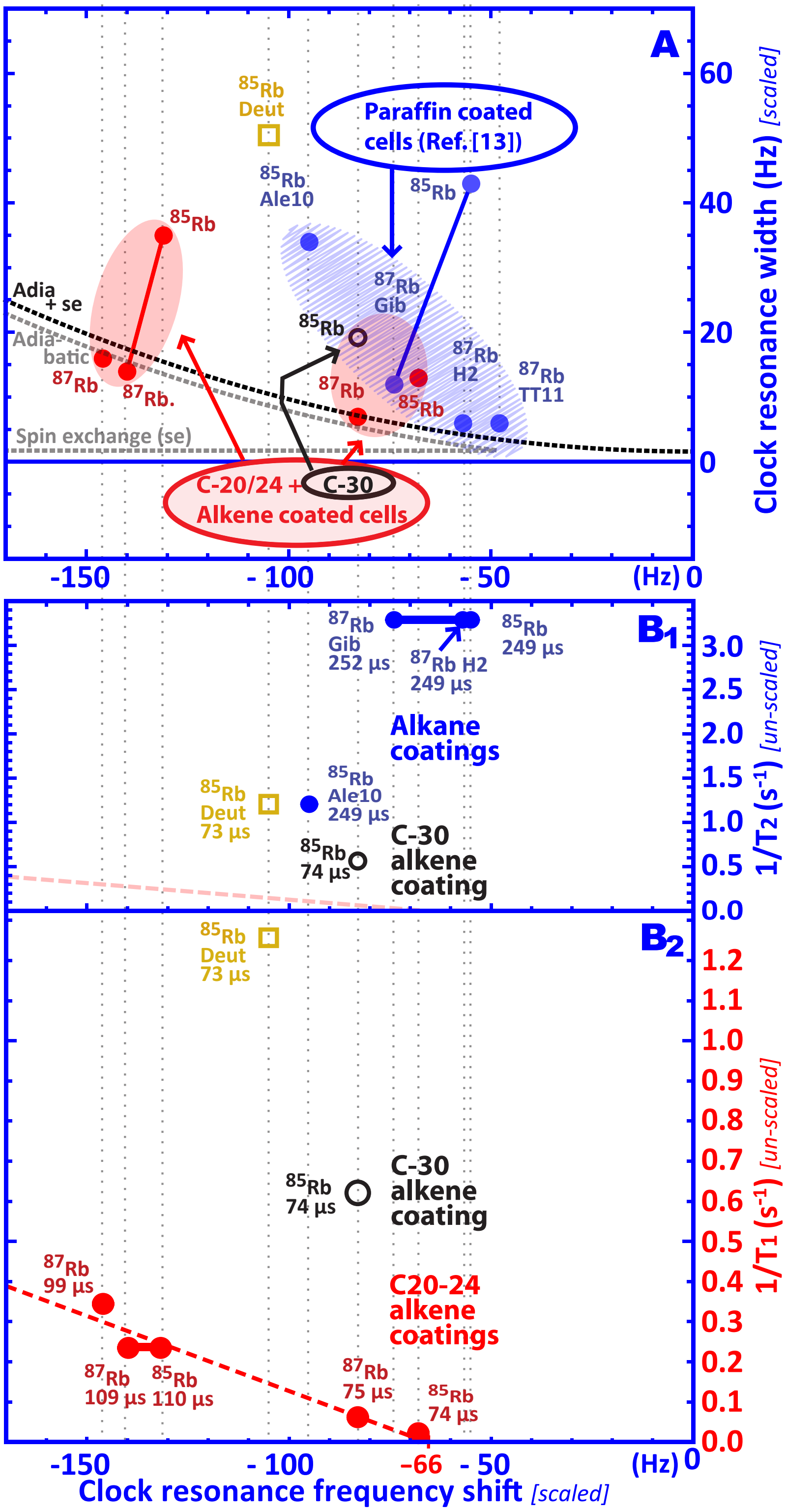

Figure 6.4: Figs. A, B1 & B2: The C-30 and deuterated paraffin coated-cells data are shown as a circle and a square, respectively. The vertical dotted lines serve to guide the eye.
Fig. A: Dependence of the hyperfine clock-resonance scaled-linewidth on the hyperfine scaled-frequency shift. The data are scaled (Sec. 6.5) to a 1-in. spherical cell at 25°C and to the hyperfine frequency of the ^{85}Rb species. The oval shapes serve to group cells with similar characteristics. Solid oval: alkene coated cells with Zeeman polarization relaxation times T_1 ranging approximately between 2 to 60 s. Hashed oval: paraffin coated cell data [64]. The dashed lines are the simulated adiabatic, spin exchange, and sum of both contributions to the hyperfine resonance linewidth. [Caption continued on next page.]

Figure 6.4 caption continued:

Figs. B1 & B2: The time between wall collisions is given in μs for each cell. Typical error bar magnitudes are given in Fig. 6.3. The two horizontal segments join ^{85}Rb and ^{87}Rb data in the cells with rubidium in isotopic abundance. Note the different vertical-axes scales in B1 and B2
Fig. B1: Dependence of the Zeeman relaxation rate $1/T_2$ on the hyperfine clock-resonance scaled-frequency shift for the three paraffin coated cells of Ref. [64] for which T_2 was measured. The alkene C-30 and deuterated-paraffin coated cells $1/T_1$ (Sec.6.5) data points are added to this figure for reference only. The light slanted dashed line is the $1/T_1$ linear fit in Fig. B2.
Fig. B2: Dependence of the Zeeman relaxation rate $1/T_1$ on the scaled hyperfine clock frequency shift in the four alkene coated cells in the present work. The alkane C-30 and deuterated-paraffin coated cells data do not follow the same linear dependence observed in the alkene C20-24-coated cells and are not part of the linear fit. [Data/analysis/project-management (2009-12): E. Corsini - Collaboration: T. Karaulanov - P.I. Dr. Budker - Valuable discussions with V. Acosta, M. Ledbetter, B. Patton, K. Tsigutkin, and D. Dounas-Fraser].

6.7 Interpretation

6.7.1 Hyperfine resonance width and frequency shift

We have investigated the ground state hyperfine transition in four C20-24 and one C-30 alkene coated vapor cells. How do the results answer the question “Is long relaxation time due to a short wall-dwelling time?” and fulfill the motivation pertaining to “application of alkali vapor coated cells to secondary frequency standard”, introduced in Sec. 6.1.

The alkene cells do not have a smaller hyperfine transition frequency shift. If we assume that the average cell-wall adsorption energy is nearly constant and independent of the coating property (Sec. 6.3), then from Eqs. (6.1), (6.3), & (6.4), the alkene's long-lived Zeeman polarization property is not caused by a cell-wall dwelling time shorter than for the alkane coatings.

This result points to the possibility that the factor governing the Zeeman relaxation is not the cell-wall dwelling time, but is instead a smaller RMS magnitude of the average fluctuations ΔE_{w} of the cell-wall adsorption energy E_{w}. Bouchiat and Brossel had reached the same conclusion for alkane coasted cells [34].

A possible explanation for the cell-wall dwelling time being similar in alkene and alkane coatings is the curing process which is performed at ~60° C and which is part of the manufacture of paraffin and alkene coated cells. During that process alkali atoms are absorbed into and/or on the coating. One may hypothesize that the alkene and alkane coatings are modified by the curing process to a final surface structure, which causes approximately the same cell-wall dwelling time, but has a different degree of uniformity.

Since the alkene coating-induced clock resonance frequency shift is not measured to be small, the coating's temperature dependence and stability will need to be assessed to determine whether alkene coatings offer an advantage for applications to secondary time standards.

The near-agreement between the scaled width of the clock resonance and the predicted value (dotted line on Fig. 6.4A) for the ^{87}Rb-filled cells, but not for the ^{85}Rb-filled cells may be an artifact of the normalization step derived from Eqs. (6.8), (6.11), & (6.12). The near-50% discrepancy for ^{85}Rb could come from sources of relaxation that are additional to the adiabatic and spin exchange effects, and fixed in nature, such as the stem-effect. Fixed contributions make a relatively larger contribution to the scaled hyperfine resonance width of ^{85}Rb, whose hyperfine frequency is approximately half that of ^{87}Rb (the scaling factor is quadratic in the ratio of the hyperfine frequencies).

6.7.2 Zeeman relaxation and hyperfine resonance frequency shift

The results in Sec. 7.4 showed that alkane and alkene coatings had comparable hyperfine frequency shift, leading to the conclusion that the approximately up to two orders of magnitude longer Zeeman relaxation time of the alkene coatings was not caused by a shorter cell-wall dwelling time (Eqs. [6.3] & [6.4]). However, in the four C20-24 alkene coated cells (which have comparable geometric factors), we observe that within the range of hyperfine frequency shifts there appears to be a linear dependence on the Zeeman linewidth (Fig. 6.4B2); which means that in alkene-coated cells the wall dwelling time $\bar{t}$w plays a role in determining the Zeeman linewidths of the cells. A similar linear dependence for alkane coated cells has not been observed [64]. The different observation may be due to the homogeneity of the history and manufacture of the alkene cells (prepared following the procedure described in Ref. [23], within a few-month period), in contrast to the history of the four alkane cells in Ref. [64] (manufactured over several decades and coated by different techniques).

Bouchiat and Brossel also inferred, from their observations in alkane coated cells, a near-linear dependence of the Zeeman linewidth $1/T_1$ on the wall dwelling time $\bar{t}_\mathrm{w}$ [34],

$$\frac{1}{T_1} \propto \frac{\bar{t}_\mathrm{w}}{\bar{t}_\mathrm{w} + \bar{t}_\mathrm{c}} \cdot (H_\mathrm{o})^2 \,, \tag{6.13}$$

where H_o is the RMS amplitude of the magnetic field fluctuation on the surface as "seen" by the alkali atoms.

If we assume that $\mathit{\Delta} E_\mathrm{hf}$ does not vary significantly from cell to cell (as assumed in Sec 7.5), one may apply the linear relationship $1/T_1 \propto \Delta\nu$ (Eqs. 6.13 and 6.8) to a family of cells, which explains the results in the four alkene coated cells pertaining to this work. We conclude that, within the constraint stated above, a shorter wall dwelling time $\bar{t}_\mathrm{w}$ in alkene coated cells is related to a narrower Zeeman linewidth $1/T_1$ as shown on Fig. 6.4B2.

We observe that the characteristic of the cell with ~60 s Zeeman relaxation time (Tab. 6.1) is equivalent to a hypothetical "perfect coating" combined with one ring-shaped gap between the cell volume and the cell reservoir through an imperfectly fitted stem-lock. A 2.3 μm wide, 2 mm diameter gap circumscribing the stem-lock, through which we assume the alkali atoms reach the cell reservoir (which scrambles the atoms' atomic polarization), is equivalent (at room temperature) to a $\sim$60 s Zeeman relaxation time. We may then interpret the -66 Hz offset (Fig. 6.4) as being the hyperfine frequency shift corresponding to the minimum cell-wall adsorption time $\bar{t}_\mathrm{w}$ and to near-zero Zeeman linewidth, and corresponding to the characteristics of an ideal alkene coating.

6.8 Hypothesis and model

In this appendix we propose a hypothesis to explain the observed linear dependence of the Zeeman linewidth on the cell-wall dwelling time and the -66Hz hyperfine transition frequency shift offset (Fig. 6.4B2), we hypothesize two different length and time scales pertaining to the alkali atoms adsorbed on the cell-wall coating.

The first, (short length/fast time scale) originates from the average difference $\mathit{\Delta} E_\mathrm{w}$ in the adsorption energy E_w between adsorption sites. The adsorbed atoms hop from one site to another (length scale) at an average rate, $1/\bar{t}_\mathrm{hop}$ (time scale), governed by the transverse thermal energy (Eq. 6.2). The hopping subjects the atoms to a time varying magnetic field $H(t)$ (from the coating's hydrogen nuclei). Bouchiat and Brossel identified $H(t)$ as being the primary relaxation mechanisms in alkane coatings, and identified the ratio of time scales of cell-wall dwelling to time between hops, $t_\mathrm{w}/t_\mathrm{hop} \simeq 10$ [34].

The second, (long length/slow time scale) pertains to the average distance traveled by the alkali atoms through random walk during one adsorption event. We hypothesize that the alkene cell-wall surface has a near-uniform adsorption energy which does not subject the atoms to large fluctuation in the magnetic field $H(t)$ when the atoms hop from one site to another. The near-uniform adsorption energy may be due to the higher alkene vapor pressure with the alkene molecules being themselves adsorbed preferentially at the sites with the largest cell-wall adsorption energy, making the adsorption energy more uniform. In this scenario the near-uniform adsorption energy allows adsorbed atoms to undergo many more hops per unit time (Eq. 6.2) than in alkane coatings, and smaller fluctuations in $H(t)$. In this hypothesis the atoms "glide" over the wall surface and the primary relaxation mechanism is the atoms' random encounters with a distribution of discrete "relaxation centers".

One could hypothesize that the relaxation centers are islands of alkali atoms on the surface (as was noted by Rampulla *et al* [113]), or islands of "uncured" coating. Alternatively the relaxation centers could be connected to the alkene molecule's unsaturated double bond (C=C), which was first thought to be Zeeman relaxation inducing, but instead gave up to two orders of magnitude longer Zeeman relaxation times. Alkalinization of the double bond (observed by Balabas *et al* [21]) may form in an island-like pattern. The encounter of the atoms with the island boundaries could be the source of large fluctuations in the adsorption energy E_w and in the magnetic field $H(t)$ ("seen" by the adsorbed alkali atoms), and would cause both Zeeman relaxation and hyperfine transition frequency shift. In this hypothesis the relaxation centers are the common cause for the Zeeman relaxation and for the hyperfine frequency shift, and explain their linear dependence. The quality of alkene coatings (the Zeeman linewidth) is a measure of the density of discrete islands of relaxation centers.

In this hypothesis the -66 Hz offset is the hyperfine frequency shift corresponding to the minimum cell-wall adsorption time $\bar{t}_{\mathrm{w}}$ and near-zero Zeeman linewidth, and would correspond to the characteristics of the ideal alkene coating with no relaxation centers. One may then liken adsorbed atoms on the surface of an ideal coating as a surface superfluid [1]. The cell exhibiting a Zeeman relaxation time of ∼60 s (Tab. 6.1) would have a near-ideal coating with just one such relaxation center, namely the alkali reservoir through an imperfectly fitted stem-lock. If the gap circumscribing the lock in that cell is a ring 2.3 μm wide and 2 mm in diameter, then the measured relaxation rate is the one caused by the atoms reaching that single relaxation center through that gap.

To summarize, in this hypothesis the Zeeman relaxation in alkane and alkene coated cells comes from two distance/time scales. One scale is related to the hopping-induced time varying magnetic field, which is dominant in alkane coated cells. The other scale is related to the random walk and encounter with an island of relaxation center, and is the dominant factor in alkene coated cells.

To test this hypothesis one could use magnetic decoupling as was done by Bouchiat and Brossel in the context of alkalis and paraffin (Sec. 6.2B), by Romalis and Lin [120] for mercury and paraffin coating, and by Driehuys *et al* [66] for xenon and paraffin coating. Magnetic decoupling would result in a dependence of the Zeeman relaxation time T_1 on the magnetic field showing two main steps, indicating the respective contributions to the Zeeman relaxation mechanism coming from the average hopping time (first time scale), and from the average random-walk time to reach a relaxation center (second time scale).

Surface nuclear magnetic resonance (NMR) could be another testing tool using the techniques pertaining to Knight shift and chemical shift. Knight shift involves a few percent shift in the NMR frequency due to the orientation of conduction electron spins near the top of the Fermi distribution, and is much larger than chemical shift [108, 136]. Knight shift would be the signature of islands of alkali metals on the cell-wall.

6.9 Conclusion

We have investigated the ground state hyperfine transition frequency shift and width in four C20-24 alkene-coated cells and compared the results with those in four alkane coated cells [64]. We found comparable frequency shift with alkene and alkane cells and observed a linear dependence of the alkene coated cells' Zeeman linewidths on the hyperfine frequency shift, a dependence which was not observed in the alkane coated

---

[1] The idea of 2D superfluidity was first formulated by M. Balabas.

cells. The linear dependence has a -66 Hz offset which may indicate the cell-wall dwelling time in an ideal coating having near-zero Zeeman linewidth.

We proposed a model involving two length/time scales both present in alkane and alkene coated cells; the short/fast one is dominant in alkane and the long/slow one is dominant in alkene. The short/fast scale follows from the work by Bouchiat *et al*, involves large adsorption energy differences between adsorption sites, and describes the primary Zeeman relaxation mechanism as large fluctuations in the magnetic field "seen" by the adsorbed atoms hopping from site to site. The long/slow scale involves a near-uniform adsorption energy on which the atoms "glide" between adsorption sites and describes the primary relaxation mechanism as islands (coating defects) of "relaxation centers" of alkali atoms or of uncured coating, with large spatial fluctuations in the adsorption energy and in the magnetic field at the islands' boundaries. Alternatively the islands may be sites where the alkali atoms are adsorbed for longer periods of time (corresponding to the μs dwelling time-scale observed by Wu *et al*). In the limit of no relaxation centers, the adsorbed atoms may constitute a surface superfluid [2].Techniques in magnetic decoupling and in surface science NMR would be well suited to further elucidate the long-standing questions pertaining to the relaxation mechanisms in anti-relaxation coated alkali vapor cells.

The present observation of the association of narrower Zeeman linewidths with shorter wall-dwelling times in alkene coated cells, may shed new understanding as to the surface dynamics governing the interaction of alkali atoms and alkene coatings.

6.10 Acknowledgements

The authors are grateful to M. Bouchiat, S. Seltzer, M. Ledbetter, S. Pustelny, V. M. Acosta, A. Shmakov, B. Patton, K. Tsigutkin, K. Jensen, D. Dounas-Frazer, D. English, A. Jarmola, N. Leefer, A. Park, and G. Iwata for helpful discussions. This work was supported by NSF (grant PHY-0855552) and by the U.S. Department of Energy through the LBNL Nuclear Science Division (Contract No. DE-AC03-76SF00098).

---

[2] The idea of 2D superfluidity was first formulated by M. Balabas.

Chapter 7

Search for plant biomagnetism (magnetophytography) with a sensitive magnetometer

We call the measurement of plant biomagnetism, **magnetophytography**, following the Greek root and suffix tradition prevailing in biomagnetism[1](Fig. 7.3).

Related publication
Journal: Jour. App. Phys. 109, 074701 (2011)
Title: Search for plant biomagnetism with a sensitive magnetometer
Authors: E. Corsini[1], and N. Baddour[1], and J. H. Higbie[2], and B. Lester[3], P. Licht[4], and B. Patton[1], and M. Prouty[5], and D. Budker1, 6
Affiliations:
[1]Department of Physics, University of California, Berkeley, CA 94720-7300
[2]Bucknell university, 701 Moore Avenue, Lewisburg, PA 17837
[3]Department of Physics, California Institute of Technology, Pasadena, CA 91125
[4]UC Botanical Garden, University of California, Berkeley, CA 94720
[5]Geometrics Inc., 2190 Fortune Drive, San Jose, CA 95131
[6]Nuclear Science Division, Lawrence Berkeley National Laboratory, Berkeley CA 94720
pacs: 87.18-h, 87.63-d, 87.80-y, 87.85.fk
Keywords: biomagnetism, magnetophytography, atomic magnetometer, titan arum, corpse flower

---

[1] ‘Magnetophytography”, follows the custom in biomagnetism of forming the word from a Greek root and suffix -gram: “cardio’-’ from the Greek *kardio* (heart); “encephalo-” from the Greek *enképhalos* (brain); “neuro-” from the Greek *nuron* (nerve); then follows “phyto-” from the Greek *phuton*” (plant); the suffix, “-gram/graphy” is from the Greek *gramma* (indicating something recorded).

Abstract

In this chapter we report what we believe is the first experimental limit placed on plant biomagnetism. Measurements with a sensitive atomic magnetometer were performed on the Titan arum *(Amorphophallus titanum)* inflorescence, known for its fast bio-chemical processes while blooming. We find that the magnetic field from these processes, projected along the Earth's magnetic field, and measured at the surface of the plant, is $\lesssim 0.6\ \mu$G.

7.1 Introduction

With the advent of sensitive magnetometers, the detection of biological magnetic signals has added a new dimension to the understanding of physiological and biological processes by providing more information about the source of the associated electrical currents than surface electrodes[53, 54].

Biomagnetism was pioneered [122] in the 1960s. Baule and McAfee at Syracuse, New York, and Surguladze, in Moscow, made the first measurements of magnetocardiography (MCG) in 1963 and 1965 respectively. Magnetic fields from the heart, the result of cardiac action potential with electrical current densities that can reach approximately 100 Am^{-2} , are on the order of 1 μG, when measured at or near the skin surface.

The first measurements of magnetoencephalography (MEG), was made by D. Cohen at M.I.T., in a magnetically shielded environment with an induction coil (before the availability of the superconductor quantum interference detection [SQUID]). Cohen later improved the signal to noise using an improved magnetic shielded room and a SQUID (which had recently been developed by James Zimmerman [48]). Magnetic fields associated with human brain functions, are of the order of 1 nG. MEG has allowed a new understanding in the organization of neural systems underlying memory, language, and perception, as well as the diagnosis of related disorders[116].

The observation of the magnetic field from an isolated sciatic nerve of a frog, using a SQUID, was measured by Wiskswo and Freeman at Vanderbilt University in 1980 (Fig. 7.1). The magnetic field from a nerve impulse is of the order of 1nG.

Superconducting quantum interference device (SQUID) magnetometers have been leading the field of ultra-sensitive magnetic field measurements since the 1960s [48, 49]. The successful use of SQUIDS in early bio-magnetic measurements motivated their continued use in a variety of sensitive biomagnetic field measurements. To increase the signal to noise, improved mu-metal magnetic shields were found to be essential in early measurements; however later experiments returned to partial shielding and used an array of sensors to cancel the background magnetic field and gradients.

However, resonant magneto-optics and atomic magnetometry[42] have experienced a resurgence driven by technological developments, specifically by the advent of reliable,

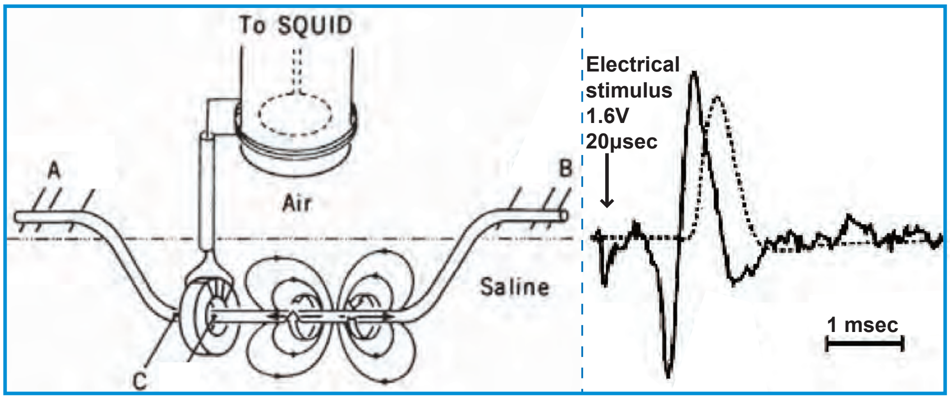

Figure 7.1: Magnetic field from an isolated frog sciatic nerve: first measurement made by Wiskswo and Freeman in 1980 [141]. Left: the nerve action potential propagates left to right. The magnetic and electric fields are shown as wide and narrow arrows around the nerve, respectively. The magnetic field is measured with the toroidal coil "C" connected to a transfer coil wound around the Dewar containing the superconducting quantum interference device (SQUID). Right: in this data the initial impulse is negative and is applied at location "A"; the magnetic field (solid line) and electric potential (dashed line), referenced to the saline bath, are measured at location "B".

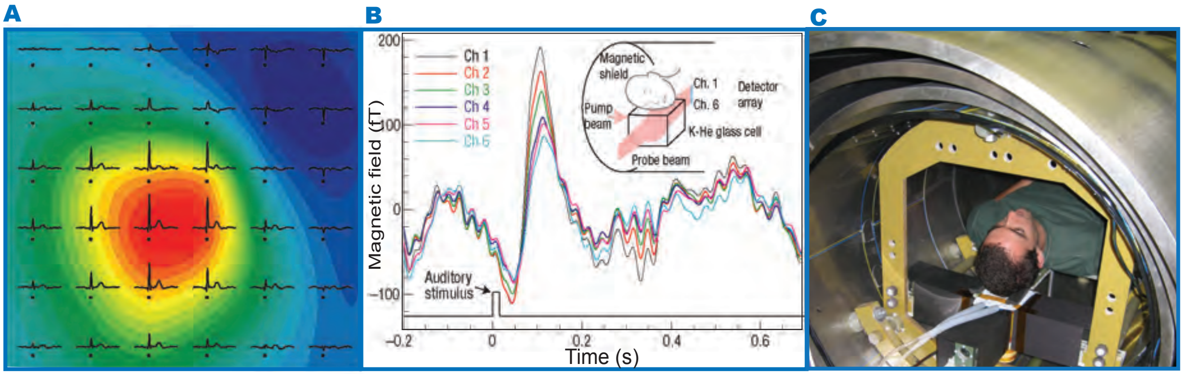

Figure 7.2: Examples of magnetocardiography (A) [30] and magnetoencephalography (B) [144] recorded with a sensitive atomic magnetometer. A: the normal component of the magnetic field of the heart beat was measured sequentially at 36 grid points 4 cm apart and averaged over 100 heartbeats. The color contour map represents the spatial distribution of the magnetic field at the time of the R-peak (strongest magnetic field). Cesium vapor cells at 30°C were used in the cardiomagnetometer. B: Potassium vapor cells at 180°C and the SERF regime were used in the encephalomagnetometer. A multichannel photodetector was used to simultaneously measure the magnetic field's spatial distribution. C: The magnetic shield used for the MEG measurement (Micah Ledbetter [when a graduate student at Princeton], was one of the human subjects in the experiment) [42].

inexpensive, and easily tunable diode lasers, and by refinements of the techniques for producing dense atomic vapors with long-lived polarized ground-states. These advances have enabled atomic magnetometers to achieve sensitivities rivaling, and in the 2000s, even surpassing that of the SQUID.

Atomic magnetometers have a dynamic range from near-zero field to Earth's magnetic field in a bandwidth from DC to several kHz [13, 83, 85], and in contrast to SQUIDs, which require cryogenic cooling and measure the relative magnetic flux through a pick-up loop, operate near room temperature and measure the absolute magnetic field directly by relating it to a frequency and to fundamental physical constants. Currently, the atomic magnetometer with the highest sensitivity is the spin-exchange relaxation-free (SERF) magnetometer, whose demonstrated sensitivity exceeded 10^{-11} G/$\sqrt{\text{Hz}}$ in 2010 (a world record)[59]. The projected sensitivity fundamental limits of SERF magnetometers is below 10^{-13} G/$\sqrt{\text{Hz}}$ [17, 94, 123, 38]. SERF magnetometers also offer the possibility of spatially resolved measurements with sub-millimeter resolution [133].

The advance in atomic magnetometers performance and their ease of operation has allowed them to be used to make biomagnetic measurements traditionally performed with SQUIDs. The first movie of the temporal dynamics of the human cardiomagnetic field map using an atomic magnetometer was made by A. Weis *et al* in 2003 [30] (Fig 7.2A). The first MEG measurement also using an atomic magnetometer was made by M. Romalis *et al*, at Princeton University in 2006 [42] (Fig. 7.2B).

In summary sensitive biomagnetic field measurements have enabled remarkable advances in magnetoencephalography, magnetoneurography, and magnetocardiography [52, 103, 30] and continue doing so. A natural extension in the rapidly progressing field of biomagnetism is the investigation of plant biomagnetism (Fig. 7.3).

To our knowledge, no one has yet detected a magnetic field from a plant, a fact which motivated this work. Biochemical processes, in the form of ionic flows and time varying ionic distributions, generate electrical currents and time-varying electric fields, both of which produce a magnetic field. However, in contrast to muscle contraction and brain processes, which have a characteristic time scale shorter than one second, plant bioprocesses span several minutes to several days and the expected magnetic field from such processes is correspondingly smaller. Detection of such small magnetic fields, together with the difficulty of providing the cryogenic support required for SQUIDS, make a sensitive atomic magnetometer the preferred choice.

Cultivation of the plant has allowed botanists to study the Titan Arum and its uncommon transformation during the rare blooming years. One of the three most notable characteristics is its size; the tallest recorded bloom occurred at the Stuttgart Zoological and Botanic Garden, Germany, in 2005, and was measured at 2.94m (nine feet, six inches).

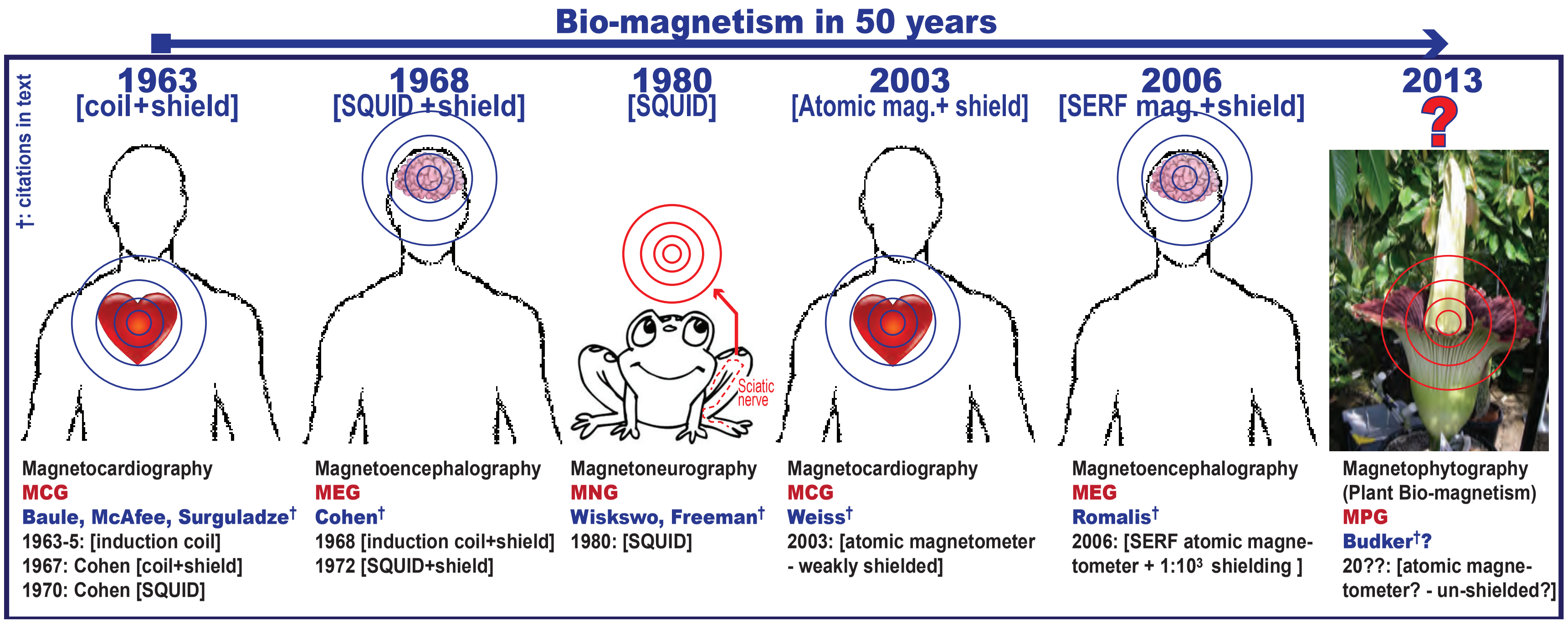

Figure 7.3: Bio-magnetism, 1963-present, a 50-year evolution, (see also figures 7.1 & 7.2). The detection of magnetic fields from bio-processes has become an integral and essential part of medicine. SQUIDs and magnetic shielding have been at the root of the rapid progress made in bio-magnetism. The recent advances ion atomic magnetometry promise a comparable sensitivity without the costly and bulky cryogenic infrastructure.

Figure 7.4: The titan arum (or *Amorphophallus titanum*), nicknamed ‘Trudy’, in full bloom on June 23, 2009, at the University of California Botanical Garden. The Geometrics G858 magnetometer sensors are visible behind the plant on the left [Photograph: E Corsini]

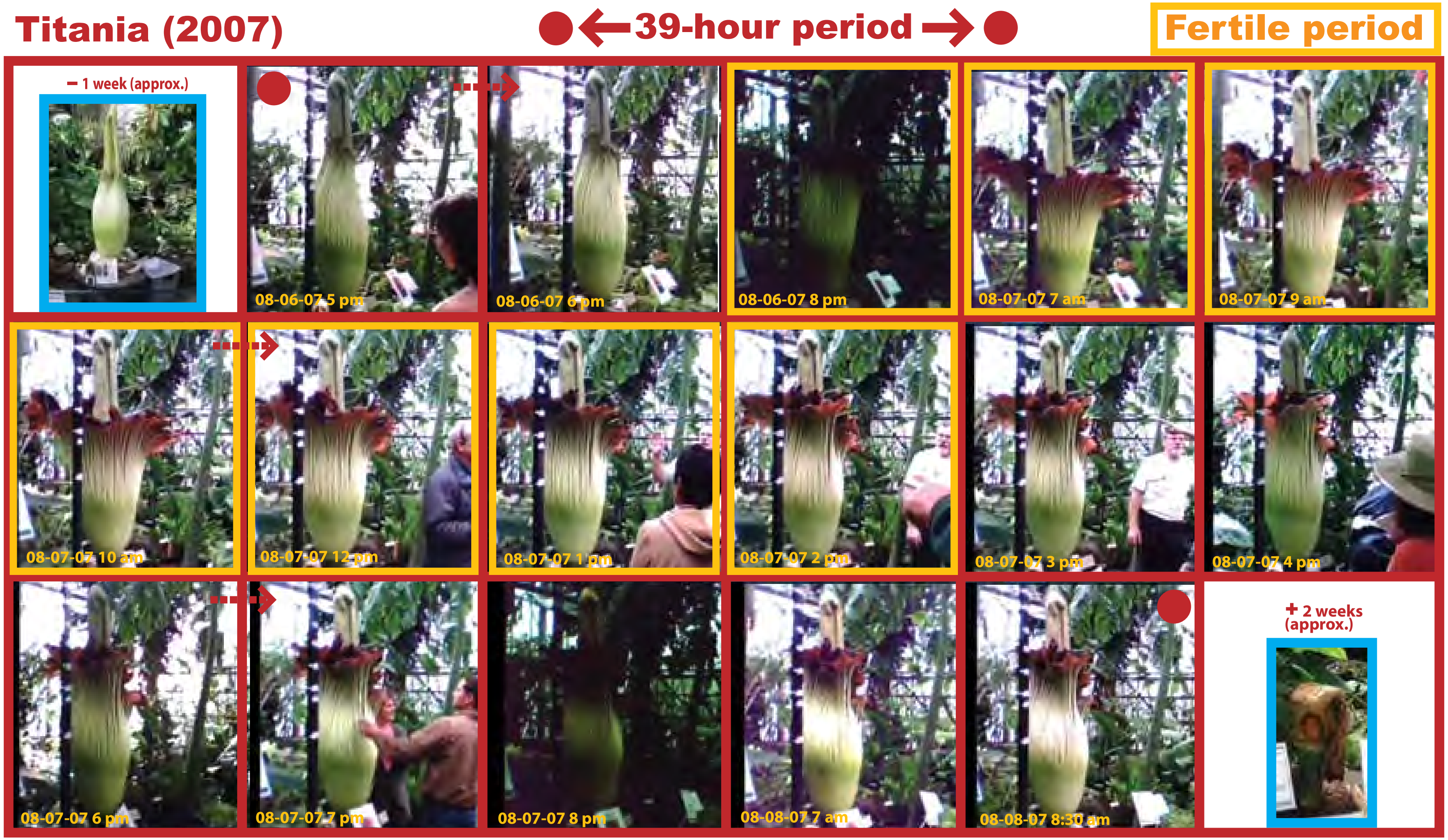

Figure 7.5: The titan arum's blooming cycle and fertile period. The representative time sequence was photographed with a flower nicknamed "Titania", at the U.C. Botanical Garden, in the summer of 2007. The opening and the closing of the spathe (on Aug. 6th at ~8:PM, and Aug 7th at ~2pm, respectively) mark the beginning and the end of the fertile cycle. The spathe then withers and the fertilized florets become seed-bearing fruit. [Photographs: E Corsini, J. Higbie]

The next unusual characteristic is the bloom's distinctive stench of cadaverine and putrescine, lasting up to twelve hours after it fully opens, which has given it the name *bunga bangkai* ("corpse-flower") in Indonesian [92]. The smell combined with the spathe's dark purple coloration lure in carrion-eating beetles and flesh-flies that are the putative pollinators.

To mitigate these challenges we turned to a family of plants that exhibit fast bio-processes and thermogenic characteristics while blooming [131]. We selected the Titan Arum, or *Amorphophallus titanum*, which is a tuberous plant with the largest known un-branched inflorescence in the world. The inflorescence's single flowers ($\sim$ 500 female and $\sim$ 500 male), located at the base of the spadix and enrobed in the spathe, together function as a single plant and flower. It is indigenous only to the Indonesian tropical forests of Sumatra, and grows at the edges of rainforests near open grasslands. The tuber weighs up to 150 lbs, and grows into a single leaf up to 20 feet tall during the vegetative years. Reproduction (flowering) may occur every few years after the plant has matured for six years or more [35].

The third striking feature is the rise and thermoregulation of the spadix temperature, which can reach up to 30°C above ambient temperature in intervals lasting about 30 minutes over the plant's 12-hour long fertile cycle (Fig. 7.5) [26]. The heat stimulates the activity of pollinator insects and helps disseminate the scent [8, 131]. The Titan Arum's characteristics, including large size and fast biochemical processes, and the availability of a specimen nearing its blooming phase at the University of California Botanical Garden at Berkeley, CA, made it an attractive candidate for this investigation.

7.2 Order of magnitude estimate of expected bio-magnetism

On a weight-specific basis, plant thermogenesis approaches the rate of heat production exhibited by flying birds and insects; it originates from a large intake of oxygen entering the florets by diffusion [131, 132]. The Titan Arum has distinct thermal zones extending $\gtrsim 1$ m upwards from the florets located at the spadix base. To estimate a possible scale of the plant bio-magnetism, we hypothesize a favorable-case scenario (from the point of view of generation of a magnetic field), modeled by a bi-directional ionic transport of oxidation/reduction chemical reactants. We approximate this ionic transport by two long parallel wires located at the core of the spadix and separated by a distance $d = 10\ \mu$m (a characteristic plant cell size).

The work required to raise the temperature of a characteristic mass $m = 1$ kg of plant material (mostly water) by $\Delta T \approx 10$°C above the ambient environment is:

$$W = \Delta T m c \simeq 42 \text{ kJ}, \tag{7.1}$$

where $c = 4.2$ kJ/kg is the specific heat of water. In a characteristic thermogenic time interval of $t \sim 30$ min this corresponds to a power of:

$$P = \frac{W}{t} \approx 20 \text{ W}, \tag{7.2}$$

which is commensurate with the calorimetry measurements performed with other thermogenic plants [130].

Assuming 1 eV per oxidation event [125], the magnetic field induced by the bi-directional currents at the nearest gradiometer sensor, positioned at a distance D = 20 cm from the plant core, is:

$$B \propto \frac{Pd}{D^2}, \tag{7.3}$$

which leads to an expected magnetic field magnitude on the order of 30 μG.

The magnetic field variations due to bio-magnetic processes are expected to occur on a time scale ranging from 15 to 30 minutes; the output of the magnetometer can therefore be averaged over one minute intervals. This would give a sensitivity better than 100 nG per point using the atomic magnetometer (described in section 7.3), which is more than sufficient to resolve the magnetic field in this scenario.

7.3 Experimental set up and environment

The plant chosen for the experiment, nicknamed "Trudy" (Fig. 7.4), was blooming for the second time at fourteen years of age, had reached a peak height of ∼ 2 m, and was kept in a heated greenhouse approximately $8 \times 8 \times 8$ m^3 in size. The experimental environment includes four main types of magnetic-field noise, each one being on a different time scale. The San Francisco Bay Area Rapid Transit electric-train system (BART) causes fluctuations in the magnetic field on the order of 0.5 mG on a time scale ranging from a fraction of a second to a minute; those fluctuations are absent from ∼1 AM to 5 AM when BART suspends operation. Visitors, during the garden opening hours (9 AM - 5 PM), cause magnetic field fluctuations on a several second to a minute time scale. Sudden displacement of the plant pot and/or the magnetic sensors add stepwise changes in the magnetic field and gradients. Another intermittent magnetic field noise is caused by the greenhouse temperature regulation mechanism which includes two electric heaters and two large fans located near the ceiling of the greenhouse; a thermostat turns on the heaters and fans every 15 to 30 minutes maintaining a temperature ranging from 25°C to 30°C throughout the greenhouse. This causes corresponding sudden spikes and stepwise magnetic field and gradient variations.

The experimental setup is shown in Fig. 7.6. A commercial G858 Geometrics cesium atomic magnetometer/gradiometer was selected for the experiment. The G858 is a scalar (as opposed to a vector) sensor, and measures the projection of the magnetic field onto the prevailing field axis[115, 2]. The G858 has a sensitivity of 100 nG (at 1 second cycle rate), a temperature dependence of 500nG/C°[6], and an operating principle derived from the techniques pioneered by Bell and Bloom [31, 28].

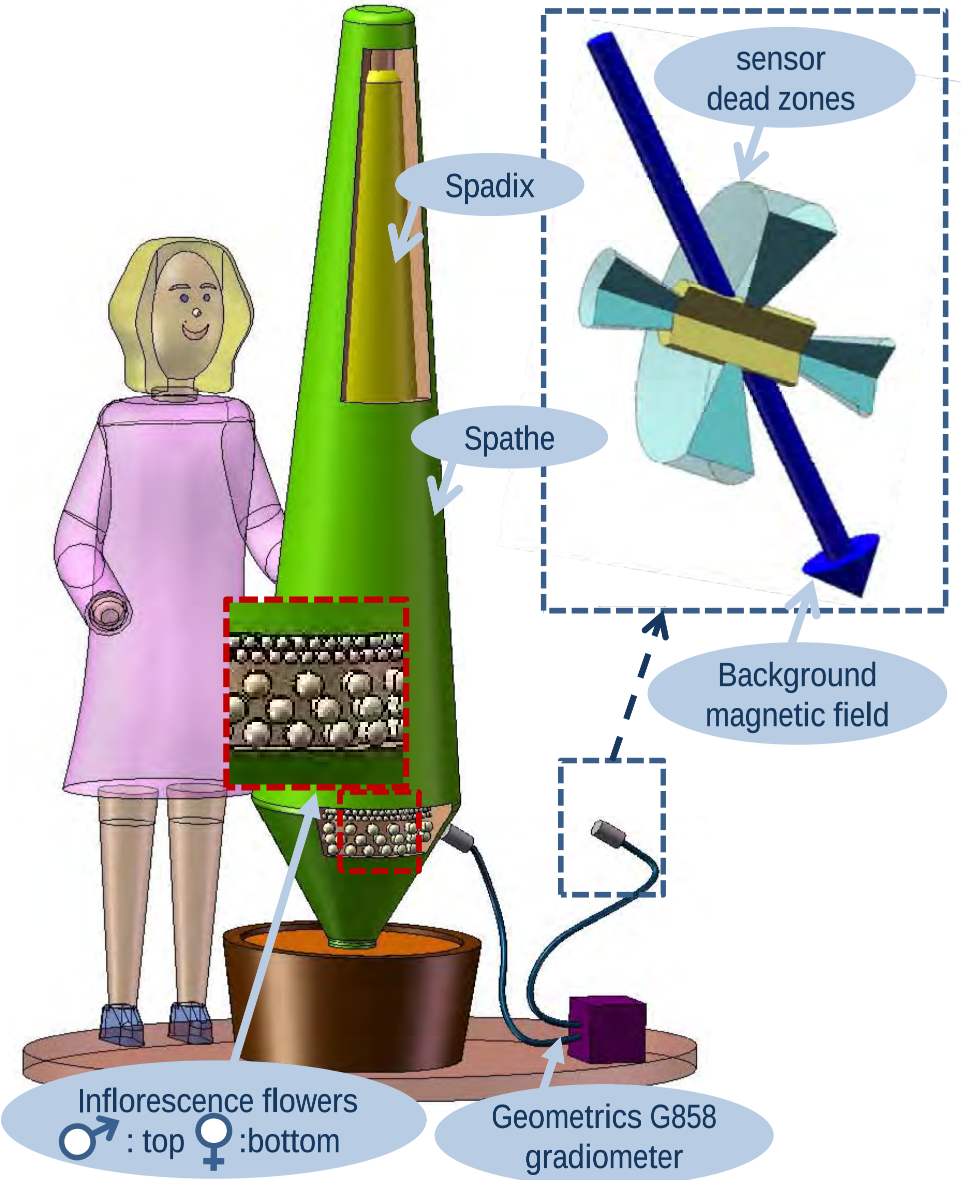

Figure 7.6: Experimental setup: The Geometrics G858 atomic gradiometer is positioned with one sensor near the spathe where pollination occurs. The other sensor is used to subtract the ambient magnetic field noise. [Insert: Each sensor's dead sensing zones (light blue) lie within 30° of the sensor's axis and within 30° of the plane perpendicular to it. The downward pointing arrow indicates the direction of the ambient magnetic field.] The sensor axes are parallel and $\sim 45°$ to the ambient magnetic field, which is inclined $\sim 60°$ to the vertical and commensurate to the local Earth magnetic field [4]. [3D drawing: E Corsini]

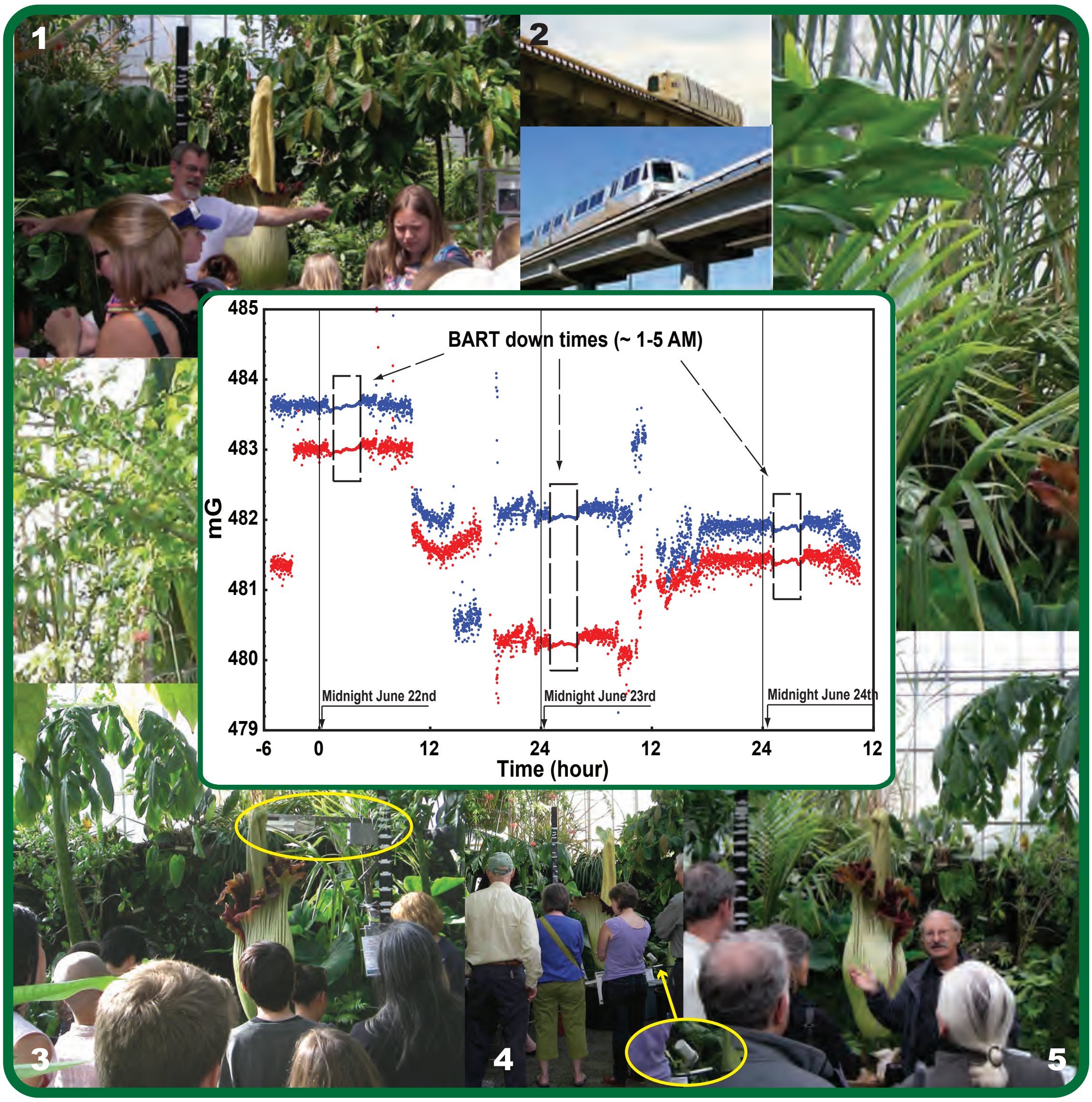

Figure 7.7: Center/Plot: data from the two magnetometer channels spanning three days. The local Earth magnetic field is ∼500 mG. The three rectangular boxes indicate the magnetically quiet periods when the BART operations are suspended from ∼1-5 AM. Discontinuities in the data correspond to shifting of the plant and/or the magnetometer sensor heads. Large magnetic-field fluctuations are seen during the U.C. Botanical Garden open hours (9 AM - 5 PM). The difference between the two magnetometer channels depends on their position relative to the ambient magnetic field gradients. (1,3,4,5): public showings and the BART electric train (2) contribute to the daytime fluctuations and discontinuities in the magnetic field recorded by the G858 Geometrics magnetometer sensors. Oval insert in 4: the Geometrics sensor which serves to subtract the ambient Earth's magnetic field. 3: photograph from an earlier attempt (Aug 2007) at measuring plant bio-magnetism, with a pair of GMR (giant magneto-resistance) three-axis magnetic sensors (Honeywell HMC2003), in another Titan arum nicknamed "Titania", housed in the same tropical-house at the UC Berkeley Botanical Garden. 4-oval: GMR sensors positioned next to the tip of the spadix - GMR electronics are to the right enclosed in a grey bud-box. 3 - upper left: the Titan arum blooms every 5-10 years; on the off-years it grows into a leaf up to 20 feet in height. 5: Paul Licht, UC Berkeley Botanical Garden Director delivering a mini-lecture on the Titan arum. [Data/project management: E. Corsini - Collaboration: V. Acosta, N. Baddour, J. Higbie, B. Lester, P. Licht, B. Patton, M. Prouty - Photographs: E. Corsini - PI: D. Budker].

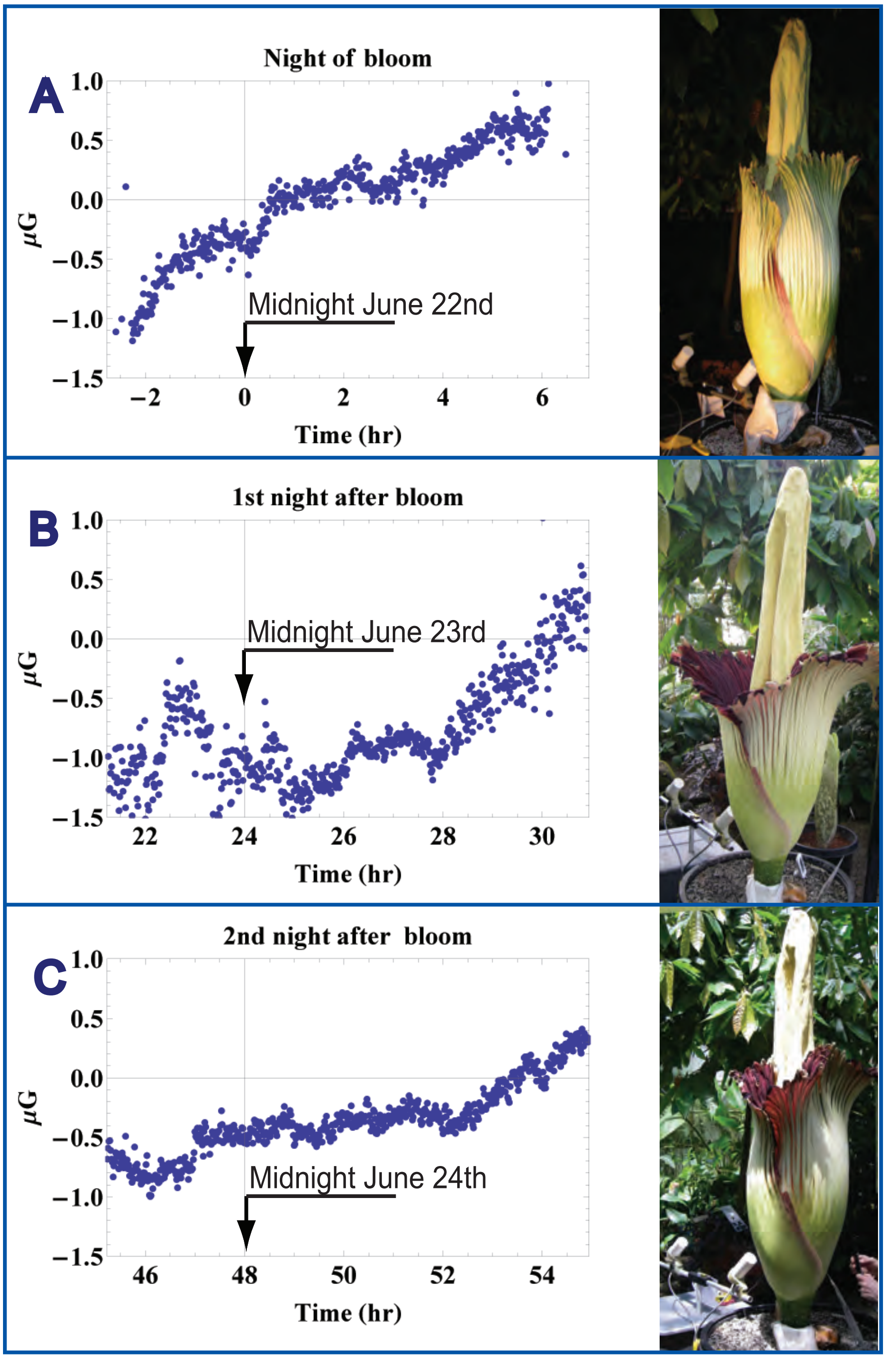

Figure 7.8: Gradiometer signal (difference magnetic field). (A): 9 hr segment: night of bloom. (B&C): for comparison, same 9 hr segments on the following two nights. To the right: photographs showing the development of the bloom; (A): night of bloom/taken at ~9:30pm, within ~1 hour of the beginning of the bloom; (B,C): representative day-time photographs. Data averaged over one minute intervals. We attribute the overall magnetic field increase to a gradual change in temperature and corresponding residual temperature dependence of the sensor (0.5 μG/°C). The time scale of that drift is significantly longer then the time scale we expect from the plant biomagnetic activity. On each of the three nights, the magnetic field noise at 1 mHz, in a 0.5 mHz bandwidth (corresponding to events lasting ~10-30 min), is $\approx$ 0.6 $\mu\mathrm{G}_{\mathrm{rms}}$. [Data/analysis/project management: E. Corsini - Collaboration: V. Acosta, N. Baddour, J. Higbie, B. Lester, P. Licht, B. Patton, M. Prouty - Photographs: E. Corsini - PI: D. Budker].

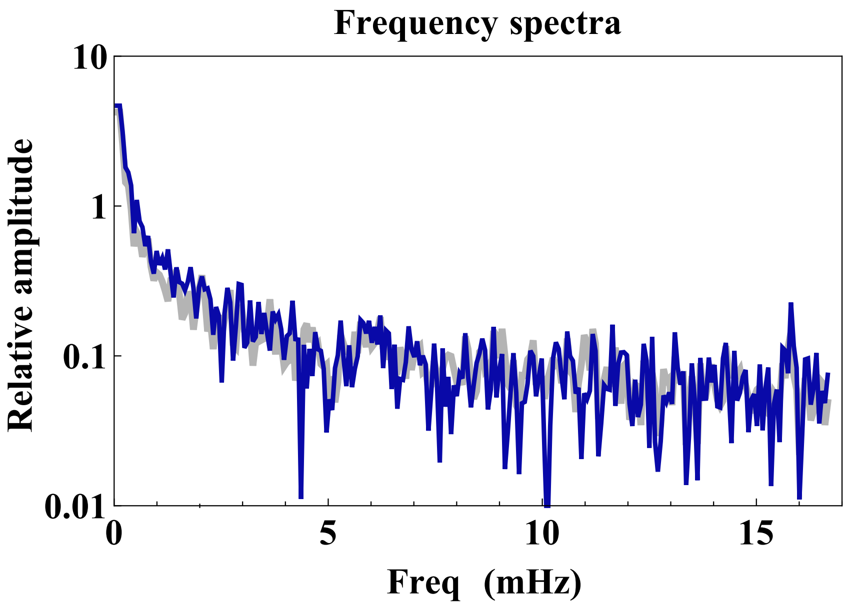

Figure 7.9: (Frequency spectra of data shown in Fig. 7.8. Dark (blue): night of bloom (Fig. 4A). Light (gray): average of subsequent two nights (Figs. B-C). A biomagnetic event of a magnitude larger than 0.6 μG and lasting 10-30 minutes would appear as a feature between 0.5 and 1.5 mHz rising above the overall 1/f noise. [Data/Analysis/project management: E. Corsini - Collaboration: V. Acosta, N. Baddour, J. Higbie, B. Lester, P. Licht, B. Patton, M. Prouty - PI: D. Budker]

One sensor was positioned $\sim$ 5 cm from the spathe near the location where pollination and thermogenesis occur and where we speculate the plant bio-magnetic activity may be strongest. The other sensor was positioned $\sim$ 0.5 m from the plant, served to subtract the ambient magnetic field.

A static magnetic field gradient throughout the greenhouse was measured to be approximately 10 μG/cm and added a constant offset between the outputs of the two magnetometer sensors, which depended on the positioning of the sensors in relation to the gradient direction. The sensor axes were aligned to have the ambient magnetic field direction fall outside the magnetometer dead zones (which lie within 30 degrees of the sensor axis and within 30 degrees of the plane perpendicular to it).

7.4 Results

Figure 7.7 shows the outputs from the two gradiometer channels. Data were collected over a period of three consecutive days starting on the evening of June 22, 2009. We visually observed the anthesis (beginning of the blooming phase) at approximately 9 PM on the night of June 22. Midnight on that night is zero on the time axis. Discontinuities in the data were caused by inadvertent moving of the pot and/or the sensors. The gaps in the data occurred during data downloading and apparatus maintenance. The BART-free time periods ($\sim$1 - 5 AM) are clearly visible as relatively magnetically quiet periods on each of the two magnetometer channels. Large magnetic field fluctuations are also visible during the Garden open hours (9 AM - 5 PM). Figure 7.8 shows the difference magnetic field, as measured by the two sensors. Three segments of data are shown, from 9 PM to 6 AM, on three consecutive nights, starting on the night of the bloom. The power spectrum of the first segment is shown in Fig. 7.9. The amplitude of the magnetic field noise at 1 mHz in a 0.5 mHz bandwidth (frequency range equivalent for events lasting from 10 to 30 minutes) is 0.6 μG, and was similar for all three nocturnal time segments.

7.5 Discussion, simulation, conclusion, and outlook

The above result sets an upper bound of 0.6 μG on the amplitude of bio-magnetism from the plant while blooming, projected onto the ambient magnetic field direction, for events in the 10 to 30-minute cycle range ($\sim$1 mHz), and at a distance of $\sim$ 5 cm from the surface of the spathe. Within the framework of the simple model of section 7.2, this is significantly lower than the expected magnetic field. However the plant bi-directional ionic currents in the model may instead be distributed in a more complex geometry than the two parallel wire model used in this analysis and with correspondingly more magnetic field cancelation. In a limiting case, there is no net magnetic field if the ionic flow is modeled by a core current enclosed by a cylindrically distributed, opposite, and counter-propagating current. The Titan Arum spadix does not have perfect cylindrical symmetry and one may expect a departure from total cancelation of the magnetic field.
To visualize a 10 to 30-minute magnetic field event we added a simulated 15-minute (FWHM), Gaussian-shaped, 1-μG fluctuation to the data recorded during the night of the bloom. Figures 7.10 & 7.11 & 7.12 in the appendix show the data in 70-min slices with 50% overlap in the time domain (left) and in the frequency domain (right).

To further investigate plant biomagnetism, greater magnetic field detection sensitivity is necessary. Several options are possible: using an array of micro sensors to better locate and resolve the source of the magnetic field and to more effectively subtract the fluctuations and drift of the ambient magnetic field and its gradients; moving to a more isolated environment that is removed from public access and electrical devices, magnetically shielding the plant to eliminate the fluctuations of the magnetic field and gradients, and/or selecting a smaller plant with fast bio-processes like the Sensitive Plant *(Mimosa pudica)* or the Sacred Lotus *(Nelumbo nucifera)*. A smaller plant size would facilitate the complete coverage of the thermogenic zones. Concurrently measuring the spatial distribution and the variations of the plant temperature with an infrared camera and correlating that measurement to the magnetic field measurement would correspondingly yield a better sensitivity.

7.6 Acknowledgments

In this chapter we acknowledge the University of California Botanical Garden staff, in particularly we thank Paul Licht, the director, who generously granted us access and after-hours access to the garden facilities; We also acknowledge stimulating discussions with Robert Dudley from the department of Integrative Biology, with Lewis Feldman, Steve Ruzin, and Peggy Lemaux from the department of Plant and Microbial Biology, and with Philip Stark from the Department of Statistics, at University of California, Berkeley. Invigorating exchanges with our colleague Todor Karaulanov helped the understanding of the processes at hand. This project was funded by an ONR MURI fund and by the U.S. Department of Energy through the LBNL Nuclear Science Division (Contract No. DE-AC03-76SF00098).

7.7 Appendix to Chapter 7

A simulated 15-minute, 1 μG magnetic field signal is added to the magnetic field data (9 hour segment) on the night of the bloom (Fig. 7.8A). The data in the 9 hour segment (with the added 1 μG signal) are divided into 70-minute time-windows with 50% overlap; the Fourier transform is computed for each time window. The sequence of time-windows data and Fourier transform are shown in Figs 7.10, 7.11, & 7.12 & 7.13. For more sensitive measurements increased magnetic field noise cancelation, with additional sensor heads, will be needed.

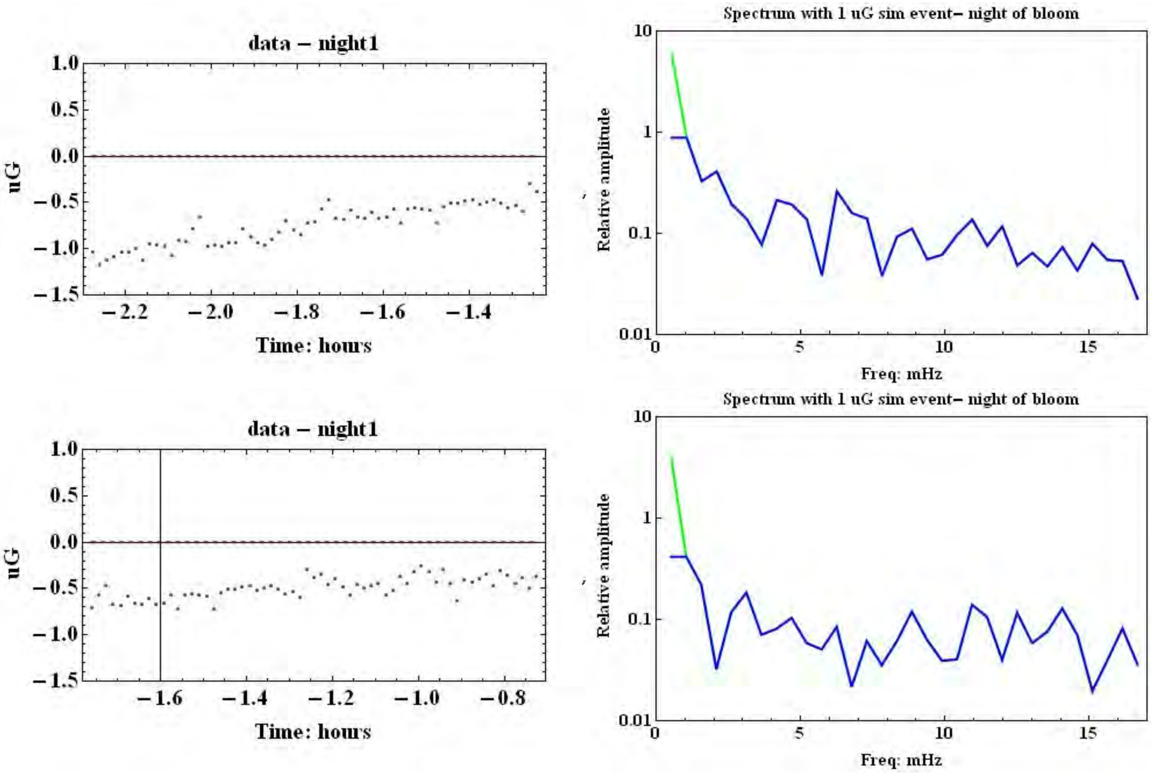

Figure 7.10: Part 1/4 - Simulated 15 min long (FWHM), 1 μG, Gaussian-shaped, magnetic fluctuation (red dotted line) added to the 9 hour-long data recorded during the night of the bloom (blue dotted line). The green dotted line is the sum data. Left: data in 70 min consecutive time slices with 50% overlap. Right: time slice's Fourier transform of the 70 min data (same color scheme). The 15-min 1-μG event rises above the $1/f$ noise between 0 and 5 mHz. [Simulation/project management: E. Corsini - Collaboration: V. Acosta, N. Baddour, J. Higbie, B. Lester, P. Licht, B. Patton, M. Prouty - PI: D. Budker].

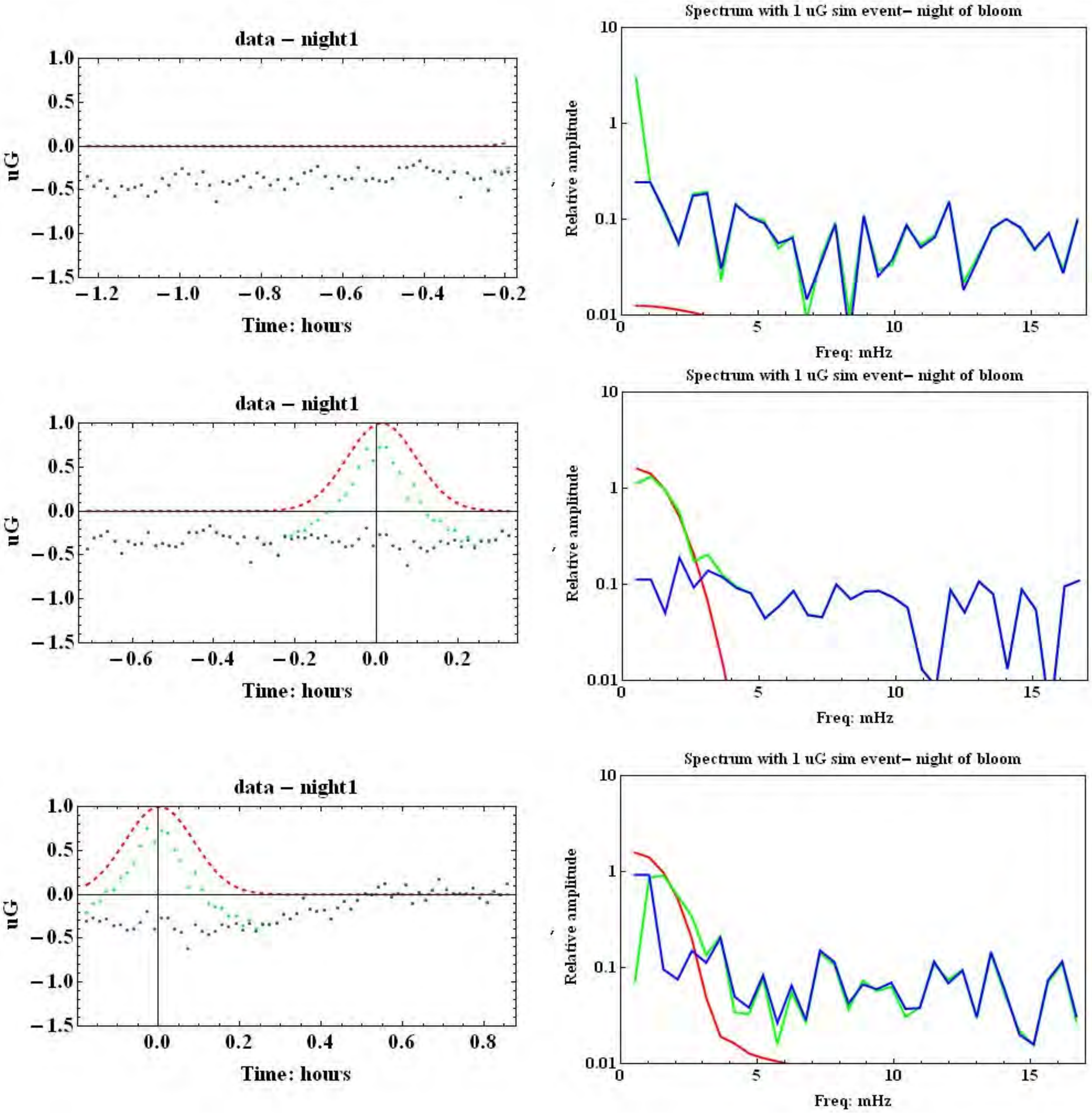

Figure 7.11: Part 2/4 - Continuation of figure 7.10

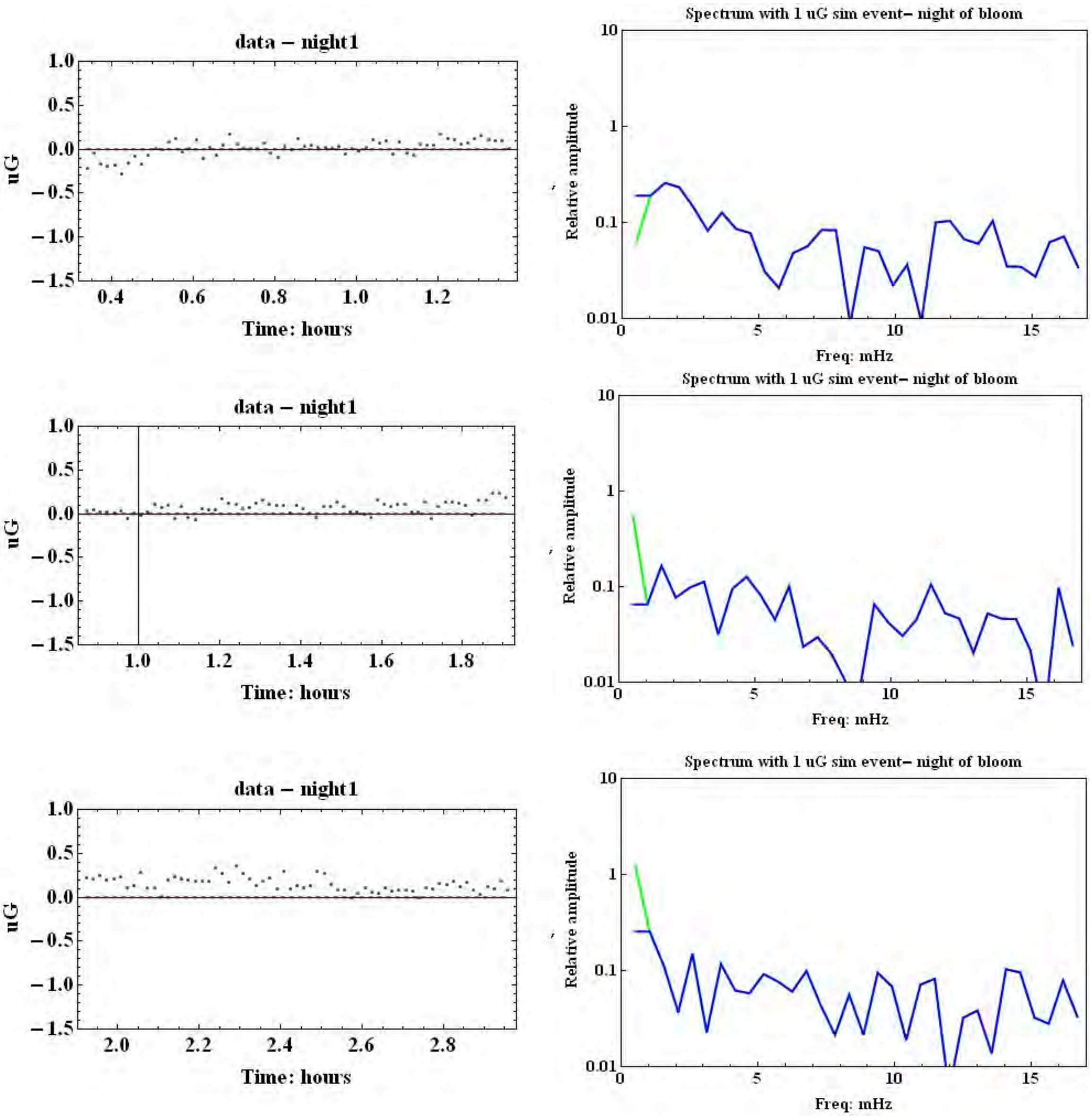

Figure 7.12: Part 3/4 - Continuation of figure 7.11

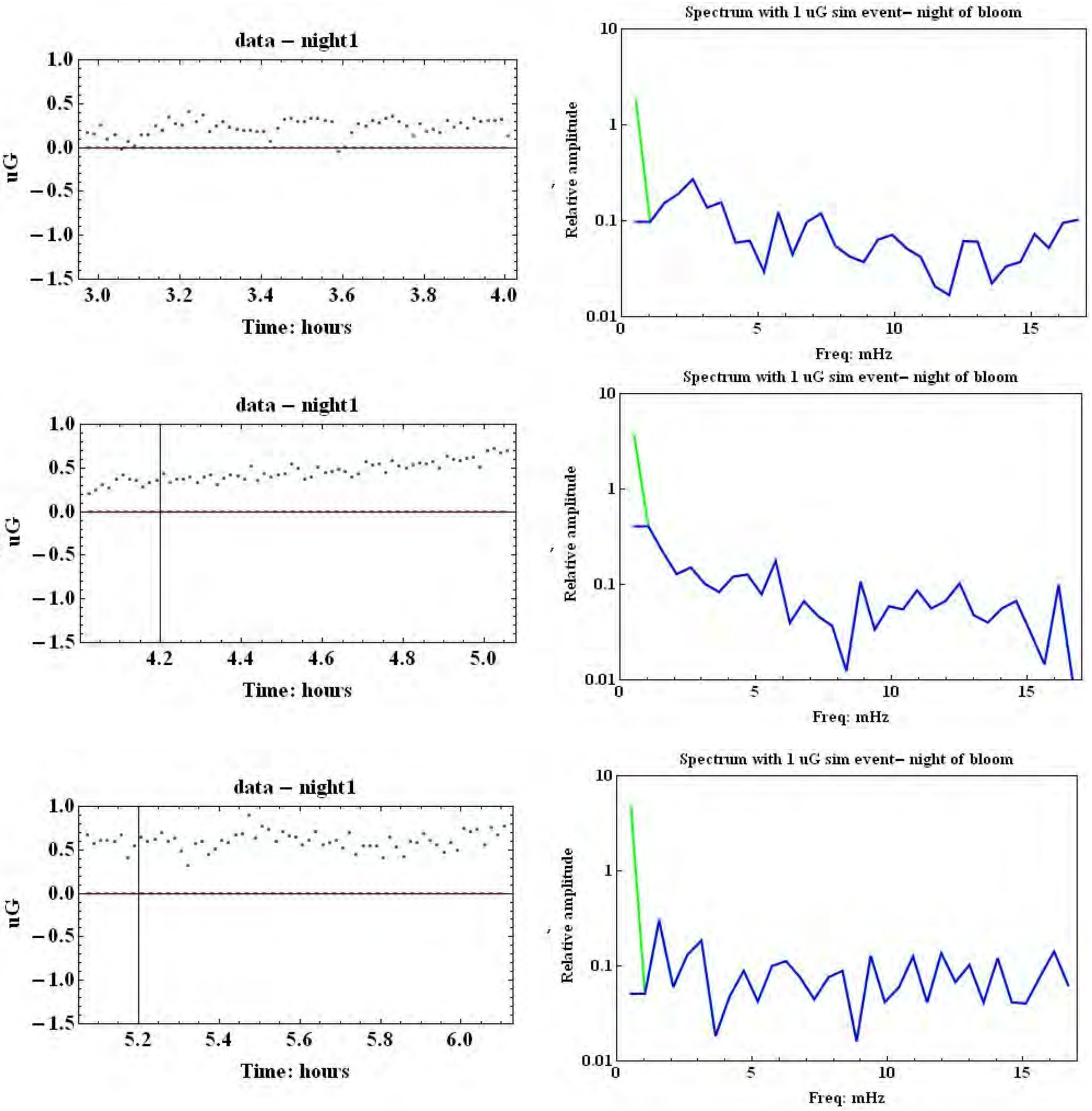

Figure 7.13: Part 4/4 - Continuation of figure 7.12

Conclusion

This work briefly described the origin of atomic magnetometry, and showed that it probes (in energy equivalent units) temperatures (or energies) eight orders of magnitude colder than the current largest Hadron Collider is hot.

We showed that the coupling of the electron's Zeeman energy sublevels to the external magnetic field, and optical pumping, are the basis of atomic magnetometry (nonlinear Faraday effect). We showed the sharp contrast of the Faraday linear and nonlinear effects with laser-cooled atoms.

We presented an application of atomic magnetometry with a self-oscillating all-optical configuration with direct applications to sensitive field measurements. We showed the design and construction of a field-able optical multi-configurable-platform to test the configuration. Preliminary field measurements revealed the challenges and multi-facets of Earth's field atomic magnetometry, confirmed the high bandwidth of the all-optical self-oscillation magnetometer scheme, and underlined the necessity of having a field-able, stable, and versatile platform to investigate geomagnetism in the field.

We then realized a laboratory-based multi-functional magnetometer platform to investigate, in a well-controlled and magnetically shielded environment, optimization techniques and systematics pertaining to configurations probing non-zero magnetic fields, and in particular the geomagnetic range. We presented preliminary measurements giving further indications of the many facets and challenges of Earth's field magnetometry. In particular these measurements showed the self-oscillation magnetometer configuration as a diagnostic tool. The measurements confirmed the necessity of having a versatile and multi- and rapid- re-configurable platform to effectively probe and investigate the large optimization-parameter space of magnetometry from zero to geomagnetic range and beyond.

We then turned to the very specific investigation of anti-relaxation coatings, a key component in atomic magnetometers. We investigated the surface property of an alkene-based coating, which had recently shown two orders of magnitude improvements in the Zeeman relaxation rate, as compared to paraffin coatings. Promising small hyperfine frequency shift with applications to atomic clocks further motivated our investigation; however the measurements revealed that the alkene cell-wall dwelling time was similar to the paraffin coatings. However we noted that, within several alkene coated cells, the Zeeman relaxation rate had a linear dependence on the cell-wall dwelling time, bringing new insight as to the surface science pertaining to anti-relaxation coatings.

Finally we reported an application of sensitive atomic magnetometry to the domain of plant biomagnetism, including the keen response from broad and scientific audiences. That response (exemplified in Fig. 8.14) shows an on-going urge and drive to measure what our senses cannot. It is a drive that goes back through the ages, and is exemplified by the manufacture, approximately 150 years ago, of an array of magnetometers to make synchronous magnetic field measurements at different locations throughout Europe. One of these magnetometers is preserved in the museum at the Collegium Maius in Kraków (Fig. 8.15).

To close, the realm of atomic magnetometry's applications extends far and wide; it ranges from sensitive magnetic field measurements of bio-processes, to probing new physics at very low energy (the dual of the same new physics probed at high energy). This range of applications places atomic magnetometry (with room-temperature alkali vapor cells and with laser-cooled atoms) at the leading edge of today's research.

theberkeleyan
THIS WEEK ON CAMPUS

April 12, 2011

Great news for baseball Bears
Cal baseball is here to stay, after all, thanks to donors who pledged some $9 million to spare the team from the budget ax. "Our supporters stuck with us and wouldn't take no for an answer," said coach David Esquer, who surprised his players with the news Friday at a Tucson hotel.
Read the full article...

Bridging Berkeley's budget gap
Chancellor Birgeneau recently unveiled a strategy to balance the campus's books "by utilizing all of the resources at our disposal." John Wilton, Berkeley's new vice chancellor for administration and finance, explains how administrators plan to meet the latest round of financial challenges in 2011-12.
Read the full article...

Magnetic fields of dreams?
Berkeley physicists, using some of the most sensitive detectors available, hope to close "an obvious gap in science" by sniffing out minuscule magnetic fields they suspect might be produced by plants. Their first efforts failed. But they're not giving up.
Read the full article...

CAMPUS NEWS

Countdown to Cal Day
Explore Cal on Saturday with some 40,000 friends and 300 events.

Construction work at Memorial Stadium gains ground
More progress, less noise. Photo gallery.

Gates, Hewlett grant for online ed
Foundations pledge $748,000 for UC pilot project in online instruction.

New Chevron achievement award
Oil giant teams with CAA to promote science, tech, engineering and math.

PEOPLE

Astronomer's Guggenheim
Prestigious fellowship goes to Professor Martin White.

Biologist wins two campus awards
Britt Glaunsinger recognized for outstanding contributions in research, teaching, service.

RESEARCH

Big boost for sun power
Energy Dept. gives $25 million to group led by Berkeley and Stanford.

Berkeley physicist turns up 'surprising' climate-change data
ScienceInsider Q&A with Richard Muller.

Steering away from danger
New site lets users find info on California's 130,000 major car crashes from 2000-2008.

Latino pre-school enrollment down
Recession-related reversal has implications for nation's workforce, researchers say.

STUDENT LIFE

Learning to love gamelan
Class in Indonesian ensemble is one of the music department's most popular courses.

BREAKING NEWS
NewsCenter.berkeley.edu

CAMPUS CALENDAR
Events.berkeley.edu

News tips or feedback? Please contact us at e-news@berkeley.edu

Managers & supervisors: *Please print and post a copy of this newsletter for any staff who don't have access to email.*

Figure 8.14: Sensing magnetic fields, inaccessible to our senses, remains at the forefront of common interest. In the Berkeleyan U.C. Berkeley campus newspaper, gauging by the order of the listing, our report of 2011 on the magnetic field upper bound of plant biomagnetism [(C) - Ch. 7], ranks equal to Cal Berkeley's legendary sports program (A), to the university budget crisis (B), and ahead of the controversial topic of "global warming" (D).

Figure 8.15: From Jagiellońska street (lower-left), entering the courtyard of the Collegium Maius (top), one of the original buildings of Uniwersytet Jagielloński [(UJ) - founded in 1364 - one of the oldest universities in Europe], past painful memories embedded in the varnish of the Aula Bobrzańskiego wooden seats (mid-left), though an ancient door (mid-right), up a flight of stairs, behind glass doors (lower-right), is preserved a magnetometer (lower-center) dating back to 1874. It is one of several that formed an array deployed throughout Europe to make synchronous magnetic field measurements. [The label reads: Magnetomtr M. Meyerstein, Gettinga, około, 1874] [Photographs: E. Corsini]

Bibliography

[1] 2010 CODATA Recommended Values of the Fundamental Physical Constants.
url: fhttp://physics.nist.gov/constants.

[2] Cesium Optically pumped magnetometers, Basic Theory of Operation.
url: ftp://geom.geometrics.com/pub/mag/Literature/M-TR91.pdf.

[3] Delrin low wear low friction.
url: plastics.dupont.com/plastics/pdflit/europe/delrin/DELLWLFe.pdf.

[4] Estimated Value of Magnetic Declination.
url: http://www.ngdc.noaa.gov/ geomagmodels/Declination.jsp.

[5] Gem Systems - Supergrad gradiometers.
url: http://www.gemsys.ca/prod_supergrad.htm.

[6] Geometrics - G-858 magMapper.
url: http://www.geometrics.com/geometrics-products
/geometrics-magnetometers/g-858-magmapper/.

[7] Geometrics - Magnetometer datasheets.
url: http://www.geometrics.com/geometrics-products
/geometrics-magnetometers/magnetometer-datasheets/.

[8] Inflorescence Terminology.
url: http://waynesword.palomar.edu/terminf1.htm.

[9] Magnetic Plants - Are plants magnetic?
Scientists at the University of Berkeley have recently tried to find out.
url: http://www.physicscentral.com/explore/multimedia/podcast.cfm?uid=20110505050957.

[10] Roithner Laser-Technik Vienna, Austria.
url: http://www.roithner-laser.com/.

[11] Rubidium 87 D Line Data.
url: http://steck.us/alkalidata (revision 2.0.1, 2 May 2008).

[12] Ulm Photonics, Ulm, Germany.
url: http://www.ulm-photonics.de/.

[13] V. Acosta, M. P. Ledbetter, S. M. Rochester, D. Budker, D. F. J. Kimball, D. C. Hovde, W. Gawlik, S. Pustelny, J. Zachorowski, and V. V. Yashchuk. Nonlinear magneto-optical rotation with frequency-modulated light in the geophysical field range. *Phys. Rev. A*, 73(5):53404–1–8, 2006.

[14] Wojciechowski Adam. *Adam Wojciechowski - doctoral Thesis.* PhD thesis, Jagiellonian University, 2011.

[15] C. Affolderbach, A. Nagel, S. Knappe, D. Jung, C. Wiedenmann, and R. Wynands. Nonlinear spectroscopy with a vertical-cavity surface-emitting laser (VCSEL). *App. Phys. B*, 70:407–413, 2000.

[16] E. B. Alexandrov, M. V. Balabas, D. Budker, D. S. English, D. F. Kimball, C.-H. Li, and V. V. Yashchuk. Light-induced desorption of alkali atoms from paraffin coating. *Phys. Rev. A*, 66:042903, 2002.

[17] J.C. Allred, R.N. Lyman, T.W. Kornack, and M.V. Romalis. High-sensitivity atomic magnetometer unaffected by spin-exchange relaxation. *Phys. Rev. Lett.*, 89, 2002.

[18] J. M. Amini and H. Gould. High Precision Measurement of the Static Dipole Polarizability of Cesium. *Physical Review Letters*, 91(15):153001, October 2003.

[19] E. Arimondo. *Progress in Optics, edited by E. Wolf*, volume 35. Elsevier, Amsterdam, 1996.

[20] E. Arimondo and P. Inguscio, M. Violino. Experimental determinations of the hyperfine structure in the alkali atoms. *Rev. Mod. Phys.*, 49, 1977.

[21] M. V. Balabas. *Physical Bases for Reception of Anti-relaxationCoatings and Study of Antirelaxation Coatings Surfaces and the Nature of it's Interaction with Alkaline Atoms.* PhD thesis, Vavilov State Optical Institute, 1995.

[22] M. V. Balabas, K. Jensen, W. Wasilewski, H. Krauter, and L. S. Madsen. High quality anti-relaxation coating material for alkali atom vapor cells. *Opt. Exp.*, 18(6):5825, 2010.

[23] M. V. Balabas, T. Karaulanov, M. P. Ledbetter, and D. Budker. Polarized alkali-metal vapor with minute-long transverse spin-relaxation time. *Phys. Rev. Lett.*, 105(7):070801, 2010.

[24] Grigory I. Barenblatt. *Scaling.* Cambridge University Press, first edition, 2003.

[25] Grigory I. Barenblatt. *Flow, Deformation and Fracture.* In preparation, 2012.

[26] W. Barthlott, J. Szarzynski, P. Vlek, W. Lobin, and N. Korotkova. A torch in the rain forest: thermogenesis of the titan arum. *Plant Biology*, 11(4):499–505, 2009.

[27] W. E. Bell and A. L. Bloom. Optical detection of magnetic resonance in alkali metal vapor. *Phys. Rev.*, 107:1559–1565, 1957.

[28] W. E. Bell and A. L. Bloom. Optically driven spin precession. *Phys. Rev. Lett.*, 6:280–281, 1961.

[29] C. J. Berglund, L. R. Hunter, D. Krause, Jr., E. O. Prigge, M. S. Ronfeldt, and S. K. Lamoreaux. New Limits on Local Lorentz Invariance from Hg and Cs Magnetometers. *Physical Review Letters*, 75:1879–1882, September 1995.

[30] G. Bison, R. Wynands, and A. Weis. A laser-pumped magnetometer for the mapping of human cardiomagnetic fields. *Appl. Phys. B.*, 76(4):325–328, 2003.

[31] A. L. Bloom. Principle of operation of the rubidium vapor magnetometer. *Appl. Opt.*, 1:61–68, Jan 1962.

[32] J.H. Boer. *The Dynamical Character of Adorption.* Oxford, fourth edition, 1968.

[33] M.A. Bouchiat. *Etude par Pompage Optique de la Relaxation d'Atomes de Rubidium.* PhD thesis, École Normale Supérieure, 1964.

[34] M.A. Bouchiat and J. Brossel. Relaxation of optically pumped rb atoms on paraffin-coated walls. *Phys. Rev.*, 147(1):41–54, 1966.

[35] D. Bown. *Aroids: Plants of the Arum Family.* Timber-Press, 2000.

[36] G. I. Brenblatt and V. M. Prostokishin. Scaling laws for fully developed turbulent shear flows. Part 2. Processing of experimental data. *J. Fluid Mech.*, 248:521–529, 1993.

[37] J. Brewer, V. G. Bordo, M. J. Kasprowicz, and H.-G. Rubahn. Dynamics of alkali-metal atom photodesorption from polymer thin films. *Phys. Rev. A*, 69:062902, 2004.

[38] D. Budker, W. Gawlik, D. F. Kimball, S. M. Rochester, V. V. Yashchuk, and A. Weis. Resonant nonlinear magneto-optical effects in atoms. *Rev. Mod. Phys.*, 74(4):1153–1201, 2002.

[39] D. Budker, W. Gawlik, D. F. Kimball, S. M. Rochester, V. V. Yashchuk, and A. Weis. Resonant nonlinear magneto-optical effects in atoms. *Rev. Mod. Phys.*, 74(1153-1201), 2002.

[40] D. Budker, D. F. Kimball, S. M. Rochester, V. V. Yashchuk, and M. Zolotorev. Sensitive magnetometry based on nonlinear magneto-optical rotation. *Phys. Rev. A*, 62(4):043403, October 2000.

[41] D. Budker, D. F. Kimball, V. V. Yashchuck, and M. Zolotorev. Nonlinear magneto-optical rotation with frequency-modulated light. *Phys. Rev. A*, 65(055403), 2002.

[42] D. Budker and M. Romalis. Optical magnetometry. *Nature Physics*, 3(4):227–234, 2007.

[43] D. Budker, V. Yashchuk, and M. Zolotorev. Nonlinear Magneto-optic Effects with Ultranarrow Widths. *Physical Review Letters*, 81:5788–5791, December 1998.

[44] Dmitry Budker, Derek F. Kimball, and David P. Demille. *Atomic Physics. An Exploration through Problems and Solutions.* Oxford, second edition, 2008.

[45] Sticker Bumper. Forever pets. *Wag More Bark Less*, 2012.

[46] J. Camparo. The rubidium atomic clock and basic research. *Physics Today*, 39:33–39, 2007.

[47] W. Chalupczak, R. M. Godun, P. Anielski, A. Wojciechowski, S. Pustelny, and W. Gawlik. Enhancement of optically pumped spin orientation via spin-exchange collisions at low vapor density. *Phys. Rev. A*, 85:043402, 2012.

[48] J. Clarke and A. Braginski. *The SQUID Handbook, Vol. I.* Wiley, 2004.

[49] J. Clarke and A. Braginski. *The SQUID Handbook, Vol. II.* Wiley, 2006.

[50] P. Clausing. *Thesis.* PhD thesis, University of Leiden, 1928.

[51] P Clausing. Thesis. *Ann d. Physik*, 7:489–521, 1930.

[52] D. Cohen. Magnetoencephalography: detection of the brain's activity with a superconducting magnetometer. *Science*, 175:664–66, 1972.

[53] D. Cohen. Measurements of the magnetic fields produced by the human heart, brain, and lungs. *IEEE Trans. Magnetics*, 11:694–700, 1975.

[54] D. Cohen and Cuffin N. Demonstration of useful differences between magnetoencephalogram and electroencephalogram. *Electroen. Clin. Neuro.*, 56:38–51, 1983.

[55] C. Cohen-Tannoudji and F. Laloë. Modification de la matrice polarisation d'un faisceau lumineux lors de la traverse d'une vapeur atomique soumise au pompage optique. - première et deuxième partie. *J. Physics (Paris)*, 28(505,722), 1967.

[56] E. Corsini, V. M. Acosta, N. Badour, J. Higbie, B. Lester, P. Litch, B. Patton, M. Prouty, and D. Budker. Search for plant biomagnetism with a sensitive magnetometer. *J. App. Phys.*, 109:074701, 2011.

[57] E. Corsini, M. Balabas, T. Karaulanov, and D. Budker. Hyperfine frequency shift and zeeman relaxation in alkali vapor cells with anti-relaxation alkene coating. *In preparation*, 2012.

[58] K. L. Corwin, Z.-T. Lu, C. F. Hand, R. J. Epstein, and C. E. Wieman. Frequency-Stabilized Diode Laser with the Zeeman Shift in an Atomic Vapor. *Applied Optics*, 37:3295–3298, May 1998.

[59] H. B. Dang, A.C. Maloof, and M. V. Romalis. Ultrahigh sensitivity magnetic field and magnetization measurements with an atomic magnetometer. *Appl. Phys. Lett.*, 97(151110):557, 2010.

[60] J.H. de Boer. *Dynamical Characternof of Adsorption.* Oxford, second edition, 1968.

[61] H. G. Dehmelt. Modulation of a light beam by precessing absorbing atoms. *Phys. Rev.*, 105:1924–1925, 1957.

[62] H. G. Dehmelt. Slow spin relaxation of optically polarized sodium atoms. *Phys. Rev.*, 105(5), 1957.

[63] W. Demtröder. *Laser Spectroscopy.* Springer, fourth edition, 2008.

[64] B. Dima, L. Hollberg, D.F. Kimball, J. Kitching, S. Pustelny, and V. V. Yashchuk. Microwave transitions and nonlinear magneto-optical rotation in anti-relaxation-coated cells. *Phys Rev. A*, 71(012903), 2005.

[65] R. Drampyan, S. Pustelny, and W. Gawlik. Electromagnetically induced transparency versus nonlinear faraday effect: Coherent control of light-beam polarization. *Phys Rev, A*, 80(033815), 2009.

[66] B. Driehuys, G. D. Cates, and W. Happer. Surface relaxation mechanisms of laser-polarized xe129. *Phys. Rev. Lett.*, 74(24):4943–4946, 1995.

[67] J. Dupont-Roc and C Haroche, S. andCohen-Tannoudji. Detection of very weak magnetic fields (109 gauss) by 87rb zero-fi eld level crossing resonances. *Appl. Opt.*, 1:61–68, 1962.

[68] M. Faraday. Experimental researches in electricity vol. iii - london, uk, 1855.

[69] M. Fleischhauer, A. Imamoglu, and J. P. Marangos. Electromagnetically induced transparency: Optics in coherent media. *Rev. Mod. Phys.*, 77(633), 2005.

[70] S. Franke-Arnold, M. Arndt, and A. Zeilinger. Magneto-optical effects with cold lithium atoms. *J. Phys. B - A.M.O. Phys.*, 34(12):2527–2536, 2001. Times Cited: 8.

[71] W. Franzen. Spin relaxation of optically aligned rubidium vapor. *Phys. Rev.*, 115(4):850–856, 1959.

[72] H. N. Freitas, M. Orias, and Chevrollier M. Lspectroscopy of cesium atoms adsorbing and desorbing at a dielectric surface. *Appl. Phys. B*, 75:703–709, 2002.

[73] W. Gawlik, R. Kowalski, R. Neumann, and F. Träger. Observation of the electric hexadecapole moment of free na atoms in a forward scattering experiment. *Optics Communications*, 12:4, 1974.

[74] W. Gawlik, W. Krzemień, S. Pustelny, D. Sangla, J. Zachorowski, M. Graf, A. O. Sushkov, and D. Budker. Nonlinear magneto-optical rotation with amplitude modulated light. *Appl. Phys. Lett.*, 88(131108), 2006.

[75] Wojciech Gawlik. *O Rozpraszaniu Do Przodu Promieniowania Rezonansowego Przez atomy sodu [Observation of nonlinear Farday effect in a sodium vapor in a forward scatterign experiment].* PhD thesis, Jagiellonian University, 1975.

[76] S Gozzini and A. Lucchesini. Light-induced atomic desorption (liad) del potassio in film di siloxano. *Proc. Soc. Ital. di Fisica*, page 114, 2001.

[77] M. T. Graf, D. F. Kimball, S. M. Rochester, K. Kerner, C. Wong, D. Budker, E. B. Alexandrov, M. V. Balabas, and V. V. Yashchuk. Relaxation of atomic polarization in paraffin-coated cesium vapor cells. *Phys. Rev. A*, 72:023401, 2005.

[78] W.C. Griffith, S. Knappe, and J. Kitching. Femtotesla atomic magnetometry in a microfabricated vapor cell. *Optics Exp.*, 18(26):27167, 2010.

[79] S. Groeger, G. Bison, J.-L. Schenker, R. Wynands, and A. Weis. A high-sensitivity laser-pumped M_x magnetometer. *European Physical Journal D*, 38:239–247, May 2006.

[80] J. S. Guzman, A. Wojciechowski, J. E. Stalnaker, K. Tsigutkin, V. V. Yashchuk, and D. Budker. Nonlinear magneto-optical rotation and zeeman and hyperfine relaxation of potassium atoms in a paraffin-coated cell. *Phys. Rev. A*, 74:053415, 2006.

[81] V. Handerek, H. McArdle, T. Willats, Psaila N., and L. Laycock. Experimental Retroreflectors with Very Wide Field of View for Free-Space Optical Communication. *2nd EMRS DTC Tech. Conf.*, B25, 2005.

[82] W. Happer. Optical pumping. *Re. Mod. Phys.*, 44:169–249, 1972.

[83] J. M. Higbie, E. Corsini, and D. Budker. Robust, high-speed, all-optical atomic magnetometer. *Rev. of Sci. Instrum.*, 77(11):113106, 2006. Times Cited: 2.

[84] C. Hovde, V. M. Acosta, E. Corsini, J. Higbie, M. P. Ledbetter, and D. Budker. Nonlinear magneto-optical rotation for sensitive measurement of magnetic fields. *OSA BioMed*, page JMA44, 2008.

[85] C. Hovde, B. Patton, E. Corsini, J. Higbie, and D Budker. Sensitive optical atomic magnetometer based on nonlinear magneto-optical rotation. *Proc. SPIE-Int. Soc. Opt. Eng.*, 7693:769313 (10 pp.), 2010.

[86] C. Hovde, B. Patton, E. Corsini, O. Versolato, S. Rochester, and D. Budker. Heading error in an alignment-based magnetometer. *Proc. SPIE Soc. Opt. Eng.*, page 8046, 2011.

[87] T. Isayama, Y. Takahashi, N. Tanaka, K. Toyoda, K. Ishikawa, and T. Yabuzaki. Observation of larmor spin precession of laser-cooled rb atoms via paramagnetic faraday rotation. *Phys Rev, A*, 59(4836), 1999.

[88] J. D. Jackson. *Classical Electrodynamics.* Wiley, third edition, 1998.

[89] K. Jensen, V. M. Acosta, Higbie J. M., M. P. Ledbetter, S. M. Rochester, and D. Budker. Cancellation of nonlinear zeeman shifts with light shifts. *Phys. Rev. A*, 79(2):023406, 2009.

[90] T. Karaulanov, M. T. Graf, D. English, S. M. Rochester, Y. Rosen, K. Tsigutkin, D. Budker, M. V. Balabas, D. F. Jackson Kimball, F. A. Narducci, S. Pustelny, and V. V. Yashchuk. Controlling atomic vapor density in paraffin-coated cells using light-induced atomic desorption. *Phys. Rev. A*, 79:012902, 2009.

[91] V. Kierman. Article of faith fails aero engineers. *NewScientist*, 150(2029):5, 1996.

[92] Geoffrey C. Kite. Inflorescence odour of the foul-smelling aroid helicodiceros muscivorus. *Kew Bulletin, Springer*, 55(1):237–240, 2000.

[93] S. Knappe, V. Shah, P. D. D. Schwindt, L. Hollberg, and J. Kitching. Nonlinear magneto-optical rotation and zeeman and hyperfine relaxation of potassium atoms in a paraffin-coated cell. *Appl. Phys. Lett.*, 85:9, 2004.

[94] I.K. Kominis, T.W. Kornack, J.C. Allred, and M.V. Romalis. A subfemtotesla multichannel atomic magnetometer. *Nature*, 422:596–599, 2003.

[95] T. W. Kornack, R. K. Ghosh, and M. Romalis. Nuclear spin gyroscope based on an atomic co-magnetometer. *Phys. Rev. Lett.*, 95:230801, 2005.

[96] G. Labeyrie, C. Miniatura, and R. Kaiser. Large faraday rotation of resonant light in a cold atomic cloud. *Phys. Rev. A*, 64(3):033402/1–7, 2001. Times Cited: 0.

[97] M. Ledbetter, S. Pustelny, D. Budker, M. Romalis, J. Blanchard, and A. Pines. Liquid-state nuclear spin comagnetometers. *arXiv:1201.4438v2[physics-atom-ph]*, 2012.

[98] M. Ledbetter, T. Theis, J. Blanchard, H. Ring, P. Ganssle, S. Appelt, B. Bluemich, A. Pines, and D. Budker. Near-zero-field nuclear magnetic resonance. *Phys. Rev. Lett.*, 107:107601, 2011.

[99] Changmin Lee, G. Z. Iwata, J. Corsini, Higbie, E., S. Knappe, M. Ledbetter, and D. Budker. Small-sized dichroic atomic vapor laser lock (DAVLL). *Rev. Sci. Instr.*, 82:043107, 2011.

[100] D. Macaluso and O. M. Corbino. Light traversing metallic vapours in a magnetic field. *Comptes Rendus Hebdomadaires des Seances de l'Academie des Sciences*, pages 548–551, 1898.

[101] H. Margenau, P. Fontana, and L. Klein. Frequency shifts in hyperfine splitting of alkalis caused by foreign gases. *Phys. Rev.*, 115(1):87–92, 1959.

[102] A. B. Matsko, D. Strekalov, and L. Maleki. Magnetometer based on the opto-electronic microwave oscillator. *Optics Communications*, 247:141–148, March 2005.

[103] Gary G. Matthews. *Cellular Physiology of Nerve and Muscle.* Wiley-Blackwell, fourth edition, 2002.

[104] H. Metcalf and Peter van der Straten. *Laser cooling and Trapping.* Springer, first edition, 2002.

[105] M. Meucci, E. Mariotti, P. Bicchi, and D. L. Marinelli, C.and Moi. Light-induced atom desorption. *Europhysics Lett.*, 25(9):639–643, 1994.

[106] S. A. Murthy, D. Krause, Jr., Z. L. Li, and L. R. Hunter. New limits on the electron electric dipole moment from cesium. *Physical Review Letters*, 63:965–968, August 1989.

[107] J. Nash and F. A. Narducci. Linear magneto-optic rotation in a cold gas. *J. Mod. Opt.*, 50:2667, 2003.

[108] B. Patton, K. Ishikawa, Y.-Y. Jau, and W. Happer. Intrinsic Impurities in Glass Alkali-Vapor Cells. *Phys. Rev. Lett.*, 99:027601, 2007.

[109] B. Patton, O. Versolato, C. Hovde, E. Corsini, J. M. Higbie, and D. Budker. A remotely interrogated all-optical rb87 magnetometer. *preprint*, 2012.

[110] B. Patton, O. Versolato, C. Hovde, E. Corsini, J. M. Higbie, S. Rochester, , and D. Budker. Heading error of an alignment-based rubidium magnetometer. *in preparation*, 2012.

[111] S. Pustelny, D. F. Jackson-Kimball, S. M. Rochester, V. V. Yashchuck, and D. Budker. Influence of magnetic-field inhomogeneity on nonlinear magneto-optical resonances. *Phys. Rev. A*, 74:063406, 2006.

[112] C. Rahman and H. G. Robinson. Rb 0-0 hyperfine transition in evacuated wall-coated cell at melting temperature. *J. Quantum Elec.*, QE-23(4):452–454, 1987.

[113] D.M. Rampulla, E. Oncel, Y.W. Yi, S. Knappe, and S.L. Bernasek. Effects of organic film morphology on the formation of rb clusters on surface coatings in alkali metal vapor cells. *App. Phys. Lett.*, 94:041116, 2009.

[114] N.F. Ramsey. Resonance experiments in successive oscillatory fields. *Rev, Sci. Inst.*, 28:57, 1957.

[115] Pavel Ripka. *Magnetic sensors and magnetometers.* Artech, 2001.

[116] T.P. Roberts, G.L. Schmidt, M. Egeth, L. Blaskey, M.M. Rey, Edgar J.C, and S.E Levy. Electrophysiological signatures: Magnetoencephalographic studies of the neural correlates of language impairment in autism spectrum disorders. *Int. J. Psychophysiology*, 68:149–160, 2008.

[117] H. G. Robinson, E.S. Ensberg, and H. G. Dehmelt. Preservation of spin state in free atom-inert surface collisions. *Bull. Am. Phys. Soc.*, 3:9, 1958.

[118] S. M. Rochester and D. Budker. Atomic polarization visualized. *American Journal of Physics*, 69:450–454, April 2001.

[119] M. V. Romalis, W. C. Griffith, J. P. Jacobs, and E. N. Fortson. New Limit on the Permanent Electric Dipole Moment of ^{199}Hg. *Physical Review Letters*, 86:2505–2508, March 2001.

[120] M. V. Romalis and L. Lin. Surface nuclear spin relaxation of hg199. *J. Chem. Phys.*, 120(3):1511, 2004.

[121] S. S. Wildermuth, S. Hofferberth, S. Lesanovsky, I. Groth, J. Krüger, P. Schmiedmayer, and I. Bar-Joseph. Sensing electric and magnetic fields with bose-einstein condensates. *Appl. Phys. Lett.*, 88(264103), 2006.

[122] Y.D. Safonov, V.M. Provotorov, V.M. Lub, and L.I Yakimenkov. Electrophysiological signatures: Magnetoencephalographic studies of the neural correlates of language impairment in autism spectrum disorders. *Bull. Exp. Biol. Med.*, 64:1022–1024, 1967.

[123] I. M. Savukov and M. V. Romalis. Effects of spin-exchange collisions in a high-density alkali-metal vapor in low magnetic fields. *Phys. Rev. A*, 71(2):023405, 2005.

[124] A.K. Schmakov, T. Karaulavov, M. V. Balabas, S. M. Rochester, S. Pustelny, and D. Budker. Apparatus for rapid characterization of alkali vapor cells. *To be Publised*, 2011.

[125] Dirk Schulze-Makuch and Louis Irwin. *Life in the universe, Expectations and Constraints.* Wiley, second edition, 2008.

[126] P. D. D. Schwindt, L. Hollberg, and J. Kitching. Self-oscillating rubidium magnetometer using nonlinear magneto-optical rotation. *Rev. Sci. Instr.*, 76:126103, 2005.

[127] S. J. Seltzer, D. J. Michalak, M. H. Donaldson, M. V. Balabas, S. L. Barber, S. K. Bernasek, M.-A. Bouchiat, A. Hexemer, A. M. Hibberd, D. F. Jackson Kimball, C. Jaye, T. Karaulanov, F. A. Narducci, S. A. Rangwala, H. G. Robinson, A. K. Shmakov, D. L. Voronov, V. V. Yashchuk, A. Pines, and D. Budker. Investigation of antirelaxation coatings for alkali-metal vapor cells using surface science techniques. *J. Chem. Phys.*, 133:144703, 2010.

[128] S. J. Seltzer, D. M. Rampulla, S. Rivillon-Amy, Y. J. Chabal, S. L. Bernasek, and Romalis M. V. Testing the effect of surface coatings on alkali atom polarization lifetimes. *J. App. Phys.*, 104:103116, 2008.

[129] G. W. Series. Should resonance curves in optical pumping be doppler-broadened? *Proc. phys. Soc.*, 88(995), 1966.

[130] R. Seymour. Analysis of heat production in a thermogenic arum lily, philodendron selloum, by three calorimetric methods. *Thermochimica Acta*, 193:91–97, 1991.

[131] R. Seymour. Plants that warm themselves. *Sci. Am.*, 276(3):104–109, 1997.

[132] R. Seymour. Diffusion pathway for oxygen into highly thermogenic florets of the arum lily philodendron selloum. *J. Exp. Botany.*, 52(360):1465–1472, 2001.

[133] Vishal Shah, Svenja Knappe, Peter D. D. Schwindt, and John Kitching. Subpicotesla atomic magnetometry with a microfabricated vapour cell. *Nature Photon.*, 1(11):649–652, 2007.

[134] M. L. Terraciano, M. Bashkansky, and F. K. Fatemi. Faraday spectroscopy of atoms confined in a dark optical trap. *Phys. Rev. A*, 77:063417, 2008.

[135] M. L. Terraciano, M. Bashkansky, and F. K. Fatemi. A single-shot imaging magnetometer using cold atoms. *Opt. Express*, 16(13062), 2008.

[136] C. H. Townes, Conyers Herring, and W. D. Knight. The effect of electronic paramagnetism on nuclear magnetic resonance frequencies in metals. *Phys. Rev.*, 77:852, 1950.

[137] C. H. Townes, Conyers Herring, and W. D. Knight. Some suggestions concerning the production and detection by optical means of inequalities in the populations of levels of spatial quantization in atoms. application to the stern and gerlach and magnetic resonance experiments. *J. Phys. Radium*, 11:255–265, 1950.

[138] E. Ulenski and Z. Wu. Measurement of dwell times of spin polarized rubidium atoms on octadecyltrichlorosilane- and paraffin-coated surfaces. *App. Phys. Lett.*, 98:201115, 2011.

[139] J. Vanier and C. Audoin. *The Quantum Physics of Atomic Frequency Standards.* Adam Hilger, 1989.

[140] M. Vengalattore, J. M. Higbie, S. R. Leslie, J. Guzman, L. E. Sadler, and D. M. Stamper-Kurn. High-resolution magnetometry with a spinor bose-einstein condensate. *Phys. Rev. Lett.*, 98(200801), 2007.

[141] J. P. Wikswo and J. A. Freeman. Magnetic field of a nerve impulse. *Science*, 208:53–55, 1980.

[142] Adam Wojciechowski, Eric Corsini, Jerzy Zachorrowski, and Wojciech Gawlik. Nonlinear faraday rotation and detection of superposition states in cold atoms. *Phys. Rev. A*, 81(053420), 2010.

[143] R. Wynands, C. Affolderbach, J. Hollberg, L. Kitching, S. Knappe, and M. Sthler. VCSELs in nonlinear spectroscopy: making optical magnetometers and atomic clocks practical. *IEEE LEOS Newsletter*, 10:29–30, 2001.

[144] H. Xia, A. B. Baranga, D. Hoffman, and M. V. Romalis. Magnetoencephalography with an atomic magnetometer. *Appl. Phys. Lett.*, 89:211104, 2006.

[145] S. Xu, S. M. Rochester, V. V. Yashchuk, M. H. Donaldson, and D. Budker. Construction and applications of an atomic magnetic gradiometer based on nonlinear magneto-optical rotation. *Review of Scientific Instruments*, 77(8):083106, August 2006.

[146] V. V. Yashchuck, D. Budker, and J. R. Davis. Laser frequency stabilization using linear magneto-optics. *Rev. Sc. Inst.*, 71(2):341, 2000.

[147] V. V. Yashchuk, S. K. Lee, Z. Poperno, D. Budker, and D.F. Jackson-Kimball. *Optical Magnetometry.* Cambridge University Press, 2012.

[148] A. N. Youdin, D. Krause, Jr., K. Jagannathan, L. R. Hunter, and S. K. Lamoreaux. Limits on Spin-Mass Couplings within the Axion Window. *Physical Review Letters*, 77:2170–2173, September 1996.

[149] K.F. Zhao, M. Schaden, and Z. Wu. Method for measuring the dwell time of spin-polarized rb atoms on coated pyrex glass surfaces using light shift. *Phys Rev. Lett.*, 103(073201), 2009.

Appendix A - Acknowledgements: Qualification Examination and Dissertation Committees

Professor Eugene D. Commins **Qualification exam Committee and Dissertation committee member**

E-mail commins@berkeley.edu – eugenecommins@earthlink.net
Phone: 1 (510) 642-2305
Campus Office: 257 Birge Hall
Position: Professor Emeritus, Dept. of Physics, University of California, Berkeley
Research: Atomic, Molecular And Optical Physics
Education: Ph.D., Columbia University (1958).
Selected awards: Member, National Academy of Sciences;
Fellow: American Academy of Arts and Sciences, A.A.A.S., A.P.S
Berkeley Campus Distinguished Teaching Awards 1963, 1979.
Publications (book) Weak Interactions of Leptons and Quarks, Cambridge University Press 1983
Personal homepage http://www.physics.berkeley.edu/research/faculty/commins.html

Professor Holger Müller **Qualification Exam Committee Chair Dissertation committee member**

E-mail hm@berkeley.edu
Phone**:** 1 (510) 664-4298
Campus office: 301C Old-Leconte Hall
Position: Assistant Professor Atomic, Molecular, and Optical Physics, University of California, Berkeley
Former position: Postdoc in the group of Steven Chu at Stanford.
Research: Atomic, Molecular And Optical Physics
Education Ph.D.Humboldt-University, Berlin
Selected awards: First patent at age 14.
Alexander von Humboldt foundation fellow
Advisor: Achim Peters.
Personal homepage: http://physics.berkeley.edu/research/mueller/
Research page: http://www.physics.berkeley.edu/research/faculty/mueller.html

Professor Grigory Isaakovich Barenblatt **Qualification exam Committee and Dissertation committee member**

E-mail: gibar@math.berkeley.edu
Phone: 1 (510) 642-4162
Campus office: 735 Evans Hall
Present position: Professor in Residence, Dept of Mathematics, University of California, Berkeley
Former position (selected): Head Dept. of Plasticity, Institute of Mechanics, Moscow University
Head, dept., Institute of Oceanology, USSR Academy of Sc.
G.I. Taylor Professor of Fluid Mechanics, University of Cambridge
Education: Ph.D. (1953), D. Sc. (1957), Professor (1962): Moscow University
Master of Arts (1993): Cambridge University
Scientific Advisor: A N. Kolmogorov
Research: Applied mathematics- mathematical physics
Research topics (selected): Fracture Mechanics, Theory of fluid and gas flows in porous media, Mechanics of non-classical deformable solids, Turbulence, Self-similarities. Nonlinear waves & intermediate asymptotics

Honors (selected):
1975 Foreign Honorary Member, American Academy of Arts & Sciences
1984 Foreign Member, Danish Center of Applied Mathematics & Mechanics
1988 Foreign Member, Polish Society of Theoretical & Applied Mechanics
1989 Doctor of Technology Honoris Causa at the Royal Institute of Technology, Stockholm, Sweden
1992 Foreign Associate, U.S. National Academy of Engineering
1993 Fellow, Cambridge Philosophical Society
1993 Member, Academia Europaea
1994 Fellow, Gonville and Caius College, Cambridge; (since 1999, Honorary Fellow)
1995 Lagrange Medal, Accademia Nazzionale dei Lincei
1995 Modesto Panetti Prize and Gold Medal 1997 Foreign Associate,.S. National Academy of Sciences
1999 G.I. Taylor Medal, U.S. Society of Engineering Science
1999 J.C. Maxwell Medal and Prize, International Congress for Industrial and Applied Mathematics
2000 Foreign Member, Royal Society of London 2005 Doctor of Civil Engineering Honoris Causa at the Torino Polytechnic Institute, Italy
2005 S.P. Timoshenko Medal, American Society of Mechanical Engineers
2009 Honorary Fellow, International Congress on Fracture

Publications
Theory of unsteady filtration of fluids and gases (1974); Nedra publishing House, Moscow
Similarity, Self-similarity, and intermediate Asymptotics. (1978); Gidromeyeoizdat Publishing House, Leningrad
Similarity, self-similarity, and intermediate asymptotics (1970); Consultants Bureau, Plenum press, New York, London
Mathematical theory of combustion and explosions (1980); NaukaPublishing House, Moscow
The motion of fluid and gases in naturalstrata (1984); Nedra PublishingHouse, Moscow
The mathematical Theory of combustion and explosions (1985); Consultants Bureau, Plenum press, New York
Dimensional analysis (1987); Gordon and Breach Science Publishers, New York, London, Paris, Montreaux, Tokyo
Theory of fluid flows through natural rocks (1990); Kluwer Academic Publishers, Dordrecht, Boston, London
Scaling phenomena in fluid mechanics. (1994); Cambridge University press
Scaling, self-similarity, and intermediate asymptotics..(1996);Cambridge University press
Scaling (2003); Cambridge University Press
Self-similar Phenomena – Dimensional Analysis and Scaling (2009); Publishing House “intellect”, Dolgoprudny
Flow, Deformation and Fracture; Cambridge University press (in preparation)

Personal homepage: http://math.berkeley.edu/~gibar/index.html
Selected publications: http://math.berkeley.edu/~gibar/barenblatt_paper_mono.html
Member of Editorial Boards: http://math.berkeley.edu/~gibar/index.html#members

Figure A.1: Dissertation and qualification exam committees (as per pesonal web-page - p1/2).

Professor Charles H. Townes **Qualification Exam Committee member**

Email: cht@ssl.berkeley.edu
Phone: 1 (510) 642-1128
Campus office: 557 Birge Hall
Position: Professor In The Graduate School, University of California, Berkeley (Prof. at Berkeley since 1967)
Research: Astrophysics
Education: Ph.D., California Institute of Technology, (1939)
Selected awards: Nobel Prize in Physics, 1964.
Member National Academy of Sciences
Group Site: http://isi.ssl.berkeley.edu
Research url: http://www.physics.berkeley.edu/research/faculty/townes.html

Professor Dmitry Budker **Dissertation committee co-Chair**
Qualification exam committee member

E-mail: budker@berkeley.edu
Phone: 1 (510) 643-1829
Campus Office: 273 Birge Hall
Position: Professor, Department of Physics, University of California at Berkeley,
Faculty Scientist, Nuclear Science Division, LBNL
Research: Atomic, Molecular And Optical Physics
Education: Ph.D. in Physics, University of California at Berkeley (1993)
MS in physics with honors, Novosibirsk State University (1985)
Selected awards: 1994 APS Award for Outstanding Doctoral Thesis Research in Atomic, Molecular, or Optical Physics
NSF CAREER award
Fellow of the American Physical Society
UC Berkeley Miller Professor (2003-2004).
Thesis advisor: Professor Eugene D. Commins.
Publications: Atomic Physics, An Exploration of Problems and Solutions, Oxford, 2004.
Optically Polarized Atoms: Understanding light-atom interactions, Oxford, 2010
Personal homepage: http://budker.berkeley.edu/index.html

Dissertation
Co-Chairmanship

Joint Kraków-Berkeley
Atomic Physics
and Photonics
Laboratory

Professor Wojciech Gawlik **Dissertation committee co-Chair**
Qualification Exam Committee participant

E-mail: gawlik@uj.edu.pl
Phone: 48(12)6635656
Fax: 48(12)6338494
Address: Zakład Fotoniki, Instytut Fizyki UJ, Reymonta 4, 30-059 Kraków, Poland
Campus office: Room 358
Present position: **(1992)** Professor Dr. hab., Institute of Physics, Jagiellonian University, Krakow, Poland
Head of Dept of Photonics-Institute of Physics
Former positions (selected)(1998) Visiting Fellow, JILA, NIST, & University of Boulder, Colorado, USA
(1991) Visiting Professor, Ecole Normale Superieure, Paris, France
(1978) Senior Visiting Fellow, Reading University, UK
(1972) Assistant Professor, Heidelberg University, Germany
Education: Msc. (1970), Ph.D (1975), habilitation (1980) [subject: Physics]: Jagiellonian University
Thesis adviser: Prof. Dr. Danuta Kunisz
Dept homepage: http://www.if.uj.edu.pl/ZF
Research: [Optical cooling and trapping of neutral atoms]
[Nonlinear magneto-optics]
[Optical nonlinear effects in dense atomic vapours]
[Medical and biological effects of low-level laser radiation]
Publications: http://www.if.uj.edu.pl/ZF/qnog/

Figure A.2: Dissertation and qualification exam committees (as per pesonal web-page - p2/2).

Appendix B - Acknowledgements Inspirations and Mentorship

Figure B.1: The University of California, Berkeley, has been a beacon of forward thinking, and continues to challenge the status-quo and to advance the frontier of knowledge; in particular the Physics Department, which holds 9 of the total 22 Nobel prize winners at Cal.
1-6:The Occupy Movement at Cal (Nov 2011). 7-15: The Monday Physics Colloquium. 11: Robert Birgeneau, UC Berkeley Chancellor and Physics Professor12: Steve Chu, 1997 Nobel Laureate Nobel Laureate in Physics and UC Berkeley professor (now the 12th United States Secretary of Energy). 13: George Smoot 2006 Nobel Laureate in Physics and UC Berkeley professor. 14: Visiting theoretical physicist and cosmologist, Stephen Hawking. 15: Visiting astrophysicist and cosmologist, Martin Rees. 16: Richard Muller, UC Berkeley professor. 17: (Alex) Alexei Filippenko, Saul Perlmutter, and Richard Muller, at the 2011 Physics Nobel Laureate reception at UC Berkeley. 18: Saul Perlmutter's 2011 Physics Nobel Laureate reception [Photographs: E. Corsini].

wojciech.gawlik

Thursday, May 05, 2011

Maerick
I am back at the office 12:38 PM
tried everything in 325L 12:38 PM

Maerick
porjector, mic, video, skype .. 12:39 PM

Call to wojciech.gawlik, duration 15:11. 12:40 PM

Call from wojciech.gawlik 1:42 PM

wojciech.gawlik
New voice message, duration 00:12 1:42 PM

Call to wojciech.gawlik, duration 03:08. 1:43 PM

Monday, May 09, 2011

Maerick
awaiting your connection 12:58 PM

Call from wojciech.gawlik, duration 1:32:15. 12:58 PM

Figure B.2: The dedication and inspiration provided by the qualification committee and dissertation committee members and by my colleagues are an intrinsic and foundational part of this work, and as such deserve to be documentted and acknowledged. A few selected examples are shown below and on the next page.
A: Dr. Wojciech Gawlik acting as qualification exam committee member via Skype teleconference, late night (in Kraków), prior to a full day managing his lab and teaching classes.
B: Todor Karaulanov (postdoc at UC Berkeley). One of the two mentors to whom I owe most of my success. the other mentor is shown in (G,H)
C,D: Amir Waxman (visiting postdoc) on one of our 5-mile, 1000-foot elevation, firetrail runs in the Berkeley hill (top: midpoint, between us, the UC Berkeley campanille is barely seen 1000-feet below. bottom: waiting for the bus ride downhill).
E: Dr Mikhail Balabas, Physics professor at the S. I. Vavilov State Optical Institute, St. Petersburg, 199034 Russia (during one of his several month-long visits to UC Berkeley), combining the art of glass blowing (and a simple oven - rightmost photograph) with science, to investigate surface-science effects which have not been elucidated in the last 50 years.
G: Trecking through snow and ice at Morskie Oko with Adam Wojciechowski, when not working in the lab (F). Adam is the graduate student (now postdoc) who provided training and mentorship in laser-cooled atoms, and who shared his extensive knowledge of Polish history and culture.
H: Dr. Holger Müller (UC Berkeley professor in physics and dissertation and qualification exam committee member) presenting his results on a test of Einstein's equivalence principle, and fielding disputative questions from Nobel Laureate Dr. Cohen-Tannoudji (2010 I.C.A.P. conference, Cairns, Queensland, Australia) [Photographs: E. Corsini].

Figure B.3: A: Dr. Barenblatt, UC Berkeley professor in mathematics, at lunch (Faculty club) with his students after his closing spring 2012 lecture (Math275) [the logarithmic law, pertaining to sheer flow, and which he disproved, is firmy crossed-out on the board behind].
B: the three-day Physics Dept. hike at the Jagiellonian University in kraków terminating around a bonfire in the Tatras mountains.
C,H,D: Dr. Eugene D. Commins' (UC Berkeley professor in physics) first retirement party, shown teaching Statistical Mechanics (211 - Fall 2004) - before being requested an encore to teach 221A/B Quantum Mechanics - twice recipient of the University of California Distinguished Teaching Award (the only professor in the UC Berkeley history of that award, to receive it twice). The awards are displayed in Pimentel Hall, UC Berkeley.
E: Jerzy (Jurek) Zachorowski (Jagiellonian University physics professor), one of the twelve life-appointed Wavel castle Zygmunt Royal Bell ringer.
F: Wojtek Gawlik (Jagiellonian University full professor [Poland's president appointed] in physics), and his wife Danuta (Danka). Dr Gawlik realized the first BEC in Poland.
G: Micah Ledbetter (postdoc at UC Berkeley) who initiated me to the guelling 5-mile 1000-foot inclined fire-trail run (on the trail in May 2012).
I: Dmitry (Dima) Budker (UC Berkeley professor in physics) playing to heal and soothe the heart and the soul. [Photographs: E. Corsini].

Figure B.4: A,n: Dr. Littlejohn, UC Berkeley professor and theorist, teaching graduate level Quantum Mechanics (221B - Class of Spring 2012 [E Corsini (not part of the class) video-recorded the lectures (I) - the lectures are vailable on Dr Littlejohn's course website]).
B: Victor Acosta (colleague and graduate student) sharing his scientific insight and daily-life common-sense.
C,D,E: Claudia Trujillo, Donna Sakima, Anne Takizawa (Undergraduate Adviser, Graduate Student Affairs Officer, Student Affairs Officer), whose many tasks, indispensable to the successful completion of the present work, would be long to list.
F: Krzysztof Brzozowski (colleague graduate student) and fiancé Anna Barzyńska (now Krzysztof and Anna Brzozowsci), during one of their invitations to their parents' chalet in the mountains by Bielsko.
G: Elvia Palabrica, one of the many dedicated workers keeping the physics building spotless and supplies replenished.
H: Stephen Pride Raffel (staff support services), purchasing wizzard at the UC Berkeley Department of Physics.
I,J,K: Duy Le Ba, Geoffrey Iwata, and Andrey Shmakov, three UC Berkeley undergraduate students who offered dedication and expertise.
L: Brigitte Lossing, Director of Campus Recreation at the UC Berkeley RSF, dedicated to users of recreational sports facilities; in particular to the 8-9pm lap swimmers (Fig. D.1).
H: Susana Wong, at Unit-3, manager at the UC Berkeley housing and dining residential department, expert at easing students through housing logistics and hurdles.
J: Michael (Misha) Solarz, "independent-minded contractor" at UC Berkeley, who constructed the workspace pertaining to Chapter 5.
[Photographs: E. Corsini].

Appendix C - Acknowledgements: Physics Department's Technical Support Teams

E-Shop

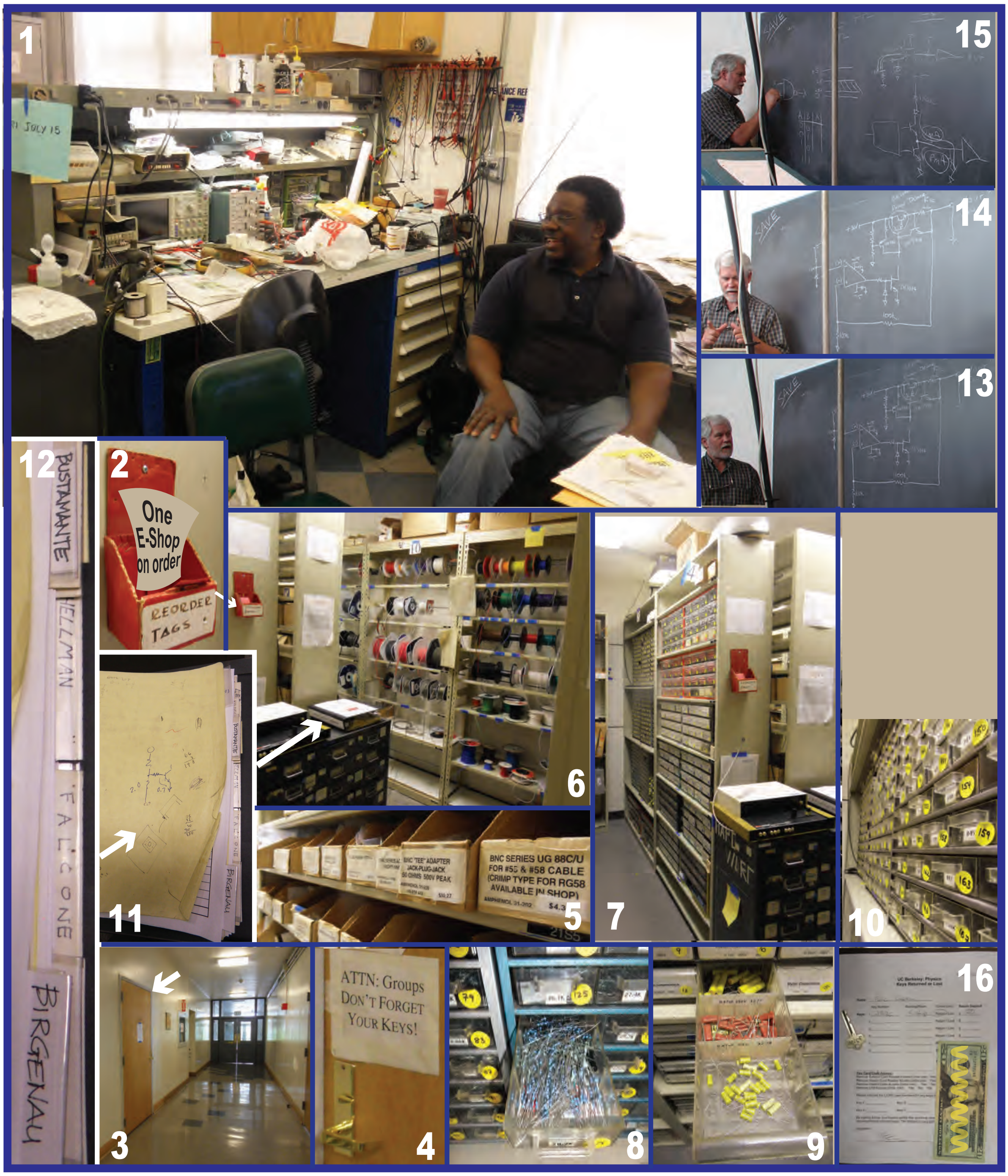

Figure C.1: 1: Levern Garner (electronic engineer) at his work station, 2: re-order tag box, 3,4: e-Shop stock-room door 5-10: e-Shop stock-room, 11,12: parts sign-out binder, 13-15: John Davis' (electronic engineer) legendary summer e-course 16: to the dismay of experimentalists: the e-Shop was terminated on June 30, 2011 / stock-room key refund [David gallegos was another key personnel - no suitable photograph available]. [Photographs: E. Corsini].

Student and Main Machine Shops

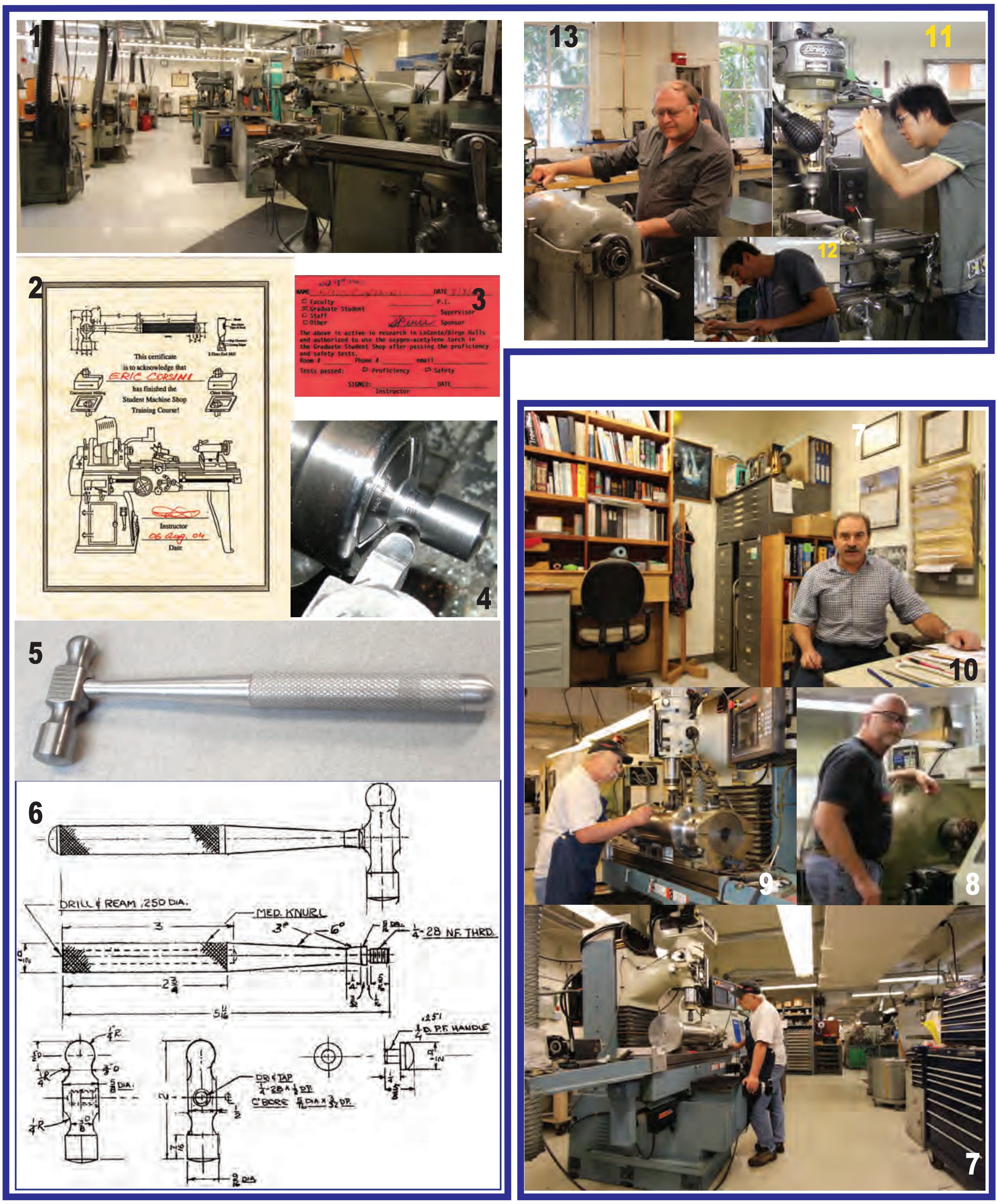

This certificate
is to acknowledge that
ERIC CORSINI
has finished the
Student Machine Shop
Training Course!

Instructor
06 Aug. 04
Date

NAME ______ DATE ______
☐ Faculty ______ P.I.
☒ Graduate Student ______ Supervisor
☐ Staff ______ Sponsor
☐ Other

The above is active in research in LeConte/Birge Halls and authorized to use the oxygen-acetylene torch in the Graduate Student Shop after passing the proficiency and safety tests.

Room # ______ Phone # ______ email ______

Tests passed: ☐ Proficiency ☐ Safety

SIGNED: ______ DATE ______
Instructor

Figure C.2: 1: student machine shop. 13: Joseph Kant, student machine shop director since 1989. 4-6: the "hammer", which completion certificates (2,3) entitles unlimited access to the student machine shop (11,12), entails a variety of lathing and milling tecniques (4). 7-10: main machine shop. 10: Marco Ambrossini: main machine shop director since 2003. 7,9: Carllisle Warner ("Warner" - engineer) machined most parts pertaining to Chapter 5-Part I. 8: Mike Brown (engineer) machined most parts pertaining to Chapter 4-Part I [Photographs: E. Corsini].

Appendix D - Closing Acknowlegements

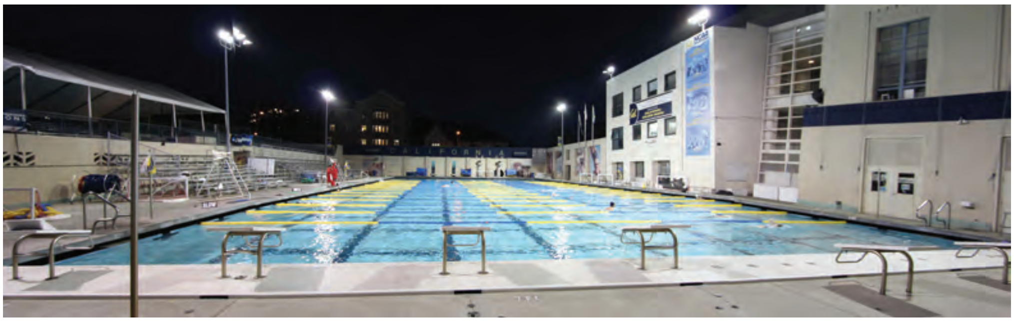

Figure D.1: UC Berkeley Recreational Sports Facilities Olympic pool

The closing of this work is dedicated
to the 8:00pm to 9:00pm swimming partners (UC Berkeley, RSF pool),

In particular to: **Peter Schwartz,**
[B.S. UC Berkeley; Ph.D. Ohio State University],
[L.B.L. Research Scientist/Mathematician - Numerical Solutions to PDE],
for his challenging questions pertaining to my field of study.
and to,
Tom Clark,
[B.A., University of Michigan; M.A., University of Cambridge]
[English Poetry Professor, Writer],
Bob Yu,
[B.S (Engineering); Phi-Beta-Kappa, M.B.A., Hass School, UC Berkeley]
[General manager, Hymnody and Bible House],
Mervyn Wong,
[B.Sc. University of Canterbery; Ph.D. Harvard University]
[L.B.L. Staff Scientist],
Mark Chow,
[B.S. (Zoology), UC Berkeley; MBA: S.F. State]
[Financial Services, Photographer],
Erik Olson,
[B.A. (logic), UC Berkeley, Teaching Credentials],
[High School teacher]
and, **John**,

who, along the years, and many a-time,
have offered a much-needed, end-of-the-day, morale booster.

Appendix E

Figure E.1: Where it began and continues...(Dedication [Front Matter])